TECHNISCHE UNIVERSITÄT MÜNCHEN
LEHRSTUHL FÜR AERODYNAMIK UND STRÖMUNGSMECHANIK

Development and Analysis of an Elasto-flexible Morphing Wing

Benoît Béguin

Vollständiger Abdruck der von der Fakultät für Maschinenwesen der Technischen Universität München zur Erlangung des akademischen Grades eines

Doktor-Ingenieurs

genehmigten Dissertation.

Vorsitzender:	Univ.-Prof. Dr.-Ing. Florian Holzapfel
Prüfer der Dissertation:	
1.	apl. Prof. Dr.-Ing. Christian Breitsamter
2.	Univ.-Prof. Dr.-Ing. Mirko Hornung

Die Dissertation wurde am 28.05.2014 bei der Technischen Universität München eingereicht und durch die Fakultät für Maschinenwesen am 06.11.2014 angenommen.

Foreword

The present work originates from my time as PhD student at the Institute of Aerodynamics and Fluid Mechanics of the Technische Universität München. I would like to thank apl. Prof. Christian Breitsamter for giving me the opportunity to work on the fascinating area of morphing wings and for being my first examiner. I appreciated his support and availability all along the project. I also acknowledge Prof. Mirko Hornung for being the second examiner, and Prof. Florian Holzapfel for being the chairman of the oral examination.
Further, I would like to thank all colleagues for the great atmosphere and the interesting technical and personal discussions we had during this time. Also, I would like to thank Wolfgang Lützenburg and his team from the institute's workshop for the realization of the wind tunnel model and for their continuous support during the numerous test campaigns. Last but not least, a big thank you to all students who did their semester projects with me.
The financial support of this work by the Deutsche Forschungsgemeinschaft is gratefully acknowledged.
I dedicate this work to my family, their inestimable support and encouragement greatly contributed to the completion of this work.

Abstract

Form-variable wings have a large potential to improve efficiency and extend mission capability of aircrafts. In this context, the present work focuses on the development and analysis of a biologically inspired morphing membrane wing made up of an articulated frame structure with an elasto-flexible membrane cover spanned on it forming the aerodynamic surface. This design allows achieving large variations of the planform and airfoil geometry to adapt the aerodynamic characteristics to varying flight conditions. While the configuration of the articulated structure determines the wing planform in terms of aspect ratio and sweep angle, the membrane cover passively adapts to the changing shape, providing thus seamless wing contour. However, the wing surface deflects under aerodynamic load and the airfoil shape is not fixed in advance but results from the fluid-structure interaction. This wing has a potential application for subsonic unmanned air vehicles.

The objectives are to determine the aerodynamic characteristics of this type of wing construction as a function of the planform configuration and membrane deformation, and to gain a detailed understanding of its aero-elastic behavior. For this, a combination of wind tunnel tests and numerical simulations is used. The wind tunnel tests are carried out with a semi-span model of the wing having a maximum span of one meter. The measurement techniques include force measurements, flow field measurements, surface flow visualization methods, and surface deflection measurements. The numerical methods include on the one hand rigid wing simulations based on potential flow modeling for the assessment of the theoretical wing characteristics as a function of the wing planform, and on the other hand two-dimensional simulations of elastic membrane airfoil sections taking into account the fluid-structure interaction for a detailed analysis of the fundamental aero-elastic behavior of the wing. For this, a self-developed code based on an analytical formulation of the membrane equilibrium coupled with the flow solver Xfoil is used.

The analysis of the membrane deformation reveals that the wing geometry (camber and thickness) is highly sensitive to the flow conditions (dynamic pressure, angle of attack, Reynolds number). Accordingly, the aerodynamic characteristics show a pronounced dependency on the flow conditions. The membrane deformation mainly leads to non-linear lift polars and delayed stall characteristics. The latter is due to the passive adaption of the wing surface to the separated flow at large angle of attack. Beside this, the effect of planform morphing on the aerodynamic characteristics at a given flow condition occurs as expected from rigid wing theory. For instance, a reduction of the aspect ratio leads to smaller lift, reduced zero-lift drag, and larger lift-dependent drag. As a result, changing the wing planform can be effectively used to shift the lift-to-drag ratio characteristics and adapt the wing performance to varying flight conditions. However, the effective aerodynamic benefit depends on the flow conditions due to the membrane deformation. In order to improve this and to provide additional control over the wing shape, several solutions are tested including a continuous variation of the membrane pre-stress, a membrane cover with increased stiffness, and a membrane cover with rigid battens. The results show that the wing shape and its aerodynamic characteristics can be effectively manipulated using a membrane cover with tailored structural properties.

Übersicht

Formvariable Flügel haben ein großes Potenzial zur Verbesserung der Effizienz und zur Erweiterung der Flugenveloppe von Flugzeugen. In diesem Kontext beschäftigt sich die vorliegende Arbeit mit der Entwicklung und Analyse einer biologisch inspirierten Flügelkonfiguration, mit der großskaligen Änderungen der Grundriss- und Profilgeometrie erreicht werden können. Der Flügel besteht aus einer Gelenkstruktur mit einer darüber gespannten elasto-flexiblen Bespannung. Während die Konfiguration der Gelenkstruktur die Grundrissgeometrie des Flügels im Hinblick auf Streckung und Pfeilung festlegt, passt sich die elasto-flexible Bespannung der Grundrissform passiv an. Damit weist der Flügel stets eine glatte Oberfläche auf. Die hohe Flexibilität der Bespannung führt darüber hinaus dazu, dass sie sich unter Last verformt. Das Flügelprofil ergibt sich somit aus der Interaktion der Bespannung mit der Umströmung. Dieser Flügel hat eine potenzielle Anwendung für unbemannte Flugzeuge.

Die Ziele dieser Arbeit sind einerseits die Bestimmung der aerodynamischen Eigenschaften dieses Flügelkonzeptes als Funktion der Grundrisskonfiguration und der Membranverformung, und andererseits die Gewinnung eines fundierten Verständnisses zu dessem aero-elastischen Verhalten. Die Untersuchungen basieren auf einer Kombination von Windkanalversuchen und numerischen Simulationen. Die Windkanaluntersuchungen wurden an einem Halbflügelmodell mit einer maximalen Spannweite von einem Meter durchgeführt. Die experimentellen Methoden umfassen Kraftmessungen, Strömungsfeldmessungen, Oberflächenströmungsvisualisierung und Deformationsmessungen. Die numerische Methoden umfassen potentialströmungsbasierte Berechnungen zur Untersuchung der theoretischen Eigenschaften des Flügels als Funktion der Grundrissgeometrie sowie zwei-dimensionale Simulationen von elastischen Membranflügelprofilen unter Berücksichtigung der Fluid-Struktur-Interaktion. Dafür kommt ein selbstentwickeltes Verfahren zum Einsatz, das auf einem mit dem Strömungslöser Xfoil gekoppelten analytischen Modell der Membranstruktur basiert.

Die Analyse der Membranverformung zeigt, dass Wölbung und Dicke des Flügels stark von den Anströmbedingungen (Staudruck, Anstellwinkel, Reynoldszahl) abhängen. Dementsprechend weisen die aerodynamischen Eigenschaften eine ausgeprägte passive Staudruckabhängigkeit auf. Im Wesentlichen führt die Verformung der Flügeloberfläche zu nicht-linearen Auftriebspolaren sowie zu verzögertem und milderem Ablöseverhalten. Letzteres ist auf die passive Adaption der Flügelkontur an die abgelöste Strömung zurückzuführen. Trotz der ausgeprägten Staudruckabhängigkeit bewirkt die aktive Änderung des Flügelgrundrisses die erwartete Beeinflussung der aerodynamischen Eigenschaften. Konfigurationen mit kleiner Streckung weisen vergleichsweise einen kleineren Auftriebsanstieg, einen kleineren Nullwiderstand und einen größeren auftriebsinduzierten Widerstand auf. Dadurch wird eine Gleitzahlanpassung ermöglicht. Die jeweilige Effizienzsteigerung gegenüber einem grundrissgleichen Starrflügel hängt jedoch stark von der Verformung der Flügeloberfläche ab. Um dies zu verbessern und eine größere Kontrolle über die Flügelgeometrie zu ermöglichen, wurden verschiedene Methoden betrachtet. Eine kontinuierliche Veränderung der Membranvorspannung, eine modifizierte Bespannung mit erhöhter Steifigkeit und eine modifizierte Bespannung mit integrierten Versteifungselementen wurden getestet. Die Ergebnisse zeigen, dass die Eigenschaften des Flügels durch eine maßgeschneiderte Gestaltung der Bespannung effektiv beeinflusst werden können.

Résumé

Les ailes à géométrie variable ont un grand potentiel pour améliorer l'efficacité des aéronefs et étendre leur enveloppe de vol. Dans ce contexte, le présent travail porte sur le développement et l'analyse d'un concept d'aile bionique basé sur l'utilisation d'une membrane élastoflexible tendue sur une structure articulée. La configuration de la structure articulée détermine la géométrie plane de l'aile en termes d'allongement et d'angle de flèche. La voilure élastoflexible s'adapte naturellement au contour imposé par la structure, confèrant ainsi une surface aérodynamique lisse.

Les objectifs de ce travail sont de déterminer les caractéristiques aérodynamiques de l'aile en fonction de sa configuration et de comprendre de manière détaillée son comportement aéroélastique, en particulier d'étudier l'effet de la déformation de la voilure sur ses performances. L'étude est basée d'une part sur des tests en soufflerie et d'autre part sur des simulations numériques. Les tests en soufflerie sont effectués sur un modèle de l'aile ayant une envergure maximale de un mètre. Les méthodes expérimentales comprennent des mesures de force, des mesures de champs de vitesses, de la visualisation d'écoulement de surface et des mesures de déformation par stéréophotogrammétrie. Les méthodes numériques comprennent d'une part des simulations basées sur la méthode potentielle pour étudier de manière théorique les caractéristiques de l'aile, et d'autre part des simulations aéroélastique de profils pour l'étude plus fondamentale de son comportement.

L'analyse de la déformation de la voilure révèle que la cambrure et l'épaisseur de l'aile sont très sensibles aux conditions d'écoulement (vitesse, angle d'incidence et nombre de Reynolds). Par conséquent, les caractéristiques aérodynamiques de l'aile dépendent fortement de la vitesse de l'écoulement. En particulier, la déformation de la voilure provoque des non-linéarités dans les courbes de portance ainsi qu'un décrochage retardé. Ce dernier est dû à l'adaptation passive de la voilure lorsque l'écoulement décroche à haute incidence. Afin de limiter la dépendance passive des performances de l'aile et de mieux pouvoir contrôler sa géométrie, il est nécessaire de modifier les propriétés de la voilure élastoflexible. Par exemple, une régulation continue de la précontrainte de la voilure et des modifications plus fondamentales de sa structure telles qu'une modification locale de sa rigidité montrent qu'il possible de contrôler les performances de l'aile. Concernant l'influence de la configuration plane de l'aile, les résultats montrent que celle-ci provoque bel et bien l'effet attendu sur la portance et la traînée. Par conséquent, la variation de la configuration permet d'ajuster la finesse de l'aile à différentes conditions de vol et optimiser son efficacité aérodynmique.

Contents

List of Figures

List of Tables

Nomenclature

Latein symbols	**Description**	**Units**
$Æ$	aspect ratio	-
b	wing span	m
C_D	drag coefficient	-
C_f	skin friction coefficient	-
C_L	lift coefficient	-
C_l	section lift coefficient	-
C_m	pitching moment coefficient	-
C_p	pressure coefficient	-
c	chord length	m
$\bar{c}$	mean chord length	m
c_r	root chord length	m
D	drag force	N
E	endurance	s
E_m	membrane elasticity modulus	Pa
e_s	span efficiency factor	-
F_T	engine thrust	N
F_x	force in the x direction	N
F_y	force in the y direction	N
F_z	force in the z direction	N
f	airfoil camber	m
g	gravity constant	m^2s^{-1}
h	focal length	m
K_m	pre-stress to dynamic pressure ratio	-
K	lift-dependent drag factor	-
L	lift force	N
l	section lift	Nm^{-1}
m	pitching moment	Nm
O	perspective center	
P	object point	
q_∞	free-stream dynamic pressure	Pa
Re	Reynolds number	-
R	range	m
$\mathbf{R}$	rotation matrix	

r	turn radius	m
S	wing area	m^2
s	camber line	m^2
T	membrane tension	Nm^{-1}
t	thickness	m
U_∞	free stream velocity	ms^{-1}
u	velocity component in x	ms^{-1}
V	flight speed	ms^{-1}
v	velocity component in y	ms^{-1}
W	aircraft weight	N
w	velocity component in z	ms^{-1}
x	coordinate in chordwise direction	m
x_{ac}	aerodynamic center	m
x_f	location of the maximum camber	m
x_t	location of the maximum thickness	m
y	coordinate in spanwise direction	m
z	vertical coordinate	m

Greek symbols	**Description**	**Units**
α	angle of attack	$^\circ$
β	wing twist	$^\circ$
Γ	circulation	m^2s^{-1}
γ	section circulation	ms^{-1}
δ	boundary layer displacement thickness	m
ε	strain	$^\circ$
θ	polar coordinate	$^\circ$
λ	taper ratio	-
ν	kinematic viscosity	m^2s^{-1}
ξ	leading-edge spar tilt angle	$^\circ$
ρ	air density	kgm^{-3}
σ	stress	Pa
ϕ	sweep angle	$^\circ$
Ω	parameter of the articulated wing structure	$^\circ$
ω	vorticity	s^{-1}

1 Introduction

1.1 Form-variable aircrafts

The close relation between the geometry of an aircraft and its flight performance is a major issue in aircraft design. In fact, a given configuration is associated with a unique set of aerodynamic characteristic values and, consequently, with a single flight condition with optimal performance. The only way to overcome this is to provide the airframe with the capability of modifying its outer shape during flight. For this reason, the development of form-variable aircraft structures plays an important role since the beginning of aviation history (Weisshaar et al. [1], Vasista et al. [2]).

The most common form-variable technologies encountered in current aircraft designs are high-lift devices and variable sweep wings. The deployment of high lift devices effectively extends the flight envelope in the low speed range by allowing the airplane to fly at velocities below the stall speed of the cruise configuration. In contrast, variable sweep wings are used to extend the flight envelope in the upper range of flight speeds by mitigating drag divergence at supersonic speeds. Beside these two well established technologies, a large number of research programs were and are concerned with the development of advanced form-variable structures to further improve efficiency and extend mission capability of aircrafts. The Mission Adaptive Wing (MAW) developed in the 1980's in frame of the joint U.S Air Force/NASA/Boeing Advanced Fighter Technology Integration research program (AFTI) is a well known example (cf. Fig. 1.1). In addition to variable sweep, the MAW features variable camber capability which allows the wing to take a large cambered airfoil for subsonic speed, a supercritical airfoil for transonic speed and a symmetric airfoil for supersonic speed (Gilbert [3], Smith et al. [4]). Flight tests with a modified version of the F-111 fighter aircraft demonstrated significant performance improvements by minimizing penalties at off-design conditions compared to the baseline wing (Hardy et al. [5]). However, the complexity and additional weight associated with the MAW made it not viable for commercial applications at this time.

More recently, the NASA's Morphing Program was a large platform which concentrated on the development of a broad range of technologies to enable efficient and multi-point adaptability in flight vehicles (Wlezien et al. [6], McGowan et al. [7]). Several advanced multi-functional adaptive structures such as Distributed Shape Change Effector Array (Raney et al. [8], [9]) were considered. Also, biologically inspired form-variable aircraft structures played an important role in this program (McGowan et al. [10]). In the field of civil aviation, the European AWIATOR research program (Aircraft Wing with Advanced Technology Operation, 2002-2007) was concerned with the integration of advanced technologies into existing transport aircraft configurations. As part of this program, the aerodynamic effect of adaptive mini trailing-edge

devices (Mini-TEDs) was investigated (Richter et al. [11], Dargel et al. [12]). Wind tunnel and flight tests carried out with the Airbus A340 transport aircraft including Mini-TEDs in form of adaptive mini split-flaps showed improved maximum lift and maximum lift-to-drag ratio. Also in the field of civil aviation, a recent example illustrating the integration of extended form-variable capability into conventional configurations is given by the new Airbus A350 aircrafts. The wings are equipped with adaptive dropped-hinge trailing-edge flaps which are not uniquely used to provide high-lift capability at take-off and landing but also to adjust the wing camber during flight for a better control of the load distribution and improved overall aerodynamic efficiency (Criou [13]).

A large number of works are also dealing with the development of form-variable structures for the replacement of conventional control surfaces by a single deformable structure. The main goal is to avoid inefficiencies due to discontinuities and gaps. For instance, the concept of "active aero-elastic wings" based on aerodynamically induced wing twist to provide roll control is discussed by Pendelton [14]. This technology has been applied in frame of the joint U.S Air Force/Boeing/NASA Active Aeroelastic Wing flight research program (AAW, 1996-2005). Flight tests with the X-53 experimental aircraft, a modified version of the F/A-18, demonstrated improved performance due to the reduced weight as well as improved aircraft roll control compared to the baseline wing design (Pendelton et al. [15]). Further studies focus on wing twist actuated by an internal mechanism instead of using the aerodynamic forces (Pecora et al. [16], Khot et al. [17]). Hingeless flaps, based on the deformation of a compliant structure as illustrated in Fig. 1.2, are also the subject of several investigations (Monner et al. [18], Gandhi et al. [19]). Aerodynamic benefits such as delayed laminar to turbulent transition, larger maximum lift, and increased control effectiveness compared to conventional control surfaces were already demonstrated in several studies (Breitsamter [20], Hetrick et al. [21]).

The broad spectrum of advanced form-variable wing technologies mentioned so far are mainly based on the extension of existing configurations. In parallel to this, a large amount of resources is spent for the development of radically new form-variable aircraft configurations (Rodriguez [23], Thill et al. [22]). Such developments are mainly related to unmanned air vehicle (UAV) and micro air vehicle (MAV) applications. Although the large potential lying in such new designs is obvious from the aerodynamic point of view, technical realizations are still a critical issue because state-of-the-art technologies are not sufficient (Moorhouse et al. [24], Valasek [25]). The Next Generation Morphing Aircraft Structures research program (N-MAS), a joint Defense Advanced Research Projects Agency/U.S Air Force project, focused on the development of morphing UAVs capable of radical shape changes for multi-mission capability (Bowmann [26]). The two morphing aircrafts developed in frame of this program are the Morphing Flight-vehicle Experiment (MFX) and the Z-wing concepts (cf. Fig. 1.3). The wings of the MFX concept are based on an articulated truss structure combined with a flexible skin material to achieve large variation of the wing planform shape (Flanagan et al. [27]). Flight tests conducted in 2006 demonstrated in-flight shape changing capability. The Z-wing is based on a vertical folding of the wings to achieve radical configuration changes. At this stage, wind tunnel tests were conducted to assess the functionality of the complex wing structure under real

aerodynamic loads (Ivanco et al. [28]).
In the field of micro air vehicles, biologically inspired adaptive configurations are playing an important role. The main reason for this is that MAVs operate at conditions similar as natural flyers. In particular, low Reynolds number aerodynamics and unsteady flow environment resulting from atmospheric turbulence are typical characteristics of the conditions to which MAVs are subjected. In Abdulrahim [29] and Grant et al. [30], gull-like morphing MAV configurations using multiple-joint structures are considered to achieve large geometry changes (cf. Fig. 1.4). Flight tests demonstrated net effects of the morphing on the flight performance values such as climb angle, glide angle, stall characteristics, turning capabilities, and crosswind rejection. In addition to this, several studies have shown that aero-elastic effects resulting from the inherent flexibility of the wing structure of natural flyers play an important role in their outstanding flight performance (Song et al. [31], Waldmann et al. [32], Hu et al. [33], and Shyy et al. [34]). Mainly, the passive shape adaption to varying flow conditions and to atmospheric turbulences acts like a natural flow control mechanism delaying stall and providing enhanced longitudinal stability. In order to provide MAVs with similar features, several concepts are based on wing structure made out of a thin flexible membrane (Waszak et al. [35], Hays et al. [36], and Yongsheng et al. [37] , [38]).
Beside their recent application for MAVs, membrane wings were already considered in past developments for their adaptivity and lightweight characteristics. For instance, several institutions were involved in the development of wings based on the “double membrane sailwing” concept consisting of a rigid leading-edge spar, a trailing-edge wire, and a fabric cover stretched between them (cf. Fig. 1.5). In addition to the lightweight and the simple construction, results from several investigations showed that this type of wing features good aerodynamic characteristics. It was therefore considered as a competitive alternative to conventional wings for low speed applications (Maughmer et al. [39], Fink [40]). The tension of the trailing-edge wire and the structural properties of the fabric can be used to control several geometric and aerodynamic properties of the wing (Muray et al. [41], [42]).

In this context, the present work deals with the development and analysis of a biologically inspired adaptive membrane wing for subsonic UAV applications. The particularity of the concept investigated here is that it allows for large changes in both the wing configuration and the camber. A description of the concept is given in the next section.

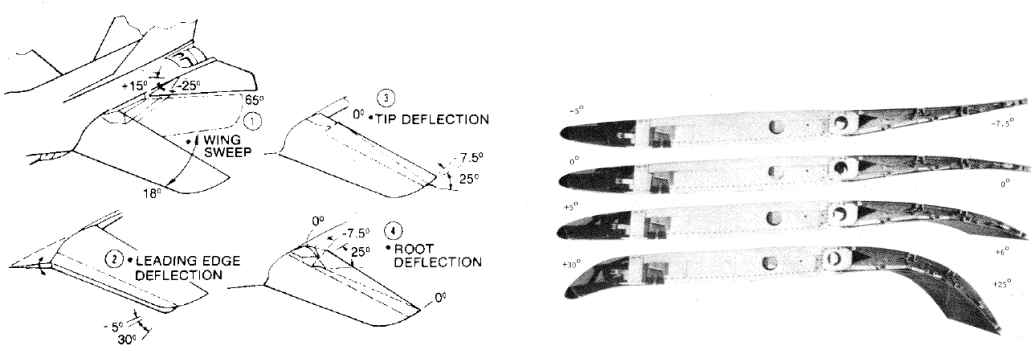

(a) Variable geometry functions (b) Defected wing shapes

Figure 1.1: Illustration of the AFTI F-111 Mission Adaptive Wing [3].

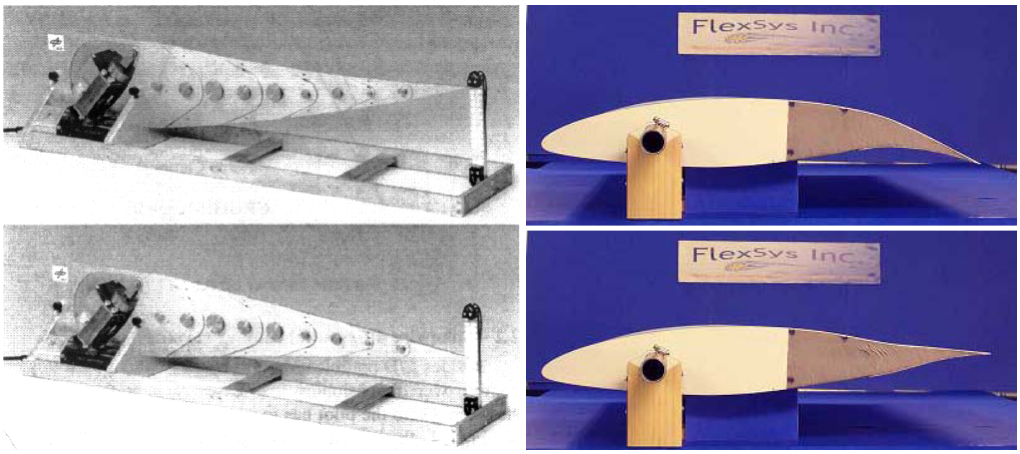

(a) Monner et al. [18] (b) Hetrick et al. [21]

Figure 1.2: Hingeless flaps concepts for variable camber trailing-edge.

(a) MFX morphing UAV [27] (b) Z-wing UAV [28]

Figure 1.3: Morphing UAVs from the N-MAS program.

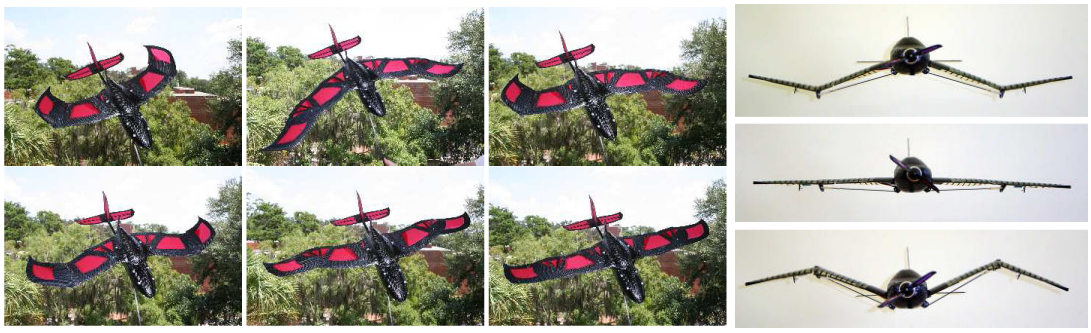

(a) Multiple-joint variable-sweep wing [30] (b) Variable twist and gull wing [29]

Figure 1.4: Biologically inspired morphing MAVs.

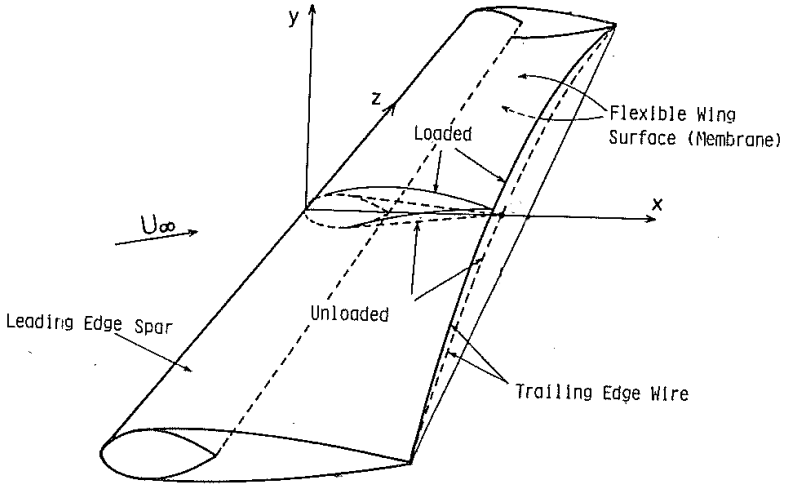

Figure 1.5: Double membrane sailwing [41].

1.2 Scope of the present work

1.2.1 Elasto-flexible morphing wing concept

The present work deals with the development and analysis of an adaptive wing for lightweight subsonic UAV application. The concept proposed here, described as the "elasto-flexible morphing wing", is illustrated in Fig. 1.6. It consists of an articulated inner structure with an elasto-flexible membrane cover spanned on it forming the actual aerodynamic surface. This particular wing construction is inspired from the wing of a pterosaur (Padian [43]). Although this is still a strongly disputed conclusion among the paleontologists, the survival of these flying reptiles over millions of years (late Triassic to the end of the Cretaceous Period, 220 to 65 million years ago) is believed to be due to their outstanding flight capabilities (Wilkinson [44], McMasters [45]). The fact is that fossils of these flying reptiles indicate that the wing skin was invested with a dense array of fibers, which could have played a role in the adaption of the wing shape. However, the purpose of the present work is to develop a technical application based on the main structure of this paragon rather than the reproduction of a real pterosaur wing. The combination of large planform variation with an elasto-flexible wing surface represents a unique and not yet explored adaptive wing design.

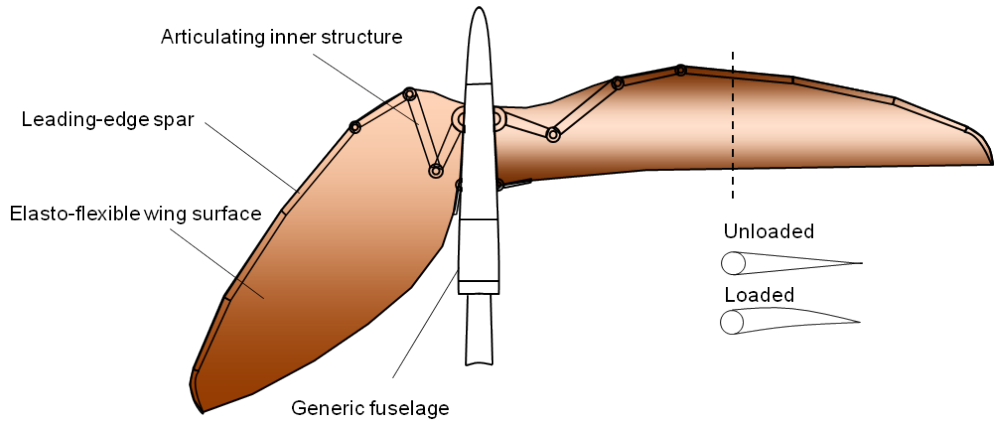

Figure 1.6: Sketch of the elasto-flexible morphing wing concept [65].

The articulated inner structure consists of four segments described as the upper arm, the lower arm, the hand, and the long finger per analogy to the biological paragon. The configuration of the structure determines the planform geometry of the wing which can be continuously changed between a wing with a large span and no sweep, and wing with a shorter span and large sweep angle. Compared to a simpler sweep wing with a single joint at the root, the present design offers a larger flexibility to adjust the wing planform. For instance, an independent variation of the wing span and sweep angle can be realized. The planform variation aims to alter the aerodynamic characteristics and adapt the performance to varying mission requirements. Indeed, configurations with large span are known to be advantageous for mission segments requiring long endurance, whereas configurations with small span are rather advantageous for mission segments requiring larger flight speed [46]. Further, the articulated structure can also be used to twist the wing for control purpose.

The elasto-flexible membrane used for the wing surface adapts passively to the planform shape imposed by the articulated structure, providing thus seamless wing contour. To achieve this with reasonable actuation force, a highly elastic membrane material is required. However, due to this property, the wing surface is expected to deflect under aerodynamic loading, and, thus, the airfoil shape is not determined in advance as for a conventional rigid wing but results from the interaction between the membrane and the surrounding airflow. The structural design of the membrane cover is therefore a critical aspect of this wing concept. In a first investigation stage, the wing characteristics resulting from the purely passive adaption of the wing surface to varying flow conditions are focused on. In a more advanced concept stage, advantage can be taken of the flexibility of the wing surface to control the camber using battens and actuators integrated in the wing surface.

1.2.2 Objectives and methods of investigation

The main objectives of the present work are on the one hand to obtain a comprehensive database of the aerodynamic characteristics of the wing as a function of the planform geometry, membrane deformation, and cover design, and on the other hand to gain a detailed understanding of its aero-elastic behavior. To achieve these objectives, a combination of wind tunnel tests and numerical simulations is used.

The wind tunnel tests are carried out with a generic semi-span model of the wing having a maximum span of one meter. The experimental techniques include force measurements, particle image velocimetry, surface flow visualization, and surface deflection measurements by stereo-photogrammetry. The force measurements are used to obtain a comprehensive database of the aerodynamic characteristics of the longitudinal motion and assess the global wing performance. The particle image velocimetry measurements are used to measure the flow field in the near wake of the wing with the main goal to analyze the spanwise load distribution which can be derived from the velocity field. The surface flow visualization techniques include wool tufts method to analyze the flow separation, and microphone probe experiments to detect the laminar to turbulent transition of the boundary layer. Finally, the surface deformation measurements are used to analyze the deflected wing shapes as a function of the aerodynamic load. In particular, the correlation of the deflected wing geometry with the aerodynamic characteristics obtained from the force measurements allows for a detailed analysis of the aero-elastic behavior of the wing. The wind tunnel model, the experimental techniques, and the test conditions are described in chapter 2.

The numerical investigations carried out in this work include rigid wing simulations to obtain a theoretical database showing the influence of the planform geometry on the wing characteristics as well as simulations taking into account the fluid-structure interaction for the detailed analysis of the aero-elastic wing behavior. The rigid wing simulations are based on potential flow modeling. The fluid-structure simulations concentrate on the investigation of two-dimensional elastic membrane airfoils representing a section of the wind tunnel model. The method used for this is based on an analytical formulation of the membrane equilibrium coupled with the flow solver Xfoil. The numerical techniques are described in chapter 3.

1.3 Theoretical background

This section provides theoretical background information in aerodynamics and flight mechanics to present the relations existing between the geometry of a wing, its aerodynamic characteristics, and the flight performance of the aircraft. The theory presented in the following is based on Refs. [46], [47], and [48].

1.3.1 Wing geometry definitions

The geometry of a wing can be characterized by a set of parameters describing its planform and its out-of-plane geometry. Figure 1.7 illustrates a generic wing planform. It is defined by the planform area, S, the wing span, b, the chord length distribution along the span, $c(y)$, and the sweep angle distribution, $\phi_{1/4}(y)$, measured at the quarter chord line. The aspect ratio of the wing is defined as $AR = b^2/S$, the mean chord length as $\bar{c} = S/b$, and the taper ratio as $\lambda = \frac{c_t}{c_r}$.

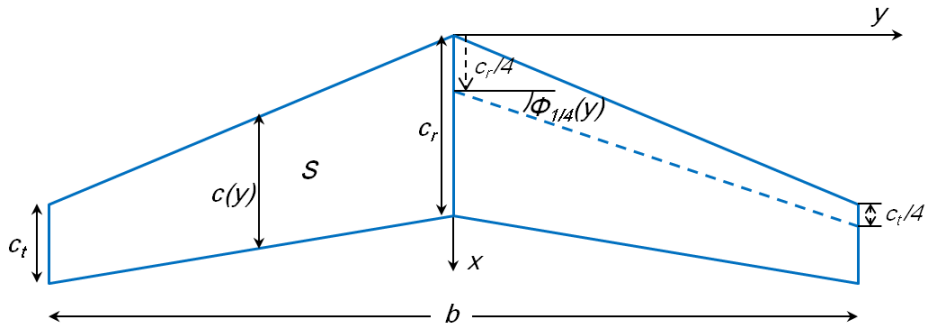

Figure 1.7: Generic wing planform and the parameters associated with it.

The out-of-plane geometry is determined by the airfoil shape and by the twist distribution. As illustrated in Fig. 1.8, the airfoil shape is described by the camber line, $s(x)$, and the thickness distribution, $t(x)$. The main geometric parameters associated with the airfoil are the maximum camber, f, the maximum thickness, t, and the locations along the chord at which the maxima occur, x_f and x_t, respectively. The wing twist, $\beta(y)$, is defined as the orientation of the chord line at a given spanwise section relative to the chord line of the root section as illustrated in Fig. 1.9.

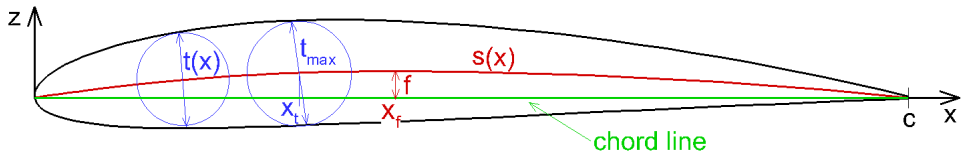

Figure 1.8: Description of the geometry of an airfoil.

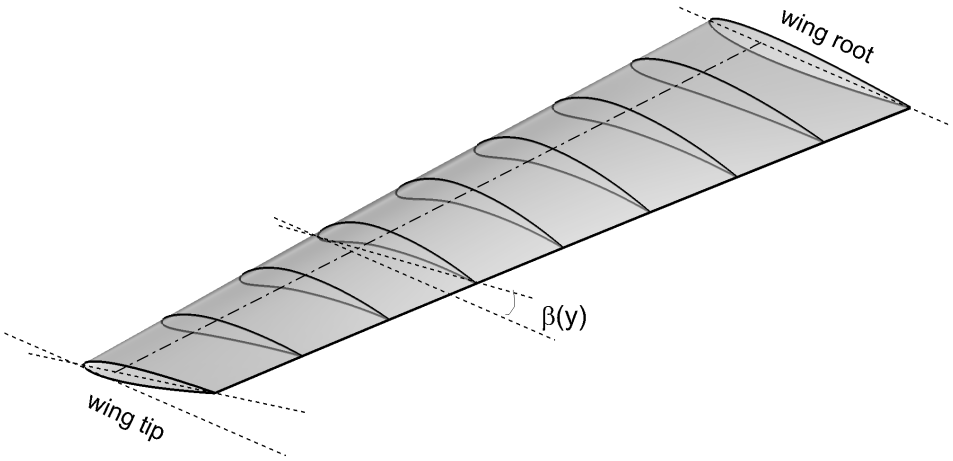

Figure 1.9: Example of a three-dimensional wing shape with spanwise varying airfoil shape and twist.

1.3.2 Overview of aerodynamics

The discussion presented here about the aerodynamic characteristics of wings is limited to the longitudinal motion according to the investigations performed in this work. The forces and moments associated with the longitudinal motion are the lift force, L, the drag force, D, and the pitching moment, m (cf. Fig. 1.10). They depend mainly on the angle of attack, α, and the free-stream velocity, U_∞. Further, the aerodynamic forces and moments are usually expressed in dimensionless coefficient form, allowing for a more fundamental description of the aerodynamic characteristics than the absolute values. The definitions of the lift, the drag, and the pitching moment coefficients are given in Eqs. 1.1.

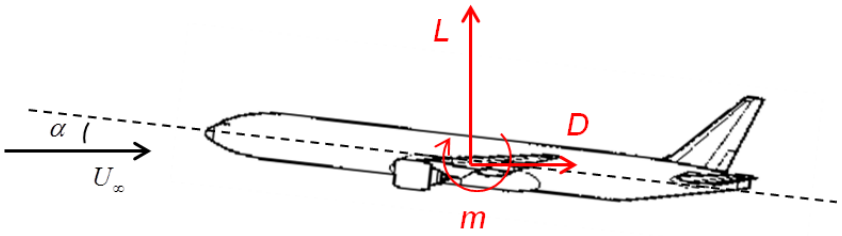

Figure 1.10: Illustration of the aerodynamic forces, moment, and principal degrees of freedom associated with the longitudinal motion of an aircraft.

$$\begin{aligned} C_L &= \frac{L}{\frac{1}{2}\rho U_\infty^2 S} \\ C_D &= \frac{D}{\frac{1}{2}\rho U_\infty^2 S} \\ C_m &= \frac{m}{\frac{1}{2}\rho U_\infty^2 S\bar{c}} \end{aligned} \tag{1.1}$$

1.3.2.1 Lift distribution

Before the lift, drag and pitching moment characteristics of the wing are discussed, the concept of spanwise lift distribution is introduced. The lift distribution, $l(y)$, indicates the lift per unit span produced by each airfoil section along the span. It is a fundamental aspect of the aerodynamic characteristics of a wing because on the one hand, it influences the aerodynamic efficiency in terms of the production of vortex-induced drag (cf. section 1.3.2.4), and on the other hand, it determines the aerodynamic load (bending moment) on the wing structure. Figure 1.11 illustrates the generic shape of a lift distribution, which usually has its maximum near or at the wing root and tends to zero at the wing tips due to the pressure balance between upper and lower wing surfaces occurring there. The relation between the lift distribution and the total lift force, L, is given by Eq. 1.2.

$$L = \int_{-b/2}^{b/2} l(y)dy \tag{1.2}$$

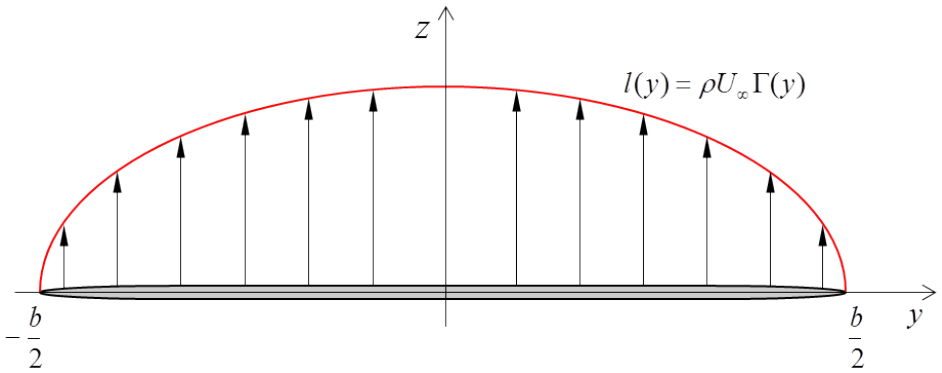

Figure 1.11: Illustration of the generic shape of a lift distribution.

The theoretical aspects related to the lift distribution can be analyzed by using Prandtl's lifting line theory associated with planar wings (i.e. no camber and no twist). In frame of this theory, the vorticity generated by a planar wing of finite span is modeled by a planar vortex sheet composed of horseshoe vortices attached to the wing surface as illustrated in Fig. 1.12. In this model, the sum of the bound vortices leads to the circulation distribution $\Gamma(y)$, which is related to the lift distribution by the Kutta-Joukowski theorem as indicated in Eq. 1.3. Further, the circulation $\Gamma(y)$ is related to the strength of the trailing vortex sheet, $\gamma(y)$, as indicated by Eq. 1.4. This

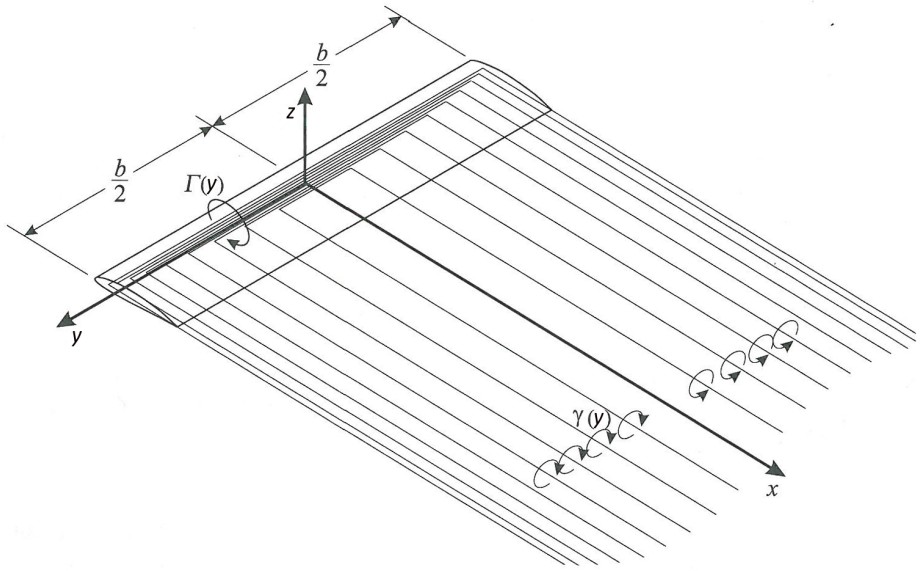

Figure 1.12: Prandtl's model for the bound vorticity and the trailing vortex sheet generated by a wing of finite span [48].

theoretical result is important because it indicates that the lift distribution can be determined from the strength of the trailing vortex sheet, which is a quantity that can be experimentally determined from flow field measurements in the near wake of the wing (Hubel [49]).

$$l(y) = \rho U_\infty \Gamma(y) \tag{1.3}$$

$$\gamma(y) = \frac{d\Gamma(y)}{dy} \tag{1.4}$$

Prandtl's lifting line theory predicts that optimal aerodynamic performance in terms of minimum vortex-induced drag is obtained with an elliptical lift distribution. As a result, the elliptical lift distribution serves as a reference in aerodynamic studies and its comparison with the lift distribution associated with a given wing is a measure of the aerodynamic efficiency in terms of vortex-induced drag production. A criterion for this is given by the span efficiency factor, e_s, which measures the harmonic distortion of $l(y)$ compared to a pure ellipse. The definition of e_s is given by Eq. 1.5, where the coefficients l_n are the coefficients of the Fourier sine series representation of $l(y)$ given in Eq. 1.6. These coefficients can be computed by Eq. 1.8 with the coordinate transformation given in Eq. 1.7. In the elliptical case, only the coefficient l_1 is non-zero and the span efficiency factor is equal to one. For other distributions, the series contains also non-zero coefficients for $n > 1$ and, consequently, the span e_s is smaller than one.

$$e_s = \frac{l_1^2}{\sum_{n=1}^{\infty} n l_n^2} \tag{1.5}$$

$$l(y) \rightarrow l(\theta) = \sum_{n=1}^{\infty} l_n sin(n\theta) \tag{1.6}$$

$$y = \frac{b}{2} cos(\theta) \tag{1.7}$$

$$l_n = \int_{-\pi}^{\pi} l(\theta) sin(n\theta) d\theta \tag{1.8}$$

For analysis purposes, the spanwise distribution of the aerodynamic load can be represented by the $C_l c(y)$ distribution, which is obtained by dividing $l(y)$ by the free-stream dynamic pressure as indicated in Eq. 1.9. This distribution is interpreted as the product of the local lift coefficient $C_l(y)$ times the local chord length $c(y)$. The fact that $C_l c(y)$ does not depend on the flow conditions makes it more suitable for a fundamental description of the dependency of the lift distribution on the wing geometry. Finally, the total lift coefficient is related to the $C_l c(y)$ distribution by the relation given in Eq. 1.10.

$$C_l c(y) = \frac{l(y)}{\frac{1}{2}\rho U_\infty^2} = \frac{2\Gamma(y)}{U_\infty} \tag{1.9}$$

$$C_L = \frac{1}{S} \int_{-b/2}^{b/2} C_l c(y) dy \tag{1.10}$$

The shape of the lift distribution is practically influenced by all aspects of the wing geometry (planform and out-of-plane geometry). In the case of planar wings, i.e. without camber or twist, the shape of the lift distribution and the span efficiency factor are independent of the angle of attack. This is not true anymore in the presence of twist or with varying camber along the span, in which case e_s can show a significant dependency on α. In the following, the theoretical dependency of the lift distribution and of the span efficiency factor on the principal parameters of the wing planform are discussed. For this, results from simulations of planar wings with trapezoidal planforms and varying aspect ratio, sweep angle and taper ratio based on potential flow modeling (vortex lattice method, cf. section 3.1) are used.

The influence of the taper ratio (λ) for wings with no sweep (i.e. $\phi = 0$) and an aspect ratio of 10 is shown in Fig. 1.13a. Decreasing λ leads to a larger aerodynamic loading at the wing root and lower aerodynamic loading at the wing tip. The span efficiency factor (cf. Fig. 1.13b) decreases with increasing aspect ratio and is maximum for λ values around 0.4.

The influence of the sweep angle on the lift distributions for wings with an aspect ratio of 10 and a taper ratio of 0.4 is shown in Fig. 1.14a. An increase of the sweep angle leads to a lower loading at the wing root and a larger loading at the wing tip. The influence of the sweep angle on the span efficiency factor for different aspect ratios and constant taper ratio of $\lambda = 0.4$ is shown in Fig. 1.14b. This diagram predicts that the highest values of e_s are reached for sweep angles between 0° and 10° depending on the aspect ratio.

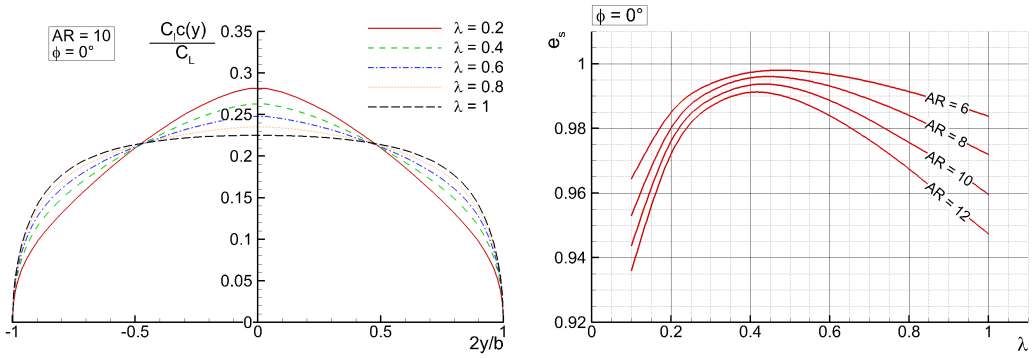

(a) (b)

Figure 1.13: Effect of λ and $\mathcal{AR}$ on the lift distributions and the span efficiency factor (planar trapezoidal wings with $\phi = 0^{\circ}$).

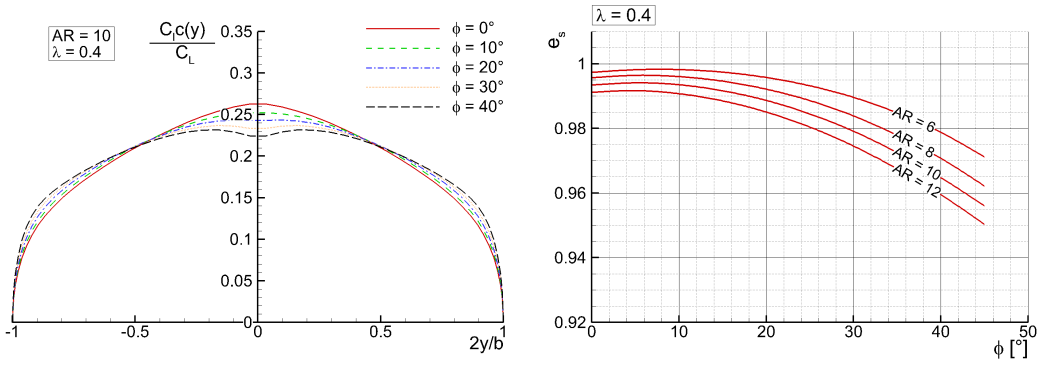

(a) (b)

Figure 1.14: Effect of ϕ and $\mathcal{AR}$ on the lift distributions and the span efficiency factor (planar trapezoidal wings with $\lambda = 0.4$).

1.3.2.2 Lift polar

The lift polar represents the dependency between the lift force and the angle of attack, $C_L(\alpha)$. The general shape of a lift polar is illustrated in Fig. 1.15a. For a rigid wing, the lift coefficient varies linearly with the angle of attack in the attached flow regime and the lift polar is represented by the linear relation given in Eq. 1.11. The fundamental aerodynamic parameters associated with the lift characteristics of a wing are the slope of the lift curve, $C_{L,\alpha}$ and the zero-lift angle of attack, α_0. The lift coefficient at $\alpha = 0$, C_{L0} is a further relevant parameter associated with the lift polar. It is dependent on $C_{L,\alpha}$ and α_0 as indicated in Eq. 1.11. At some larger angle of attack, the lift curve is no more linear due to flow separation, and the lift begins to decrease (stall). The maximum lift coefficient, C_{Lmax}, and the angle of attack at which it occurs, α_{max}, are two further parameter associated with the lift polar.

$$C_L = C_{L,\alpha}(\alpha - \alpha_0) = \underbrace{C_{L0}}_{-C_{L,\alpha}\alpha_0} + C_{L,\alpha}\alpha \quad (\alpha < \alpha_{max}) \tag{1.11}$$

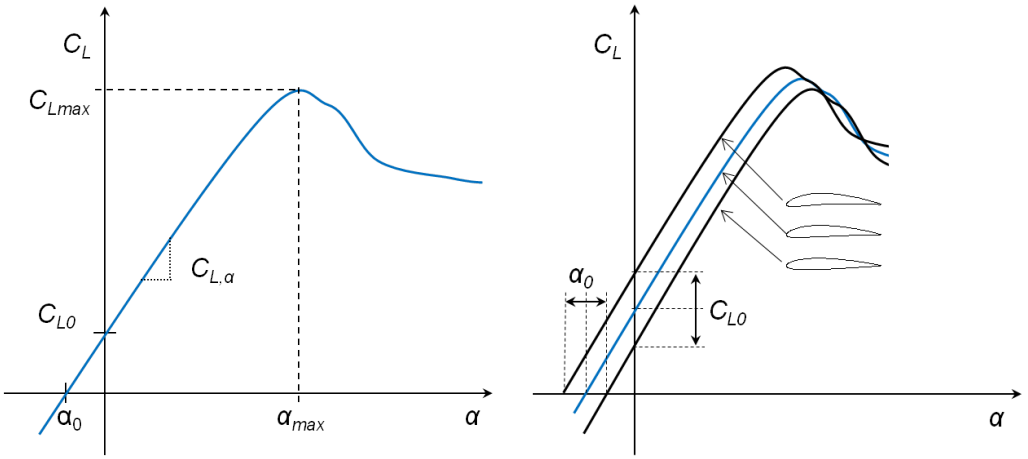

(a) Sketch of a lift polar

(b) Effect of the camber on α_0 and C_{L0}

Figure 1.15: Illustration of a lift polar.

The zero-lift angle of attack, α_0, is essentially a function of the out-of-plane geometry of the wing (camber and twist). The qualitative dependency of α_0 and C_{L0} on the camber illustrated in Fig. 1.15b and shows that C_{L0} increases with increasing camber. The slope of the lift curve ($C_{L,\alpha}$) is mainly influenced by the planform shape of the wing. Figure 1.16 presents the theoretical dependency of $C_{L,\alpha}$ on the wing planform. The values shown here come from vortex lattice simulations (cf. section 3.1). Both diagrams show that $C_{L,\alpha}$ decreases with decreasing aspect ratio. Figure 1.16a shows that the influence of λ is rather weak but nevertheless, $C_{L,\alpha}$ exhibits an optimum for taper ratios between 0.2 and 0.4 depending on the aspect ratio. Figure 1.16b shows that the sweep angle has a significant influence on $C_{L,\alpha}$. Indeed, the lift curve slope decreases with increasing sweep angle.

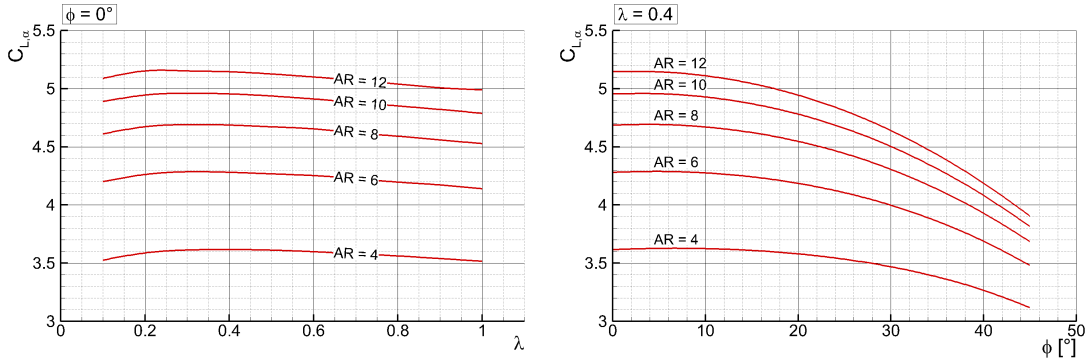

(a) Effect of λ and $\mathcal{AR}$ with $\phi = 0^\circ$

(b) Effect of ϕ and $\mathcal{AR}$ with $\lambda = 0.4$

Figure 1.16: Theoretical dependency of the lift curve slope on the principal parameters of the planform geometry (planar trapezoidal wings).

1.3.2.3 Pitching moment and aerodynamic center

Figure 1.17a shows the generic shape of the pitching moment characteristics of a wing (C_L vs. C_m plot). For rigid wings, the pitching moment is a linear function of the lift coefficient prior

to flow separation (i.e. for $C_L < C_{Lmax}$) and is modeled by the linear relation given in Eq. 1.12. The parameters associated with the pitching moment characteristics are therefore the pitching moment at zero lift, C_{m0}, and the slope of the curve, $\frac{dC_m}{dC_L}$.

$$C_m = C_{m0} + \frac{dC_m}{dC_L} C_L \quad (C_L < C_{Lmax}) \tag{1.12}$$

$$\frac{(x_{ac} - x_{ref})}{\bar{c}} = -\frac{dC_m}{dC_L} \tag{1.13}$$

The value of C_{m0} depends principally on the out-of-plane geometry of the wing. A wing with a positive camber is generally associated with negative values of C_{m0} and vice versa. In contrast, the slope is principally influenced by the planform shape. However, it also depends on the position x_{ref} where the pitching moment is measured. As illustrated in Fig. 1.17b, a particular value of x_{ref} is the position where the pitching moment is independent of C_L, i.e. $\frac{dC_m}{dC_L} = 0$ and C_m takes a constant value equal to C_{m0}. This particular position is defined as the aerodynamic center, x_{ac}, and represents the limit where the slope of the pitching moment characteristics changes its sign. If the pitching moment characteristics are known at an arbitrary reference position x_{ref}, the position of the aerodynamic center relative to x_{ref} can be calculated using the relation given in Eq. 1.13. The aerodynamic center is an important aerodynamic parameter of a wing for the study of the longitudinal stability of an aircraft.

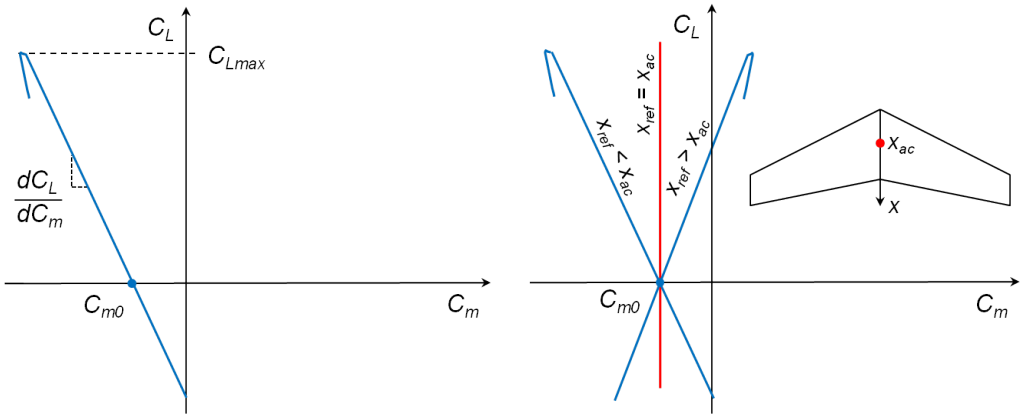

(a) Sketch of the pitching moment characteristics

(b) Dependency of the slope on the reference position

Figure 1.17: Illustration of the pitching moment characteristics.

The position of the aerodynamic center is influenced mainly by the planform shape of the wing. Figure 1.18 illustrates the dependency of $\frac{dC_m}{dC_L}$ and of x_{ac} on the planform geometry for planar wings with trapezoidal planforms obtained from simulations with a vortex lattice method. The slope of the pitching moment curve decrease with increasing sweep angle. Consequently, the aerodynamic center moves backwards. This trend is more pronounced for larger values of the aspect ratio.

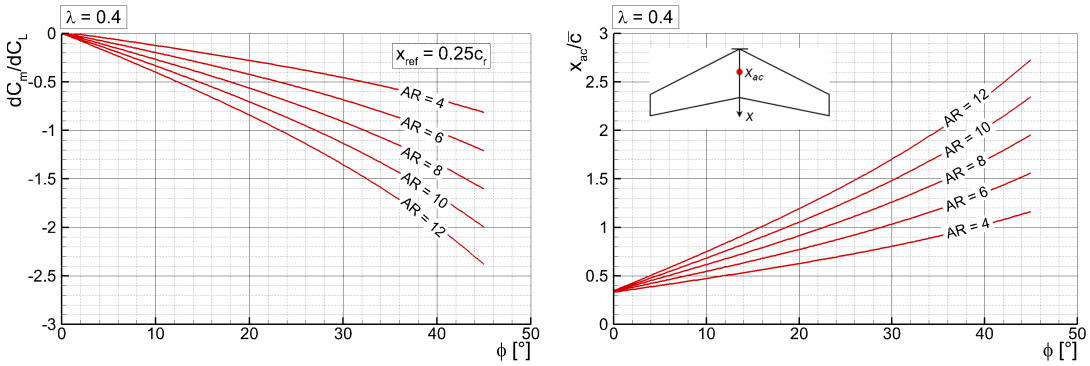

(a) (b)

Figure 1.18: Theoretical dependency of the pitching moment characteristics on the aspect ratio and sweep angle for planar wings with trapezoidal planform and constant taper ratio ($\lambda = 0.4$).

1.3.2.4 Drag polar

The drag force acting on a rigid wing is usually modeled as a quadratic function of the lift as given in Eq. 1.14. The first term of the right hand side, C_{D0}, is the zero-lift drag coefficient and accounts for the drag at $C_L = 0$. The second term accounts for the lift-dependent part of the drag which varies with the square of the lift coefficient multiplied by the lift-dependent drag factor K. Per definition, Eq. 1.14 represents a symmetric drag polar because it does not contain any linear term. Indeed, the linear lift-dependency of the drag is very small in practice and can be ignored for a simplified presentation of the drag characteristics. The generic shape of the drag polar is shown in Fig. 1.19.

$$C_D = C_{D0} + KC_L^2 \quad (C_L < C_{Lmax}) \tag{1.14}$$

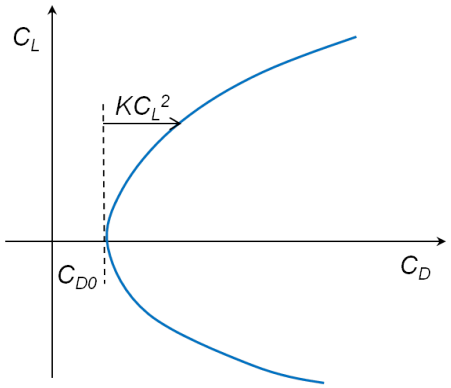

Figure 1.19: Illustration of the quadratic drag polar.

The total drag, C_D, can be decomposed in two distinct contributions which are the parasite drag, C_{Dp}, and the vortex induced drag, C_{Dv}, as indicated by Eq. 1.15. Both C_{Dp} and C_{Dv} are modeled

as quadratic functions of the lift as shown in Eqs. 1.16 and 1.17. The parasite drag is due to the viscosity of the fluid. It includes the skin friction as well as the imbalance in pressure forces due to flow separation. Its magnitude is therefore influenced by aspects such as the wetted area of the wing (skin friction) and the airfoil camber and thickness (flow separation). The vortex-induced drag results from the production of lift. It accounts for the kinetic energy contained in the trailing vortex sheet in the wake of a lifting surface.

$$C_D = C_{Dp} + C_{Dv} \tag{1.15}$$

$$C_{Dp} = C_{Dp0} + K_p C_L^2 \tag{1.16}$$

$$C_{Dv} = C_{Dv0} + K_v C_L^2 \tag{1.17}$$

In Eq. 1.16, the first term of the right hand side, C_{Dp0}, accounts for the friction drag and the imbalance in pressure forces due to flow separation at zero lift. The second term with the proportionality constant K_p represents the lift-dependent part of the parasite drag, which is due to the variation in skin friction and pressure forces as the lift changes. In Eq. 1.17, C_{Dv0} accounts for the vortex-induced drag at zero lift, which is usually small but non-zero except in the case of a planar wing with no camber and no geometrical twist. The second term of the right hand side with the proportionality factor K_v accounts for the lift dependent part of the vortex-induced drag, which is uniquely dependent on the planform geometry of the wing. A theoretical relation for this factor known from Prandtl's lifting line theory is given in Eq. 1.18. The influence of the wing planform geometry on K_v in Eq. 1.18 is given by an explicit dependency on the aspect ratio, and by the presence of the span efficiency factor, e_s, which was introduced in section 1.3.2.1. This illustrates well the influence of the lift distribution on the drag, and the fact that in frame of Prandtl's lifting line theory, the vortex induced drag is minimum for a wing with an elliptical lift distribution (i.e. e_s = 1). For lift distributions other than elliptical, e_s is smaller than one and the vortex induced drag is larger accordingly.

$$K_v = \frac{1}{\pi \mathcal{A} e_s} \tag{1.18}$$

The total drag is obtained by summing up the expressions for C_{Dp} and C_{Dv} according to Eq. 1.15. The composition of the zero-lift drag coefficient, C_{D0}, and of the lift-dependent drag factor, K, is given in Eqs. 1.19 and 1.20.

$$C_{D0} = C_{Dp0} + C_{Dv0} \tag{1.19}$$

$$K = K_p + \underbrace{\frac{1}{\pi \mathcal{A} e_s}}_{K_v} \tag{1.20}$$

In practice, C_{Dp0} is much larger than C_{Dv0} and C_{D0} is dominated by the parasite drag coming from the skin friction and pressure drag due to flow separation. The absolute magnitude of the

skin friction is directly proportional to the wing area S. However, this dependency is not directly reflected by the drag coefficient because it scales with S per definition (cf. Eq. 1.1). In contrast, the effect of the imbalance in pressure forces due to flow separation is fully reflected in C_{D0}. Beside the dependency on the Reynolds number, this part of the zero-lift drag is principally influenced by the wing span and the airfoil shape (thickness and camber). For instance, general requirements for low parasitic drag are small aspect ratio and thin airfoil. The lift-dependent drag coefficient (cf. Eq. 1.20) is usually dominated by the vortex induced drag. Consequently, wings with large aspect ratio are advantageous to minimize the lift-dependent drag, which is opposite to the requirement for low parasitic drag.

1.3.2.5 Lift-to-drag ratio characteristics

The most important measure of the aerodynamic efficiency of a wing is the lift-to-drag ratio, L/D. An expression for it derived from the relation of the quadratic drag polar (cf. Eq. 1.14) is given in Eq. 1.21. Figure 1.20 illustrates the generic shape of the L/D vs. C_L characteristics, which is characterized by the maximum lift-to-drag ratio, $(L/D)_{max}$, and by the lift coefficient at which $(L/D)_{max}$ occurs, $(C_L)_{LDmax}$. Expressions for these two parameters derived analytically from Eq. 1.21 are given in Eqs. 1.22 and 1.23. From the discussion of the drag polar presented in section 1.3.2.4, it is known that a wing geometry associated with low values of C_{D0} usually exhibits large values of K and vice versa. Consequently, Eq. 1.23 emphasizes the large impact the choice of the wing geometry has on the flight condition with optimal aerodynamic efficiency represented by $(C_L)_{LDmax}$ because C_{D0} and K appear on different sides of the fraction. A wing with a large aspect ratio is typically associated with larger values of $(C_L)_{LDmax}$ than a wing with a low aspect ratio. The effect of the wing geometry on $(L/D)_{max}$ depends on the relative variation of C_{D0} and K with the wing geometry. However, it is known from practice that wings with large aspect ratios and large camber exhibit larger values of $(L/D)_{max}$ than wings with low aspect ratios.

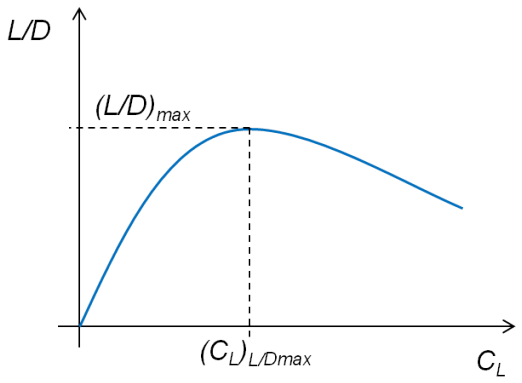

Figure 1.20: Illustration of the lift-to-drag ratio characteristics.

$$\frac{L}{D} = \frac{C_L}{C_D} = \frac{C_L}{C_{D0} + KC_L^2} \tag{1.21}$$

$$\left(\frac{L}{D}\right)_{max} = \frac{1}{\sqrt{4C_{D0}K}} \tag{1.22}$$

$$(C_L)_{LDmax} = \sqrt{\frac{C_{D0}}{K}} \tag{1.23}$$

1.3.3 Overview of flight mechanics

In the following, the influences of the geometric configuration on global flight performance criteria such as minimum and maximum speeds, range, endurance, and minimum turn radius are discussed. As illustrated in Fig. 1.21, the flight performance of an aircraft depends on three different aspects of its design: the geometrical configuration, the weight, and the propulsion power. For a given morphing aircraft, it is assumed that an in-flight modification of the wing geometry affects only the aerodynamics, whereas the weight and the power remain unchanged. For this reason, aspects related to the weight and the propulsion are not considered explicitly in the following discussion.

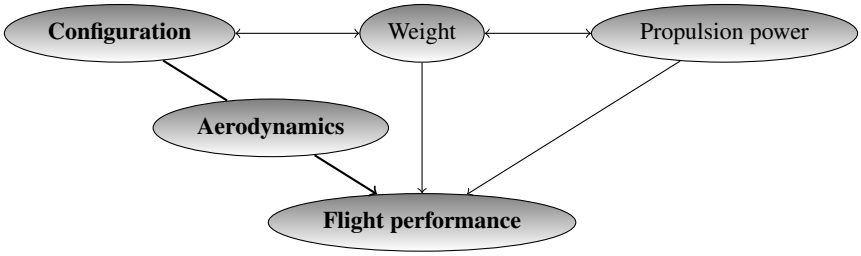

Figure 1.21: Overview of the principal design aspects influencing the flight performance.

The flight performance is directly dependent on the lift and the drag forces. Equations 1.24 and 1.25 give expressions for the absolute magnitude of these forces as a function of the flight condition (U_∞, ρ), and of the geometric configuration represented explicitly by the wing area, S, and indirectly by the aerodynamic coefficients C_L, C_{D0}, and K.

$$L = \frac{1}{2}\rho U_\infty^2 S C_L \tag{1.24}$$

$$D = \frac{1}{2}\rho U_\infty^2 S (C_{D0} + KC_L^2) \tag{1.25}$$

1.3.3.1 Minimum and maximum speeds

As indicated by Eq. 1.24, a reduction of the flight speed must be compensated by an increase of the lift coefficient in order to keep the lift force constant and equal to the weight W. However, the lift coefficient can be only increased up to C_{Lmax} as discussed in section 1.3.2.2, and the minimum speed is the speed at which the required lift coefficient equals to C_{Lmax}. This relation is expressed by Eq. 1.26 which is obtained by setting $C_L = C_{Lmax}$ in Eq. 1.24. It shows that V_{min} is inversely proportional to the square root of the product of S and C_{Lmax}. Consequently,

a minimization of V_{min} requires configurations with a large planform area and/or with a large maximum lift coefficient.

$$V_{min} = \sqrt{\frac{2W}{\rho S C_{L,max}}} \propto \frac{1}{\sqrt{SC_{L,max}}} \tag{1.26}$$

The maximum speed is reached when the drag is equal to the maximum thrust the engines can generate, here defined as F_{Tmax}. From this, Eq. 1.27 gives an expression for the maximum speed, V_{max}, which is obtained by setting $D = F_{Tmax}$ in Eq. 1.25 and solving for the speed. This expression indicates that V_{max} is in first line inversely proportional to the square root of the product of the planform area and the zero-lift drag coefficient. The influence of the product $C_{D0}K$ in the square root of the nominator is assumed to be small. As a result, configurations with a small planform area and/or a small parasite drag are required for large maximum speed.

$$V_{max} = \left(\frac{F_{Tmax} + W\sqrt{(F_{Tmax}/W)^2 - 4C_{D0}K}}{\rho S C_{D0}} \right)^{\frac{1}{2}} \propto \frac{1}{\sqrt{SC_{D0}}} \tag{1.27}$$

1.3.3.2 Range and endurance

The range of an aircraft, R, is defined as the distance it can cover on one load of fuel. It can be estimated using the Breguet's formula[1] given in Eq. 1.28, where sfc represents the specific fuel consumption of the engine, W_0 the weight of the aircraft with empty tanks and W_1 the weight with full tanks. The parameter related to the aircraft configuration is the lift-to-drag ratio, to which R is proportional.

The endurance, E, defined as the amount of time that an airplane can stay in the air on one load of fuel, is given by Eq. 1.29. This relation is very similar to that for the range and shows that the endurance is also proportional to the lift-to-drag ratio. As a result,the range and the endurance can be optimized by choosing wing configurations associated with large lift-to-drag ratio L/D.

$$R = \frac{V}{sfc}\frac{L}{D} ln\left(\frac{W_0}{W_1}\right) \propto \frac{L}{D} \tag{1.28}$$

$$E = \frac{1}{sfc}\frac{L}{D} ln\left(\frac{W_0}{W_1}\right) \propto \frac{L}{D} \tag{1.29}$$

1.3.3.3 Turn radius

The turn radius measures the ability of an aircraft to change the direction of its flight path and is a relevant performance metrics related to maneuver flight. Here, only a level turn is considered (i.e. a turn with constant altitude). An expression to estimate the minimum turn radius, r_{min}, is

[1] Valid for non-powered flight conditions. In the case of powered flight, the range and the endurance depend further on the type of propulsion [46].

given in Eq. 1.30. It indicates that the minimum turn radius is in first line proportional to the ratio of the lift-induced drag factor K to the wing area S. The influence of the product $C_{D0}K$ in the square root of the denominator is assumed to be small. Consequently, minimizing r_{min} requires a wing with large planform area and/or configuration associated with a small lift-induced drag factor.

$$r_{min} = \frac{4KW}{g\rho S\sqrt{(T/W)^2 - 4KC_{D0}}} \propto \frac{K}{S} \tag{1.30}$$

2 Experimental techniques and test setups

2.1 Wind tunnel model

This section presents the semi-span wind-tunnel model that was developed on the basis of the sketch shown in Fig. 1.6 for the experimental investigations.

2.1.1 Articulated structure

The articulated structure of the wind tunnel model is shown in Fig. 2.1 and the nomenclature of its components is detailed in Table 2.1. The load bearing elements consist of the upper arm segment (1), the lower arm segment (2), the hand segment (3), and the finger segment (4). These components are connected to each other by the shoulder joint (5), the elbow joint (6), the hand joint (7), and the finger joint (8). The whole structure can be rotated at the shoulder about the y-axis, and the finger segment can be rotated about its own axis to change the wing twist. However, the twist was not varied during this work. The linkages (9) and (10), connecting the lower arm (2) with the bed plate (11), and the upper arm (1) with the hand segments (3), respectively, are used to make the movement of the structure elements interdependent. Like this, the configuration of the whole structure can be altered by rotating the lower arm segment (1) about the shoulder joint (5). The single degree-of-freedom used to set the planform shape is therefore the angle Ω indicated in Fig. 2.1. A 50 W stepper motor (12) with a planetary gearbox (13) and a worm gear (14) are used to change the angle Ω and actuate the structure. The angle between the hand and the finger segments was fixed to 10° during all the investigations carried out in this work. The bar (15) is used to define the leading-edge between the hand segment and the root section of the wing. This element plunges through a hole made in the bed plate (11) depending on the position of the hand segment. The trailing-edge of the wing consists of a telescopic spar (16) which length passively adapts to the configuration of the articulated structure (cf. Fig. 2.2a). Further, the trailing-edge spar (16) is attached at the wing root to a linear screw guide (17) used to set the root chord length c_r (cf. Fig. 2.2b). This degree-of-freedom is mainly used to adjust the pre-stress of the membrane cover used for the wing surface (cf. section 2.1.3). Finally, the bed plate is welded to a shaft (18) allowing to fix the model in the test section of the wind tunnel. The articulated structure was developed with the help of the Computer Aided Design (CAD) software CATIA (cf. Fig. 2.1a), and was manufactured in the workshop of the Institute of Aerodynamics and Fluid Mechanics of the Technische Universität München. All elements are made out of steel, except the hand and finger segments which are made out of aluminium.

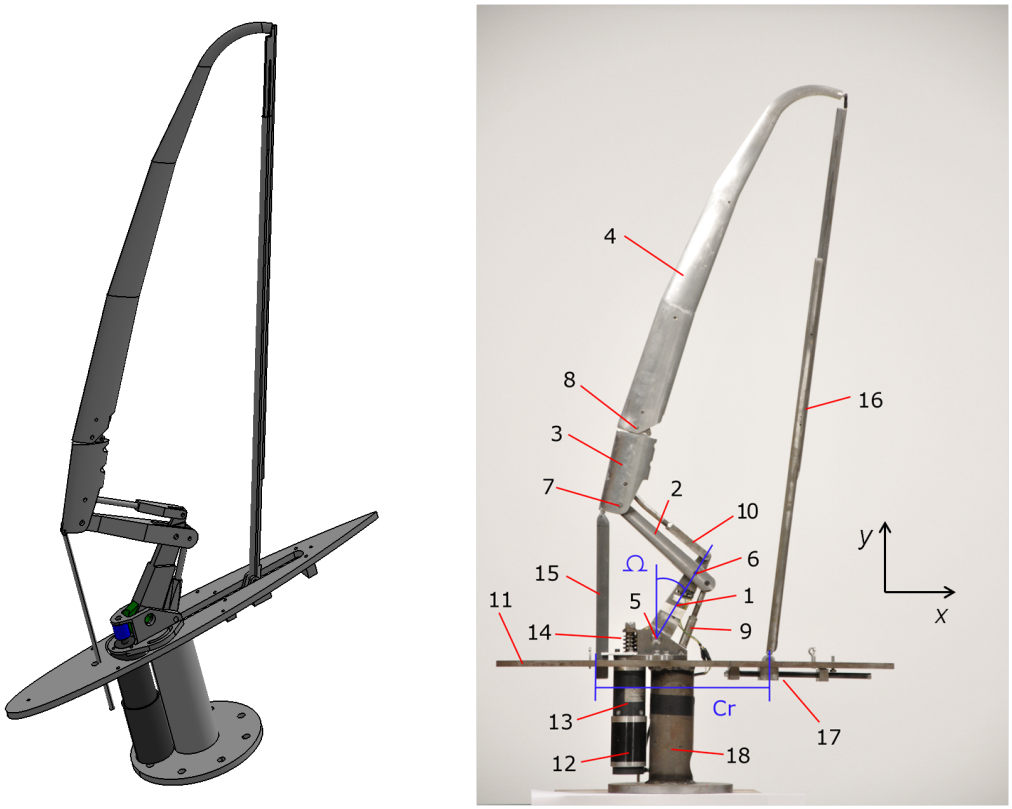

(a) CAD model of the articulated wing structure (CATIA)

(b) Structure of the real model

Figure 2.1: Description of the articulated structure of the morphing wing model.

1	upper arm segment	10	linkage 2
2	lower arm segment	11	bed plate
3	hand segment	12	stepper motor
4	finger segment	13	planetary gearbox
5	shoulder joint	14	worm gear
6	elbow joint	15	inner leading-edge segment
7	hand joint	16	telescopic trailing-edge spar
8	finger joint	17	linear screw guide
9	linkage 1	18	fixation shaft

Table 2.1: Nomenclature of the components of the articulated structure indicated in Fig. 2.1b.

The elements 3, 4, and 15 of the articulated structure are forming the leading-edge of the wing. Therefore, the cross-section geometry of these components plays an important role because it determines the pressure distribution around the leading-edge and their design required special attention during the development of the wind-tunnel model. An appropriate geometry for these elements was obtained from numerical simulations carried out with the method presented in section 3.2. This study indicated that an asymmetric geometry has to be used in order to mitigate the intensity of the suction peak around the leading-edge. The geometry used for the wind-tunnel model is shown in Fig. 2.2c. It consists of two superposed half-ellipses with different minor

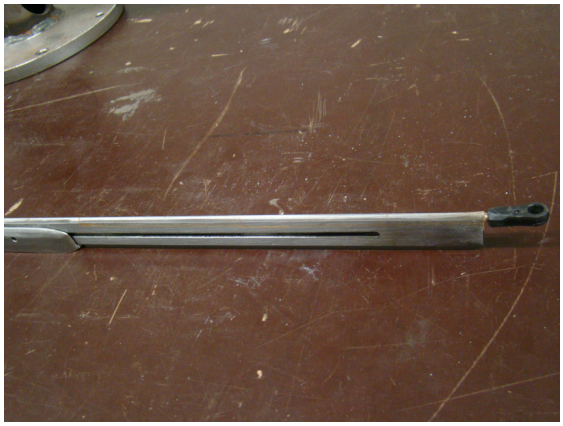

(a) Telescopic trailing-edge spar

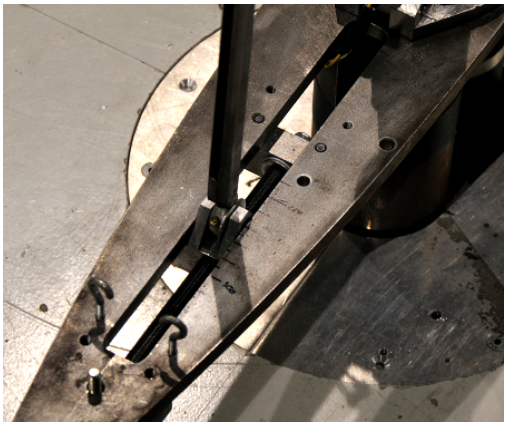

(b) Linear screw guide used to modify the root chord length

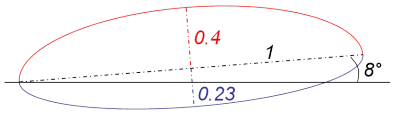

(c) Cross-section of the leading-edge spar

(d) Illustration of the construction of a wing section

Figure 2.2: Details of the wing structure.

axes and inclined of 8° about the leading-edge. The length of the spar is around 20 to 25% of the local wing chord. Finally, Fig. 2.2d illustrates the shape of an airfoil section that results when the membrane is spanned on the wing structure.

The articulated structure described above is the last and most advanced version. However, the development up to this version took several steps. In the following, the main steps of its evolution are presented. Figure 2.3a shows the first version of the wing structure. The main differences compared to the last version are at the trailing-edge and in the inner part of the leading-edge. The spar used to form the trailing-edge had a fixed length and was attached to the leading-edge spar. At the leading-edge, a short spar attached to the hand segment was used instead of the plunging spar. As a result, the wing structure formed a closed frame only when it is fully retracted, in which case the trailing-edge spar and the small spar attached to the hand segment touch the bed plate at the wing root. Preliminary wind tunnel tests with this version of the wing structure showed strong vibrations of the membrane in the inner part of the wing where the structure is open. In order to improve this, the telescopic trailing-edge spar was developed and a plunging element in the inner part of the leading-edge was introduced to provide a closed frame for the membrane cover independently of the configuration of the articulated structure (second version, cf. Fig. 2.3b). This led to significant improvements of the behavior in terms of membrane vibration. In this version, the plunging element at the leading-edge consists of a simple rounded bar with a diameter of 8 mm. The trailing-edge spar is attached at a fixed position on the bed plate corresponding to a root chord length of 0.27 m. Further, in the first and the second versions, the wing chord was not aligned with the x-axis due to the way the hand segment was attached to the lower arm segment. This results in a negative twist of approximately -1.7° as illustrated in

Fig. 2.3c.

Compared to the second version, the third and last version shown in Fig. 2.1 features several improvements. First, a modification of the lower arm segment was made in order to properly align the leading-edge spar and remove the negative twist. Second, the plunging-element in the inner part of the leading-edge was replaced by a profiled spar having the same geometry as the hand and finger segments. Third, the linear screw guide at the wing root was introduced to allow for a modification of the root chord length. Beside this, the first and the second versions feature the same planform characteristics.

The results presented in chapter 5 were obtained with the second version of the structure which has the negative twist of -1.7°, the fixed root chord length of 0.27 m, and the rounded spar in the inner part of the leading-edge. The results presented in chapters 4 and 6 were obtained with the third and last version of the wing structure.

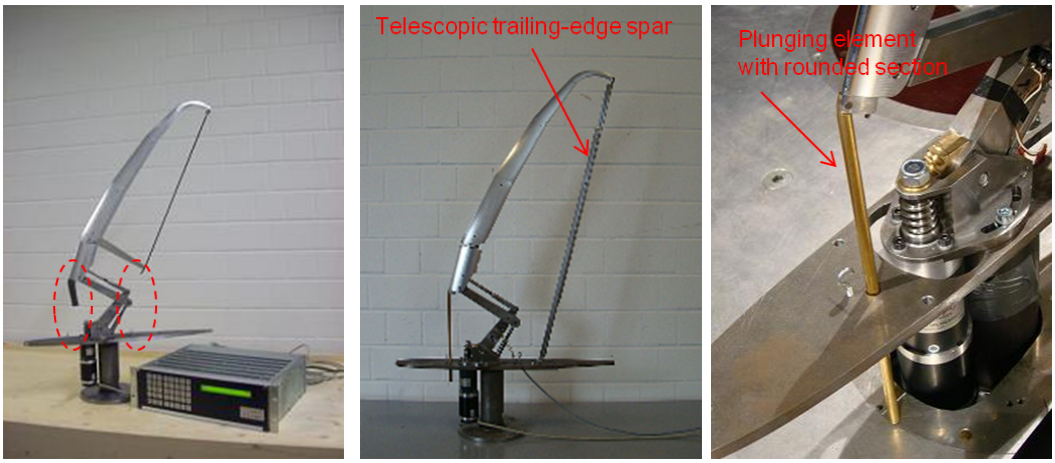

(a) First version

(b) Second version

(c) Effect of the misalignment of the leading-edge spar on the wing twist

Figure 2.3: Evolution of the articulated wing structure.

2.1.2 Planform morphing characteristics

The planform geometry of the wing is determined by the configuration of the articulated structure, which depends on the two degree-of-freedoms Ω and c_r. Ω is allowed to vary between 20° and 60°, and c_r between 0.24 m and 0.3 m. Figure 2.4 illustrates different shapes of the structure for several values of these parameters. With Ω = 20°, the wing planform has the largest span and almost no sweep. For this reason, it is denominated as the “straight wing” configuration. With Ω = 60°, the wing has the smallest span and the largest sweep angle. This configuration is denominated as the “swept-back wing”. Figure 2.4c presents an intermediate configuration

obtained with $\Omega = 40^{\circ}$ as well as the effect of the root chord length on the wing planform.

(a) $\Omega = 20^{\circ}$, $c_r = 0.27$ m (straight wing)

(b) $\Omega = 60^{\circ}$, $c_r = 0.27$ m (swept-back wing)

(c) $\Omega = 40^{\circ}$, $c_r = 0.24$ m and $c_r = 0.3$ m (intermediate configuration)

Figure 2.4: Illustration of different configurations of the articulated structure.

Figure 2.5 presents the geometric characteristics of the wing planform as a function of the parameters Ω and c_r. The black lines highlight the geometric characteristics corresponding to $c_r = 0.27$ m because most of the experimental tests were conducted with this value of c_r. A variation of the root chord length was only used to affect the membrane pre-stress in a later stage of the investigations. The planform area (cf. Fig. 2.5a) exhibits a maximum value of 0.242 m^2 with $\Omega = 30^{\circ}$ and $c_r = 0.30$ m, and a minimum value of 0.176 m^2 for $\Omega = 60^{\circ}$ and $c_r = 0.24$ m. The wing span (cf. Fig. 2.5b) varies linearly with Ω. It has a maximum value of 1.01 m for $\Omega = 20^{\circ}$ (straight wing) and a smallest value of 0.638 m for $\Omega = 60^{\circ}$ (swept-back wing). The wing span is not affected by a modification of the root chord length. The mean chord (cf. Fig. 2.5c) is affected by both Ω and c_r. It shows a maximum value of 0.322 m with $\Omega = 60^{\circ}$ and $c_r = 0.306$ m and a minimum value of 0.206 m for $\Omega = 20^{\circ}$ and $c_r = 0.24$ m. The aspect ratio (cf. Fig. 2.5d) decreases with increasing values of Ω according to the variation of the planform area and of the wing span. It shows also a dependency on the root chord length resulting from the effect c_r has on the planform area. The aspect ratio exhibits a maximum value of 9.79 for $\Omega = 20^{\circ}$ and $c_r = 0.24$ m, and a minimum value of 4.17 with $\Omega = 60^{\circ}$ and $c_r = 0.3$ m. Finally, the sweep angle, $\phi_{1/4}$, is shown in Fig. 2.5e. It is measured as the angle of the straight line joining the quarter-chord of the root section to the quarter-chord of the tip section. It is mainly influenced by Ω, but shows also a slight dependency on the root chord length. The sweep angle exhibits a maximum value of 37.7° with $\Omega = 60^{\circ}$ and $c_r = 0.24$ m and a minimum value of 4.6° with $\Omega = 20^{\circ}$ and $c_r = 0.3$ m.

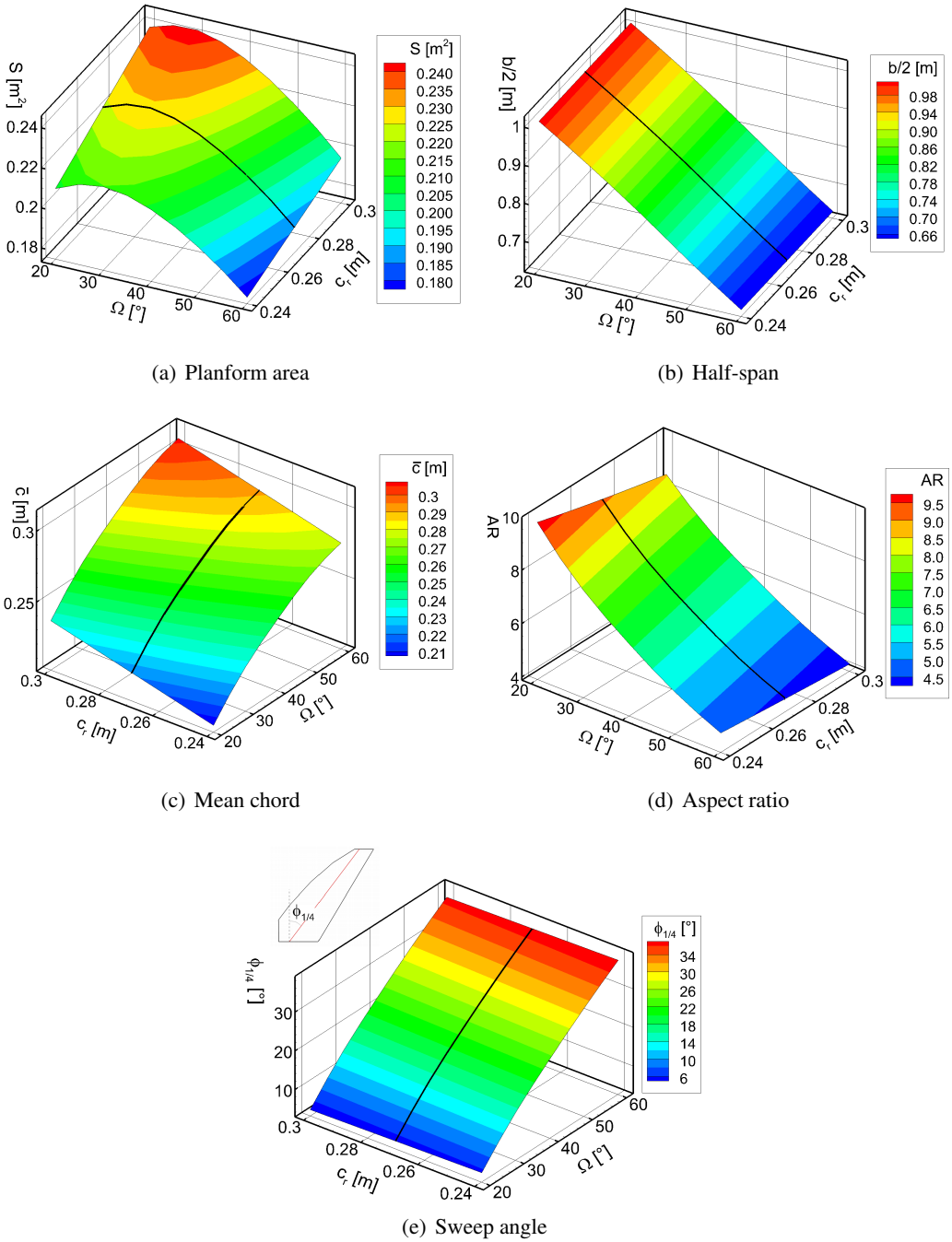

(a) Planform area

(b) Half-span

(c) Mean chord

(d) Aspect ratio

(e) Sweep angle

Figure 2.5: Geometric characteristics of the wing planform as a function of the parameters Ω and c_r of the articulated structure.

2.1.3 Elasto-flexible wing surface

2.1.3.1 Material

The membrane material used for the wing surface is a commercial off-the-shelf polyamide/elastan fabric coated on one side with a polyurethane layer (cf. Fig. 2.6a). It is provided by the textile manufacturer Eschler Textil GmbH (material number 02227) [64]. It features anisotropic stiffness, has a thickness of 0.5 mm, and a mass of 250 g/m^2. This material was chosen because it features appropriate characteristics in terms of maximum elongation, tensile strength, and elasticity for this application.

(a) Membrane material used for the wing surface

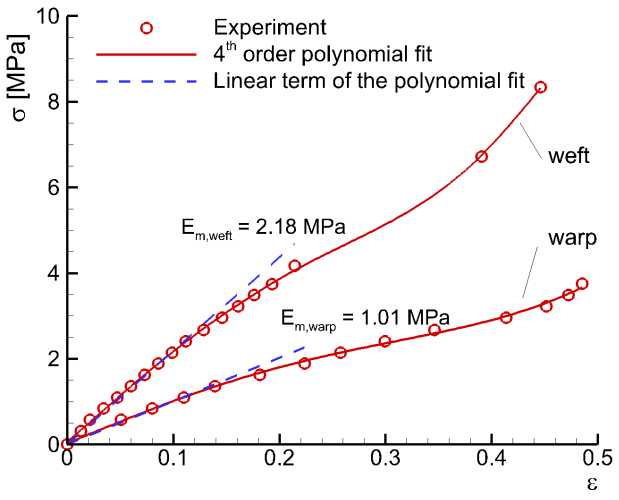

(b) Stress-strain curves obtained from unidirectional tensile tests

Figure 2.6: Description of the membrane material used for the wing surface.

The determination of the mechanical properties of textile membranes is not a trivial issue because the non-linear stress-strain behavior of such materials highly depends on the ratio of the applied load in the warp and weft directions (Uhlemann et al. [50]). As a result, complex models relying on bidirectional tensile tests are usually required for an accurate description of their elastic behavior. Such tests were not carried out within the present work. However, unidirectional tensile tests were conducted to provide an estimation of the mechanical characteristics of both principal directions of this material. The stress-strain curves obtained from these tests are shown in Fig. 2.6b. The stress, σ, is defined as the traction force divided by the width of the probes (75 mm) times the thickness of the membrane (0.5 mm). The strain is defined as the relative elongation of the probes compared to the initial probe length. The stress-strain curve corresponding to both principal directions are non-linear and can be fairly well approximated by a 4^{th}-order polynomial fit. The linear terms of these polynomials provide an estimation for the order of magnitude of equivalent elasticity moduli $E_{m,warp}$ and $E_{m,weft}$, respectively, which can be used to approximate the material law for small deformation (i.e. for $\varepsilon < 0.15$). The tensile tests indicate that the material is approximately two times stiffer in the weft direction than in the

warp direction, with $E_{m,warp}$ = 1.01 MPa and $E_{m,weft}$ = 2.18 MPa. The principal characteristics of the membrane material are summarized in Table 2.2.

	weft	*warp*
Maximum relative elongation	460%	240%
Maximum tensile force	450 N/5cm	290 N/5cm
Approximate elasticity moduli	2.18 MPa	1.01 MPa
Thickness	0.5 mm	
Mass	250 g/m^2	

Table 2.2: Overview of the properties of the membrane material used for the wing surface. The values for the maximum elongation and the tensile strength are provided by the manufacturer.

2.1.3.2 Design of the baseline membrane cover

The baseline design of the wing surface consists of a cover manufactured out of the membrane material as illustrated in Fig. 2.7a. This cover is spanned over the articulated structure of the wing and fixed to the bed plate by the metallic frame as illustrated in Fig. 2.7b. For this application, the stiffest direction (weft) of the anisotropic membrane material is oriented perpendicularly to the trailing-edge, and the weakest direction (warp) is oriented parallel to the trailing-edge. This is advantageous to mitigate the force required to change the planform shape, because the largest deformation occur in the spanwise direction. The design of the initial shape of the membrane cover is based on several criteria. On the one hand, a certain amount of pre-stress has to be guaranteed even for the configuration with the smallest span (i.e. swept-back wing, Fig. 2.4) to prevent the formation of crinkles. On the other hand, a uniform pre-stress distribution has to be achieved in the intermediate configuration. A suitable cut was determined using 2D finite elements calculations with ANSYS Mechanical APDL [51]. The deformation of the membrane in different planform configurations was simulated using several initial shapes until a suitable design was found. Figure 2.8 presents the complete wing model with the membrane cover in three different configurations with a visualization of the initial size of the membrane cover. The wing provides a seamless aerodynamic surface for all planform configurations. A generic fuselage consisting of a body of revolution is used for the aerodynamic fairing of the structure components at the wing root.

2.1.3.3 Membrane deformation as a function of the planform

The initial deformation of the membrane is an important characteristic of the wing surface because it influences its reaction to pressure loads and, thus, the deflected wing shape. In the case of the morphing wing considered here, the initial deformation is not constant but depends on the planform shape. While the dependency on the wing configuration (Ω) is more a side effect, the movable trailing-edge (c_r) is used to affect intentionally the membrane pre-stress with the goal to influence its deflection under aerodynamic load and provide additional control on the wing shape.

(a) Membrane cover

(b) Fixation of the membrane cover on the bed plate of the wing structure

Figure 2.7: Description of the membrane cover used for the wing surface.

(a) $\Omega = 20^{\circ}$, $c_r = 0.27$ m (straight wing)

(b) $\Omega = 40^{\circ}$, $c_r = 0.27$ m (intermediate configuration)

(c) $\Omega = 60^{\circ}$, $c_r = 0.27$ m (swept-back wing)

Figure 2.8: Complete wing in three different configurations with a visualization of the initial size of the membrane cover (in red).

The initial deformation of the membrane as a function of the planform shape was measured by means of photogrammetry (cf. section 2.2.4). For this, markers were placed on the wing lower side to form a grid aligned with the weft and the warp directions of the fabric. The position of the markers was then measured for a series of wing planforms using Ω values between 20° and 60° as well as root chord lengths c_r between 0.24 m and 0.3 m. From this, the membrane pre-strain in each principal direction, $\varepsilon_{0,warp}$ and $\varepsilon_{0,weft}$, were evaluated using Eqs. 2.1 and 2.2, where $l_{0,warp}$ and $l_{0,weft}$ represents the length of the grid lines in the non-deformed state, and l_{warp} and l_{weft} the length of the grid lines of the deformed membrane as illustrated in Fig. 2.9. From the pre-strain components, an approximation for the pre-stress, σ_0, can be obtained using the linear relation given in Eq. 2.3 where E_{weft} and E_{warp} are the elasticity moduli obtained from the tensile tests presented in Fig. 2.6. Although this simple relation does not account for higher order terms and bi-axial dependencies such as a Poisson ratio (not known at this stage), it still provides useful information for the analysis of the wing characteristics.

$$\varepsilon_{0,warp} = \frac{l_{warp} - l_{0,warp}}{l_{0,warp}} \tag{2.1}$$

$$\varepsilon_{0,weft} = \frac{l_{weft} - l_{0,weft}}{l_{0,weft}} \tag{2.2}$$

$$\sigma_0 = \varepsilon_{0,weft} E_{m,weft} + \varepsilon_{0,warp} E_{m,warp} \tag{2.3}$$

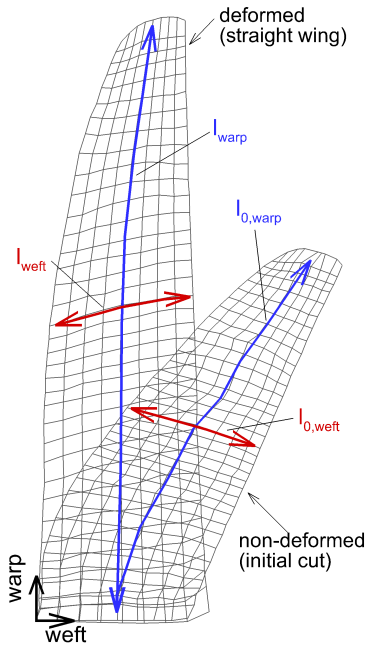

Figure 2.9: Definition of the membrane pre-strain in each principal direction of the fabric.

Figures 2.10 and 2.11 show the pre-strain in the warp and in the weft directions occurring with the straight wing (Ω = 20°), the intermediate configuration (Ω = 40°), and the swept-back wing (Ω = 60°) with a constant root chord length of c_r = 0.27 m. The variation of the pre-strain in the warp direction as the planform changes from the straight wing to the swept-back configuration is directly attributed to the change in wing span. The largest values of $\varepsilon_{0,warp}$ occur at the trailing-edge of the straight wing configuration (cf. Fig. 2.10a) where the membrane cover shows a relative elongation up to 0.5. Accordingly, the smallest values of $\varepsilon_{0,warp}$ occur with the swept-back wing configuration (cf. Fig. 2.10c) with relative elongations around 0.11. The intermediate configuration (cf. Fig. 2.10b) shows fairly constant values of $\varepsilon_{0,warp}$ around 0.26 over the complete wing surface. The influence of the planform on the pre-strain in the weft direction (cf. Fig. 2.11) is more complicated. Near the wing root, $\varepsilon_{0,weft}$ is the largest in the swept-back wing configuration (cf. Fig. 2.11c) with a relative elongation around 0.2. At mid-span, $\varepsilon_{0,weft}$ is the largest in the case of the intermediate configuration. In the case of the straight wing configuration, negative values of $\varepsilon_{0,weft}$ occur in an area located at 30% wing span because the wing chord there is smaller than the size of the initial membrane cut. Overall, the straight wing exhibits the smallest values of $\varepsilon_{0,weft}$ among the three planform shapes considered here. The membrane pre-stress evaluated from Eq. 2.3 is shown in Fig. 2.12. The overall largest

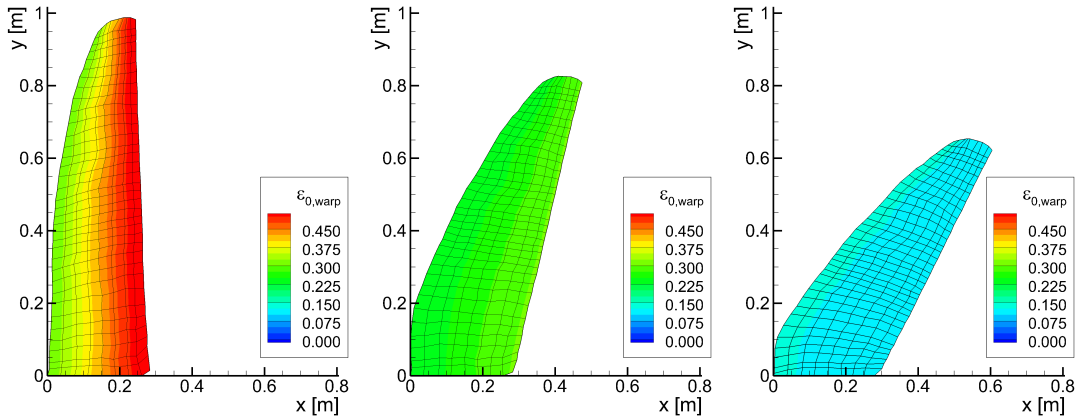

(a) $\Omega = 20^{\circ}$, $c_r = 0.27$ m (straight wing)

(b) $\Omega = 40^{\circ}$, $c_r = 0.27$ m (intermediate configuration)

(c) $\Omega = 60^{\circ}$, $c_r = 0.27$ m (swept-back wing)

Figure 2.10: Membrane pre-strain in the warp direction as a function of the wing planform.

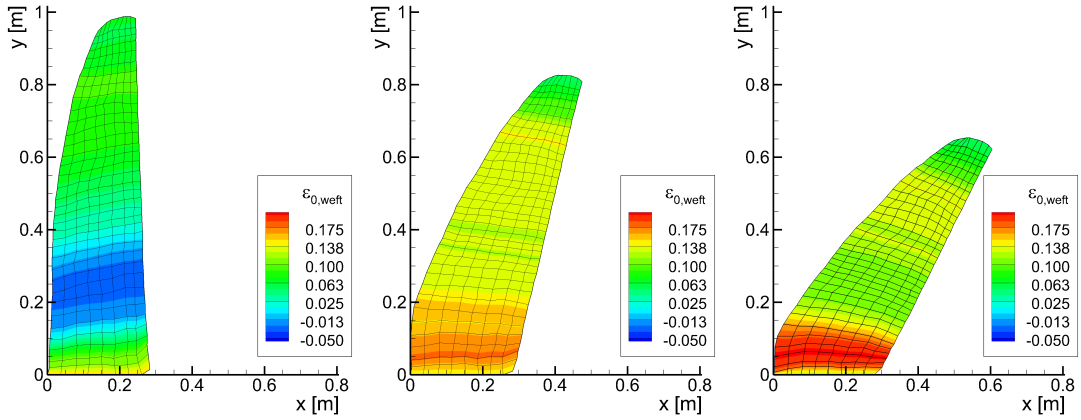

(a) $\Omega = 20^{\circ}$, $c_r = 0.27$ m (straight wing)

(b) $\Omega = 40^{\circ}$, $c_r = 0.27$ m (intermediate configuration)

(c) $\Omega = 60^{\circ}$, $c_r = 0.27$ m (swept-back wing)

Figure 2.11: Membrane pre-strain in the weft direction as a function of the wing planform.

values of σ_0 are observed at the wing root and in the upper half of the straight wing because of the large values of $\varepsilon_{0,warp}$ conditioned by the large span of this configuration. However, the straight wing exhibits also the overall smallest values of the pre-stress around 30% span, which is due to the negative values of $\varepsilon_{0,weft}$ occurring at this spanwise position (cf. Fig. 2.11a). In the case of the intermediate configuration, the pre-stress distribution is much more uniform according to the design criteria for the initial shape of the membrane cover mentioned above. In addition, this planform configuration exhibits relatively large values of σ_0 over the whole surface. In the case of the swept-back wing, the pre-stress is comparatively small over the most part of the wing surface according to the small values of $\varepsilon_{0,warp}$ resulting from the reduced span. Only near the wing root, larger values of σ_0 occur.

The results presented above indicate that the pre-stress strongly depends on the wing planform and further that it is not constant over the membrane surface. However, it is useful to represent

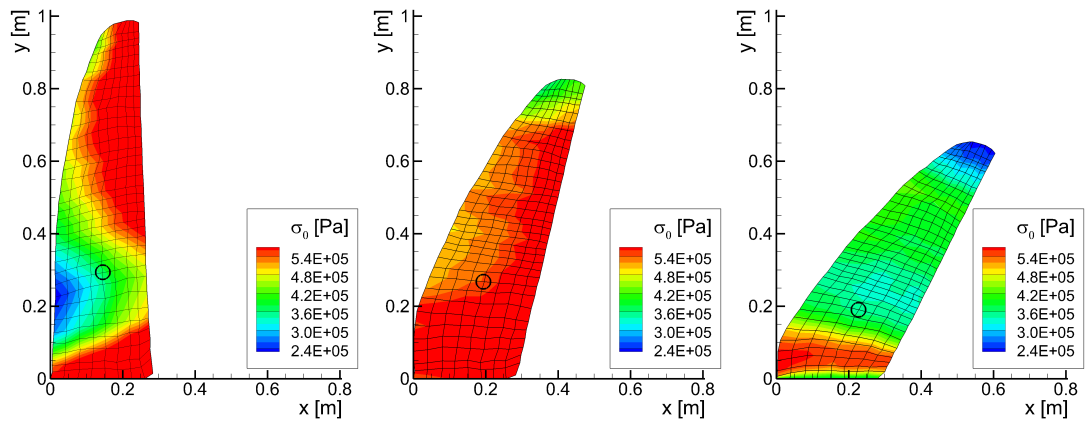

(a) $\Omega = 20^{\circ}$, $c_r = 0.27$ m (straight wing)

(b) $\Omega = 40^{\circ}$, $c_r = 0.27$ m (intermediate configuration)

(c) $\Omega = 60^{\circ}$, $c_r = 0.27$ m (swept-back wing)

Figure 2.12: Membrane pre-stress as a function of the wing planform.

the pre-strain and the pre-stress of the membrane by a single parameter for the analysis of the aero-elastic behavior of the wing. For this, the values of the pre-strain and the pre-stress at the single grid point highlighted by the black circles in Fig. 2.12 are used. This position is located at 30% span, which is the spanwise location where the largest membrane deflection occurs (cf. chapter 4).

A synthesis of the pre-strain and pre-stress characteristics of the wing surface as a function of the planform shape (Ω) and root chord length (c_r) is given in Fig. 2.13. For this, the values of $\varepsilon_{0,weft}$, $\varepsilon_{0,warp}$, and σ_0 at the grid point highlighted in Fig. 2.12 are used. The pre-strain in the warp direction decreases as Ω increases according to the corresponding change in wing span. The non-linear dependency between $\varepsilon_{0,weft}$ and Ω is due to the intrinsic variation of the wing chord as the planform changes from the straight wing to the swept-back wing configuration. At this location on the wing surface, $\varepsilon_{0,weft}$ is the largest with $\Omega = 40^{\circ}$. The negative values of $\varepsilon_{0,weft}$ occurring in the straight wing configuration ($\Omega = 20^{\circ}$) are due to the small wing chord as already mentioned above in the discussion of Fig. 2.11a. Further, $\varepsilon_{0,weft}$ increases monotonically with c_r according to the change in wing chord (cf. Fig. 2.5c). The pre-stress is the largest with the intermediate configuration corresponding to $\Omega = 40^{\circ}$. In the cases of the straight wing ($\Omega = 20^{\circ}$) and of the swept-back wing ($\Omega = 60^{\circ}$), the pre-stress is smaller and lie within the same range for both configurations.

2.1.3.4 Modified membrane covers

In addition the baseline membrane cover presented above, two further versions including specific structural modifications were considered. The goal at this stage was not to provide an optimized membrane cover and reach target performance values but rather to test the generic influence of specific modifications of the membrane structure on the wing characteristics. The modified membrane covers were tested only with the straight wing configuration.

The first modified cover has increased stiffness obtained by doubling the membrane thickness

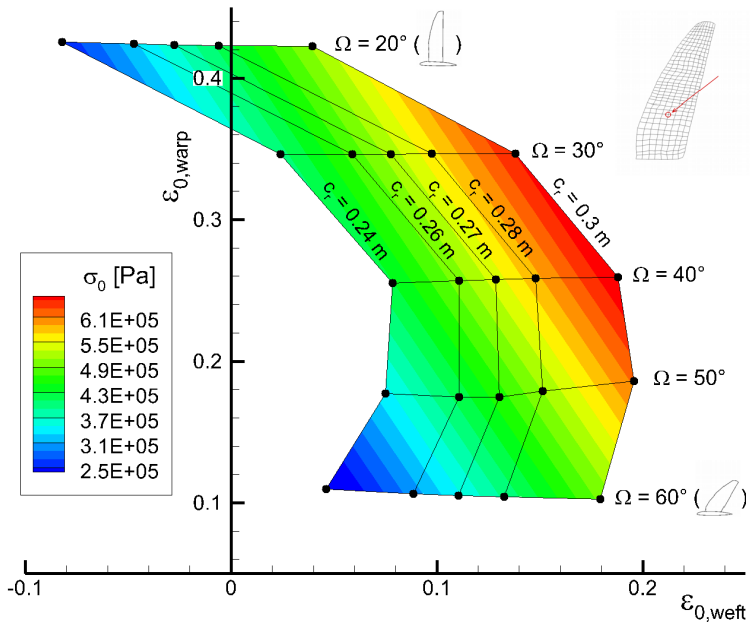

Figure 2.13: Synthesis of the membrane pre-strain and pre-stress characteristics as a function of the planform shape (Ω) and root chord length (c_r).

at three spanwise positions. For this, thin membrane strips with a width of 25 mm and made out of the same fabric are sewed on the baseline membrane cover as illustrated in Fig. 2.14a. The principal directions of these strips are oriented the same way as for the remaining cover, i.e. with the weft direction perpendicular to the trailing-edge. The three strips are placed at spanwise locations corresponding to $2y/b = 0.15$, $2y/b = 0.3$, and $2y/b = 0.45$. These positions were chosen because the membrane deflection is the largest around $2y/b = 0.3$ as is shown in chapter 4. The advantage of using thin strips placed at discrete spanwise positions instead of doubling the membrane thickness over a larger area is that like this, the membrane stiffness can be increased in the chordwise direction without affecting too much the stiffness in the spanwise direction. As mentioned above, a low stiffness in the spanwise direction is required to allow the variation of the planform with reasonable actuation force.

The second modified membrane cover uses “rigid” battens fixed to the membrane to further increase the stiffness and provide the wing surface with a pre-determined shape as illustrated in Fig. 2.14b. The battens are made out of an aluminium flat bar with a thickness of 2 mm and a width of 10 mm. They are inserted between the two membrane layers at the three locations where the membrane thickness is doubled in the first modified version of the cover (cf. Fig. 2.14c). While the battens used for the wing lower side are straight, those used for the wing upper side are cambered with a circular shape. The geometric characteristics of the cambered battens in terms of their chord length, c, and relative camber, f/c, are given in Fig. 2.15.

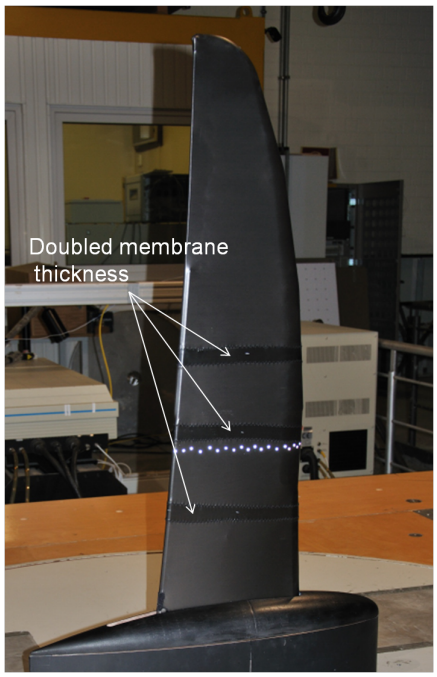

(a) Membrane with doubled thickness at three spanwise positions

(b) Cambered battens to be fixed on the wing upper side

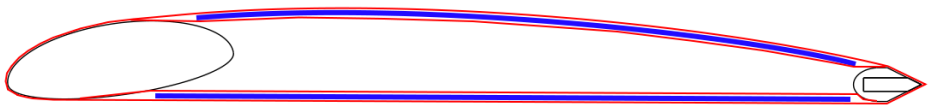

(c) Sketch of a wing section with the battens

Figure 2.14: Modified membrane covers.

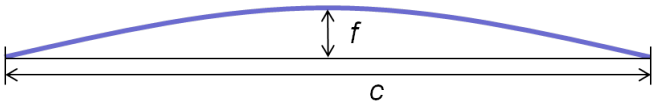

$2y/b$	f/c
0.15	0.048
0.30	0.043
0.45	0.033

Figure 2.15: Geometric characteristics of the cambered battens used for the wing upper side.

2.2 Measurement techniques

2.2.1 Force measurements

Force measurements are carried out to obtain the lift, drag, and pitching moment characteristics of the wing and to study its aerodynamic performance. For this, an external six-component strain gauge balance installed under the floor of the wind tunnel test section is used. The balance is mounted on a turning plate actuated with an electric motor to set the angle of attack α. The balance turns with the model and provides thus forces and moments F_x, F_y, and m_z in the body-fixed coordinate system as illustrated in Fig. 2.16 and the transformation given by Eqs. 2.4 and 2.5 have to be applied to obtain the lift and the drag forces. Further, the quarter chord of the root section is used as reference position for the pitching moment characteristics in this work. The transformation given by Eq. 2.6 is used to obtain it from the moment m_z. Finally, the aerodynamic coefficients are computed from the absolute forces according to their definitions given in Eq. 1.1.

The measurement range of each component as well as the precision of the balance are indicated in Table 2.3. The internal sampling rate is 200 Hz, and for the measurements performed throughout this work, an averaging time of 20 seconds was used to obtain time-averaged forces. Further details about the test conditions for the force measurements are provided in section 2.3.2.

$$L = F_y cos(\alpha) - F_x sin(\alpha) \tag{2.4}$$

$$D = F_y sin(\alpha) + F_x cos(\alpha) \tag{2.5}$$

$$m = m_z - F_y \Delta l \tag{2.6}$$

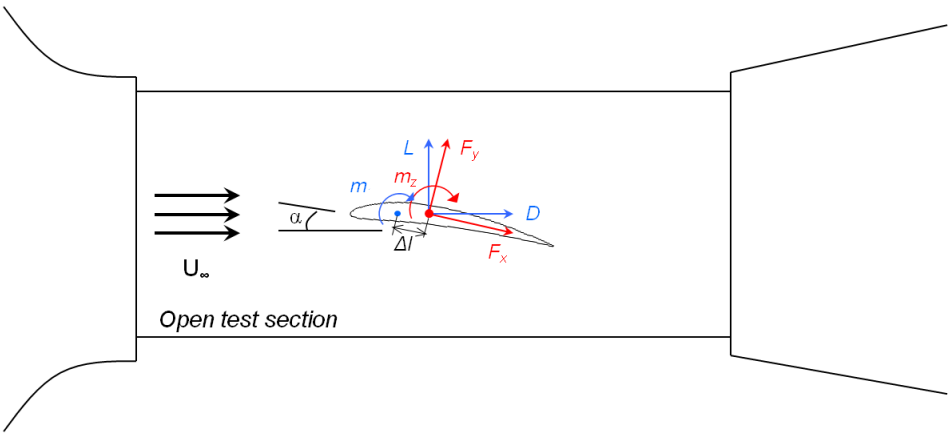

Figure 2.16: Illustration of the different coordinate systems involved in the force measurements.

2.2.2 Stereo-particle image velocimetry

Particle image velocimetry (PIV) is a non-intrusive technique for the measurement of velocity fields [52]. The basic principles of PIV are illustrated in Fig. 2.17. The flow is seeded with

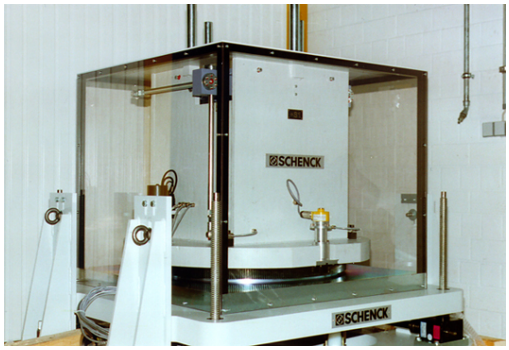

F_x	$\pm 1500\ N$
F_y	$\pm 3000\ N$
F_z	$\pm 3000\ N$
m_x	$\pm 700\ Nm$
m_y	$\pm 500\ Nm$
m_z	$\pm 700\ Nm$
Precision	0.025% of the entire range

Table 2.3: Six-component aerodynamic balance used for the force measurements.

tracer particles and a light sheet generated by a laser beam and a cylindrical lens is placed at the position where the velocity field has to be measured. The tracer particles passing through the light sheet reflect the laser light and their positions can be recorded with a camera. To determine the flow velocity, two pictures of the tracer particles taken at times t and t' are needed. The displacement of the tracer particles between the two images can be determined using cross-correlation calculations and the velocity vectors can be reconstructed using the known time interval $\Delta t = t' - t$. For the measurement of three-dimensional velocity fields, two cameras viewing with different angles on the plane defined by the light sheet have to be used (stereo-particle image velocimmetry). The three-dimensional velocity field is obtained by combining the two-dimensional vector fields obtained with each camera.

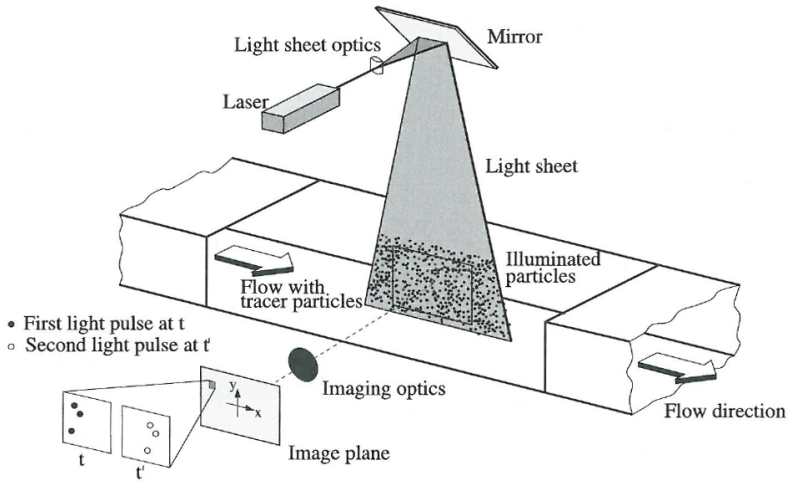

Figure 2.17: Illustration of the principles of particle image velocimetry [52].

Stereo-PIV measurements were carried out in this work to measure the velocity field in the near wake of the wing as illustrated in Fig. 2.18. The measurement plane is located at a distance half of the mean chord behind the wing tip. The light sheet is produced by a 200 mJ double-pulsed neodymium-doped yttrium aluminum garnet laser (Nd:YAG), and the positions of the tracer particles are recorded by two CCD cameras of type FlowSense 2M with a resolution of 1200×1600 pixels. The camera optics used have a focal length of 135 mm which, in combination with the distance to the measurement plane, yields a size of the measurement window of 150×300 mm

with an average resolution of 5 pixels per millimeter in the z-direction and 8 pixels per millimeter in the y-direction. As a result, the measurement of the wake of the complete wing requires the measurement plane to be moved in the y-direction using a traversing unit. The flow field is therefore composed of several measurement planes patched together. At each position, hundred instantaneous measurements were used to obtain statistically averaged flow fields. The tracer particles used consist of paraffin oil droplets with a size of 2-5 μ m generated by a seeding generator. The time interval Δt for the configuration setup used in this work was determined from the empirical formula $\Delta t = \frac{0.5 \cdot 10^{-3}}{U_\infty}$, with U_∞ being the free-stream velocity. The processing of the raw particle images into maps of 50×40 vectors was carried out with the software FlowManager based on an adaptive-correlation algorithm with 25% overlap and final interrogation areas of 32×32 pixels [53].

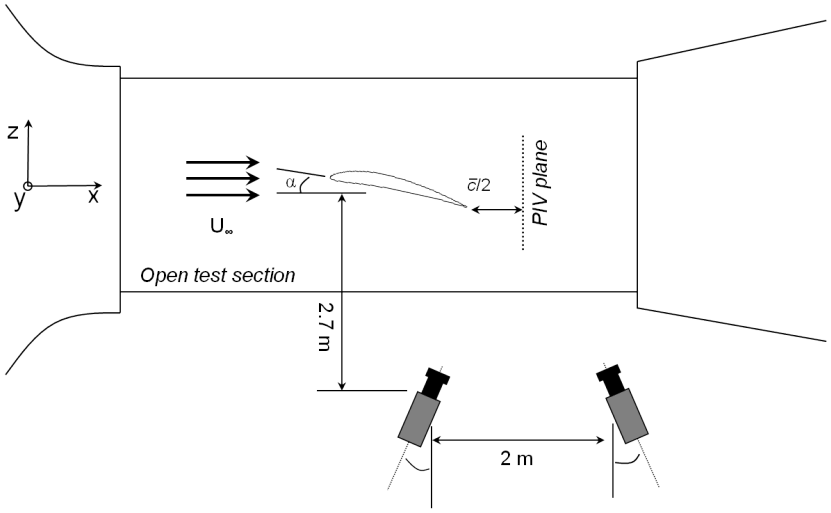

Figure 2.18: Illustration of the experimental setup for the stereo-PIV measurements.

2.2.3 Surface flow visualization techniques

2.2.3.1 Wool-tufts

The wool-tuft flow visualization technique was used to detect flow separation on the suction side of the wing and analyze its stall behavior [54]. For this, wool tufts with a length of 20 mm and a diameter of approximately 1 mm were fixed on the upper side of the wing with an averaged spacing of 25 mm. Pictures of the wing surface taken with a camera were analyzed manually to detect the regions of separated flow, which are characterized by blurred tufts coming from their unsteady movement as they are entrained by the turbulent separated flow (cf. Fig. 2.19).

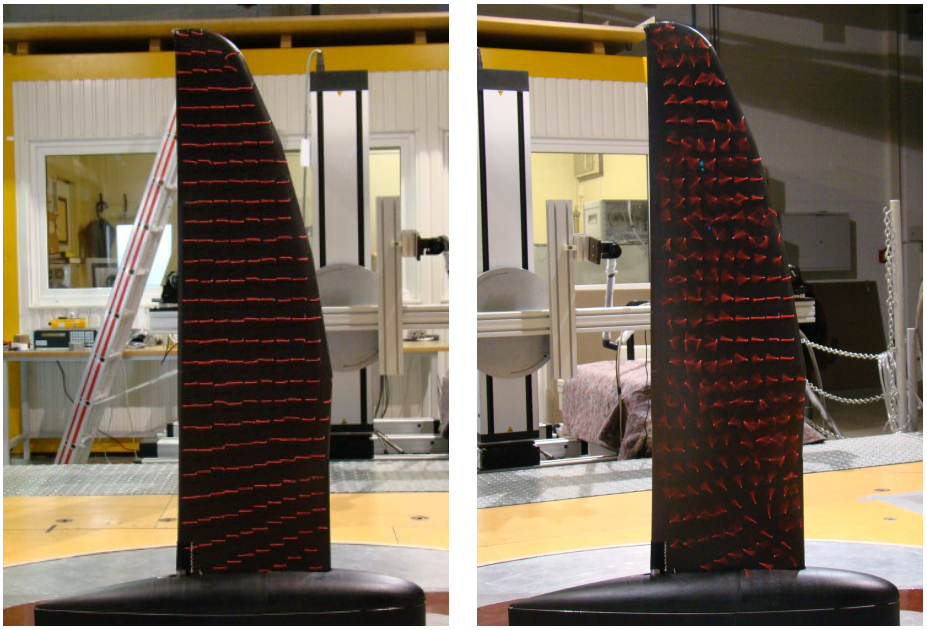

(a) Attached flow (b) Separated flow

Figure 2.19: Illustration of the wool-tufts flow visualization experiments.

2.2.3.2 Microphone probe

A microphone probe was used to detect the location of the laminar to turbulent transition of the boundary layer on the wing surface. The structure of the microphone probe is shown in Fig. 2.20. It consists of a pitot-tube with a microphone brought at its end connected to an amplifier and a speaker or a sound card for digital signal post processing. The character of the boundary layer can be determined by the type of acoustic signal captured by the microphone. In the turbulent case, the turbulent pressure fluctuations produces a characteristic noise.

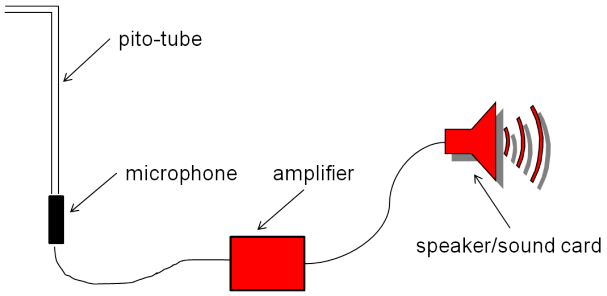

Figure 2.20: Sketch illustrating the construction of the microphone probe.

2.2.4 Stereo-photogrammetry

Stereo-photogrammetry was used to measure the deformation of the wing surface and reconstruct the three-dimensional wing shapes. Because no measurement system for this was readily available at the institute, a complete system has been developed specifically for these investigations. For this reason, the principles of stereo-photogrammetry are explained more extensively

in the following to present the method on which the self-developed measuring system is based. The theory presented in the following come from Ref. [55].

2.2.4.1 Principles of analytical photogrammetry

The fundamental equations of analytical photogrammetry are the collinearity equations. Figure 2.21 illustrates a scene where a camera surveys an object. According to the pinhole camera model, the camera is modeled by the image plane (u,v), and the perspective center O, through which all rays of light are converging. The coordinate system (x',y',z') associated with the camera regarded as a spatial object has its origin at the perspective center O, which is placed at a distance equal to the focal length $-h$ behind the image plane. The projection P' of an object point P on the image plane is defined by the intersection of the image plane with the ray of light $O-P$. In the camera coordinate system, the position of P' is given by the vector $\vec{x}'_{P'} = (x'_{P'}, y'_{P'}, -h)$ because all points on the image plane have a constant coordinate z' which is equal to the negative of the focal length. Finally, the position and the orientation of the camera in the object space coordinate system (X,Y,Z) is defined by the position of the perspective center $\vec{X}_O = (X_0, Y_0, Z_0)$ and a rotation matrix $\mathbf{R}$ containing the three Euler angles (ω, ϕ, κ) defining the orientation of the axis x', y', and z' relative to X, Y, and Z.

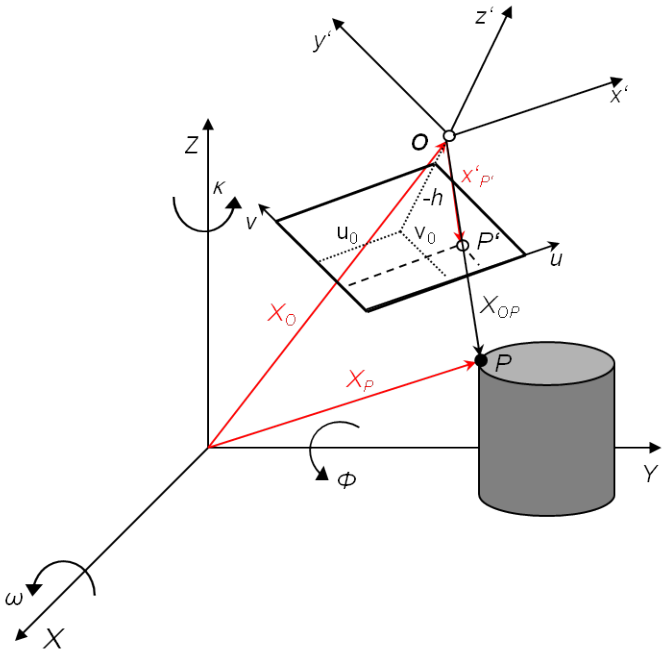

Figure 2.21: Schematic illustration of a photogrammetric scene.

The first step to derive the collinearity equations is to express the position of P in the object space as the sum of the vectors $\vec{X}_O$ and $\vec{X}_{OP}$ as shown in Eq. 2.7. Because $\vec{x}'_{P'}$ is collinear with $\vec{X}_{OP}$ (cf. Fig. 2.21), it can be used instead of $\vec{X}_{OP}$ to include information from the image space into the transformation. For this, the vector $\vec{x}'_{P'}$ must be expressed in the object space coordinate system, which is done using the rotation matrix $\mathbf{R}$, and a scaling factor m such that $||\vec{X}_{OP}|| = m||\vec{x}'_{P'}||$. The result of this substitution is given in Eq. 2.8, which expresses the position of the object point

P as a function of the position of the camera in the object space, $\vec{X}_O$, its orientation, $\mathbf{R}$, and the position of P' on the image plane, $\vec{x'_{P'}}$.

$$\vec{X}_P = \vec{X}_O + \underbrace{\vec{X}_{OP}}_{m\mathbf{R}\vec{x'}_{P'}} \tag{2.7}$$

$$\begin{bmatrix} X_P \\ Y_P \\ Z_P \end{bmatrix} = \begin{bmatrix} X_0 \\ Y_0 \\ Z_0 \end{bmatrix} + m \cdot \begin{bmatrix} r_{11} & r_{12} & r_{13} \\ r_{21} & r_{22} & r_{23} \\ r_{31} & r_{32} & r_{33} \end{bmatrix} \cdot \begin{bmatrix} x'_{P'} \\ y'_{P'} \\ -h \end{bmatrix} \tag{2.8}$$

The transformation in Eq. 2.8 requires the coordinates of the image and of the object spaces to be expressed in the same physical unit. In general, however, the image coordinate system (u,v) in which the position of P' is measured has different units and origin than the fictive camera system (x',y',z') used so far. To handle this, an additional transformation between the coordinate systems of the image plane (u,v) and of the camera (x',y',z') as given in Eq. 2.9 can be included into the transformation to obtain Eq. 2.10. There, u_0 and v_0 are the coordinates of the principal point defined as the projection of the perspective center O on the image plane (cf. Fig. 2.21), and λ_u and λ_v are scaling factors which account for the different units between the image and camera coordinates systems (scaling in x and y may be different).

$$\begin{aligned} x'_{P'} &= \lambda_u(u_{P'} - u_0) \\ y'_{P'} &= \lambda_v(v_{P'} - v_0) \end{aligned} \tag{2.9}$$

$$\begin{bmatrix} X_P \\ Y_P \\ Z_P \end{bmatrix} = \begin{bmatrix} X_0 \\ Y_0 \\ Z_0 \end{bmatrix} + m \cdot \begin{bmatrix} r_{11} & r_{12} & r_{13} \\ r_{21} & r_{22} & r_{23} \\ r_{31} & r_{32} & r_{33} \end{bmatrix} \cdot \begin{bmatrix} \lambda_u(u_{P'} - u_0) \\ \lambda_v(v_{P'} - v_0) \\ -h \end{bmatrix} \tag{2.10}$$

The collinearity equations are finally obtained by dividing the first and the second lines of Eq. 2.10 by the third one, which eliminates the unknown scaling factor m. They are given in Eqs. 2.11 and 2.12, and describe the transformation between the three-dimensional coordinates of points in object space and their projection on the image plane as a function of eleven parameters related to the photogrammetric scene. The parameters X_0, Y_0, Z_0, ω, ϕ, and κ are related to the position and the orientation of the camera in the object space and are called the parameters of exterior orientation. The remaining five parameters, h, u_0, v_0, λ_u and λ_v, are exclusively related to the camera and are called the parameters of interior orientation. The collinearity equations can be further extended with correction terms to take account of optical distortion effects, but this is out of the scope of the present discussion.

$$u = u_0 + \frac{f}{\lambda_u}\left[\frac{r_{11}(X-X_0)+r_{21}(Y-Y_0)+r_{31}(Z-Z_0)}{r_{13}(X-X_0)+r_{23}(Y-Y_0)+r_{33}(Z-Z_0)}\right] \quad (2.11)$$

$$v = v_0 + \frac{f}{\lambda_v}\left[\frac{r_{12}(X-X_0)+r_{22}(Y-Y_0)+r_{32}(Z-Z_0)}{r_{13}(X-X_0)+r_{23}(Y-Y_0)+r_{33}(Z-Z_0)}\right] \quad (2.12)$$

If the parameters of exterior and interior orientation are known, the computation of the projection of an object point on the image plane can be directly done by applying the collinearity equations. However, the reconstruction of the three-dimensional coordinates of an object point from its image coordinates is not directly possible because the collinearity equations only provide two equations for the three unknowns coordinates X, Y, and Z. In stereo-photogrammetry, the missing equations are provided by a second set of collinearity equations associated with a second image containing a projection of the object point to be reconstructed. Like this, four equations are available to compute the three unknowns X, Y, and Z. The resulting system is over-determined and usually solved using least-squares fitting.

In practical cases, however, the parameters of interior and exterior orientation are not known in advance and have to be determined during a calibration procedure which consists in applying the collinearity equations to a set of reference points with known coordinates. By doing this, the unknowns are now the eleven transformation parameters, which can be determined by least-squares fitting. However, due to the non-linear nature of the collinearity equations with respect to the transformation parameters, a non-linear least-squares fitting method is required and initial values must be provided, which may be difficult in some situations. This difficulty can be eluded by using an alternative formulation of the collinearity equations known as the Direct Linear Transformation method introduced in the following section.

2.2.4.2 Direct Linear Transformation method

The Direct Linear Transformation method (DLT) is based on a simple rearrangement of the collinearity equations, in which all non-linear combinations of the transformation parameters occurring in the collinearity equations are redefined as single coefficients. The resulting DLT equations are given in Eqs. 2.13 and 2.14, which are linear with respect to the new transformation parameters L_1 to L_{11}. The "price" for this rearrangement is solely the loss of the direct physical meaning of the transformation parameters compared to the parameters of the original collinearity equations.

$$u = \frac{L_1X + L_2Y + L_3Z + L_4}{L_9X + L_{10}Y + L_{11}Z + 1} \quad (2.13)$$

$$v = \frac{L_5X + L_6Y + L_7Z + L_8}{L_9X + L_{10}Y + L_{11}Z + 1} \quad (2.14)$$

The parameters L_1 to L_{11} are obtained during a calibration procedure for which a set of at least six control points with known coordinates are required. The DLT equations for each of the n control points ($n \geq 6$) can be rearranged in a linear system of $2n$ equations as shown in Eq. 2.15,

which can be solved for the parameters L_1 to L_{11} using a linear least-squares fitting method.

$$\begin{bmatrix} X_1 & Y_1 & Z_1 & 1 & 0 & 0 & 0 & 0 & \frac{-u_1}{X_1} & \frac{-u_1}{Y_1} & \frac{-u_1}{Z_1} \\ 0 & 0 & 0 & 0 & X_1 & Y_1 & Z_1 & 1 & \frac{-v_1}{X_1} & \frac{-v_1}{Y_1} & \frac{-v_1}{Z_1} \\ \vdots & \vdots & \vdots & \vdots & \vdots & \vdots & \vdots & \vdots & \vdots & \vdots & \vdots \\ X_n & Y_n & Z_n & 1 & 0 & 0 & 0 & 0 & \frac{-u_n}{X_n} & \frac{-u_n}{Y_n} & \frac{-u_n}{Z_n} \\ 0 & 0 & 0 & 0 & X_n & Y_n & Z_n & 1 & \frac{-v_n}{X_n} & \frac{-v_n}{Y_n} & \frac{-v_n}{Z_n} \end{bmatrix} \cdot \begin{bmatrix} L_1 \\ L_2 \\ \vdots \\ L_{10} \\ L_{11} \end{bmatrix} = \begin{bmatrix} u_1 \\ v_1 \\ \vdots \\ u_n \\ v_n \end{bmatrix} \tag{2.15}$$

For the reconstruction of the coordinates (X_i, Y_i, Z_i), at least two images containing the projection of the object point to be reconstructed are required because the object coordinates contain three unknowns and one image provides only two equations. The DLT equations corresponding to each of the m images ($m \geq 2$) can be combined to obtain the linear system of equations given by Eq. 2.16, which can be solved for the unknown coordinates (X_i, Y_i, Z_i) using a linear least-squares fitting method. For the reconstruction, the transformation parameters corresponding to each camera must have been obtained from a calibration performed in the same object space coordinate system.

$$\begin{bmatrix} u_i^{(1)}L_9^{(1)} - L_1^{(1)} & u_i^{(1)}L_{10}^{(1)} - L_2^{(1)} & u_i^{(1)}L_{11}^{(1)} - L_3^{(1)} \\ v^{(1)}L_9^{(1)} - L_1^{(1)} & v_i^{(1)}L_{10}^{(1)} - L_2^{(1)} & v_i^{(1)}L_{11}^{(1)} - L_3^{(1)} \\ \vdots & \vdots & \vdots \\ u_i^{(m)}L_9^{(m)} - L_1^{(m)} & u_i^{(m)}L_{10}^{(m)} - L_2^{(m)} & u_i^{(m)}L_{11}^{(m)} - L_3^{(m)} \\ v_i^{(m)}L_9^{(m)} - L_1^{(m)} & v_i^{(m)}L_{10}^{(m)} - L_2^{(m)} & v_i^{(m)}L_{11}^{(m)} - L_3^{(m)} \end{bmatrix} \cdot \begin{bmatrix} X_i \\ Y_i \\ Z_i \end{bmatrix} = \begin{bmatrix} L_4^{(1)} - u_i^{(1)} \\ L_8^{(1)} - v_i^{(1)} \\ \vdots \\ L_4^{(m)} - u_i^{(m)} \\ L_8^{(m)} - v_i^{(m)} \end{bmatrix} \tag{2.16}$$

2.2.4.3 Stereo-image matching

One of the main difficulties in the reconstruction of the three-dimensional coordinates lies in the proper recognition of the correct image point $P_i^{\prime(2)}$ in the second image that corresponds to a given point $P_i^{\prime(1)}$ in the first image. In most cases, this step is difficult because all points in each images look the same (as illustrated in Fig. 2.22a). Fortunately, the search for the correct point in the second image can be reduced to a search along a line by taking advantage of the principles of epipolar geometry. The main idea comes from the fact that the object point P_i, its projections $P_i^{\prime(1)}$ and $P_i^{\prime(2)}$, and the perspective centers $O^{(1)}$ and $O^{(2)}$ all lie on a common plane called the epipolar plane (cf. Fig. 2.22b). Further, this epipolar plane intersects the image planes in two lines called the epipolar lines, along which $P_i^{\prime(1)}$ and $P_i^{\prime(2)}$ are necessarily lying.
In practice, once an image point $P_i^{\prime(1)}$ has been selected in the first image, the corresponding epipolar line in the second image plane can be constructed using the known transformation parameter. In the case where only one point is lying along the epipolar line, the reconstruction of the object point P_i can be directly done using Eq. 2.16. In the case where more than one point lie along the epipolar line, further image features such as contrast, shape or color must be taken into account in order to select the correct candidate.

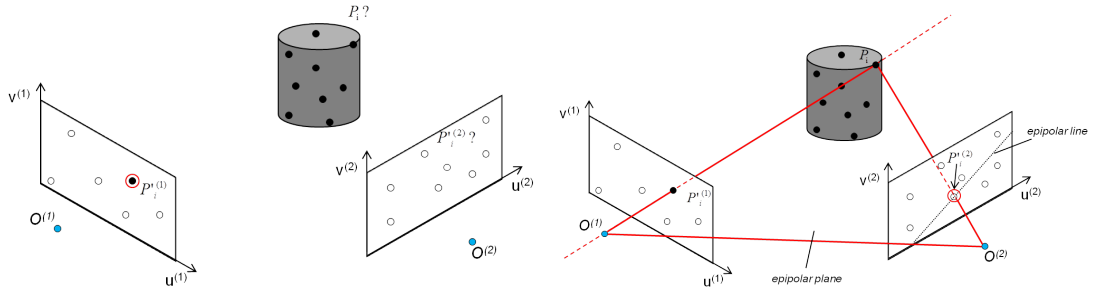

Figure 2.22: Principles of epipolar geometry for feature matching in a stereo-image pair.

2.2.4.4 Self-developed measurement system

The stereo-photogrammetry measurement system developed for the present investigation is based on the Direct Linear Transformation method presented above (cf. section 2.2.4.2). It is used to reconstruct the three-dimensional coordinates of markers placed on the wing surface. The code was implemented in Matlab, and takes advantage of some pre-implemented functions available in the image processing toolbox of this software for basic operations such as the recognition of the markers and the determination of the pixel coordinates of their center. The principles of epipolar geometry presented in section 2.2.4.3 are further implemented in the code to facilitate the recognition of corresponding markings for the reconstruction of three-dimensional coordinates.

During the development of the system as well as during the first measurements campaign, the cameras of the PIV measurement system were used (cf. section 2.2.2). Due to their given resolution and the small field of view conditioned by the available camera optics, the system had to be moved into several positions to measure a complete wing. As a result, the reconstructed wing geometries consists of several single measurements patched together. Moreover, simultaneous measurements of the upper and of the lower wing sides are not possible because the cameras had to be moved to the other side. In a later project stage, a set of four cameras with larger resolution and appropriate objectives were acquired. With this new system, both wing sides could be measured simultaneously by placing two cameras on each side of the test section. These cameras use CMOS-monochrome sensors with a resolution of 2592×1944 pixels. The focal length of 16 mm allows the complete wing to be measured in a single measurement with an averaged resolution of 2.3 pixels/mm. In order to increase the contrast and facilitate the recognition of the image points during the image processing, the markers placed on the wing surface are retro-reflective and a lighting system consisting of two 0.8 W LEDs placed on each camera were used.

For the calibration of each camera, a plane target of 1000×800 mm with an array of dots (spacing of 75 mm) was used as illustrated in Fig. 2.23. This target was moved into several z-positions to provides a three-dimensional array of points with known positions that can be used to evaluate Eq. 2.15 and obtain the eleven DLT parameters associated with each camera. The quality of the calibration can be assessed by using the transformation parameters to reconstruct the coordinates of the calibration points from the raw images of the target. With the setup used in

this work, an averaged reconstruction error lying below the pixel resolution of the cameras was obtained. Finally, the different steps involved in the procedure for the reconstruction of the wing geometry from the raw stereo-image pair are illustrated in Fig. 2.24. The mains steps consist in the recognition of the markers and their center in both images, the proper recognition of the corresponding markers, and the reconstruction of the three-dimensional coordinates from Eq. 2.16.

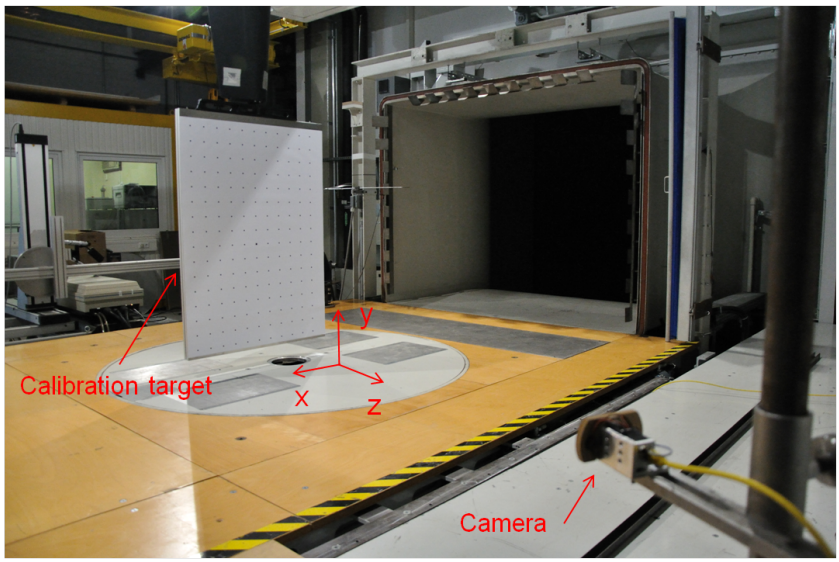

Figure 2.23: Illustration of the setup for calibration procedure of the stereo-photogrammetry measurement system.

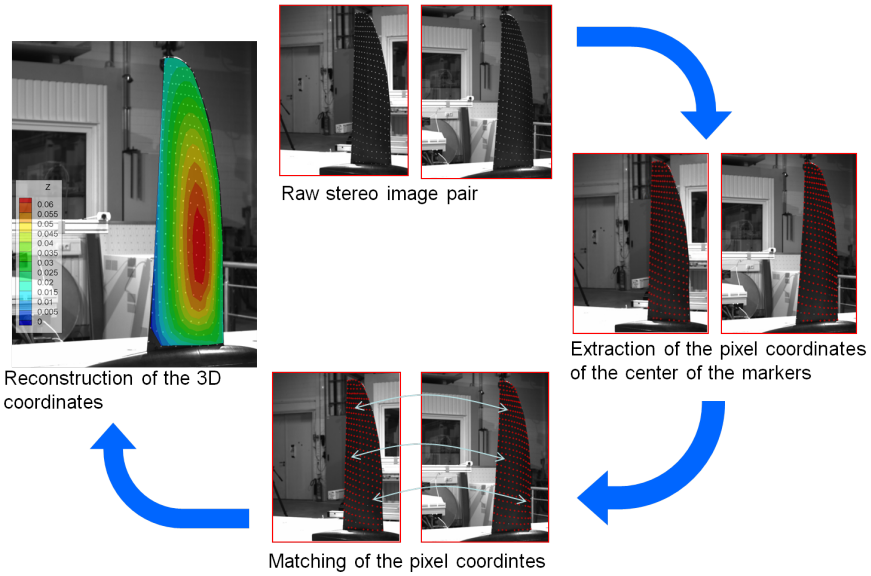

Figure 2.24: Illustration of reconstruction procedure with the stereo-photogrammetry measurement system.

2.3 Experimental setup and test parameters

2.3.1 Wind-tunnel facility and general setup

The experimental tests were carried out in the low-speed wind tunnel facility A of the Institute of Aerodynamics and Fluid Mechanics of the Technische Universität München (cf. Fig. 2.25). This Göttingen-type wind tunnel has an open test section which is 4.8 m long, 1.8 m high, and 2.4 m wide. It can generate free stream velocities up to 65 m/s with free-stream turbulence intensity below 0.4%.

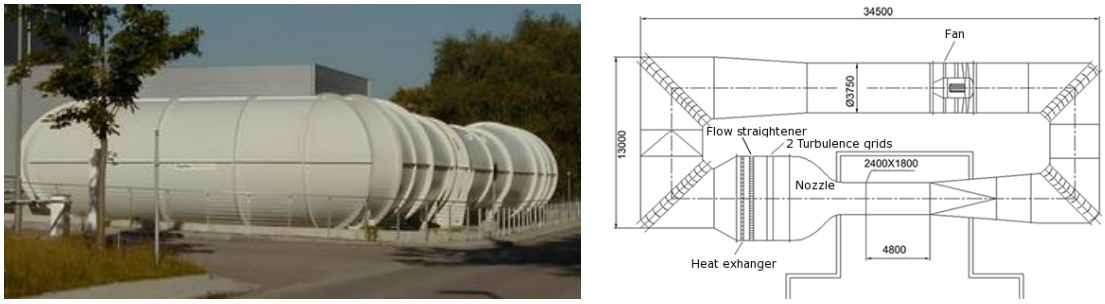

(a) View from outside

(b) Drawing showing the principal dimensions (in mm)

Figure 2.25: Illustration of the wind tunnel facility A of TU München [63].

Figure 2.26 shows the model installed in the wind tunnel test section. The wing is fixed to the aerodynamic balance placed under the floor of the test section. The wing root is elevated by 130 mm above the floor of the test section to avoid interactions with the floor boundary layer which has a thickness equal to 40-70 mm at the model position. A péniche is used for the aerodynamic fairing of the portion of the shaft exposed to the airflow as illustrated in Fig. 2.26. The péniche is only fixed to the floor of the test section and does not touch the model.

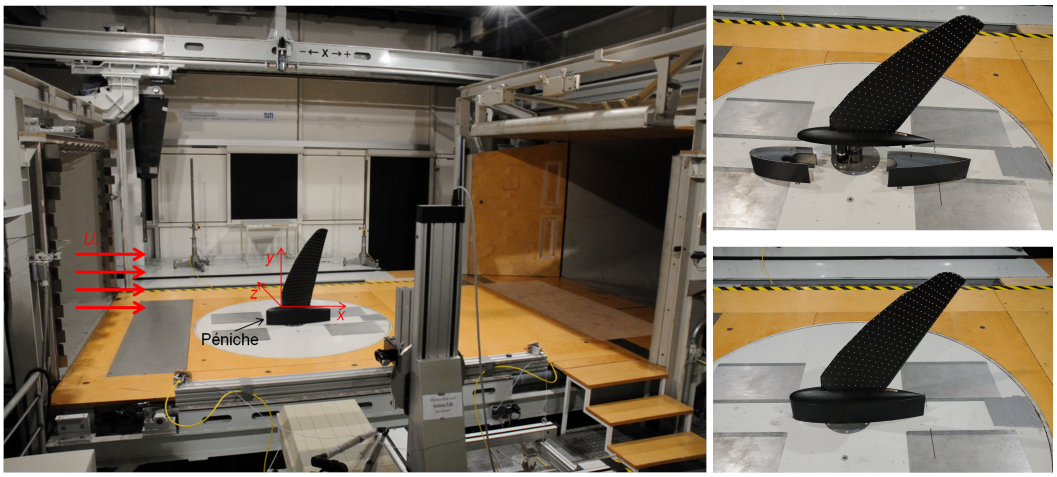

Figure 2.26: View of the wing model installed in the test section.

2.3.2 Test cases and test conditions

A total of five discrete planform configurations are considered in this work to assess the influence of the planform shape on the aerodynamic characteristics. These five configurations consist of the straight wing, the swept-back wing, and three intermediate configurations as illustrated in Fig. 2.27. The initial value of the root chord length (c_r) used for most of the tests was 0.27 m. Its variation was considered only to change the membrane pre-stress in a later stage of the investigations. For this, c_r values of 0.24 m, 0.26 m, 0.28 m, and 0.3 m were used with the straight wing, the intermediate 2, and the swept-back wing configurations. The geometric parameters of the resulting wing configurations as a function of the planform and root chord length are summarized in Table 2.4. The last column of Table 2.4 gives the values of the membrane pre-stress corresponding to the single position on the wing surface used in Fig. 2.13.

(a) Straight wing (b) Intermediate 1 (c) Intermediate 2 (d) Intermediate 3 (e) Swept-back wing

Figure 2.27: Illustration of the five wing configurations considered for the experimental tests (Ω varying with c_r = 0.27 m).

Configuration	Articulated structure		Planform parameters					Membrane
	Ω [°]	c_r [m]	S [m^2]	$b/2$ [m]	$\bar{c}$ [m]	$\mathcal{AR}$	$\phi_{1/4}$ [°]	σ_0 ($\cdot 10^5$) [Pa]
Straight wing	20	0.24	0.208	1.010	0.206	9.79	5.45	2.51
	20	0.26	0.218	1.010	0.216	9.33	5.16	3.25
	20	**0.27**	**0.224**	**1.010**	**0.221**	**9.12**	**5.02**	**3.67**
	20	0.28	0.228	1.010	0.226	8.92	4.88	4.14
	20	0.30	0.239	1.010	0.236	8.54	4.60	5.12
Intermediate 1	**30**	**0.27**	**0.229**	**0.923**	**0.248**	**7.45**	**15.00**	**5.19**
Intermediate 2	40	0.24	0.209	0.830	0.251	6.60	23.57	4.28
	40	0.26	0.217	0.830	0.262	6.35	23.27	5.01
	40	**0.27**	**0.221**	**0.830**	**0.267**	**6.23**	**23.13**	**5.41**
	40	0.28	0.226	0.830	0.272	6.11	22.98	5.83
	40	0.30	0.234	0.830	0.282	5.90	22.67	6.72
Intermediate 3	**50**	**0.27**	**0.206**	**0.731**	**0.282**	**5.18**	**30.53**	**4.61**
Swept-back wing	60	0.24	0.174	0.638	0.292	4.62	37.68	2.11
	60	0.26	0.180	0.638	0.302	4.46	37.39	3.00
	60	**0.27**	**0.183**	**0.638**	**0.307**	**4.38**	**37.26**	**3.47**
	60	0.28	0.186	0.638	0.312	4.31	37.11	3.95
	60	0.30	0.192	0.638	0.322	4.17	36.83	4.94

Table 2.4: Geometric parameters of the wing configurations considered in the experimental tests.

The wind tunnel tests were carried out at three different free-stream dynamic pressures corre-

sponding to q_∞ = 135 Pa, q_∞ = 310 Pa, and q_∞ = 545 Pa, which, using a constant air density of 1.2 kg/m^3, correspond to free-steam velocities of $U_\infty \approx$ 15 m/s, $U_\infty \approx$ 22.5 m/s, and $U_\infty \approx$ 30 m/s. The choice of these flow conditions is based on preliminary wind tunnel tests conducted to assess the amplitude of the membrane deflection. The three free-stream dynamic pressures retained lead to deformation amplitudes that can be categorized in low, middle, and large deformations, allowing thus a progressive investigation of the influence of the membrane deformation on the aerodynamic characteristics. The test conditions in terms of the free-stream dynamic pressure, free-stream velocity, and Reynolds number based on the mean chord of the two extreme wing planforms are summarized in Table 2.5. For the Reynolds number calculation, a kinematic viscosity $\nu = 1.6{\cdot}10^{-5}$ m^2/s was used. Force measurements were performed using angles of attack between -30° and +40° with steps of 1°. The blockage of the test section at the maximum angle of attack is below 4%. Therefore, blockage effects are assumed to be negligible. Tests with the remaining measurement techniques were carried out at selected angles of attack. Finally, the ratio of the membrane pre-stress to the free-stream dynamic pressure, as defined in Eq. 2.17, is a useful parameter for the analysis of the aero-elastic behavior of the wing. The values of this parameter associated with each planform configuration and flow condition are given in Table 2.6. To evaluate K_m, the values of σ_0 given in Table 2.4 are used.

$$K_m = \frac{\sigma_0}{q_\infty} \tag{2.17}$$

q_∞ [Pa]	U_∞ [m/s]	Re ($\cdot 10^6$)	
		Straight wing	Swept-back wing
135	15	0.23	0.30
310	22.5	0.345	0.45
545	30	0.46	0.60

Table 2.5: Test conditions.

The wind tunnel test campaigns carried out throughout the project can be categorized as follows. In a first stage of the investigation, the tests were carried out with the second version of the articulated wing structure (cf. section 2.1.1). The main goal was to obtain a comprehensive database of the aerodynamic characteristics as a function of the planform as well as to assess the influence of the membrane deformation. For this, force measurements were conducted with all five wing planforms listed in Table 2.4 using a constant root chord length of 0.27 m. The wool tufts and the flow field measurements were also performed in an early project stage with the same model version, but only with the straight wing and with the swept-back configurations. The results of these investigations are presented in chapter 5. All further test campaigns use the last version of the wing structure.

A test campaign was dedicated to the investigation of the effect of a variation of the membrane pre-stress on the membrane deflection. The tests included force and deformation measurements carried out on the straight wing, the intermediate 2, and the swept-back configurations using root chord lengths of 0.24 m, 0.26 m, 0.28 m, and 0.30 m. The results of these tests are presented in

$K_m = \sigma_0/q_\infty$		q_∞ [Pa]		
Configuration	c_r [m]	135	310	545
Straight wing	0.24	1859	810	461
	0.26	2407	1048	596
	0.27	**2719**	**1184**	**673**
	0.28	3067	1335	760
	0.30	3793	1652	939
Intermediate 1	**0.27**	**3844**	**1674**	**952**
Intermediate 2	0.24	3170	1381	785
	0.26	3711	1616	919
	0.27	**4007**	**1745**	**993**
	0.28	4319	1881	1070
	0.30	4978	2168	1233
Intermediate 3	**0.27**	**3415**	**1487**	**846**
Swept-back wing	0.24	1563	681	387
	0.26	2222	968	550
	0.27	**2570**	**1119**	**637**
	0.28	2926	1274	725
	0.30	3659	1594	906

Table 2.6: Values of the parameter K_m defined as the ratio of the membrane pre-stress to the free-stream dynamic pressure.

chapter 6.

The next measurement campaign was dedicated to the detailed investigation of the aero-elastic behavior of the wing. For this, force and deflection measurements were carried out simultaneously on the straight wing configuration with a constant root chord length of 0.27 m. The influence of the laminar to turbulent transition of the boundary layer on the fluid-structure interaction was also investigated within this measurement campaign. The results are presented in chapter 4.

Finally, the last measurement campaign was carried out with the alternative membrane covers presented in section 2.1.3.4. The tests included force and deformation measurements and were only carried out on the straight wing configuration with a constant root chord length of 0.27 m. These results are presented in chapter 6.

3 Numerical methods

3.1 Vortex-lattice simulations

Potential flow simulations based on the vortex-lattice method [47] were carried out to analyze the theoretical characteristics of planar rigid wings with planforms equivalent to the wind tunnel model. The program used for this is AVL (Athena Vortex Lattice [57]), a tool for the aerodynamic and flight-dynamic analysis of rigid aircraft of arbitrary configuration. Simulations were carried out for all wing configurations listed in Table 2.4 using 10 vortices in the chordwise direction and 100 vortices in the spanwise direction as illustrated in Fig. 3.1. Figures 3.2 to 3.4 as well as Table 3.1 show the simulation results in terms of the lift curve slope, the pitching moment slope, the aerodynamic center, and the span efficiency factor as a function of the wing configuration.

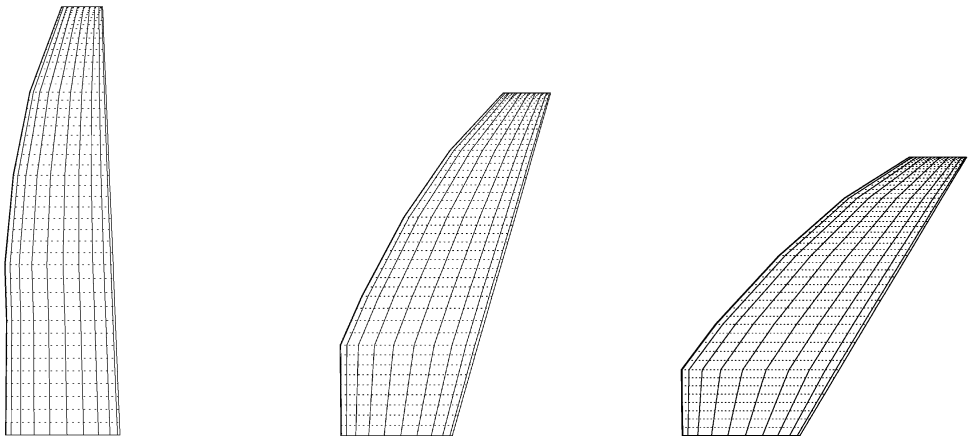

(a) Straight wing (b) Intermediate 2 (c) Swept-back wing

Figure 3.1: Wing models and discretization of the wing surface for the vortex lattice simulations.

Figure 3.2 shows the lift curve slope $C_{L,\alpha}$. It decreases as the planform changes from the straight wing to the swept-back wing configuration because of the decreasing aspect ratio. It decreases also with increasing root chord length according to the effect c_r has on the aspect ratio (Fig. 2.5d). The largest lift curve slope ($C_{L,\alpha} = 4.95$) is therefore obtained in the case of the straight wing configuration with $c_r = 0.24$ m. Accordingly, the smallest value ($C_{L,\alpha} = 3.43$) occurs in the case of the swept-back wing with $c_r = 0.3$ m.

The effect of the wing configuration on the slope of the pitching moment curve is shown in Fig. 3.3a. The reference location for the pitching moment is the quarter chord of the root section (i.e. $x_{ref} = 0.25c_r$). The quantity $\frac{dC_m}{dC_L}$ decreases as the planform changes from the straight wing

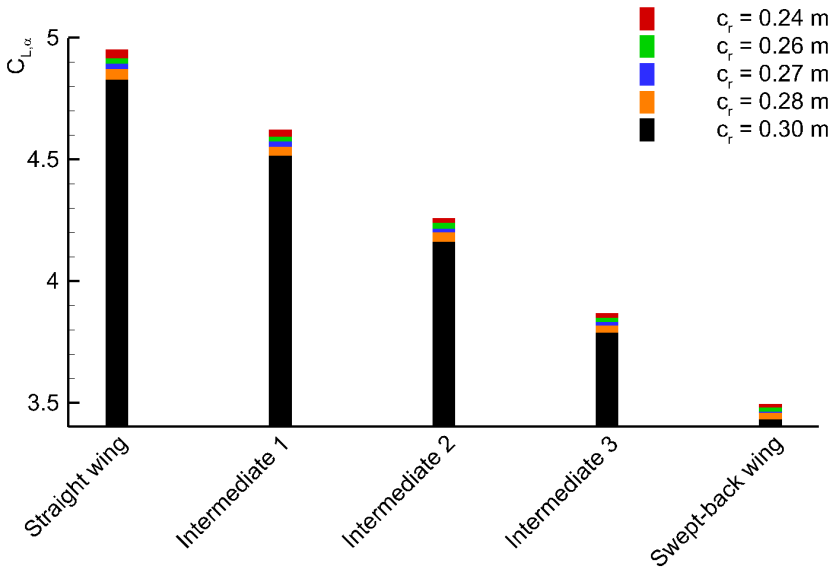

Figure 3.2: Lift curve slope as a function of the planform configuration.

to the swept-back wing configuration because of the increasing sweep angle. It also decreases with decreasing root chord length according to the effect c_r has on the sweep angle (Fig. 2.5e). Consequently, the smallest value ($\frac{dC_m}{dC_L}$ = -0.533) occurs in the case of the swept-back wing with c_r = 0.24 m, and the largest value ($\frac{dC_m}{dC_L}$ = -0.02) in the case of the straight wing with c_r = 0.3 m. The location of the aerodynamic center, evaluated from Eq. 1.13, is shown in Fig. 3.2b. Here, x_{ac} is expressed as the distance from the leading-edge of the root section. The aerodynamic center moves towards the trailing-edge as the planform changes from the straight wing to the swept-back wing configuration and with increasing root chord length according to the increasing sweep angle.

The effect of the wing planform on the span efficiency factor is shown in Fig. 3.4. The quantity e_s decreases as the planform changes from the straight wing to the swept-back wing configuration because the increasing sweep angle shifts the aerodynamic load towards the wing tip, and the resulting lift distribution differs even more from the ideal elliptical one (cf. section 1.3.2.1). Further, the highest values of e_s for a given configuration is always obtained with the largest root chord length. Therefore, the largest span efficiency factor (e_s = 0.9991) occurs with the straight wing and c_r = 0.3 m, and the smallest one (e_s = 0.9774) occurs with the swept-back wing and c_r = 0.24 m.

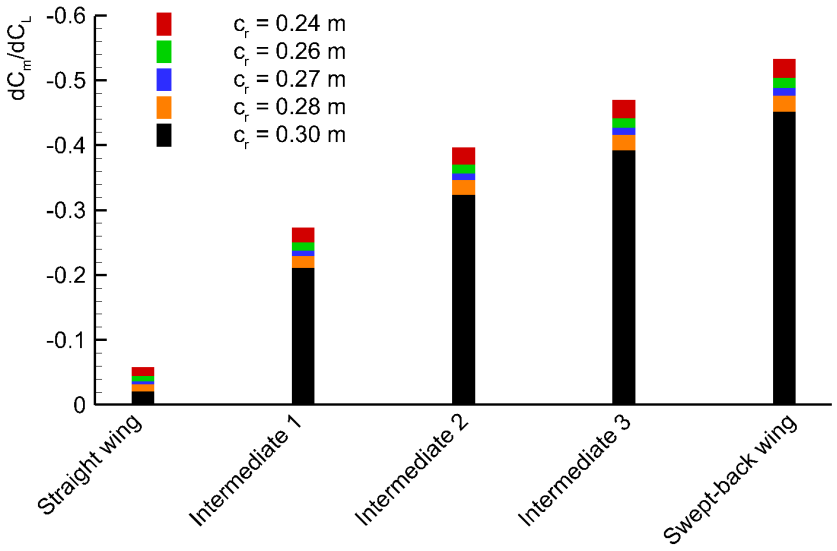

(a)

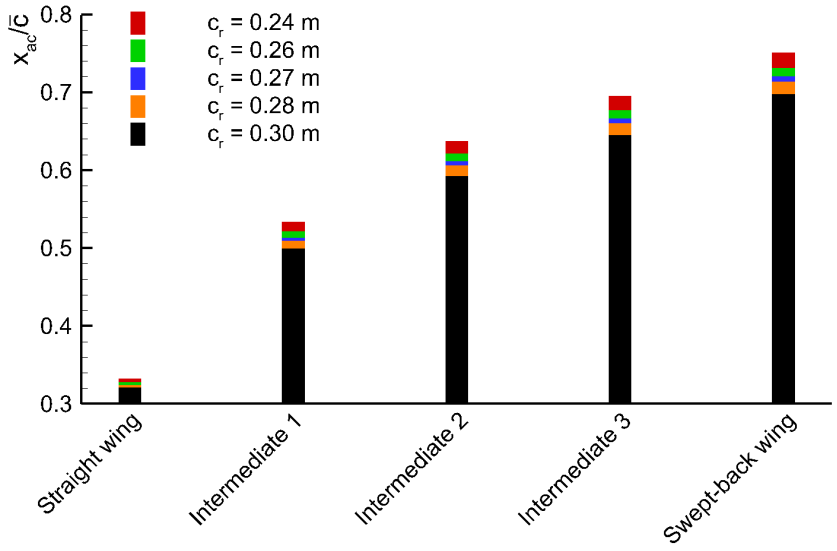

(b)

Figure 3.3: Pitching moment characteristics as a function of the planform configuration.

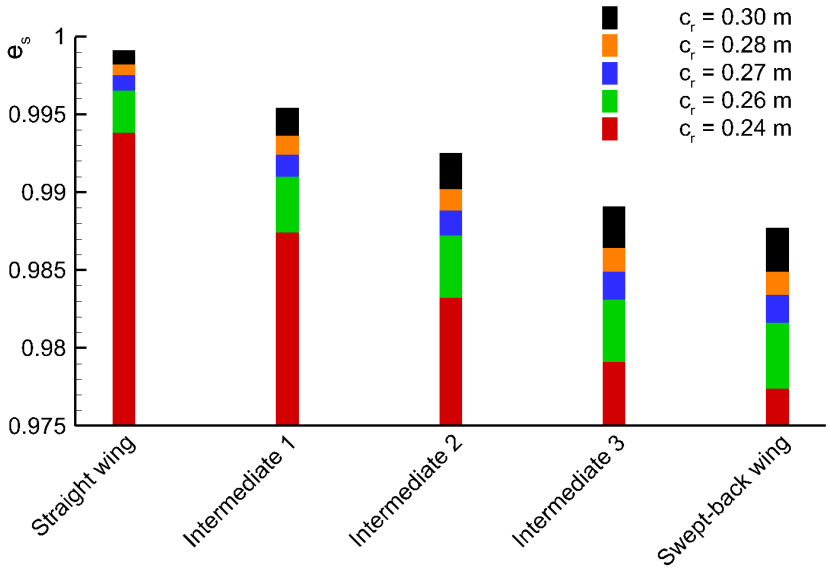

Figure 3.4: Span efficiency factor as a function of the planform configuration.

Configuration	Aerodynamic parameters				
	c_r [m]	$C_{L,\alpha}$	$\frac{dC_m}{dC_L}$	$x_{ac}/\bar{c}$	e_s
Straight wing	0.24	4.95	-0.058	0.332	0.9938
	0.26	4.91	-0.045	0.328	0.9965
	0.27	**4.89**	**-0.036**	**0.324**	**0.9980**
	0.28	4.87	-0.032	0.3243	0.9982
	0.30	4.83	-0.020	0.3212	0.9991
Intermediate 1	0.24	4.62	-0.273	0.534	0.9874
	0.26	4.59	-0.250	0.521	0.9910
	0.27	**4.57**	**-0.237**	**0.512**	**0.9924**
	0.28	4.55	-0.229	0.509	0.9936
	0.30	4.51	-0.210	0.499	0.9954
Intermediate 2	0.24	4.26	-0.397	0.638	0.9832
	0.26	4.24	-0.370	0.621	0.9872
	0.27	**4.21**	**-0.356**	**0.611**	**0.9888**
	0.28	4.19	-0.346	0.606	0.9902
	0.30	4.16	-0.323	0.592	0.9925
Intermediate 3	0.24	3.87	-0.470	0.695	0.9791
	0.26	3.85	-0.442	0.677	0.9831
	0.27	**3.83**	**-0.427**	**0.667**	**0.9849**
	0.28	3.81	-0.416	0.660	0.9864
	0.30	3.78	-0.392	0.645	0.9891
Swept-back wing	0.24	3.49	-0.533	0.751	0.9774
	0.26	3.47	-0.503	0.731	0.9816
	0.27	**3.46**	**-0.488**	**0.721**	**0.9834**
	0.28	3.45	-0.477	0.714	0.9849
	0.30	3.43	-0.452	0.697	0.9877

Table 3.1: Aerodynamic characteristics of the morphing wing as a function of the planform configuration based on vortex lattice potential flow simulations.

3.2 Fluid-structure simulation of elastic membrane airfoils

This section presents the program that was developed for the simulation of elastic membrane airfoils with a construction similar to a section of the wind tunnel model. It was initially developed with the main goal to help designing the leading-edge spar of the wind tunnel model. In a later stage of the investigation, it was also used for the detailed investigations of the aero-elastic characteristics of this type of wing construction and complement the experimental results.
This program is based on an analytical formulation for the membrane equilibrium coupled with the viscous/inviscid flow solver Xfoil [60]. The advantage is that it requires very few computational resources and simulation results are usually obtained within few seconds.

3.2.1 Elastic membrane airfoil model

The elastic membrane airfoil model introduced in the following is based on the work presented in Ref. [41]. The airfoil structure dealt with consists of a rigid leading-edge spar with a membrane wrapped around as illustrated in Fig. 3.5. The membrane has a thickness t and is assumed to be made out of a linear elastic material with a modulus of elasticity E_m. The membrane is further fixed at the leading-edge ($x = 0$) and at the trailing-edge ($x = c$). As a result, there is no structural interaction between the airfoil upper and lower sides (index u and l, respectively) and they are treated separately. Between $x = 0$ and a certain position $x = x_s$ where the membrane separates from the spar, the airfoil geometry is given by the shape of the spar (i.e. $z_{LE}(x)$). For $x > x_s$, the shape of the airfoil is determined by the deflected membrane and has to be calculated by solving the equation given by Eq. 3.1. This equation expresses the relation between the curvature of the membrane, $\frac{d^2z(x)}{dx^2}$, the pressure difference across it, $\Delta P = P_o - P_i$, and the tension in it, T. The inner pressure, P_i, is in this model assumed to be equal to the free-stream static pressure, P_∞. Finally, the tension is assumed to be constant all along the membrane, which is correct if the skin friction and the friction between the membrane and the spar are neglected.

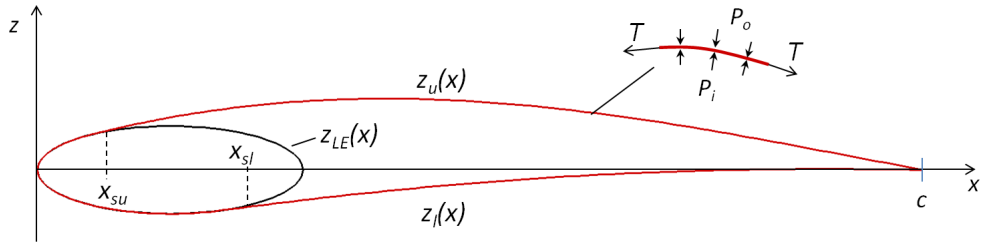

Figure 3.5: Description of the elastic membrane airfoil model.

$$\frac{d^2z(x)}{dx^2} = \frac{\Delta P(x)}{T} \tag{3.1}$$

The boundary conditions for Eq. 3.1 according to this problem are given by Eqs. 3.2 to 3.4. The condition 3.2 ensures that the membrane lies on the spar at the position where it separates from it (i.e. $x = x_s$). The condition 3.3 ensures that the separation occurs smoothly by imposing the

slope of the membrane to be the same as the slope of the leading-edge spar. The condition 3.4 fixes the coordinate of the trailing-edge at $z = 0$.

$$z(x_s) = z_{LE}(x_s) \tag{3.2}$$

$$\left.\frac{dz(x)}{dx}\right|_{x=x_s} = \left.\frac{dz_{LE}(x)}{dx}\right|_{x=x_s} \tag{3.3}$$

$$z(c) = 0 \tag{3.4}$$

The general form of the solution of Eq. 3.1 can be obtained analytically by integrating it twice between x_s and x as given by Eq. 3.5. The two integration constants that results, C_1 and C_2, and the membrane tension, T, can be determined using the boundary conditions 3.2 to 3.4. Their expression are given in Eqs. 3.6 to 3.8.

$$z(x) = \frac{1}{T}\int_{x_s}^{x}\int_{x_s}^{x}\Delta P(x)dxdx + C_1 x + C_2 \tag{3.5}$$

$$C_1 = \left.\frac{dz_{LE}(x)}{dx}\right|_{x=x_s} \tag{3.6}$$

$$C_2 = z_{LE}(x_s) - C_1 x_s \tag{3.7}$$

$$T = -\frac{\int_{x_s}^{c}\int_{x_s}^{c}\Delta P(x)dxdx}{(c-x_s)C_1 + z_{LE}(x_s)} \tag{3.8}$$

Equation 3.5 along with the expressions for the integration constants and for the tension allows to compute the shape of the membrane as a function of x_s which is still unknown. In order to determine the value of x_s giving the right solution, a further condition is required. The criteria used for this concerns the length of the membrane. In fact, all values of x_s give a solution of Eq. 3.1 that is mathematically correct, but only one leads to a membrane which length is in accordance with its elongation due to the aerodynamic load. On the one hand, the relative elongation of the deflected membrane, ε_m, is expressed by the relation given in Eq. 3.10, where l_0 and l are the lengths of the unloaded and of the deflected membranes, respectively, as illustrated in Fig. 3.6. The length of the membrane is computed with Eq. 3.9. On the other hand, the relative elongation due to the aerodynamic load, ε_T, can be calculated by Eq. 3.11. The variable ε_0 defines the initial elongation (pre-strain) of the membrane. In order to find the right value of x_s, the following procedure is used. For a given pressure distribution, the airfoil shape and the tension are computed for a series of x_s values along the leading-edge spar. For each values of x_s, the elongations ε_m and ε_T are computed. The value of x_s providing the airfoil shape that satisfies the equilibrium between the aerodynamic and the elastic forces is determined by the point where $\varepsilon_m(x_s)$ and $\varepsilon_T(x_s)$ cross.

$$l = \int_0^c \sqrt{1+\left(\frac{dz(x)}{dx}\right)^2}\,dx \tag{3.9}$$

$$\varepsilon_m = \frac{l-l_0}{l_0} \tag{3.10}$$

$$\varepsilon_T = \frac{T}{E_m t} - \varepsilon_0 \tag{3.11}$$

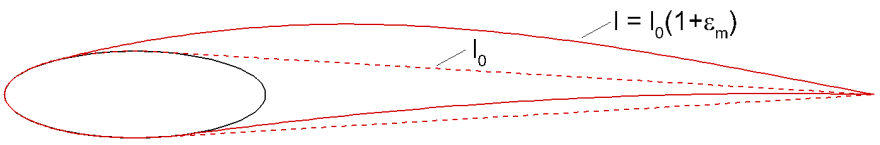

Figure 3.6: Sketch illustrating the lengths of the unloaded and of the loaded membrane.

The procedure presented for the computation of the deflected airfoil shape corresponding to a given pressure load (i.e. ΔP) has been implemented in a Matlab script. The integrations in Eqs. 3.5 to 3.8 are done using a trapezoidal method. Because the airfoil upper and lower sides are treated separately, the above procedure has to be applied twice in order to compute the complete airfoil geometry.

3.2.2 Coupling with the viscous/inviscid flow solver Xfoil

The pressure distribution around the airfoil is computed with Xfoil, an interactive program for the design and analysis of subsonic isolated airfoils (Drela [58, 59]). It is based on a linear-vorticity panel method coupled with a viscous boundary layer formulation that enables taking into account viscous effects such as parasitic drag and flow separation. As illustrated in Fig. 3.7, the two-dimensional flow field around the airfoil is constructed by superposing a free-stream flow with a vortex sheet ($\gamma(s)$) on the airfoil surface. The boundary layer is calculated from a two-equations formulation for the momentum and kinetic energy shape parameters. In turn, the influence of the boundary layer on the potential flow is modeled by superposing a source distribution ($\sigma(s)$) on the airfoil surface and in the wake to account for the mass defect. Xfoil can treat both laminar and turbulent boundary layers. The transition point can either be determined by the embedded e^N-type amplification formulation method (Ingen et al. [62]), or forced to occur at a user-defined location along the chord (x_{tr}).

In order to simulate the two-way fluid-structure interaction between the airfoil shape and the flow field, Xfoil is coupled with the elastic membrane airfoil model presented in the previous section and both solvers are executed iteratively until the airfoil lift coefficient has converged to a constant value. The flow chart diagram of Fig. 3.8 illustrates this procedure.

The inputs required by the program consist of a series of parameters related to the structure of the airfoil, and a series of parameters defining the flow condition. The structure of the airfoil is defined by the chord length, c, the geometry of the leading edge spar, $z_{LE}(x)$, the membrane

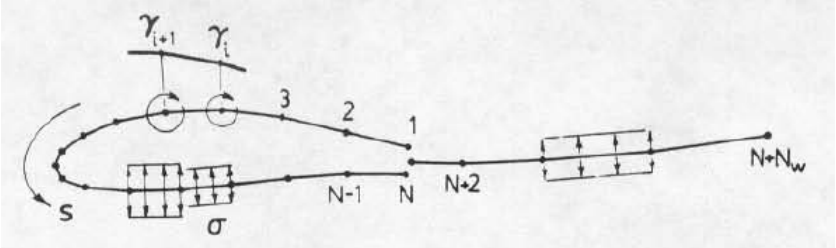

Figure 3.7: Modeling of the potential flow around an airfoil with the panel method in Xfoil [58].

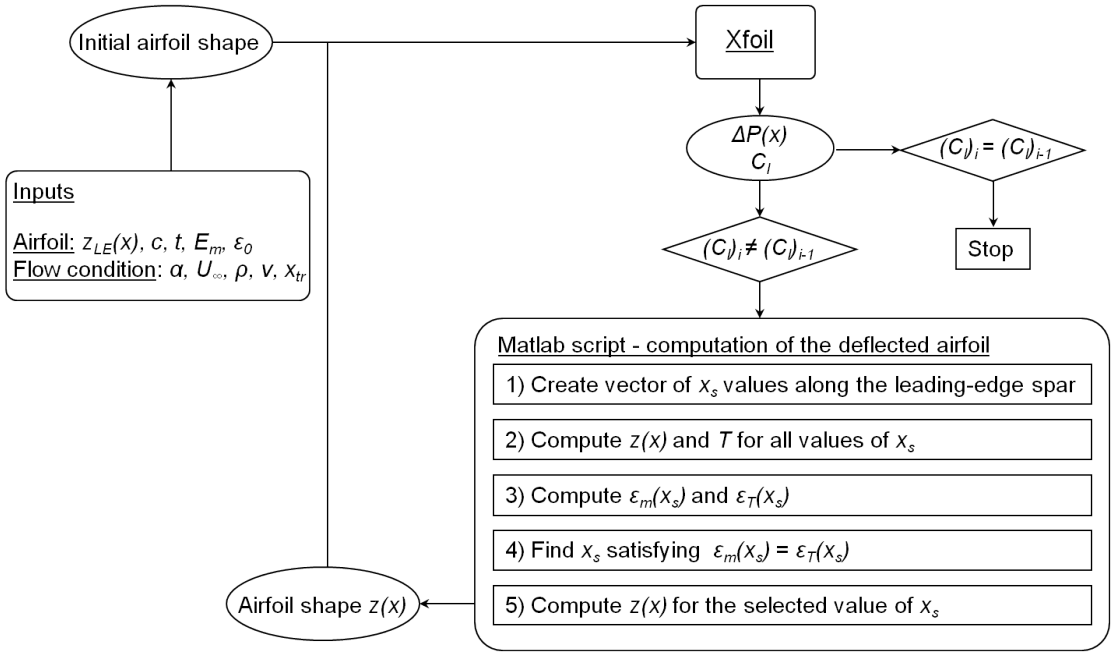

Figure 3.8: Flow chart diagram illustrating the iterative procedure to calculate the deflected shape of an elastic membrane airfoil.

thickness, t, its elasticity modulus, E_m, and the pre-strain, ε_0. The flow conditions are defined by the angle of attack, α, the free-stream velocity, U_∞, the fluid density, ρ, and the kinematic viscosity, ν. Xfoil can be executed in the viscous or in the inviscid mode, depending on whether the boundary layer has to be taken into account or if only an inviscid analysis is performed. In the inviscid mode, Xfoil only requires the angle of attack α. In the viscous mode, the Reynolds number, Re, has to be provided in addition, which is calculated from the remaining parameters as $Re = \frac{U_\infty c}{\nu}$. The last parameter, x_{tr}, can be used to set the laminar-turbulent transition at a fixed location and override the prediction from the e^N method. For the first iteration, an initial airfoil geometry with a straight membrane between the leading-edge spar and the trailing edge (unloaded membrane, cf. Fig. 3.6) is constructed and used to calculate an initial pressure distribution. The iterations are stopped when the change in lift coefficient is below a given criteria. Figure 3.9 illustrates the convergence of the program.

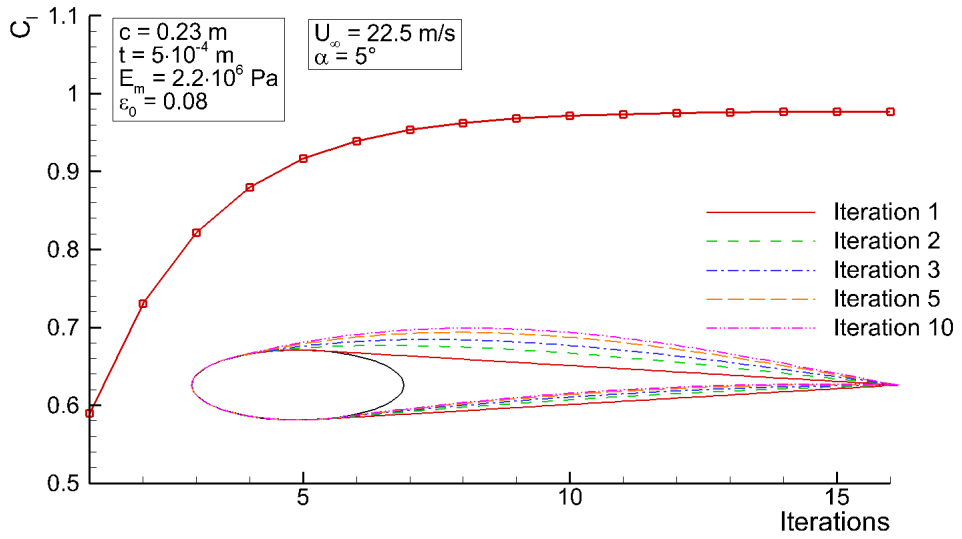

Figure 3.9: Illustration of the program convergence (inviscid simulation).

3.2.3 Design of the leading-edge spar of the wind tunnel model

The program presented above was used for the design of the leading-edge spar of the wind tunnel model (cf. section 2.1). The goal was to find a cross section geometry that avoids sharp suction peaks and strong adverse pressure gradients. To carry out this study, the leading-edge spar was modeled with two superposed half ellipses having the same principal axis, a, and different secondary axis, b_u and b_l, respectively. The spar can further be tilted with an angle ξ about the leading-edge as illustrated in Fig. 3.10. With this parameterization, a large variety of shapes can be generated by varying four parameters. The spar geometry was systematically varied until an appropriate shape satisfying the criteria of smooth pressure distribution around the leading-edge was obtained (trial-and-error procedure). An overview of the results is presented in the following to illustrate the effect of the leading-edge spar geometry on the inviscid pressure distribution.

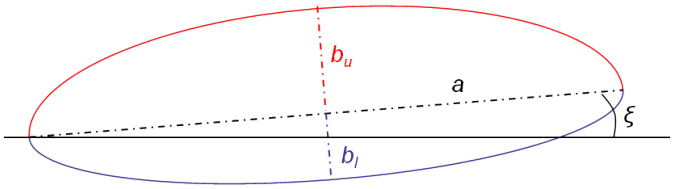

Figure 3.10: Parameterization of the leading-edge spar geometry modeled as two superposed half ellipses.

Figure 3.11 shows the deflected airfoil shapes and the corresponding pressure distributions obtained from inviscid simulations with a rounded spar, a symmetric elliptic spar, and an asymmetric spar. The latter is the one used for the wind tunnel model. The values for the membrane thickness, the elasticity modulus, and the pre-strain used for these simulations are based on the real parameters of the wind tunnel model (cf. section 2.1). The results shown here correspond to simulations carried out with an angle of attack of $\alpha = 5^{\circ}$, and at three different free-stream dy-

namic pressures which correspond to the flow conditions used in the experimental investigations (cf. section 2.3.2). The results show the large effect the flow conditions have on the amplitude of the deflection and, thus, on the airfoil geometry. This dependency is extensively discussed in chapter 4. Concerning the influence of the spar geometry on the pressure distribution around the leading edge, the results show that with a simple rounded spar (Fig. 3.11a), large suction peaks with strong adverse pressure gradients occur at the leading-edge. With the elliptic spar (Fig. 3.11b), the intensity of the suction peak is reduced but a strong adverse pressure gradient is still present behind the pressure minimum. A real improvement can only be reached with an asymmetric spar as shown in Fig. 3.11c. In this case, the rotation of the spar about the leading-edge has a similar effect on the pressure distribution than a leading-edge flap has. The geometric parameters associated with this spar, which is the one used for the wind tunnel model, are given in Table. 3.2.

Parameter	Value
a	approx. 25% of the chord
b_u	$0.4a$
b_l	$0.23a$
ξ	8°

Table 3.2: Parameters of the leading-edge spar geometry used for the wind tunnel model.

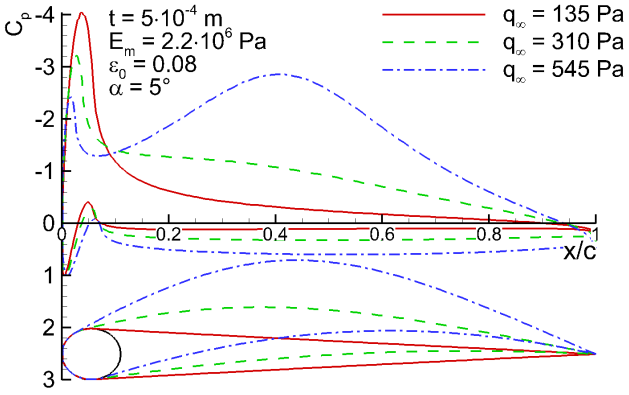

(a) Rounded

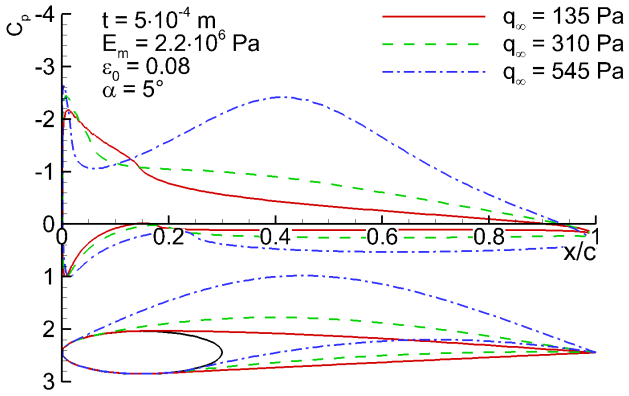

(b) Symmetric elliptic

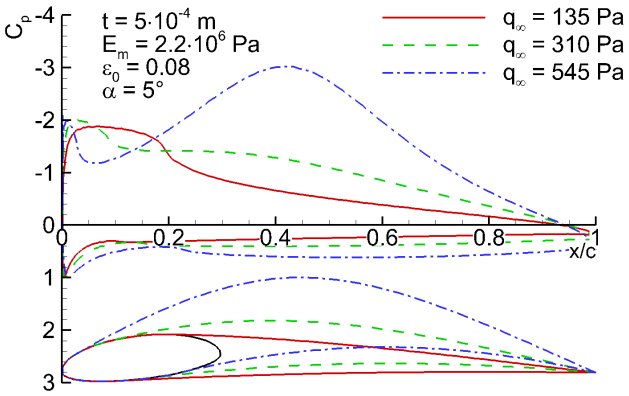

(c) Asymmetric

Figure 3.11: Influence of the leading-edge spar geometry and flow conditions on the pressure distribution and deflected airfoil shapes (inviscid simulations).

4 Aero-elastic behavior of the wing

This chapter aims at describing the aero-elastic behavior of the wing. This includes the detailed analysis of the deflected wing shapes as a function of the wing planform and flow conditions and a discussion of the resulting effects on the lift and drag characteristics. Also, the influence of the laminar-turbulent boundary layer transition on the fluid-structure interaction is discussed. The results presented in this chapter originate from measurement campaigns carried out with the last version of the wind tunnel model (cf. section 2.1.1) and with a constant root chord length of 0.27 m.

4.1 Deflection of the wing surface

4.1.1 Overview

Figure 4.1 shows the deflection of the suction and pressure sides of the straight wing configuration measured at $q_\infty = 135$ Pa, $q_\infty = 310$ Pa, and $q_\infty = 545$ Pa with $\alpha = 10^\circ$. The black dots indicate the position of the markers distributed on the wing surface for the stereo-photogrammetry measurements. The deflection Δz is defined as the difference in the z-coordinate between the loaded and the unloaded wing geometry. An area of the wing at the root of both wing sides and at the tip of the suction side are missing because the measurements were performed with the first camera system which had a limited field of view due to the available camera optics (cf. section 2.2.4.4). Finally, the deflected wing shapes presented here are reconstructed from instantaneous measurements.

At positive angles of attack, the suction force on the suction side and the pressure force on the pressure side deflect the membrane cover into the positive z-direction (i.e. $\Delta z > 0$). The maximum deflection of the suction side occurs around 30% span, and of the pressure side around 40% span. Further, the deflection of the suction side is always larger than the deflection of the pressure side. The reasons for this are that on the one hand the pressure load on the pressure side is generally smaller at positive angles of attack. On the other hand, the membrane on the pressure side touches the upper and lower arm segments of the articulated structure (cf. section 2.1.1) as it deflects, which also limits the deformation. The influence of these structure elements is visible below 20% span where the region with smaller values of Δz occur. Although similar deflection patterns occur at all free-stream dynamic pressures, the amplitude differs dramatically. At q_∞ = 135 Pa, the maximum deflection is around Δz = 0.006 m on the suction side and around Δz = 0.0035 m on the pressure side. At q_∞ = 545 Pa, the deflection is one order of magnitude larger with a maximum of Δz = 0.043 m on the suction side and Δz = 0.013 m on the pressure side.

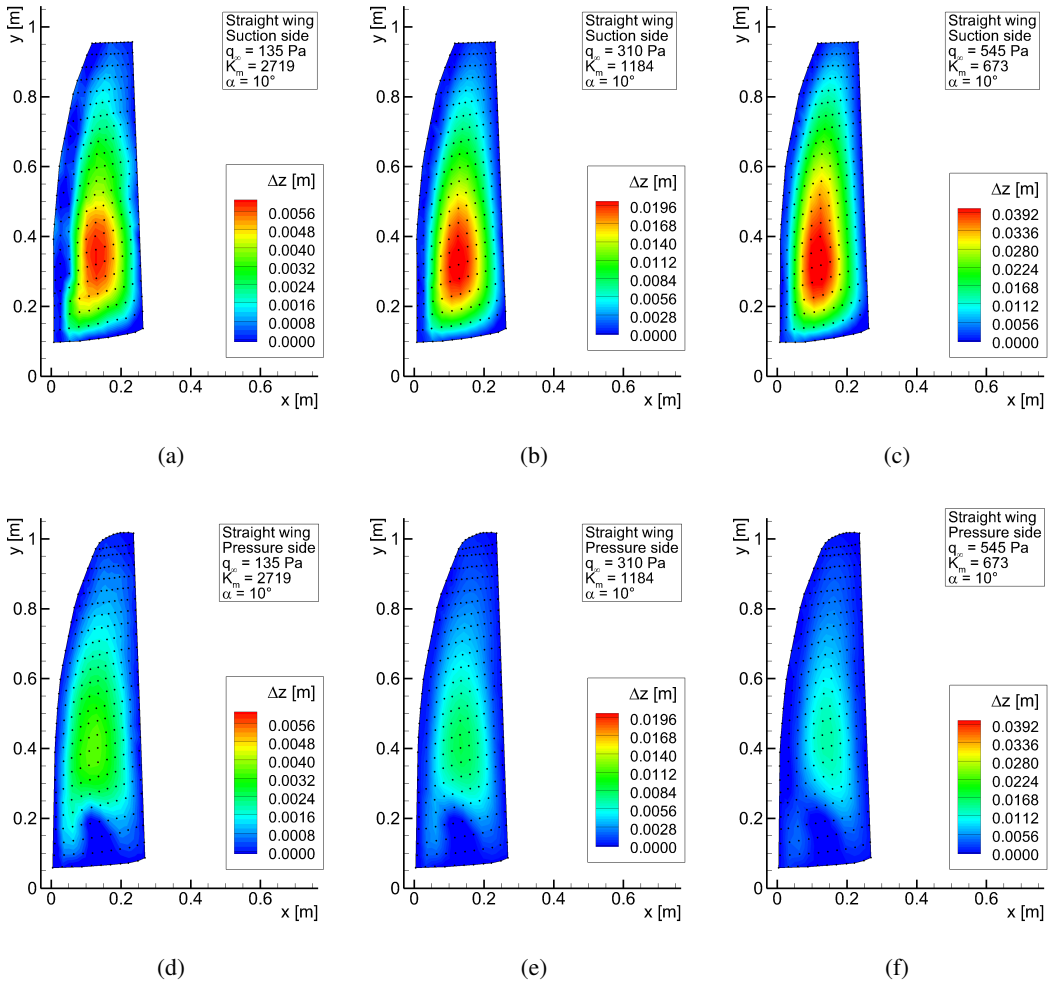

Figure 4.1: Deflection of the wing surface at $\alpha = 10^{\circ}$, straight wing configuration (instantaneous measurement).

Figures 4.2 and 4.3 show the deflection of the wing surface of the intermediate 2 and of the swept-back wing configurations, respectively. The same contour levels as in Fig. 4.1 are intentionally used for a direct assessment of the planform influence on the deflection amplitude. The membrane deflection for these configurations show similar characteristics as for the straight wing presented above. Indeed, the maximum deflection of the suction side occurs also around 30% span, and the deflection of the pressure side is also smaller. However, the amplitude of the deflection differs strongly. The intermediate 2 configuration (cf. Fig. 4.2) exhibits always the smallest deflection at a given flow condition, because the membrane pre-stress associated with this wing planform is comparatively large as discussed in section 2.1.3.3. This is also well reflected by the larger value of K_m (ratio of the membrane pre-stress to the free-stream dynamic pressure, cf. section 2.3.2) associated with this configuration. Also, the intermediate 2 configuration has a smaller aspect ratio than the straight wing and therefore the wing surface is subjected to comparatively smaller loads at equivalent flow conditions, which also contributes to the smaller deflection amplitude. The deflection of the surface of the swept-back wing (cf. Fig. 4.3) is larger than that of the intermediate 2 configuration, but also much smaller than that

of the straight wing, although it is associated with a membrane pre-stress and K_m values similar as the straight wing. In this case, the smaller deflection amplitudes are uniquely attributed to the smaller aerodynamic load conditioned by the reduced aspect ratio.
The results presented here indicate that the influence of the wing planform on the membrane deflection (i.e. the wing shape) is twofold because the planform influences simultaneously the membrane pre-stress and the aerodynamic load acting on the wing surface.

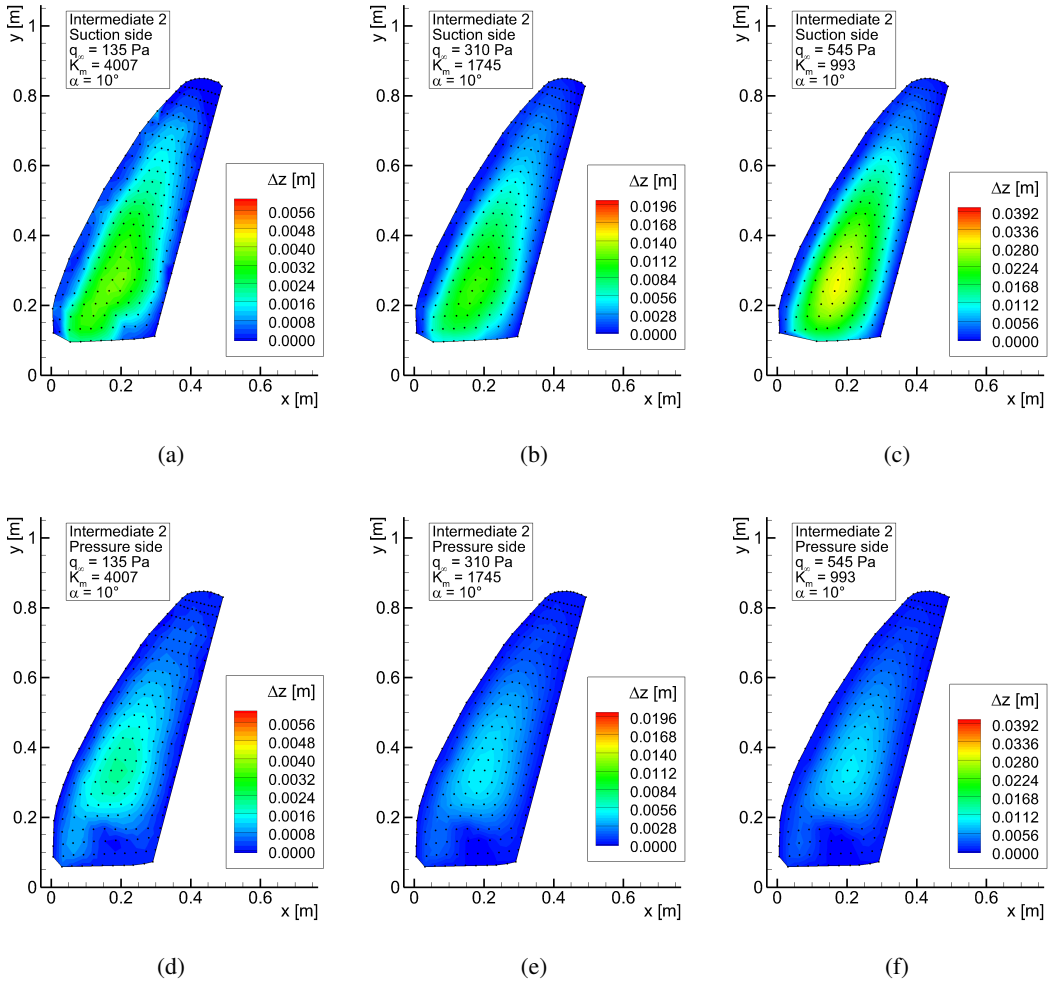

Figure 4.2: Deflection of the wing surface at $\alpha = 10^{\circ}$, intermediate 2 configuration (instantaneous measurement).

The deflection measurements performed on both wing sides can be combined to analyze the camber and thickness of the wing. Figure 4.4 shows the effect of the free-stream dynamic pressure and of the wing configuration on the geometry of a wing section located at $2y/b = 0.3$ ($\alpha = 10^{\circ}$). As discussed above, the membrane deflection at $q_{\infty} = 135$ Pa is small and the camber and thickness of the wing remain small accordingly. However, the wing shape changes dramatically as the free-stream dynamic pressure increases. The straight wing configuration exhibits comparatively the largest thickness and camber because it is associated with smaller membrane

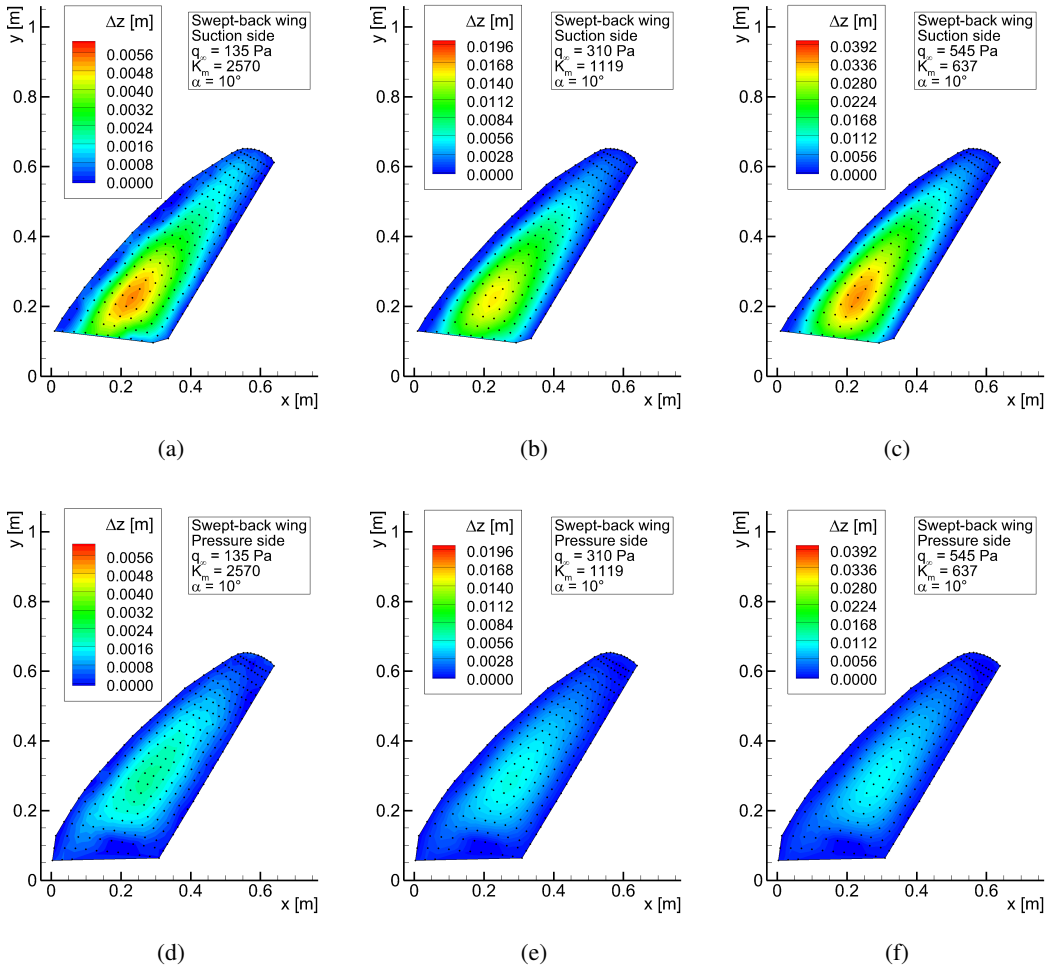

Figure 4.3: Deflection of the wing surface at $\alpha = 10^{\circ}$, swept-back wing configuration (instantaneous measurement).

pre-stress and larger aerodynamic loads due to its large aspect ratio as discussed above. The airfoil shapes corresponding to the intermediate 2 and to the swept-back configurations exhibit a much smaller camber according to the smaller deflection of the wing surface associated with these two configurations. Figure 4.5 presents a comparison of the spanwise distribution of the relative camber and relative thickness corresponding to the straight wing, the intermediate 2, and the swept-back wing configurations occurring at $\alpha = 10^{\circ}$ and with $q_{\infty} = 135$ Pa, $q_{\infty} = 310$ Pa, and $q_{\infty} = 545$ Pa. The dashed line placed at $2y/b = 0.3$ indicates the spanwise position corresponding to the airfoil shapes shown in Fig. 4.4. The maximum camber occurs always between $2y/b = 0.3$ and $2y/b = 0.4$. In contrast, the relative thickness reaches its maximum at spanwise positions below that, because the upward deflection of the pressure side is limited by the structure elements as discussed above. The membrane on the suction side is free to deflect, explaining thus the large thickness. At all flow conditions, the camber and the thickness are always the largest for the straight wing. At $q_{\infty} = 545$ Pa, this configuration exhibits a pronounced camber with a maximum of $f/c = 0.127$ and a thickness of $t/c = 0.24$ at $2y/b = 0.34$. The intermediate 2 and the swept-back wing configurations at this flow condition show more usual wing shape

with relative cambers below 0.1 and relative thicknesses around 0.12.

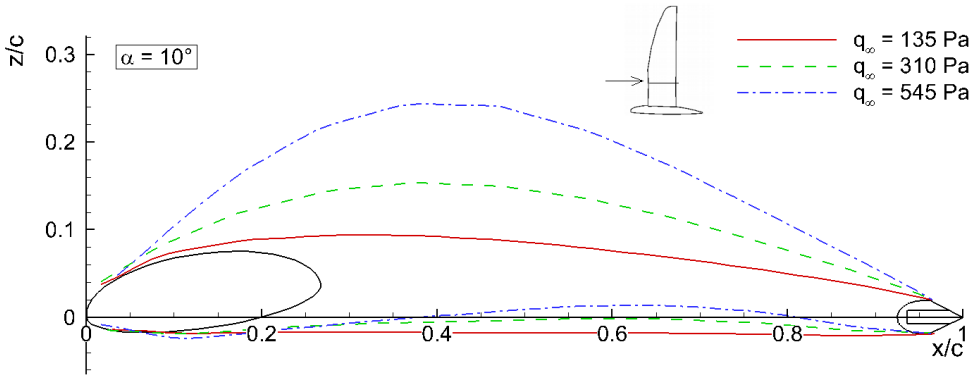

(a) Straight wing

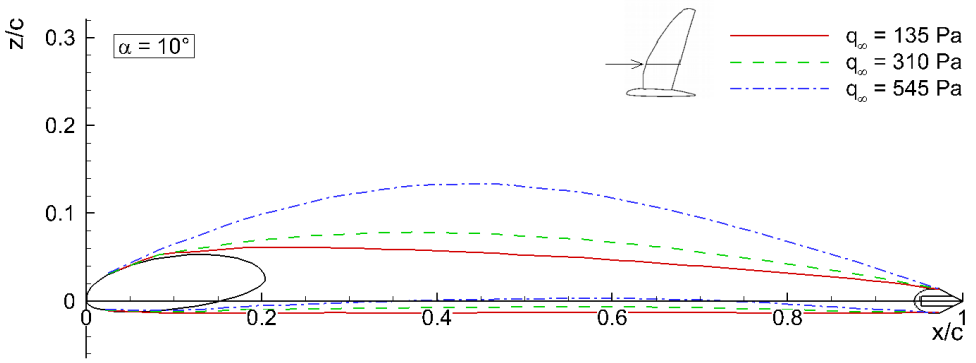

(b) Intermediate 2

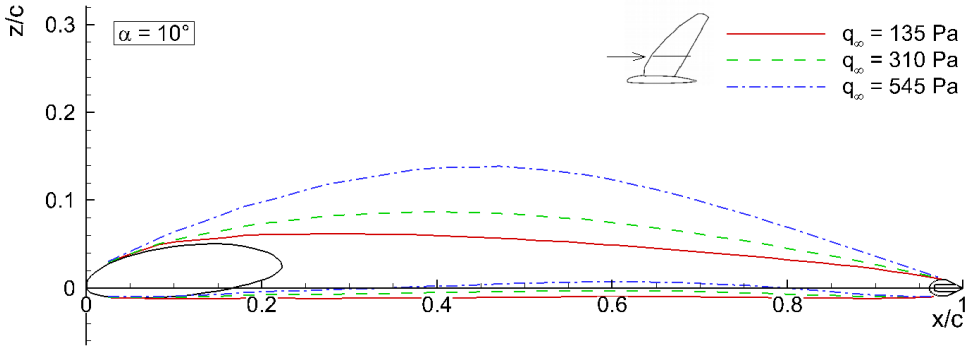

(c) Swept-back wing

Figure 4.4: Deflected airfoil shapes at $2y/b = 0.3$.

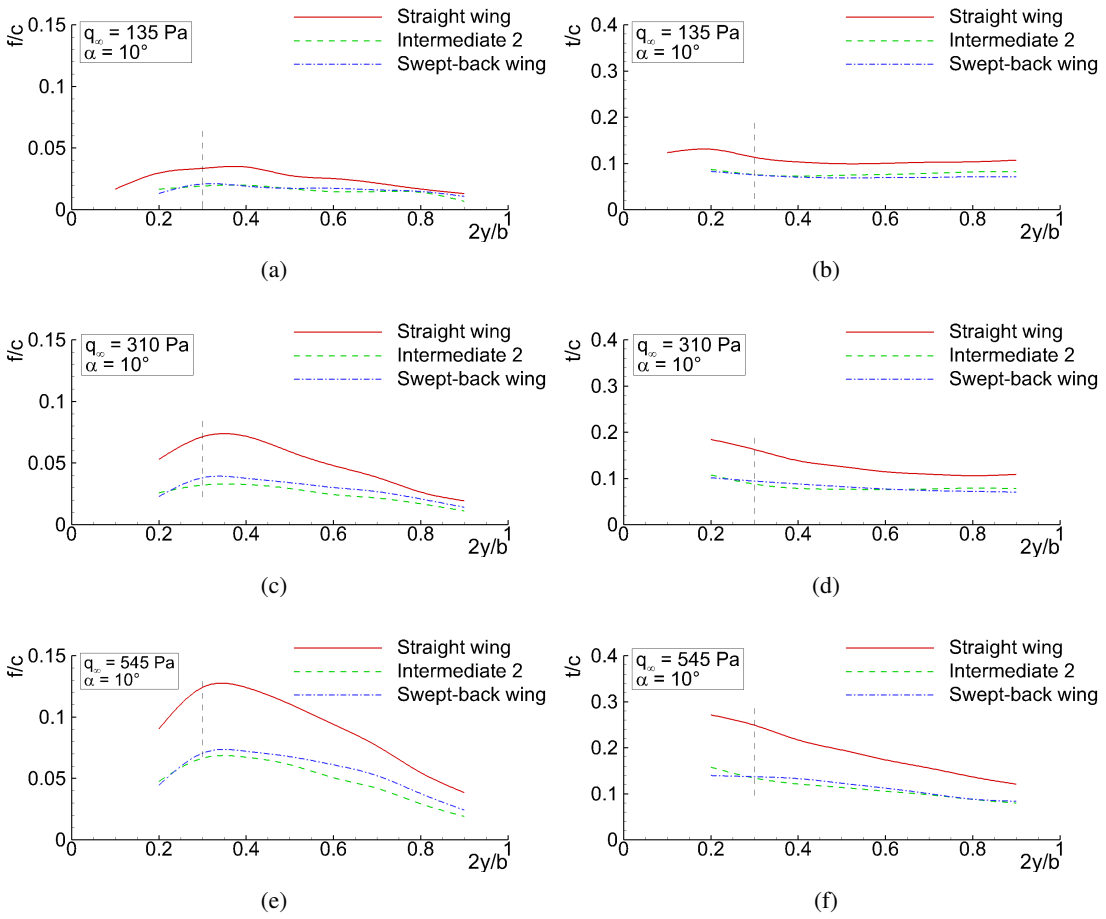

Figure 4.5: Effect of the flow conditions and planform configuration on the spanwise camber and thickness distributions.

4.1.2 Passive airfoil morphing

The results presented so far illustrated the overall dependency of the wing shape on the free-stream dynamic pressure at constant angle of attack. However, the wing shape shows a pronounced dependency on the angle of attack, too. In the following, this dependency is analyzed based on results from detailed measurements performed on the straight wing configuration. During these measurements, a single row of markers placed at $2y/b = 0.3$ was used to measure the deflected airfoil shape instead of placing markers over the complete wing surface as for the measurements presented in Figs. 4.1 to 4.3. The reason for this is that the markers disturb the surface flow, which was found to have an important impact on the fluid-structure interaction at some conditions (cf. section 4.2). Using a single row of markers allows capturing the deflected wing shapes while minimizing the disturbance of the surface flow. Further, the airfoil shapes presented in the following are statistically averaged from hundred instantaneous measurements. The standard deviation of the z-coordinate is used as a measure for the membrane vibration. Error bars indicating it are included in the plots in the case where it is significant.

Figure 4.6a presents the effect of the angle of attack on the deflected wing shapes of the straight wing measured at $q_\infty = 310$ Pa. The angle of attack influences the amplitude and the direction of

the deflection and, thus, the amplitude and the sign of the camber. At positive angles of attack, the pressure distribution around the wing is such that both the wing lower and upper sides are deflected in the positive z direction and the wing features a positive camber. At negative angles of attack, the opposite occurs since both wing sides are deflected downwards, resulting in a negative camber. At $\alpha = 0^{\circ}$, both wing sides deflects into opposite directions resulting in a fairly symmetric airfoil shape. As long as no trailing-edge flow separation occurs, the amplitude of the deflection increases with increasing angle of attack and the membrane does not vibrate significantly. As the angle of attack is further increased, trailing-edge flow separation occurs and the deflection of the wing upper side decreases as a result of the decreasing suction load associated with the separated flow (cf. Fig. 4.6b). Further, the turbulent separated flow causes significant vibrations of the wing surface as indicated by the error bars showing the standard deviation of the z coordinate of the airfoil shapes corresponding to $\alpha = 15^{\circ}$ and $\alpha = 20^{\circ}$.

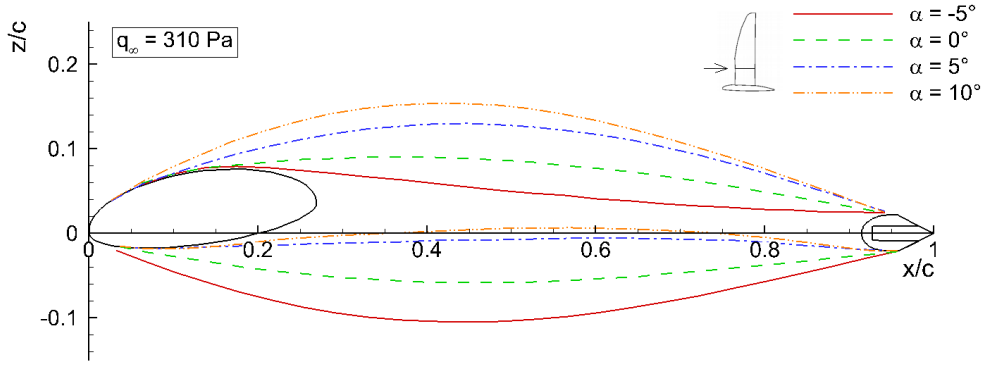

(a) Attached flow regime

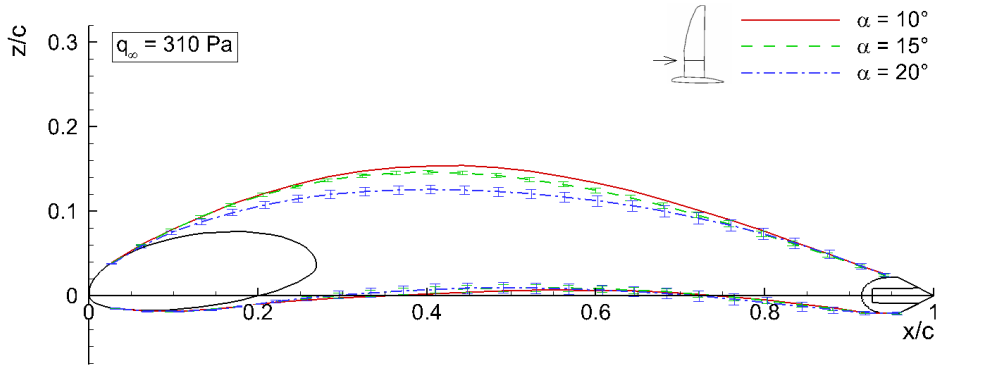

(b) Separated flow regime

Figure 4.6: Effect of the angle of attack on the deflected wing shape at constant dynamic pressure in the (airfoil section of the straight wing at $2y/b = 0.3$).

Figure 4.7 presents the relative camber, f/c, and the location of the maximum camber, x_f/c, as a function of the free-stream dynamic pressure and of the angle of attack. The parameters corre-

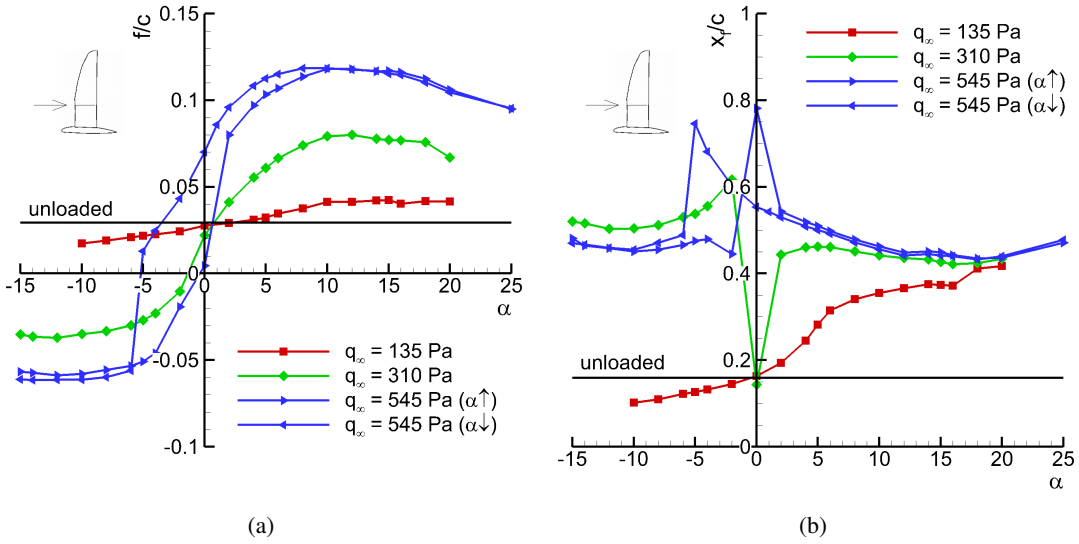

Figure 4.7: Camber characteristics of the airfoil section of the straight wing at $2y/b = 0.3$.

sponding to the undeflected airfoil section are also shown in the plots for a better assessment of the variation due to the membrane deflection. At q_∞ = 135 Pa, the camber increases linearly with the angle of attack between α = -10° and α = 10°. At α = 0°, the camber is nearly the same as in the unloaded case with f/c = 0.028. At negative angles of attack, the camber is smaller than the unloaded case but remains always positive (f/c = 0.018 at α = -10°) because the deflection of the wing lower side is not large enough to cause negative cambers. At positive angles of attack, f/c increases up to 0.041 at α = 10° and remains constant beyond that because the occurrence of trailing-edge flow separation at high angles of attack prevents a further increase of the deflection of the upper side. The location of the maximum camber (cf. Fig. 4.7b) at this flow condition moves continuously downstream with increasing α from x_f/c = 0.102 at α = -10° to x_f/c = 0.417 at α = 20°.

At q_∞ = 310 Pa, the camber exhibits a much larger dependency on the angle of attack according to the larger deflection occurring at this flow condition. With f/c = 0.022, the camber at α = 0° is slightly smaller than in the unloaded case. At positive angles of attack, the camber increases and reaches a maximum of 0.08 at α = 12°. Above this it decreases slightly due to the occurrence of trailing-edge flow separation as highlighted in Fig. 4.6b. At negative angles of attack, the camber is negative according to the large deflection of the wing lower side in the negative z direction occurring at this flow condition (cf. Fig. 4.6a). The minimum camber (f/c = -0.037) is reached at α = -12°. For angles of attack smaller than -12°, the camber does not change significantly anymore due to the occurrence of flow separation on the wing lower side. The maximum camber at this flow condition is located more downstream than at q_∞ = 135 Pa. In the positive α range, x_f/c remains fairly constant with a value around 0.45. In the negative α range, x_f/c is slightly larger with values around 0.51. Further, the x_f/c characteristic exhibits a discontinuity around α = 0° due to the rapid change in the sign of the camber.

At q_∞ = 545 Pa, a further phenomenon occurs. The measurements performed during the increas-

ing and the decreasing angle of attack slopes revealed that the wing surface can take different shapes at the same angle of attack depending on whether α is increasing or decreasing. This results in a significant hysteresis between α = -6° and α = 10°. The hysteresis is not centered around α = 0° is because an asymmetric leading-edge spar is used. A similar effect is reported in Waldmann et al. [32]. It is not necessarily related to any flow separation phenomenon and occurs independently of the hysteresis sometimes observed in the stall regime due to different locations of the separation and reattachment points (Müller et al. [61]). Figure 4.8a the two different airfoil shapes occurring at α = 0°. The airfoil corresponding to the α-increasing case is fairly symmetric according to the very small value of the relative camber shown in Fig. 4.7a (i.e. f/c = 0.006). The camber in the α-increasing case changes abruptly from f/c = 0.006 to f/c = 0.08 between α = 0° and α = 2°. As it is shown in Fig. 4.8b, this is due to the abrupt change in the direction of the deflection of the wing lower side. In contrast, the airfoil corresponding to the α-decreasing case has a large positive camber at α = 0° (i.e. f/c = 0.071). The camber in this case remains positive up to α = -5°. Between α = -5° and α = -6°, the camber decreases abruptly from f/c = 0.0128 to f/c = -0.056 because the deflection of the wing upper side changes abruptly its direction (cf. Fig. 4.8c). The airfoil shapes occurring at α = -5° has an unconventional shape with a maximum deflection of the upper side located at x/c = 0.6. This airfoil shape is stable but the wing upper side vibrates significantly as indicated by the error bars showing the standard deviation of the z coordinate. At this flow condition, the maximum camber is f/c = 0.118 and is reached at α = 10°. The minimum camber is around f/c = -0.06 and occurs at α = -10°. For angles of attack above 10° and below -10°, the camber decreases again due to the occurrence of trailing-edge flow separation. The location of the maximum camber at q_∞ = 545 Pa shows discontinuities due to the abrupt change in sign of the camber. It is located around x_f/c = 0.45 at negative angles of attack and varies between x_f/c = 0.53 and x_f/c = 0.43 in the positive α range. The hysteresis effect captured here occurs only at large aerodynamic loading in combination with low membrane pre-stress. Further investigations carried out with varying pre-stress have shown that the hysteresis becomes significant for values of the parameter K_m below 1000 as it is shown in chapter 6.

Figure 4.9 shows the airfoil thickness, t/c, and the location of the maximum thickness, x_t/c, as a function of the angle of attack and free-stream dynamic pressure. The thickness increases with the free-stream dynamic pressure as a result of the increasing amplitude of the deflection. At q_∞ = 135 Pa, the relative thickness lies between 0.102 and 0.13. At q_∞ = 310 Pa, it varies between 0.133 and 0.17. At q_∞ = 545 Pa, the maximum thickness in the negative angle of attack range is between 0.225 and 0.26. Between α = 2° and α = 14°, the thickness is significantly smaller in the α-increasing case than in the α-decreasing case. At q_∞ = 310 Pa and q_∞ = 545 Pa, the thickness at high angles of attack (i.e. $\alpha > 14°$) decreases according to the reduced amplitude of the deflection associated with separated flow. The location of the maximum thickness (cf. Fig. 4.9b) at q_∞ = 135 Pa moves monotonically towards the trailing-edge with increasing angle of attack and varies between x_t/c = 0.22 and 0.45. At q_∞ = 310 Pa and q_∞ = 545 Pa, the behavior is different because x_t/c is maximum at α = 0° and decreases above and below this angle of attack.

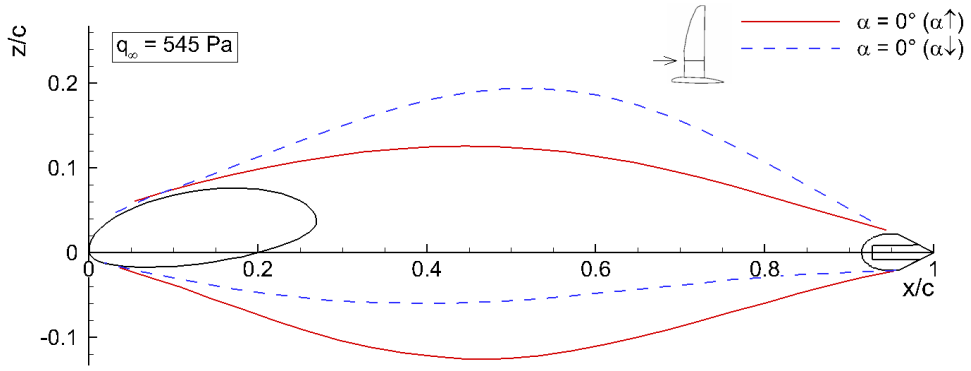

(a)

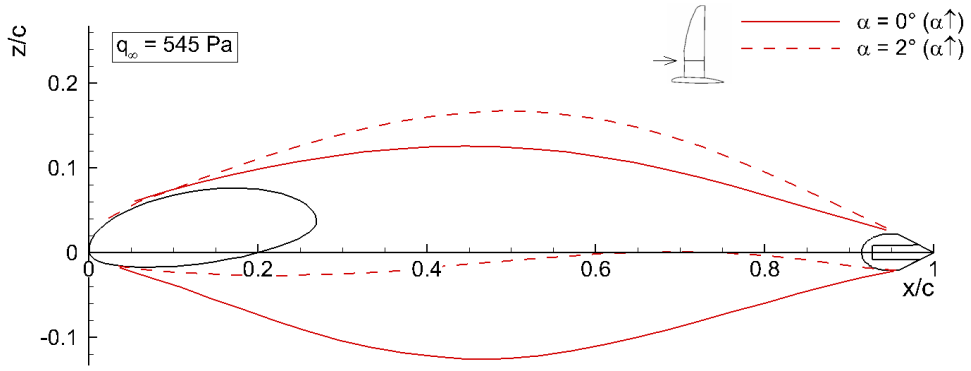

(b)

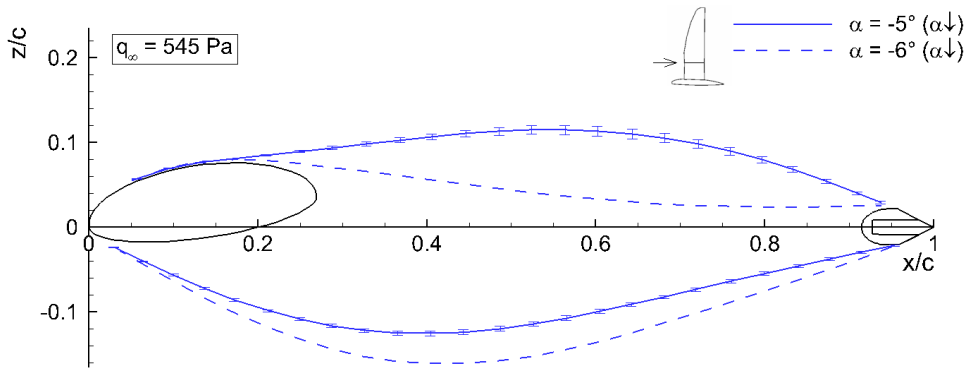

(c)

Figure 4.8: Deflected airfoil shapes at q_∞ = 545 Pa to illustrate the hysteresis effect.

4.1.3 Effects on the aerodynamic characteristics

In the following, the effect of the membrane deflection on the lift and drag characteristics is presented. For this, only the straight wing configuration is considered. The effect of the planform on the aerodynamic characteristics is discussed in detail in chapter 5. The lift and drag

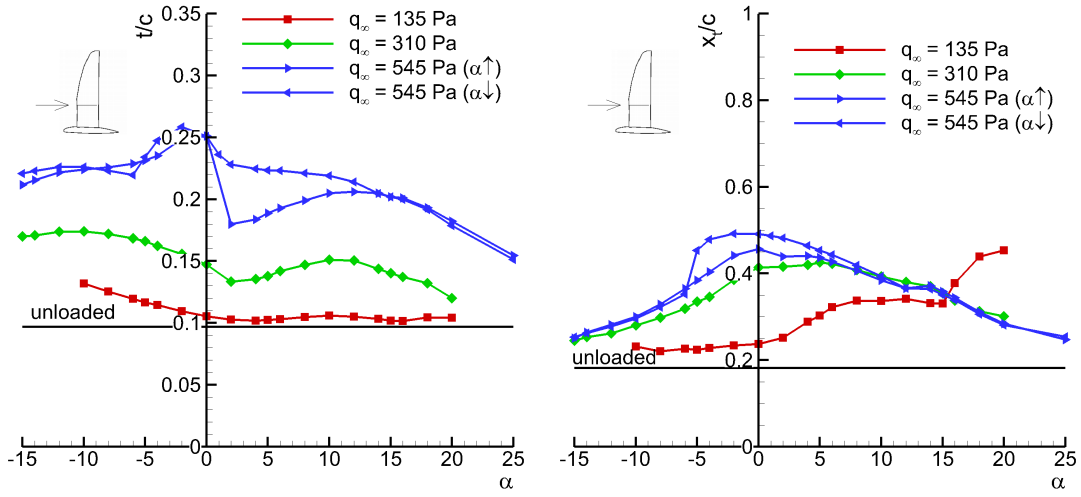

(a) (b)

Figure 4.9: Thickness characteristics of the airfoil section of the straight wing at $2y/b = 0.3$.

polars presented in the following were measured synchronously with the deflection measurements presented in section 4.1.2, thus allowing a direct correlation between the aerodynamic characteristics and the deflected wing shapes.

Figure 4.10a presents the lift polars measured at q_∞ = 135 Pa, q_∞ = 310 Pa, and q_∞ = 545 Pa. The theoretical lift curve obtained from the rigid wing simulations (cf. section 3.1) is also indicated in the plot. The aerodynamic characteristics show a pronounced dependency on the dynamic pressure which is due to the deformation of the wing surface described above. The lift curves get steeper and non-linear with increasing free-stream dynamic pressure as a result of the membrane deflection. The increasing camber leads to a decrease of the zero-lift angle and, thus, the lift at the set geometric angle of attack increases. At q_∞ = 135 Pa, the lift curve is fairly linear according to the small amplitude of the deflection occurring at this flow condition. However, it is slightly steeper than the theoretical rigid wing prediction because the camber increases slightly with increasing angle of attack (cf. Fig. 4.7). At q_∞ = 310 Pa, the lift curve exhibits a larger slope because the angle of attack dependency of the camber is much more pronounced at this flow condition. The lift at $\alpha = 0^\circ$ is almost equal to zero because a fairly symmetric airfoil shape occurs at this angle of attack. At q_∞ = 545 Pa, the different wing shapes occurring during the α-increasing and the α-decreasing phases result in a pronounced hysteresis in the lift curves. Between α = -6° and α = 2°, the lift corresponding to the α-decreasing case is much larger according to the larger camber. Outside of this range, both lift curves are similar. The onset of stall occurs between $\alpha = 10^\circ$ and $\alpha = 12^\circ$ at all three flow conditions as indicated by the flatter slope of the lift curves from this angle on. This corresponds also to the angle of attack where the maximum camber is reached (cf. Fig. 4.7). However, the behavior at higher α is strongly affected by the level of free-stream dynamic pressure. Overall, the stall occurs rather smoothly because the passive adaption of the wing surface to the separated flow acts like a natural flow control mechanism. The amplitude of this phenomenon depends on the flow conditions, and,

as a result, both C_{Lmax} and α_{max} increase with increasing free-stream dynamic pressure. At q_∞ = 135 Pa, the maximum lift coefficient is equal to 1.02 and occurs at α = 15°. At q_∞ = 310 Pa, it is equal to 1.19 and occurs at α_{max} = 17°. At q_∞ = 545 Pa, the maximum lift coefficient equal to 1.26 and occurs at α_{max} = 19° only. The drag characteristics in Fig. 4.10b are given as

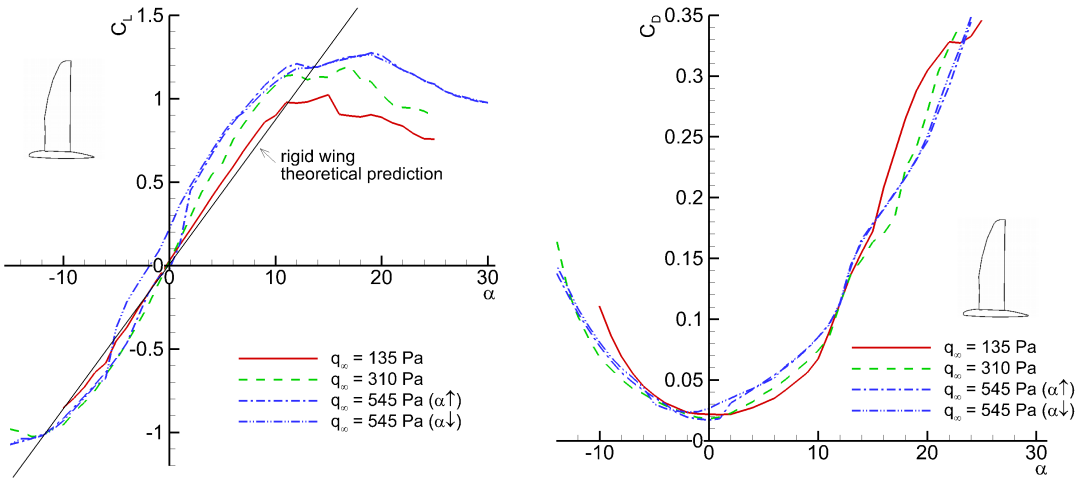

(a) (b)

Figure 4.10: Lift and drag characteristics of the straight wing configuration as a function of the free-stream dynamic pressure.

a function of the angle of attack to allow for a direct comparison with the deflected wing shapes described above. At α = 0°, the smallest drag occurs at q_∞ = 545 Pa and for the α-increasing case. However, the largest drag at this angle of attack occurs also at q_∞ = 545 Pa, but for the α-decreasing case. This is because the wing at α = 0° exhibits a large positive camber in the α-decreasing case and is therefore associated with a comparatively larger parasitic drag than the symmetric airfoil shape occurring in the α-increasing case (cf. Fig. 4.7a). At negative angles of attack, the largest drag occurs at q_∞ = 135 Pa. The smaller drag occurring at q_∞ = 310 Pa and q_∞ = 545 Pa is due to the negative cambers occurring at negative angles of attack, which result in a smaller parasitic drag than the almost undeflected wing. In the positive angle of attack range, the drag is smaller at q_∞ = 135 Pa in the attached flow regime (i.e. $\alpha < 10°$). A more detailed analysis of the aerodynamic characteristics is given in chapter 5.

4.2 Influence of the boundary layer transition

The boundary layer transition was found to have a large impact on the fluid-structure interaction. This was discovered during the deflection measurements where force measurements conducted on the wing with markers distributed over the complete surface showed important differences compared to the measurements carried out with a clean wing surface at some conditions. In this section, the location of the free transition is analyzed and the effects of a forced transition on the fluid-structure interaction is discussed. Further, numerical simulations of two-dimensional elastic membrane airfoils are presented to investigate the effect of the transition in detail.

4.2.1 Location of the free transition

Figure 4.11 indicates the location of the laminar to turbulent boundary layer transition on the suction side of the straight wing configuration detected with the microphone probe (cf. section 2.2.3) as a function of the flow conditions. At q_∞ = 135 Pa and $\alpha = 0^\circ$, the boundary layer remains laminar in the upper half of the wing. On the lower half, it becomes turbulent around $x/c = 0.5$. At positive angles of attack, the transition moves upstream. It occurs around $x/c = 0.3$ at $\alpha = 5^\circ$ and around $x/c = 0.2$ at $\alpha = 10^\circ$. At $q_\infty = 545$ Pa, the transition occurs more downstream than at q_∞ = 135 Pa. Therefore, the boundary layer remains laminar over a significant area of the wing even at $\alpha = 10^\circ$. The fact that the transition occurs later with increasing free-stream dynamic pressure is attributed to the membrane deformation and the change in camber and thickness that results. Indeed, an opposite trend would be expected for a rigid wing because the increase in Reynolds number associated to an increase of the dynamic pressure would lead to an upstream shift of the transition. As it is shown later in section 4.2.3, the transition at the Reynolds number considered here is caused by a laminar separation bubble with turbulent reattachment. The occurrence of the separation bubble is very sensitive to the pressure gradients behind the leading-edge. The larger camber associated with larger free-stream dynamic pressures (cf. Fig. 4.4) mitigates the intensity of the suction peak at the leading-edge, delaying thus the occurrence of the laminar separation bubble. As a result, the transition moves downstream.
Figure 4.12 shows the location of the transition on the suction side of the swept-back wing. At q_∞ = 135 Pa and $\alpha = 0^\circ$, the transition occurs around $x/c = 0.27$ over the complete wing and moves upstream with increasing angle of attack. At q_∞ = 545 Pa, the transition takes place at fairly the same locations as at q_∞ = 135 Pa above 30% wing span. Below this, it moves downstream as in the case of the straight wing (cf. Fig. 4.11b). This indicates that the transition on the surface of the swept-back wing is likely to be triggered by cross-flow instabilities caused by the larger sweep angle. Indeed, the transition occurs near the leading-edge independently of the free-stream dynamic pressure above 30% wing span, i.e. where the sweep-angle is large. It moves downstream with increasing dynamic pressure only near the wing root where the sweep angle is smaller.

4.2.2 Wing characteristics with forced transition

In order to measure the characteristics of the straight wing configuration with a turbulent boundary layer over the whole surface, a zig-zag tape placed behind the leading-edge on the wing suction side was used as illustrated in Fig. 4.13a. Estimations with the method presented in Ref. [56] indicate that, considering the chordwise location of the tape, the free-stream velocity, and the air kinematic viscosity, minimum disturbance heights of 0.47 mm for the flow condition at q_∞ = 135 Pa and of 0.3 mm for the flow condition at q_∞ = 545 Pa are required to trigger transition. The tape used is placed at $x/c = 0.05$ and has a thickness of 0.5 mm (cf. Fig. 4.13b). Tests including force and deflection measurements were carried out to analyze the wing characteristics with the forced transition. For the deflection measurements, a single row of markers placed at $2y/b = 0.3$ is used to reconstruct the airfoil section at this spanwise location (cf. Fig. 4.13a). In

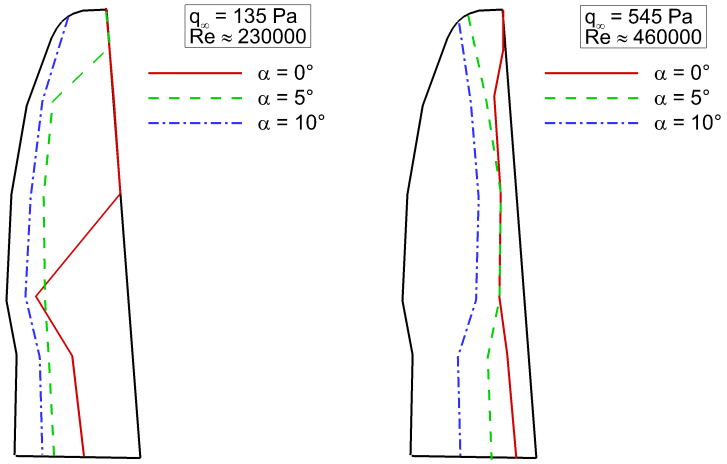

(a) (b)

Figure 4.11: Location of the laminar to turbulent boundary layer transition on the suction side of the straight wing configuration as a function of the flow conditions.

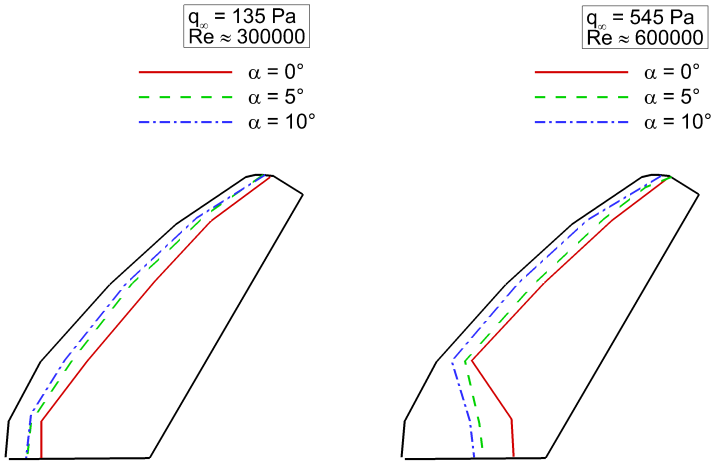

(a) (b)

Figure 4.12: Location of the laminar to turbulent boundary layer transition on the suction side of the swept-back wing configuration as a function of the flow conditions.

the following, the wing characteristics obtained with the forced transition are compared with the characteristics measured with the free transition. For this, the same results as presented in sections 4.1.2 and 4.1.3 are used. Figure 4.14 presents the lift and drag characteristics of the straight wing configuration measured with the free and with the forced transition at q_∞ = 135 Pa. At q_∞ = 135 Pa, the lift curve corresponding to the forced transition exhibits a slightly smaller slope and reaches slightly lower maximum lift coefficients compared to the free transition case. The latter can be due to the energy loss caused by the tape favoring an earlier turbulent separation. The drag is also slightly increased, which may be directly attributed to the increase in zero-lift

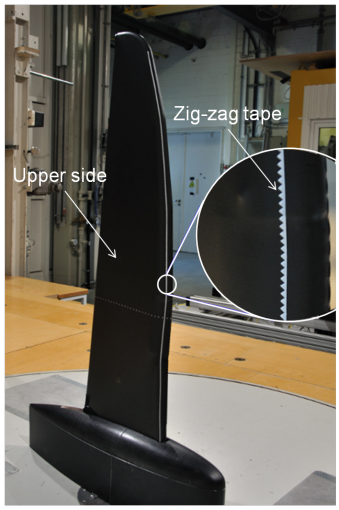

(a) Placement of the zig-zag tape on the wing

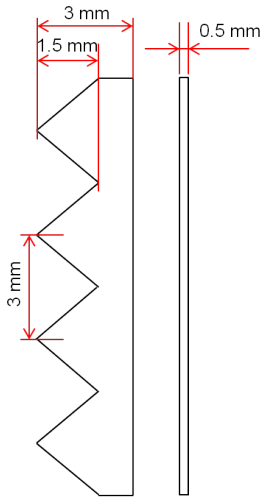

(b) Details of the tape geometry

Figure 4.13: Zig-zag tape placed on the leading-edge of the suction side to trigger transition.

drag due to the presence of the tape. However, the overall influence of the zig-zag tape is limited because the free transition at this flow condition occurs already near the leading-edge and, thus, the zig-zag tape does not significantly change the situation.In contrast, the forced transition has a profound effect on the lift and drag characteristics at q_∞ = 545 Pa (cf. Fig. 4.15). At this flow condition, the zig-zag tape changes significantly the situation because in the free transition case the boundary layer remains laminar over a large area of the wing (cf. Fig. 4.11b). The lift curve corresponding to the forced transition exhibits a much flatter slope. The hysteresis effect is also present with the forced transition, but the loop extends up to larger angles of attack than in the free transition case. The lift characteristics are, however, identical in the stall region (α > 20˚) and at negative angles of attack (α < -6˚). The latter is because the behavior at negative angles of attack is dominated by the deflection of the wing lower side where no zig-zag tape was used. The drag characteristics are also strongly affected by the location of the transition. In the negative angle of attack range, the drag is essentially similar in both cases. However, it is significantly smaller in the forced transition case for $\alpha > 0$˚.

Figure 4.16 presents the deflected airfoil shapes occurring at q_∞ = 545 Pa and $\alpha = 6$˚ with the free and with the forced transition. The deflection is significantly smaller with the forced transition, explaining thus the smaller lift and drag at positive angles of attack. Figure 4.17 shows a comparison of the camber and the thickness of the airfoil section at $2y/b = 0.3$ occurring at q_∞ = 545 Pa as a function of the angle of attack and of the transition type. As suggested by Fig. 4.16, the camber is significantly smaller with the forced transition over the whole angle of attack range, which again correlates well with the smaller lift and the smaller drag observed in Fig. 4.14c and d. The maximum camber occurring with the forced transition is nearly 14% smaller than the maximum camber occurring with the free transition. Concerning the thickness (cf. Fig. 4.17b), the trend is mixed. At negative α, the thickness is fairly the same in both cases. At positive α, the wing with the forced transition exhibits a larger thickness up to $\alpha = 5$˚. Above

this, the thickness in the free transition case is larger. The numerical investigations presented in the following section give a detailed analysis of the phenomenon observed here and provide an explanation for its occurrence.

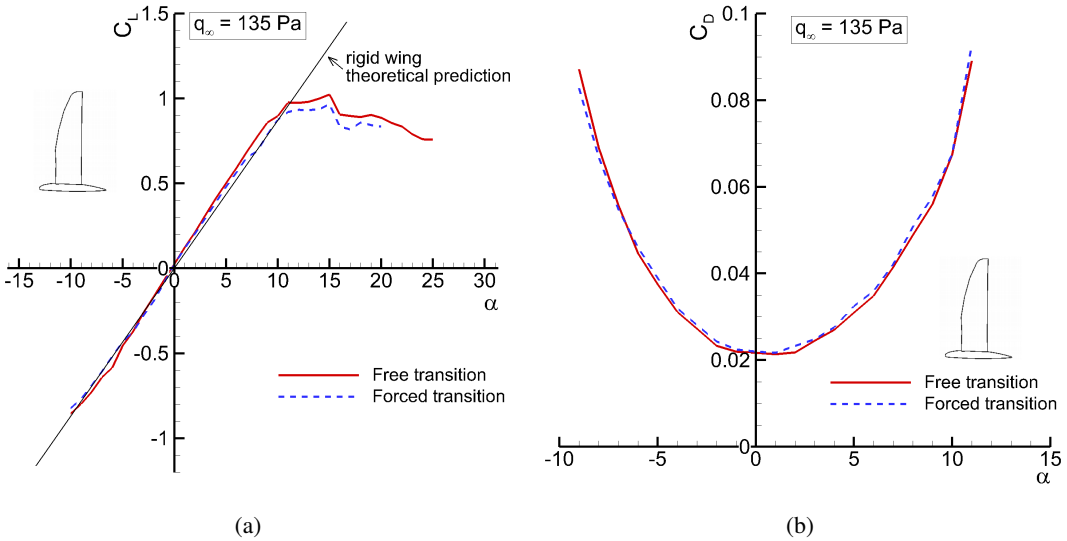

(a) (b)

Figure 4.14: Influence of the boundary layer transition on the lift and drag characteristics of the straight wing configuration at q_∞ = 135 Pa.

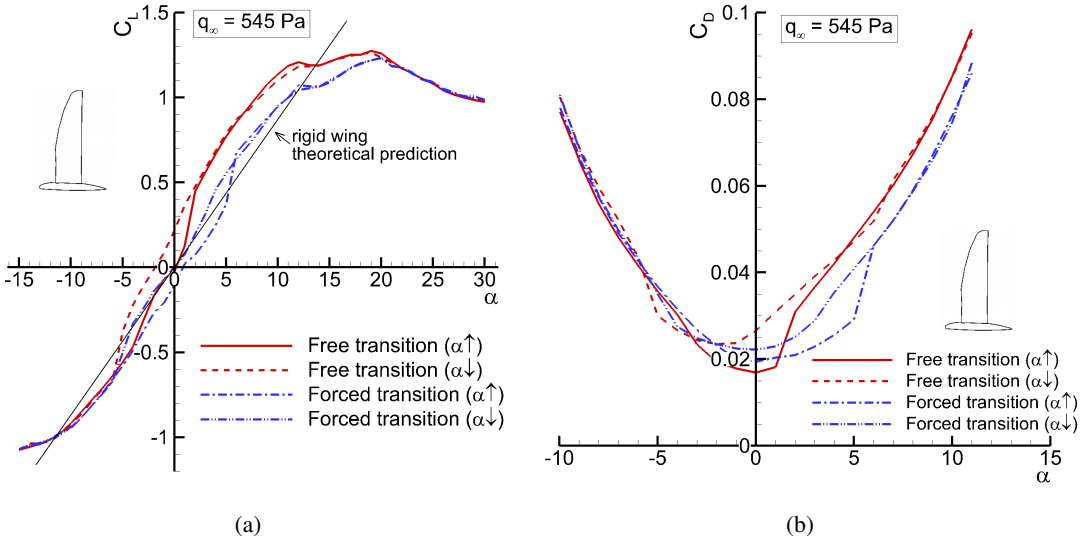

(a) (b)

Figure 4.15: Influence of the boundary layer transition on the lift and drag characteristics of the straight wing configuration at q_∞ = 545 Pa.

4.2.3 Numerical investigations

The numerical investigations presented here were carried out with the program introduced in section 3.2 to study the influence of the boundary layer transition on the fluid-structure interaction.

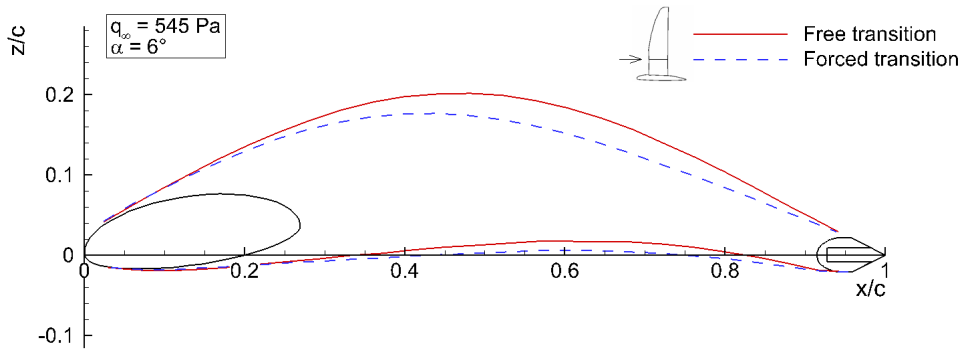

Figure 4.16: Deflected wing shapes occurring at q_∞ = 545 Pa with free and forced transition.

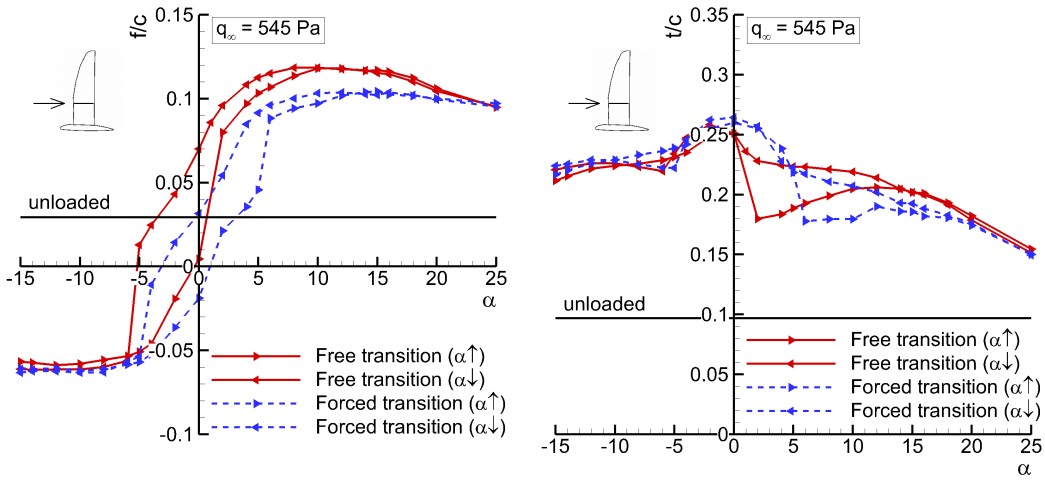

(a) (b)

Figure 4.17: Effect of the boundary layer transition on the airfoil characteristics at q_∞ = 545 Pa (wing section at $2y/b = 0.3$).

The elastic membrane airfoil considered in the simulations has the same structural characteristics as a section of the wind tunnel model concerning the leading-edge spar geometry, the membrane thickness, the elasticity modulus, and the pre-stress (cf. section 2.1.3). The flow conditions used in the simulation in terms of the dynamic pressure and Reynolds numbers are also equivalent to the experimental conditions. The influence of the boundary layer transition is investigated by running simulations with free transition (e^N method, cf. section 3.2.2) and with fully turbulent boundary layer obtained by setting the transition location to $x_{tr}/c = 0$.

Figure 4.18 presents the simulation results in terms of the lift curves (plots a and c), the relative camber (plots b and d), and location of the free transition (plot e) at q_∞ = 135 Pa and q_∞ = 545 Pa. The theoretical lift curves with a slope of 2π corresponding to a rigid airfoil are also shown for comparison. At q_∞ = 135 Pa, the lift curves obtained with the free transition exhibits a slightly larger slope and a larger maximum lift than with the forced transition. However, both curves are slightly steeper than the theoretical curve because the camber increases with the angle of

attack as shown in Fig. 4.18b. The slightly larger slope and the later stall in the free transition case were also observed in the experiment (cf. Fig. 4.14a). The camber at this flow condition increases linearly with α up to stall and stays fairly constant after that. At q_∞ = 545 Pa, the type of transition has a much larger impact on the lift and an effect similar as in the experiment occurs. Indeed the lift with the forced transition is much smaller (at least in the lower range of α) and the lift curve is steeper than with the free transition according to the smaller camber (plot d). The smaller slope associated with the forced transition case is due to the occurrence of trailing-edge flow separation as it is shown later. The lift curve corresponding to the free transition is steeper up to $\alpha = 8^\circ$ where a local lift maximum occurs. At higher angles of attack, both lift curves are fairly identical except that stall occurs earlier in the forced transition case. As it is shown in the following, the larger lift and the strong non-linearity in the free-transition case are directly related to the presence of a laminar separation bubble. The relative camber at this flow condition follows the trend of the lift because it is larger in the free-transition case up to $\alpha = 8^\circ$ and identical in both cases at higher angles of attack. Figure 4.18e shows the location of the free transition predicted by Xfoil at q_∞ = 135 Pa and q_∞ = 545 Pa. At both flow conditions, the transition moves upstream with increasing angle of attack. However, the transition at q_∞ = 545 Pa occurs much later than at q_∞ = 135 Pa up to $\alpha = 8^\circ$. Between $\alpha = 8^\circ$ and $\alpha = 10^\circ$, the location of the transition at q_∞ = 545 Pa moves rapidly upstream. This angle of attack interval corresponds also to the region where the local lift maximum occurs in Fig. 4.18c. The fact that the transition occurs later at q_∞ = 545 Pa than at q_∞ = 135 Pa is also consistent with the experimental results shown in Fig. 4.11. The detailed analysis of the deflected airfoil shapes, the pressure distributions, the skin friction coefficient, and the boundary layer thickness presented in the following provides details about the occurrence of this phenomenon. Figure 4.19 shows the deflected airfoil shapes and the corresponding pressure distributions (plots a and b), the skin friction coefficient on the suction side (C_f, plots c and d), and the boundary layer displacement thickness on the suction side (δ/c, plots e and f) corresponding to q_∞ = 135 Pa and q_∞ = 545 Pa at $\alpha = 5^\circ$ with the free and the forced transitions ($x_{tr}/c = 0$). The boundary layer displacement thickness is obtained from the two equation viscous boundary layer used in Xfoil (cf. section 3.2.2).

At q_∞ = 135 Pa, the deflection is small and the deflected airfoil shapes obtained with both transition types are identical (plot a). At q_∞ = 545 Pa, the deflection is larger than at q_∞ = 135 Pa according to the larger aerodynamic load (plot b). However, the amplitude of the deflection with the fully turbulent boundary layer is much smaller than with the free transition, according to the smaller lift shown in Fig. 4.18c. A comparison with the experimental results presented in Fig. 4.16 shows a good agreement concerning the effect of the forced transition on the amplitude of the deflection at this flow condition. Further, the short plateaus in the pressure distributions corresponding to the free transition case at both free-stream dynamic pressures (plots a and b) indicate the occurrence of local flow separation. The negative values of the skin friction (plots c and d) and the local increase of the boundary layer thickness (plots e and f) in the corresponding regions confirm this assumption. As a result, the free transition at the Reynolds numbers considered here is caused by a laminar separation bubble with turbulent reattachment. As the camber

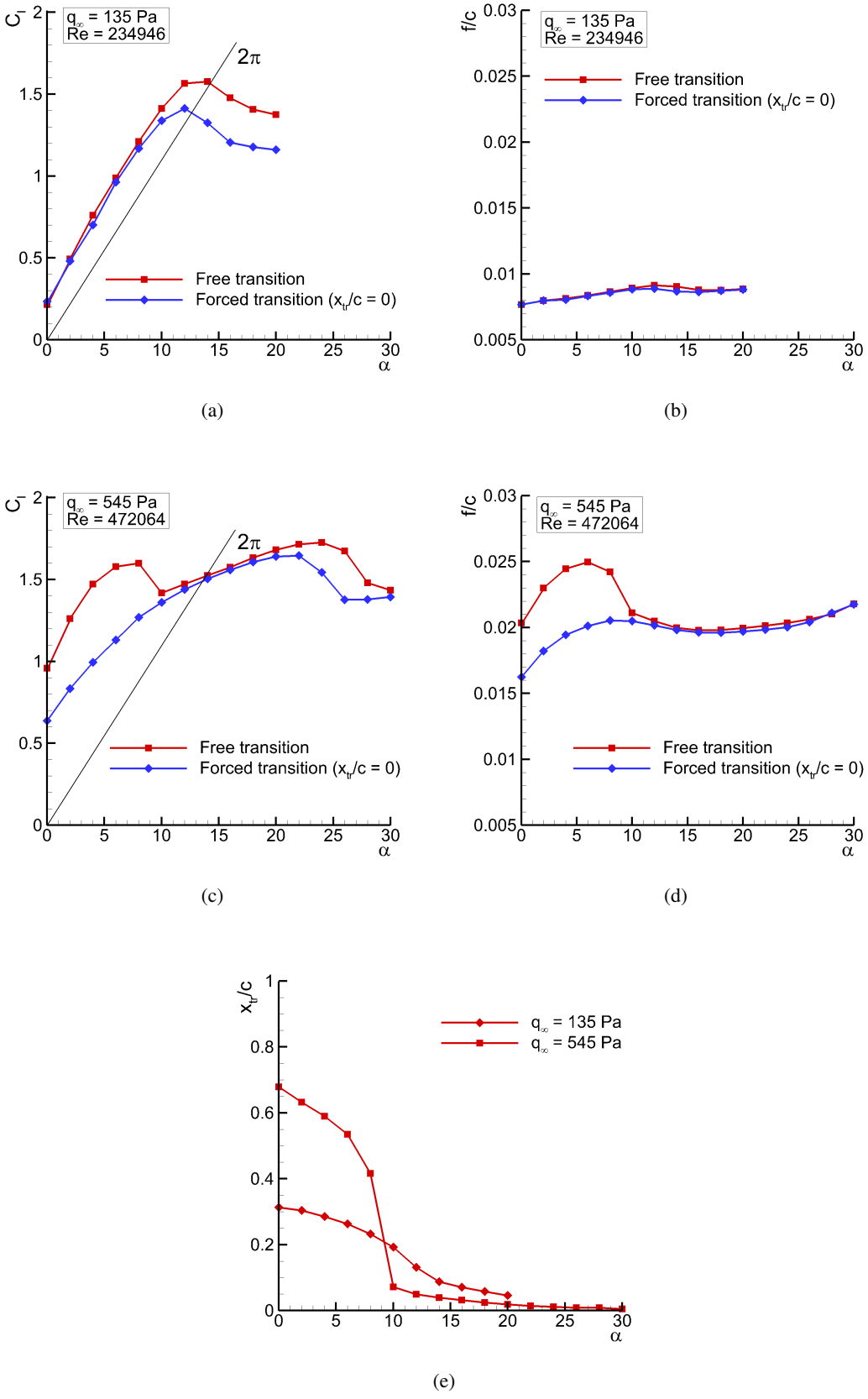

Figure 4.18: Simulation results showing the influence of the boundary layer transition on the airfoil characteristics at q_∞ = 135 Pa and q_∞ = 545 Pa.

increases due to the increasing membrane deflection, the intensity of the suction peak around the leading-edge is reduced, which delays the occurrence of the laminar separation bubble and explains the downstream shift of the transition at q_∞ = 545 Pa. In the forced transition case, there is no sign of local flow separation on the airfoil surface. However, the pressure distribution corresponding to the forced transition at q_∞ = 545 Pa exhibits a plateau in the rear part of the airfoil ($x/c > 0.75$) which indicates the occurrence of significant trailing-edge flow separation. The negative values of the skin friction coefficient in this region confirm this. Although the camber is larger in the free transition case, the flow remains attached. The significant trailing-edge flow separation occurring in the fully turbulent case is the explanation for the smaller deflection and the smaller lift. Indeed, trailing-edge flow separation reduces the suction load on the suction side and the deflection decreases accordingly. However, the fact that the flow separation occurs earlier with a fully turbulent boundary layer than in the laminar case appears to be in contradiction with the expected behavior. A closer look at the boundary layer displacement thickness (plots e and f) provides an explanation for this unexpected behavior. The occurrence of the laminar separation bubble delays the growth of the boundary layer in such a way that it is significantly thinner in the rear part of the airfoil compared to the fully turbulent case where the boundary layer thickness increases monotonically along the airfoil surface. As a result, the thinner boundary layer corresponding to the free transition case can withstand stronger adverse pressure gradients and, thus, separates later than the comparatively thicker boundary layer in the fully turbulent case. The difference in boundary layer thickness also explains the earlier stall observed in the forced transition case at q_∞ = 135 Pa (cf. Fig. 4.18a). The results presented in Fig. 4.19 showed that the laminar separation bubble occurring in the free-transition case is responsible for the larger deflection and the larger lift observed in Fig. 4.18c and d. However, the lift and the camber are larger only up to $\alpha = 8^\circ$ where the local maximum occurs. Above this, the characteristics are the same in both cases. The reason for this is that the occurrence of the laminar separation bubble is very sensitive to the angle of attack. To illustrate this, Fig. 4.20a presents the deflected airfoil shapes with the corresponding pressure distributions, and Fig. 4.20b shows the skin friction on the suction side obtained with the free transition at q_∞ = 545 Pa and $\alpha = 6^\circ$, $\alpha = 8^\circ$, and $\alpha = 10^\circ$. At $\alpha = 6^\circ$, the laminar separation bubble occurs downstream as indicated by the local plateau in the pressure distribution and by the region with negative skin friction around x/c = 0.5. At $\alpha = 8^\circ$, the suction peak at the leading-edge is larger and the laminar separation bubble occurs more upstream as indicated by the negative C_f around x/c = 0.05. Consequently, the positive influence of the delayed occurrence of the laminar separation bubble on the boundary layer thickness does not apply anymore from $\alpha = 8^\circ$ on. Accordingly, significant trailing-edge flow separation occurs as indicated by the vanishing skin friction coefficient for $x/c > 0.75$ and the deflection of the suction side decreases. At $\alpha = 10^\circ$, the separated flow area is larger and the amplitude of the membrane deflection is much smaller, thus a smaller lift results. Above $\alpha = 10^\circ$, the airfoils with both transition types have similar characteristics because the free transition takes place near the leading-edge. The discussion presented above indicates that the delayed occurrence of the laminar separation bubble responsible for the delayed onset of the trailing-edge flow separation is very sensitive to the intensity of the suction peak at the leading-edge. As a

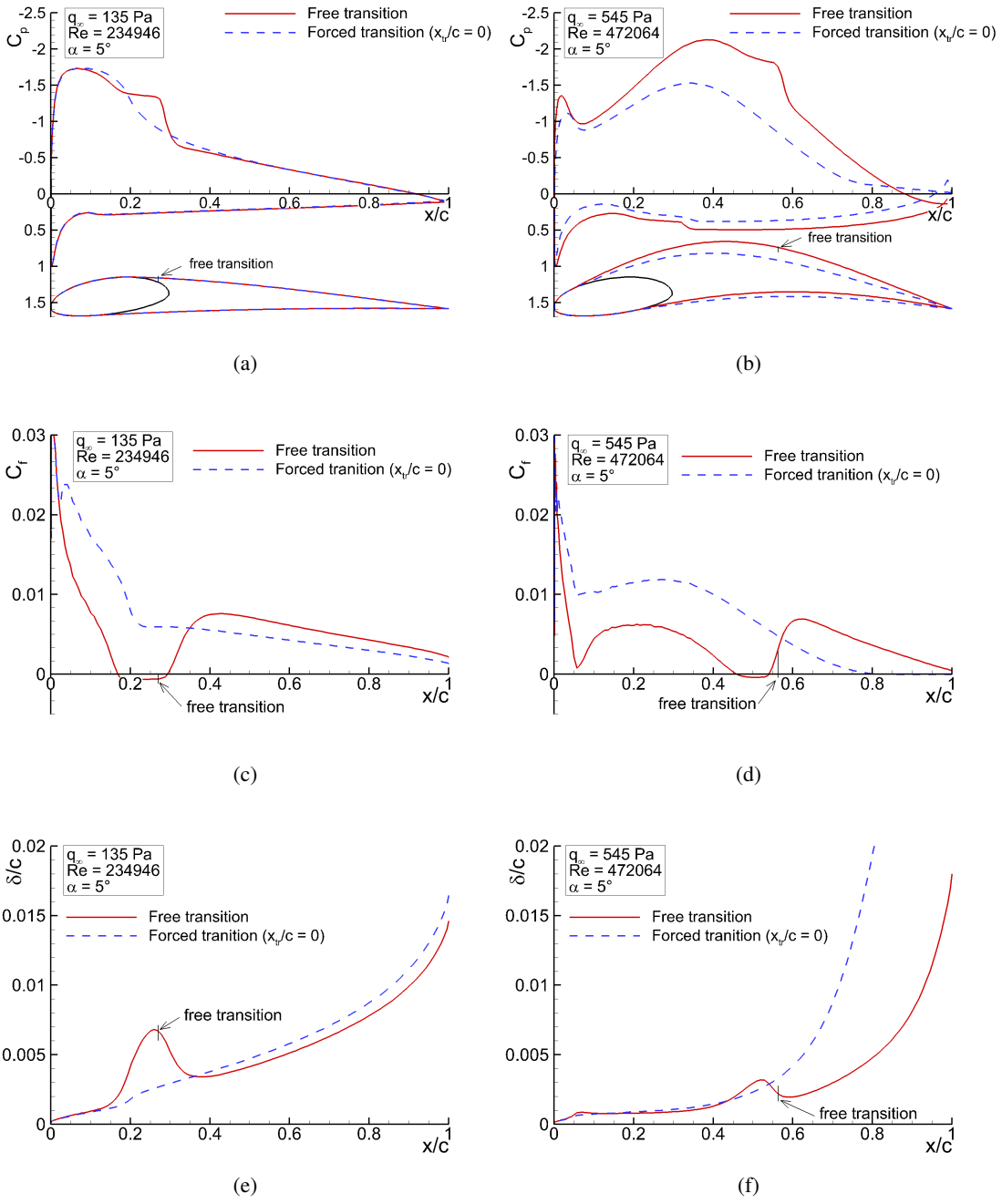

Figure 4.19: Simulation results showing the influence of the boundary layer transition on the deflected airfoil shapes, pressure distributions, skin friction (suction side), and boundary layer displacement thickness (suction side) at different flow conditions.

result, the cross-section geometry of the leading-edge spar has a direct influence on the occurrence of this phenomenon. In the present investigation, it is especially pronounced because the asymmetric geometry was designed specifically to mitigate the intensity of the suction peak (cf. section 3.2.3), allowing thus for the downstream shift of the laminar separation bubble up to relatively high angles of attack. Further, this effect occurs uniquely because the natural transition is caused by a laminar separation bubble, which in turn is directly related to the low Reynolds

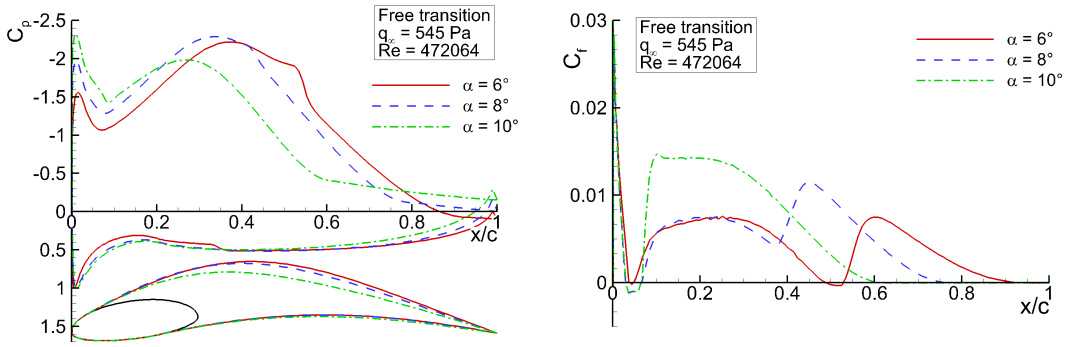

(a) (b)

Figure 4.20: Simulation results showing the effect of the angle of attack on the deflected airfoil shapes, pressure distribution, and skin friction coefficient (suction side) at q_∞ = 545 Pa.

number aerodynamics involved here. In the case where the natural transition is caused by other mechanisms as for example Tollmien-Schlichting waves at higher Reynolds numbers or cross flow instabilities due to larger sweep angle (as for the swept-back wing configuration, cf. Fig. 4.12), the location of the transition is not expected to have such a pronounced effect on the wing characteristics.

The results discussed above have some implications for the experimental results presented in this work. Mainly, the wool tufts or the markers distributed over the whole surface for the deflection measurements act like turbulators leading to turbulent surface flow. Consequently, the deflection amplitudes measured at large dynamic pressure are underestimated compared to the real deflection amplitudes occurring during the force measurements carried out with a clean surface. For instance, the deflection measurements presented in sections 4.1 and 6.1 were carried out with markers distributed over the complete wing. The deflection measurements presented in sections 4.1.2, 4.2.2, and 6.2 were carried out using less markers (i.e. single row) to reduce the disturbance on the surface flow. However, this information is only relevant for wing configurations having a small sweep angle such as the straight wing because with larger sweep angle, the transition is supposedly caused by cross flow instabilities and not by a laminar separation bubble.

5 Effect of planform morphing on the wing performance

This chapter focuses on the influence of the wing planform on the lift, the drag, and the pitching moment characteristics. Also, an evaluation of the resulting effect on the global flight performance is presented. For this, the aerodynamic characteristics of the five wing configurations listed in Table 2.4 with a constant root chord length of 0.27 m are considered. The results presented here originate from a measurement campaign carried out in an early stage of the investigations with the second version of the articulated structure, which is characterized by the slight negative twist and the rounded spar in the inner part of the leading-edge (cf. section 2.1.1). The lift, drag, and pitching moment characteristics presented in the following are averaged from the measurements performed during the increasing and decreasing angle of attack phases. Finally, all force measurements presented in this chapter were carried out with a clean wing surface and therefore correspond to the free-transition case (cf. section 4.2).

5.1 Aerodynamic characteristics

5.1.1 Lift polars and stall characteristics

Figure 5.1 shows a comparison between the lift curves corresponding to the straight wing, the intermediate 2, and the swept-back wing configurations at different free-stream dynamic pressures [66], [67]. At q_∞ = 135 Pa, the lift curve of the straight wing exhibits the steepest slope, followed by the intermediate 2 configuration and finally the swept-back wing shows the flattest curve. At this flow condition, the wing surface does not deflect significantly and the lift curve slope decreases with decreasing aspect ratio as expected from rigid wing theory (cf. section 1.3.2.2). The negative lift occurring at $\alpha = 0^\circ$ is due to the negative twist resulting from the misalignment of the leading-edge spar in the version of the model used for the measurements presented here as discussed in section 2.1.1. At q_∞ = 310 Pa and q_∞ = 545 Pa, the membrane deflection becomes significant and a large influence on the lift characteristics results. The straight wing shows always the steepest curves because in addition to the rigid wing effect of its large aspect ratio, the wing surface in this configuration experiences also comparatively large deflections according to the small membrane pre-stress and the large aerodynamic load associated with the large aspect ratio (cf. section 4.1). The lift polars at q_∞ = 545 Pa show also a pronounced non-linearity due to the delayed stall as it is discussed later. The curves corresponding to the intermediate 2 and the swept-back wing configurations at q_∞ = 310 Pa and q_∞ = 545 Pa exhibit almost identical slopes, although a smaller slope would be expected in the case of the swept-back wing considering its

reduced aspect ratio. However, the swept-back wing is associated with a smaller membrane pre-stress than the intermediate 2 configuration and, thus, it experiences comparatively larger deflections at equivalent flow conditions as highlighted in section 4.1. As a result, the influence of the aspect ratio is to a certain extent compensated by the larger camber. A quantitative discussion of the lift curve slopes as a function of the planform configuration and flow conditions is given later.

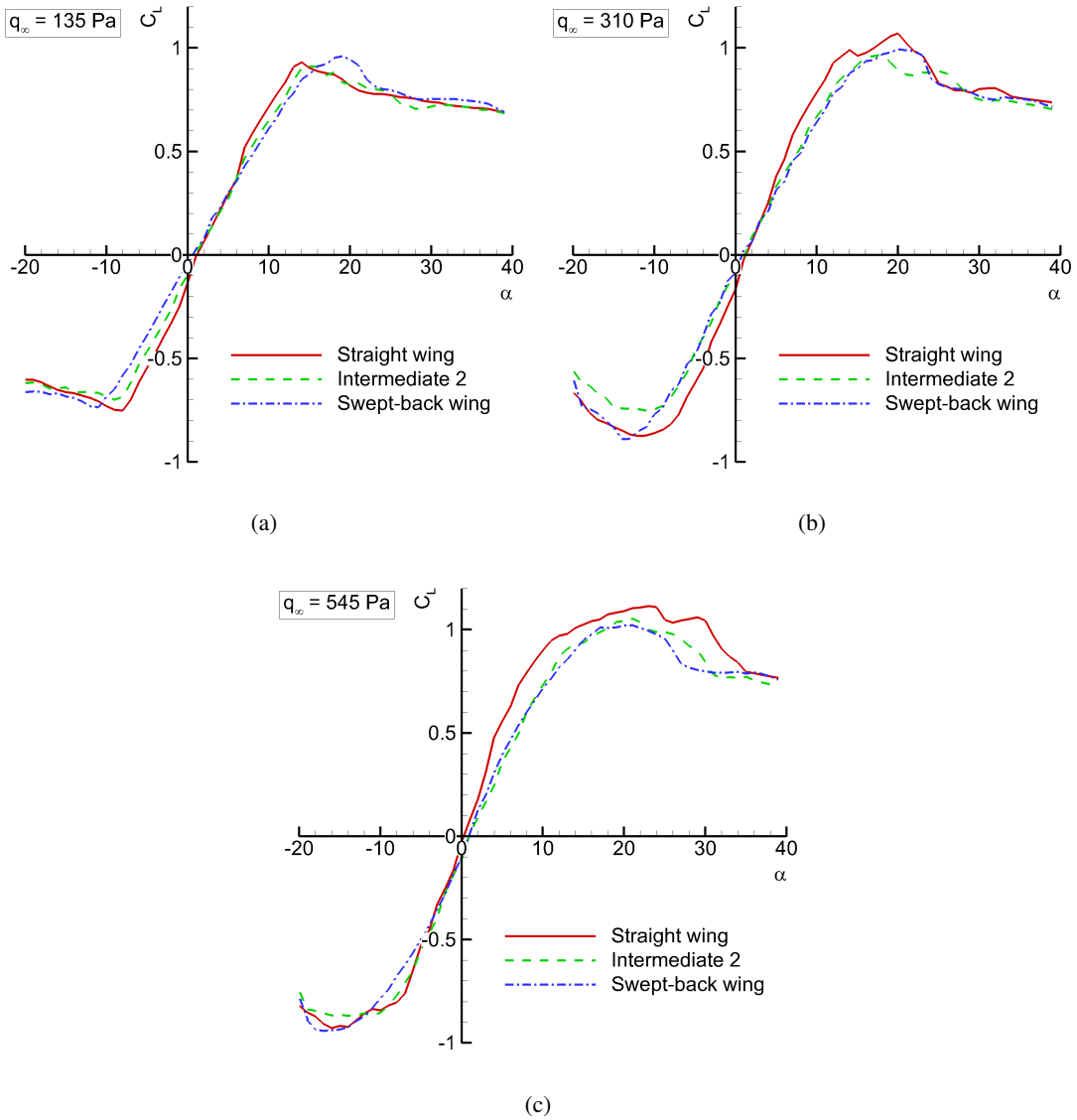

Figure 5.1: Lift polars as a function of the wing planform and free-stream dynamic pressure.

Concerning the stall characteristics, the swept-back wing at q_∞ = 135 Pa exhibits the latest stall (α_{max} = 19°) and the largest maximum lift coefficient (C_{Lmax} = 0.96) among the three configurations considered here. At this flow condition, the wing geometry is not significantly affected by the membrane deformation and, thus, the superior stall characteristics of the swept-back wing are attributed to its larger sweep angle. As the free-stream dynamic pressure increases, the stall gets overall smoother due to the increasing effect of the passive adaption of the wing shape to

the separated flow (natural flow control mechanism, cf. chapter 4). The straight wing at q_∞ = 310 Pa and q_∞ = 545 Pa shows the largest maximum lift because it experiences comparatively larger deflection of the wing surface and, thus, the natural flow control mechanism due to the membrane deformation is more pronounced. At q_∞ = 310 Pa, the local maximum around α = 14° in the lift curve of the straight wing is caused by the presence of a laminar separation bubble as explained in section 4.2.3. At q_∞ = 545 Pa, the onset of stall in the case of the straight wing occurs at α = 12° as indicated by the decreasing slope. However, the maximum lift (C_{Lmax} = 1.1) is reached at α_{max} = 24° only.

A deeper insight into the stall behavior is gained by looking at the results from the wool tuft experiments shown in Figs. 5.2 and 5.3. In the case of the straight wing at q_∞ = 135 Pa, the separation starts at the wing root at α = 10°. At α = 15°, which is already beyond the maximum lift (cf. Fig. 5.1a), a second region of separated flow occurs at the wing tip. At α = 20°, the two separated flow regions at the root and at the tip have grown and almost join each other. The flow is completely separated at α = 25°. At q_∞ = 545 Pa, the separation process is completely different according to the different wing shape (camber) associated with this flow condition (cf. section 4.1). The separation begins at α = 5° already with a small area of separated flow at the trailing-edge. It is caused by the strong adverse pressure gradient associated with the massive camber occurring at this flow condition. As the angle of attack increases, the separated flow region grows and moves from the trailing-edge towards the leading-edge but propagates rather slowly according to the smoother stall observed in the corresponding lift curve (cf. Fig. 5.1c). At α = 25°, just beyond α_{max}, the flow is still attached over a significant area of the wing. The state of completely separated flow is reached only beyond α = 30°.

The flow separation patterns corresponding to the swept-back wing are presented in Fig. 5.3. They show similar characteristics as in the case of the straight wing. At q_∞ = 135 Pa, the flow separation begins also at α = 10° at the root, and there is also a larger region of separated flow at the wing tip at α = 15°. Above α = 15°, the area of separated flow moves rapidly towards the leading-edge and the flow is almost completely separated at α = 20°, which corresponds to the angle of attack at which the maximum lift is reached (cf. Fig. 5.1a). At q_∞ = 545 Pa, the area of separated flow up to α = 15° is significantly larger than at q_∞ = 135 Pa, which is explained by the larger camber associated with the larger membrane deflection at this flow condition. However, the region of separated flow for higher angles of attack grows slower than at q_∞ = 135 Pa according to the smoother stall associated with this flow condition (cf. Fig. 5.1c).

A synthesis of the lift characteristics in terms of the lift curve slope ($C_{L,\alpha}$) and the maximum lift coefficient (C_{Lmax}) as a function of the wing planform ($\mathcal{AR}$) and flow conditions (q_∞) is presented in Fig. 5.4. In this figure, the data corresponding to the intermediate 1 and 3 configurations are also taken into account. The theoretical values of $C_{L,\alpha}$ shown in Fig. 5.4a are based on the vortex lattice simulations presented in section 3.1. The experimental values of $C_{L,\alpha}$ were obtained by fitting linear polynomials to the lift curves using only the data corresponding to the attached flow regime (-5° < α < 10°).

The lift curve slope decreases with decreasing aspect ratio as expected from rigid wing theory. At q_∞ = 135 Pa, the experimental values of $C_{L,\alpha}$ are near to the theoretical rigid wing values

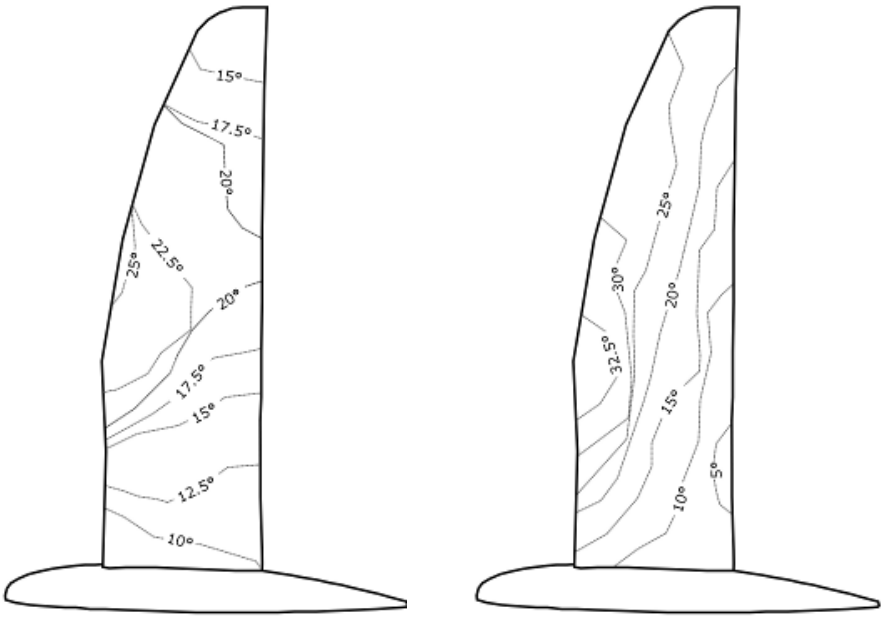

(a) q_∞ = 135 Pa (b) q_∞ = 545 Pa

Figure 5.2: Delimitation of the separated flow area on the suction side of the straight wing configuration as a function of the angle of attack.

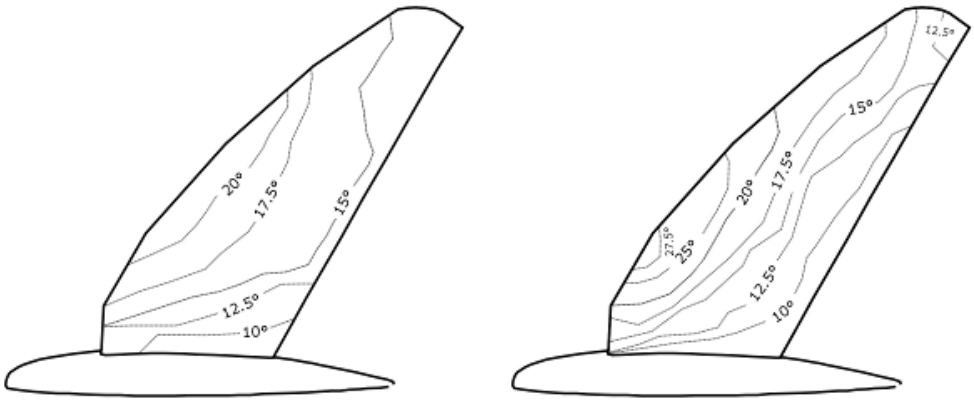

(a) q_∞ = 135 Pa (b) q_∞ = 545 Pa

Figure 5.3: Delimitation of the separated flow area on the suction side of the swept-back wing configuration as a function of the angle of attack.

because the membrane deflection is small at this flow condition and therefore does not influence the lift characteristics. As the dynamic pressure increases, $C_{L,\alpha}$ gets larger according to the increasing dependency of the camber on the angle of attack. However, the general trend concerning the influence of the wing planform remains valid at all flow conditions. The straight wing configuration ($\mathcal{AR} = 9.12$) provides the overall largest lift curve slopes with a maximum of $C_{L,\alpha} = 5.84$ at $q_\infty = 545$ Pa. The smallest slope is equal to $C_{L,\alpha} = 3.83$ and occurs in the case of the swept-back wing ($\mathcal{AR} = 4.38$) at $q_\infty = 135$ Pa.

The maximum lift coefficients as a function of the wing planform and flow conditions are shown in Fig. 5.4b. The quantity C_{Lmax} increases with increasing dynamic pressure as suggested in the discussion of the lift curves shown in Fig. 5.1. This is principally due to the increasing camber. The influence of the planform on C_{Lmax} is not the same at all flow conditions. At $q_\infty = 135$ Pa, the swept-back wing configuration ($\mathcal{AR} = 4.38$) exhibits the largest maximum lift coefficient ($C_{Lmax} = 0.96$). For higher dynamic pressures, the largest maximum lift coefficients are provided by the straight wing ($\mathcal{AR} = 9.12$) with $C_{Lmax} = 1.07$ at $q_\infty = 310$ Pa and $C_{Lmax} = 1.11$ at $q_\infty = 545$ Pa.

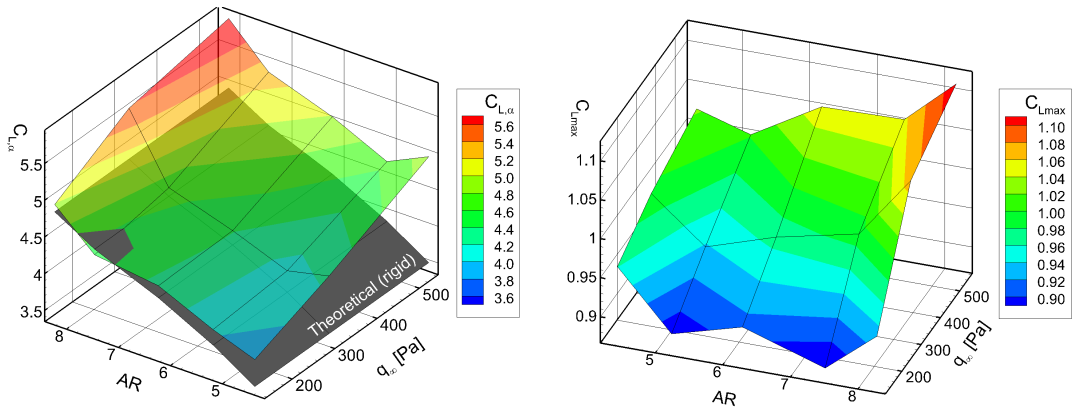

(a) (b)

Figure 5.4: Synthesis of the lift characteristics in terms of the lift curve slope ($C_{L,\alpha}$) and the maximum lift coefficient (C_{Lmax}) as a function of the planform configuration ($\mathcal{AR}$) and flow condition (q_∞).

5.1.2 Pitching moment characteristics

Figure 5.5 presents the pitching moment characteristics corresponding to the straight wing, the intermediate 2, and the swept-back wing configurations measured at different free-stream dynamic pressures. The moment reference point is located at the quarter chord of the wing root. The pitching moment at zero-lift, C_{m0}, is almost zero in all cases because the wing exhibits a fairly symmetric airfoil shape at $C_L = 0$ (cf. chapter 4). The slope of the pitching moment is always negative, which indicates that the aerodynamic center is located behind the reference point where the pitching moment is measured. The slope decreases as the planform changes from the straight wing to the swept-back configuration as a result of the increasing sweep angle, which is consistent with the theoretical expectations (cf. section 1.3.2.3). Further, the pitching moment characteristics are fairly linear up to C_{Lmax} even at large free-stream dynamic pressures.

The explanation for this is that the angle of attack dependency of the camber at large free-stream dynamic pressures affects both the lift and the pitching moment, and the non-linearities that result cancel each other when C_m is plotted against C_L.

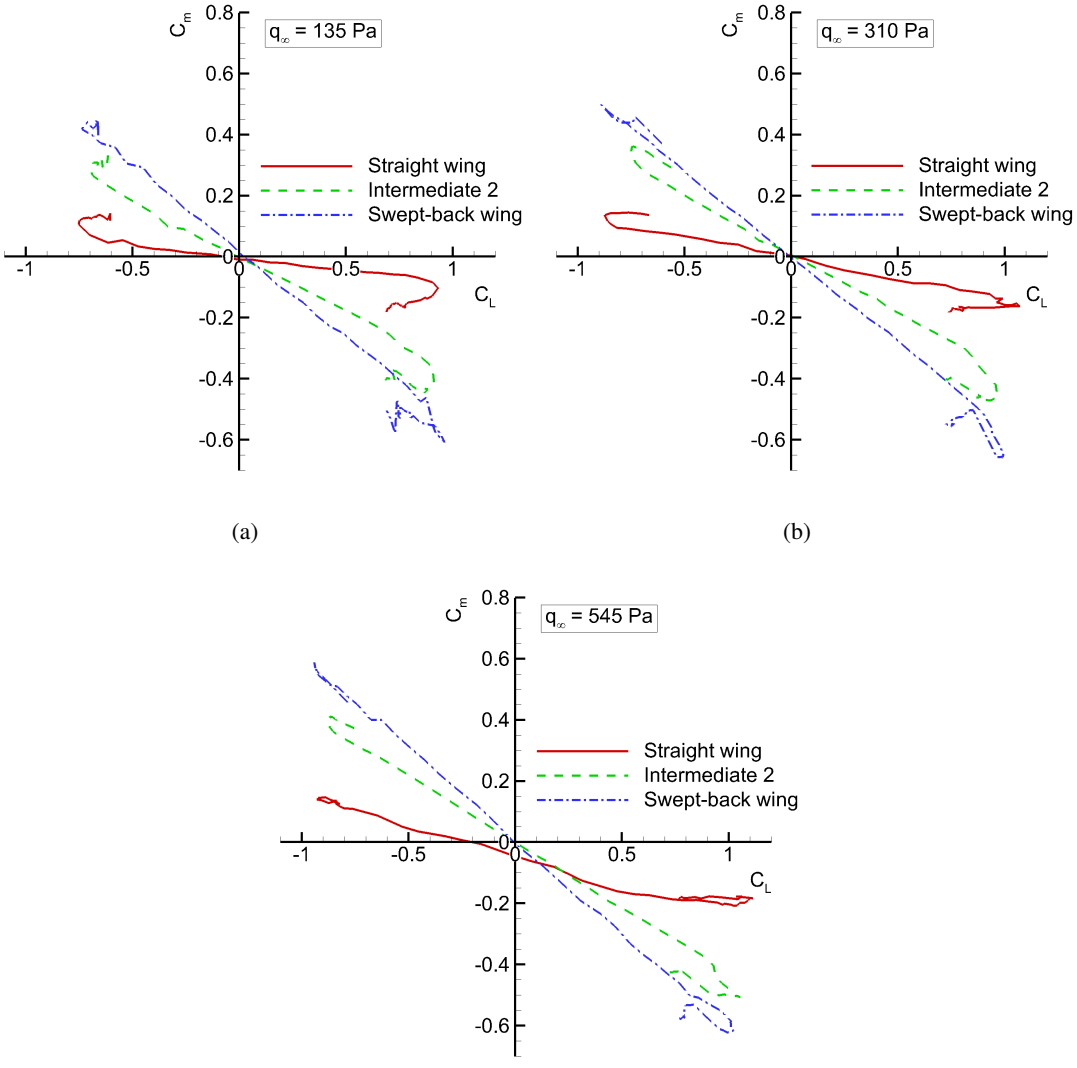

Figure 5.5: Pitching moment characteristics as a function of the wing planform and free-stream dynamic pressure.

Figure 5.6 presents a synthesis of the pitching moment characteristics in terms of the slope of the pitching moment curve, dC_m/dC_L, and the location of the aerodynamic center, $x_{ac}/\bar{c}$, as a function of the planform configuration (sweep angle $\phi_{1/4}$) and of the flow conditions (q_∞). The location of the aerodynamic center is determined according to Eq. 1.13 and is expressed as the distance from the leading-edge of the root section. The experimental values of dC_m/dC_L were also obtained by linear polynomial fitting as for the analysis of the lift characteristics presented above.

Both dC_m/dC_L and $x_{ac}/\bar{c}$ show a good agreement with the theoretical predictions (cf. section 3.1) at q_∞ = 135 Pa because the membrane deformation is not significant at this flow condition and the aerodynamic characteristics are dictated by the planform geometry. As the free-stream dynamic pressure increases, dC_m/dC_L decreases and the aerodynamic center moves towards the trailing-edge accordingly. This behavior is attributed to the angle of attack dependency of the camber, the intensity of which increases with increasing free-stream dynamic pressure. The decrease of dC_m/dC_L as well as the downstream shift of the aerodynamic center indicate that the longitudinal stability increases with increasing free-stream dynamic pressure.

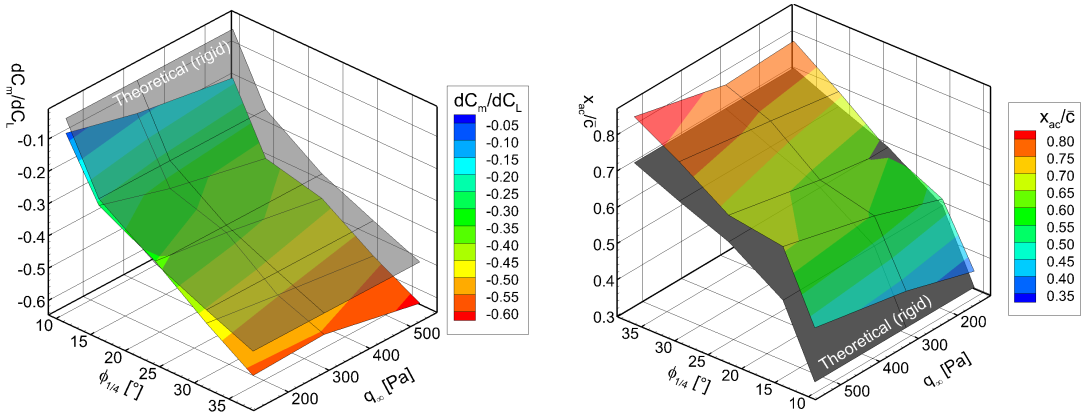

(a) (b)

Figure 5.6: Synthesis of the pitching moment characteristics in terms of the slope of the pitching moment curve (dC_m/dC_L) and the location of the aerodynamic center ($x_{ac}/\bar{c}$) as a function of the planform configuration ($\phi_{1/4}$) and flow condition (q_∞).

5.1.3 Drag characteristics

5.1.3.1 Drag polars

Figure 5.7 shows the drag polars corresponding to the straight wing, the intermediate 2, and the swept-back wing configurations at different free-stream dynamic pressures [68], [69]. At q_∞ = 135 Pa, changing the planform from the straight wing to the swept-back wing configuration causes a clear reduction in zero-lift drag and an increase in lift-dependent drag. The swept-back wing exhibits the smallest drag for $C_L < 0.5$, whereas for $C_L > 0.5$, the straight wing provides the smallest drag. At q_∞ = 545 Pa, a similar trend occurs. Moreover, all drag polars are shifted to the right and therefore the zero-lift drag at this flow condition is smaller than the zero-lift drag at q_∞ = 135 Pa. This is partly due to the increased Reynolds number, and partly to the changing camber and thickness (cf. chapter 4). At q_∞ = 310 Pa, the trend concerning the effect of the planform on the drag polar is not as clear as for the two other flow conditions. While the swept-back wing exhibits a zero-lift drag which is only slightly smaller than at q_∞ = 135 Pa, the zero-lift drag of the straight wing and of the intermediate 2 configurations are significantly smaller. As a result, the swept-back wing is associated with the largest drag over the whole range of lift coefficients. The straight wing shows the smallest drag except for $0 < C_L < 0.35$

where the intermediate 2 configuration provides slightly smaller values of C_D.

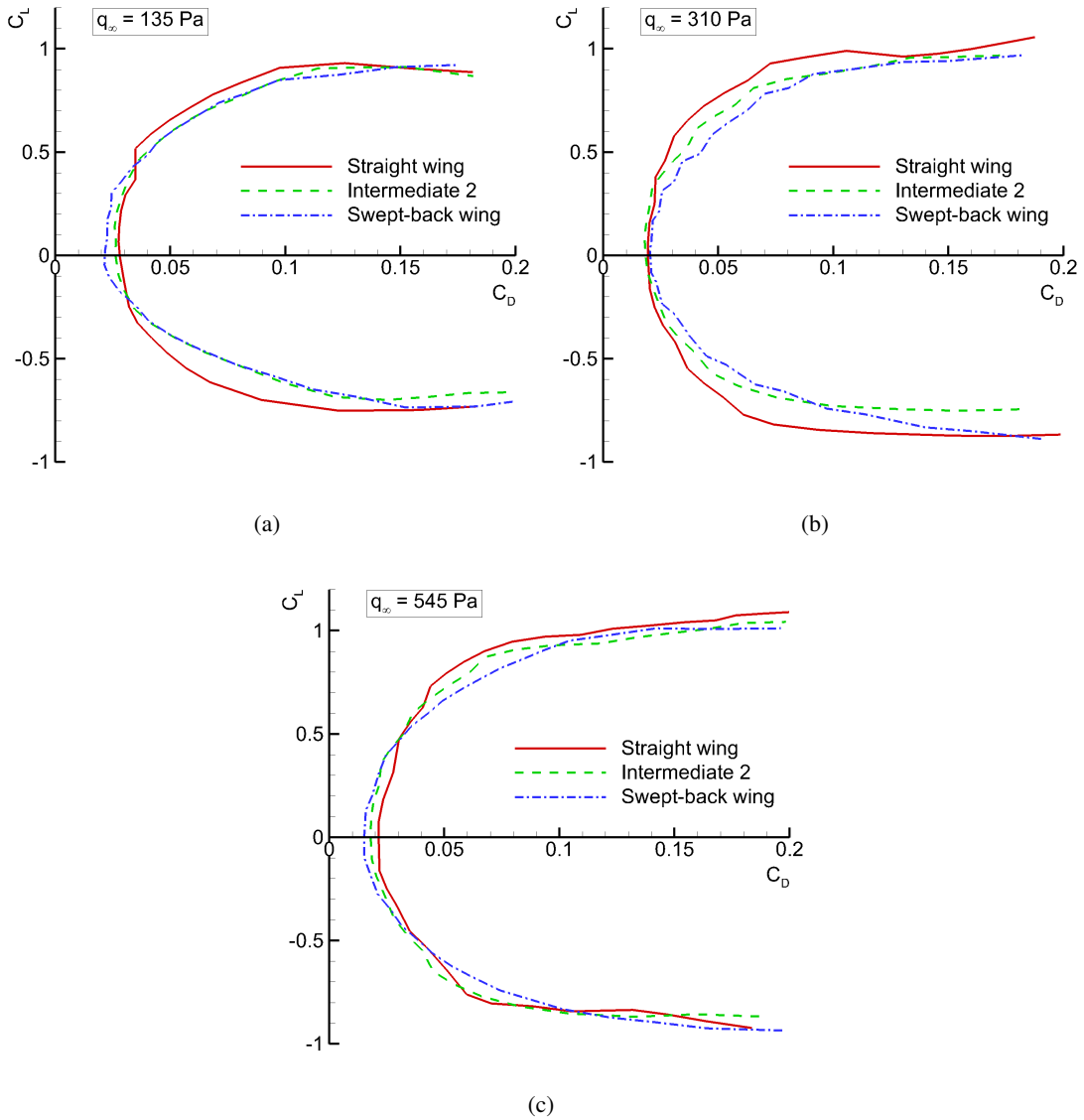

Figure 5.7: Drag polars as a function of the wing planform and free-stream dynamic pressure.

A synthesis of the drag characteristics in terms of the zero-lift drag coefficient, C_{D0}, and the lift-induced drag factor, K, as a function of the planform configuration ($\mathcal{AR}$) and flow condition (q_∞) is presented in Fig. 5.8. The parameters C_{D0} and K were obtained by fitting the quadratic drag polar model (cf. Eq. 1.14) to the experimental data. For this, only the data contained in the attached flow regime are taken into account ($-5^\circ < \alpha < 10^\circ$).

In general, the zero-lift drag decreases monotonically with increasing free-steam dynamic pressure. As mentioned above, this behavior is partly attributed to the increasing Reynolds number and partly to the membrane deformation at zero lift. Only for the straight wing ($\mathcal{AR}$ = 9.12), the smallest value of C_{D0} occurs at q_∞ = 310 Pa. As suggested by the discussion of the drag polars above, the zero-lift drag of the straight wing ($\mathcal{AR}$ = 9.12) and with the intermediate 2 con-

figuration ($\mathcal{AR}$ = 6.23) experience the largest decrease between q_∞ = 135 Pa and q_∞ = 310 Pa whereas the zero-lift drag corresponding to the swept-back wing decreases more linearly with increasing free-stream dynamic pressure. Concerning the effect of the planform, C_{D0} decreases monotonically with decreasing aspect ratio at q_∞ = 135 Pa and q_∞ = 545 Pa. However, it is almost independent of the planform at q_∞ = 310 Pa. These differences are directly attributed to the complex interaction between the planform geometry, the low Reynolds number aerodynamics, and the surface deflection which is different for each configuration. The overall largest value of C_{D0} is equal to 0.0282 and occurs in the case of the straight wing ($\mathcal{AR}$ = 9.12) at q_∞ = 135 Pa. The overall smallest value is equal to 0.0149 and occurs in the case of the swept-back wing ($\mathcal{AR}$ = 4.38) at q_∞ = 545 Pa.

The influence of the planform shape and of the flow conditions on the lift-dependent drag factor is shown in Fig. 5.8b. The quantity K increases with decreasing aspect ratio as expected from rigid wing theory. This is also consistent with the fact that the straight wing provides the smallest drag in the upper lift coefficient range (cf. Fig. 5.7). Further, K is observed to decrease with rising dynamic pressure. This is directly attributed to the larger camber the wing shows at larger free-stream dynamic pressures, which is associated with smaller parasitic drag at equivalent lift coefficient. The overall smallest value of K is equal to 0.0507 and occurs in the case of the straight wing ($\mathcal{AR}$ = 9.12) at q_∞ = 545 Pa. The overall largest value is equal to 0.0828 and occurs in the case of the swept-back wing ($\mathcal{AR}$ = 4.38) at q_∞ = 310 Pa.

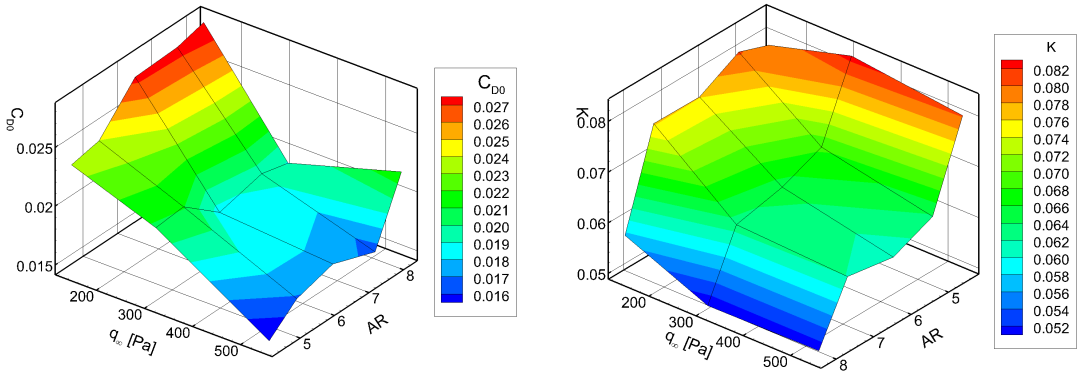

(a) (b)

Figure 5.8: Synthesis of the drag polars in terms of the zero-lift drag coefficient (C_{D0}) and lift-dependent drag factor (K) as a function of the planform configuration ($\mathcal{AR}$) and flow condition (q_∞).

5.1.3.2 Lift distribution and vortex-induced drag

In the following, the lift distributions, the span efficiency factors, and the vortex induced drag evaluated form the flow field measurements carried out in the near wake of the wing are discussed [70]. Figures 5.9a and b show exemplarily the flow field in the wake of the straight wing at $\alpha = 10^\circ$ and q_∞ = 135 Pa. From the v and w velocity components, the streamwise vorticity, ω_x, can be calculated according to Eq. 5.1. The corresponding vorticity field is shown in Fig. 5.9c

with a clear tip vortex around $y = 1$ m. From ω_x, the local contributions to the total circulation, $d\Gamma(y)$, is obtained by integrating $\omega_x dy$ along the z-direction as indicated in Eq. 5.2, where dy represents the grid spacing in the y-direction. The circulation distribution, $\Gamma(y)$, is obtained by integrating $d\Gamma(y)$ in the y-direction starting from the wing tip as indicated in Eq. 5.3. Finally, the lift distribution, $C_l c(y)$, is obtained from $\Gamma(y)$ according to Eq. 1.9. This procedure was implemented in a Matlab script using a trapezoidal method to perform the numerical integrations.

$$\omega_x = \frac{\partial v}{\partial z} - \frac{\partial w}{\partial y} \tag{5.1}$$

$$d\Gamma(y) = \int (\omega_x dy) dz \tag{5.2}$$

$$\Gamma(y) = \int_{b/2}^{y} d\Gamma(y) dy \tag{5.3}$$

Figures 5.10 and 5.11 present the $C_l c(y)$ distributions corresponding to the straight wing and the swept-back wing configurations associated with $\alpha = 5^\circ$ and $\alpha = 10^\circ$ at $q_\infty = 135$ Pa and $q_\infty = 545$ Pa. In the case of the straight wing, PIV measurements could not be obtained below $2y/b = 0.08$ due to reflections of the laser sheet with the fuselage. For the evaluation of the span efficiency factor, the missing portion of the circulation distribution is extrapolated with a constant value between the last experimental value and the root section as indicated in Fig. 5.10. A comparison between the lift coefficients obtained from the force measurements and those computed from the integration of the lift distribution according to Eq. 1.10 is given in Table 5.1. The maximum discrepancy of 13.48% indicates a fair quality of the PIV measurements.
For both wing configurations, the local lift is always significantly larger at $q_\infty = 545$ Pa than at $q_\infty = 135$ Pa, which is the direct consequence of the larger camber occurring at larger dynamic pressure as highlighted in chapter 4. Indeed, the lift distributions at constant angle of attack would be independent of the flow conditions in the case of a rigid wing. Further, the $C_l c(y)$ distributions corresponding to $q_\infty = 545$ Pa exhibit a maximum located further outboard compared to the distributions corresponding to $q_\infty = 135$. This correlates well with the shape of the camber distribution presented in Fig. 4.5. Indeed, the camber at $q_\infty = 545$ Pa is small at the wing root and increases strongly up to 30% and 40% wing span. In contrast, the camber at $q_\infty = 135$ Pa shows less variation along the span. The larger local lift at $\alpha = 10^\circ$ compared to $\alpha = 5^\circ$ is just due to the increased angle of attack. The lift distributions corresponding to the swept-back wing exhibit increased loading at the wing tip and reduced loading at the wing root compared to the lift distributions corresponding to the straight wing, which is due to the larger sweep angle (cf. section 1.3.2.1).

The span efficiency factors associated with each $C_l c(y)$ distribution and evaluated with the method presented in section 1.3.2.1 are given in Figs. 5.10 and 5.11 as well as in Table 5.1. For this, the Fourier sine series of Eq. 1.5 was truncated after 500 terms which allows for an accurate representation of the original distribution. For a given wing planform and angle of attack, the span efficiency factor is always smaller at $q_\infty = 545$ Pa than it is at $q_\infty = 135$ Pa. This indicates that the lift distributions differs even more from the ideal elliptical one as the amplitude of the

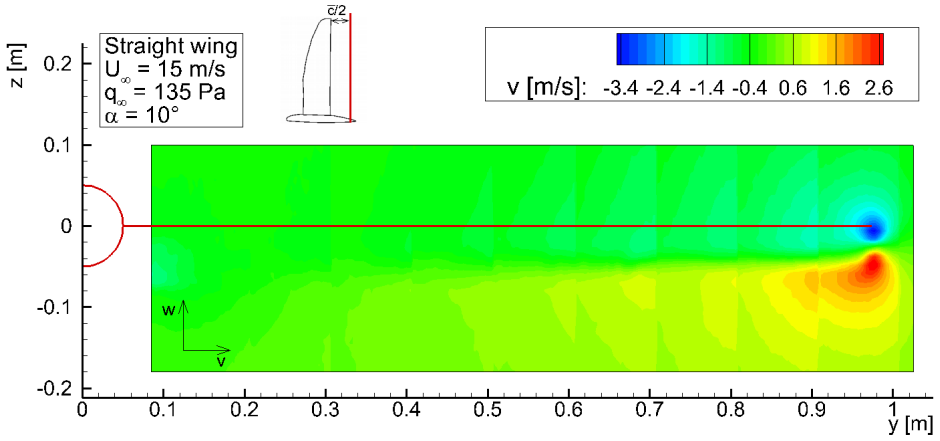

(a)

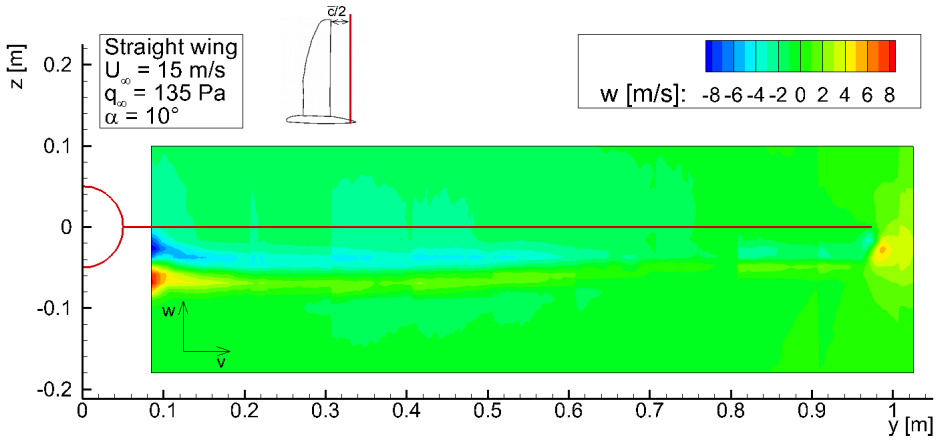

(b)

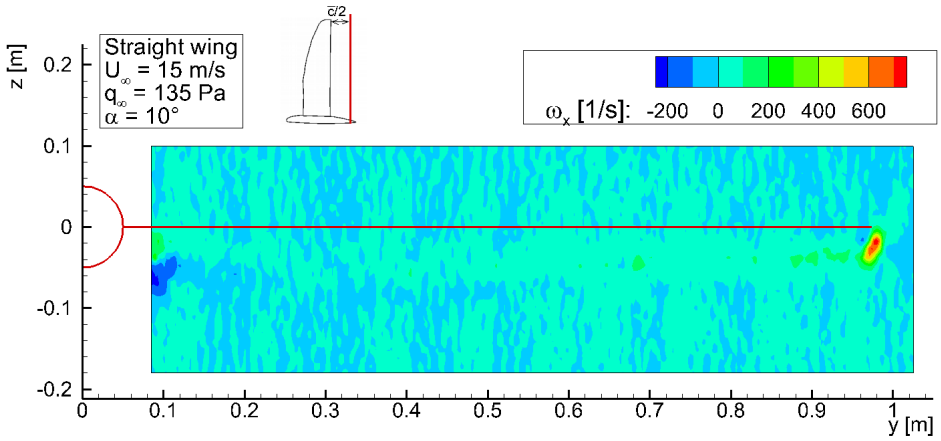

(c)

Figure 5.9: Example of results from the Stereo-PIV measurements showing the velocity and vorticity fields in the near wake of the straight wing at $q_\infty = 135$ Pa and $\alpha = 10^\circ$.

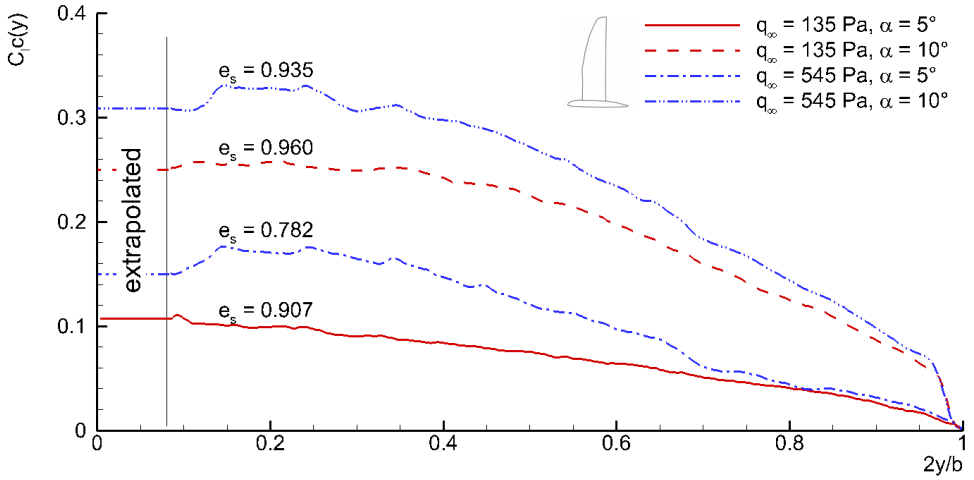

Figure 5.10: Lift distributions of the straight wing as a function of the flow conditions.

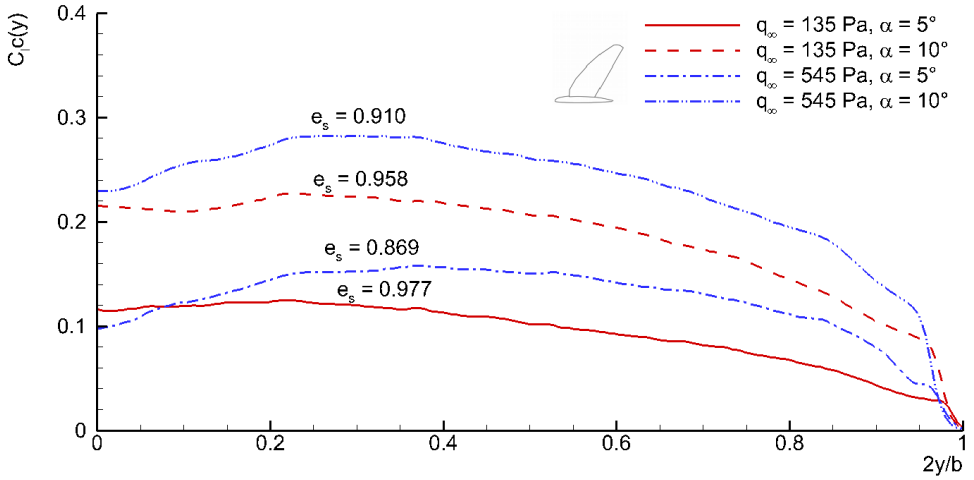

Figure 5.11: Lift distributions associated with the swept-back wing as a function of the flow conditions.

membrane deflection increases. This further shows that the contribution of the vortex drag to the total lift-dependent drag (cf. section 1.3.2.4) increases with the free-stream dynamic pressure. However, the discussion of the drag characteristics obtained from the force measurements presented above showed a significant decrease of the lift-dependent drag factor K with increasing dynamic pressure (cf. Fig. 5.8b), which may appear contradictory to the way e_s varies. The decrease in K was mainly explained by the decrease in parasitic drag associated with the larger camber occurring at larger free-stream dynamic pressures. As a result, the reduction in parasitic drag as the wing surface deforms is more important than the increase in vortex-induced drag expected from the variation of the span efficiency factor. Concerning the influence of the planform on the span efficiency factor, the theory predicts a decrease in e_s with increasing sweep angle (cf. section 1.3.2.1 and 3.1). However, no univocal trend can be recognized from the experimental results, because the dynamic pressure dependency of the wing geometry has a too large

influence on the lift distribution and overcomes the pure effect of the planform. Further, the span efficiency factors obtained from the experiment are in general smaller than the theoretical predictions based on the vortex lattice simulations. The differences are due to the fact that the simulations were based on planar wings, which is definitely not true in the case of the flexible wing. The fuselage and the péniche have also an influence on the vortex field which is not accounted for in the simulations.

The span efficiency factors can be used to evaluate the vortex-induced drag coefficients, C_{Dvi}, according to Eq. 5.4 coming from the combination of Eqs. 1.17 and 1.18. For this, the aspect ratios given in Table 2.4 and the lift coefficients obtained from the force measurement given in Table 5.1 were used. The values of C_{Dvi} as well as the ratio of the vortex-induced drag coefficient to the total drag coefficient obtained from the force measurements are given in Table 5.1. The results indicate that the contribution of the vortex induced drag is between 11% in the case of the straight wing at q_∞ = 135 Pa and α = 5° and 71% in the case of the swept back wing at q_∞ = 545 Pa and α = 10°. The contribution of the vortex-induced drag to the total drag is always larger in the case of the swept-back wing than in the case of the straight wing at equivalent flow conditions, which is principally due to the smaller aspect ratio. Finally, the contribution of the vortex-induced drag to the total drag is always larger at α = 10° than at α = 5° according to the larger lift coefficient.

$$C_{Dvi} = \frac{C_L^2}{\pi \mathcal{A} e_s} \tag{5.4}$$

Configuration	q_∞ [Pa]	α [°]	$C_{Lforcemeas.}$	$C_{Lliftdistr.}$	ΔC_L [%]	e_s	C_{Di}	C_{Dvi}/C_D
Straight wing	135	5	0.294	0.295	0.40	0.907	0.0033	0.109
		10	0.716	0.828	13.48	0.960	0.0187	0.317
	545	5	0.485	0.463	4.75	0.782	0.0105	0.297
		10	0.901	1.000	9.86	0.935	0.0303	0.447
Swept-back wing	135	5	0.303	0.321	5.68	0.977	0.0068	0.277
		10	0.612	0.631	2.94	0.958	0.0285	0.541
	545	5	0.395	0.430	8.17	0.869	0.0130	0.528
		10	0.717	0.788	9.03	0.910	0.0410	0.710

Table 5.1: Aerodynamic parameters derived from the stereo-PIV measurements.

5.1.4 Lift-to-drag ratio

Figure 5.12 presents the lift-to-drag ratio characteristics corresponding to the straight wing, the intermediate 2, and the swept-back wing configurations at different free-stream dynamic pressures. At q_∞ = 135 Pa and q_∞ = 545 Pa, the straight wing provides the largest lift-to-drag ratio for $C_L > 0.5$, whereas for $C_L < 0.5$, the largest lift-to-drag ratios are obtained with the swept-back wing. The characteristics of the intermediate 2 configuration is fairly in between. This is consistent with the drag polars presented in Fig. 5.7 and confirms the aerodynamic benefit that can be gained from the planform morphing, since changing the wing configuration can be used to increase L/D depending on the required lift coefficient. However, the pronounced

dynamic pressure dependency of the lift and drag characteristics resulting from the membrane deflection makes this aerodynamic benefit very sensitive to the flow conditions. In fact, the clear trend observed at q_∞ = 135 Pa and q_∞ = 545 Pa does not occur at q_∞ = 310 Pa. At this flow condition, the lift-to-drag ratio is dominated by the straight wing configuration over almost the whole range of lift coefficients. In this case, the superiority of the straight wing and of the intermediate 2 configurations over the swept-back wing are principally due to the smaller zero-lift drag occurring at this flow condition as mentioned in the discussion of the drag polars (cf. Fig. 5.7).

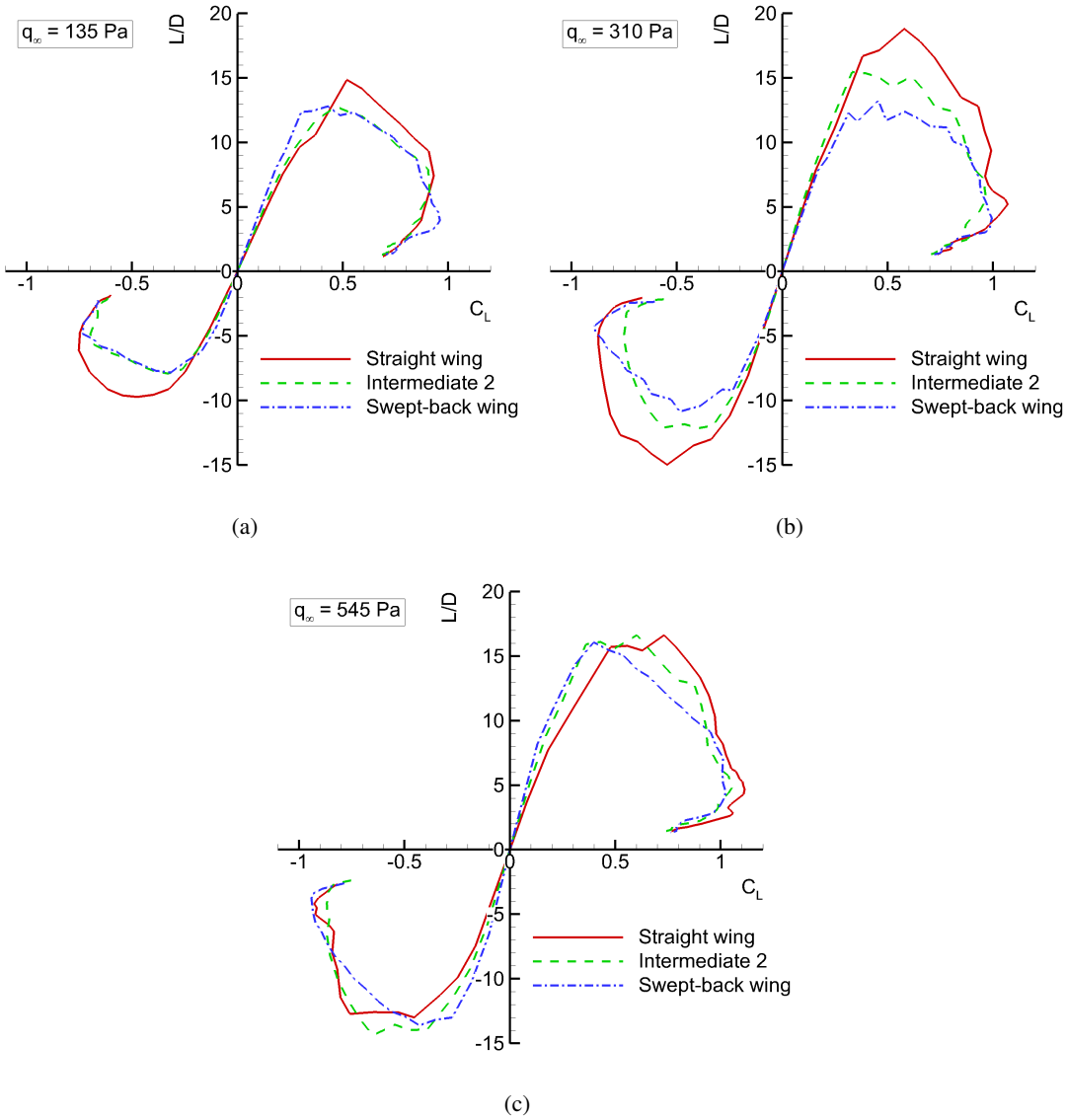

Figure 5.12: Lift-to-drag ratio characteristics as a function of the wing planform and free-stream dynamic pressure.

The highest maximum lift-to-drag ratios at q_∞ = 135 Pa and at q_∞ = 310 Pa are obtained with the straight wing configuration with values of 14.58 (at q_∞ = 135 Pa) and 18.67 (at q_∞ = 310

Pa). At q_∞ = 545 Pa, all three wing configurations exhibit similar values of $(L/D)_{max}$ around 16. These lift-to-drag ratios are relatively large considering the low Reynolds number at which the measurements were carried out (cf. Table 2.5). In the negative range of lift coefficients, the largest absolute values of L/D at q_∞ = 135 Pa and q_∞ = 310 Pa are obtained with the straight wing. At q_∞ = 545 Pa, the intermediate 2 and the swept-back wing configurations provide larger absolute values of L/D. The lift-to-drag ratios occurring in the negative range of lift coefficients are also relatively large compared to the lift-to-drag ratios occurring at positive lift coefficients because the wing takes a negative camber at negative angles of attacks as described in chapter 4. A synthesis of the lift-to-drag ratio characteristics in terms of its maximum value, $(L/D)_{max}$, as a function of the wing planform ($\mathcal{AR}$) and flow conditions (q_∞) is shown in Fig. 5.13. In this figure, the measurement results obtained with the intermediate 1 and 3 configuration are also taken into account. In general, the maximum lift-to-drag ratio increases with increasing free-stream dynamic pressure. This is attributed to both, an increase in lift and a decrease in drag as mentioned in the discussion of the lift and the drag polars in the previous sections. In the case of the straight wing only ($\mathcal{AR}$ = 9.12), the largest maximum lift-to-drag ratio occurs at q_∞ = 310 Pa with $(L/D)_{max}$ = 18.67. With the remaining configurations, a further increase of the free-stream dynamic pressure may lead to a further increase in $(L/D)_{max}$ until a maximum is reached. It indicates that the wing surface reaches an optimal deformation state in terms of the maximum lift-to-drag ratio at a given flow condition. Concerning the effect of the planform, $(L/D)_{max}$ gets in general smaller with decreasing aspect ratio. The largest values of $(L/D)_{max}$ are therefore obtained with the straight wing ($\mathcal{AR}$ = 9.12) except at q_∞ = 545 Pa where the intermediate 1 configuration ($\mathcal{AR}$ = 7.45) provides the largest value with $(L/D)_{max}$ = 17.44.

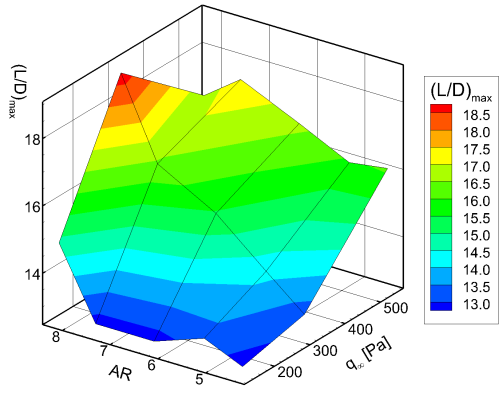

Figure 5.13: Synthesis of the lift-to-drag ratio characteristics in terms of its maximum value, $(L/D)_{max}$, as a function of the planform configuration ($\mathcal{AR}$) and flow condition (q_∞).

5.2 Flight performance criteria

In the following, the influence of the planform morphing on the flight performance criteria with respect to minimum and maximum speeds, range and endurance, and minimum turn radius (cf. section 1.3.3) is presented.

5.2.1 Minimum and maximum speeds

The minimum flight speed, V_{min}, was recognized to be inversely proportional to the square root of the wing area times the maximum lift coefficient (cf. Eq. 1.26), and the maximum flight speed, V_{max}, to be inversely proportional to the square root of the wing area times the zero-lift drag coefficient (cf. Eq. 1.27). As a result, the minimum and maximum speeds associated with a given wing planform relatively to the minimum and maximum speeds associated with the straight wing (index *sw*) can be evaluated using the relations given by Eqs. 5.5 and 5.6.

$$\frac{V_{min}}{(V_{min})_{sw}} = \frac{\sqrt{(SC_{Lmax})_{sw}}}{\sqrt{SC_{Lmax}}} \tag{5.5}$$

$$\frac{V_{max}}{(V_{max})_{sw}} = \frac{\sqrt{(SC_{D0})_{sw}}}{\sqrt{SC_{D0}}} \tag{5.6}$$

Figure 5.14 shows the relative variation of the minimum and maximum speeds with the planform configuration at the different free-stream dynamic pressures. Of course, the data points shown in this plot are associated with a fixed dynamic pressure, i.e. a fixed flight speed. However, this allows to recognize the main trend concerning the influence of the planform. Figure 5.14a indicates that the lowest minimum speed is always obtained with the straight wing according to the large planform area and the comparatively large maximum lifts associated with this configuration (cf. Fig. 5.4b). The minimum speed increases monotonically as the planform changes from the straight wing to the swept-back wing. Consequently, the swept-back wing is associated with the largest minimum speeds, expected to lie between 1.06 and 1.12 times the minimum speed of the straight wing.

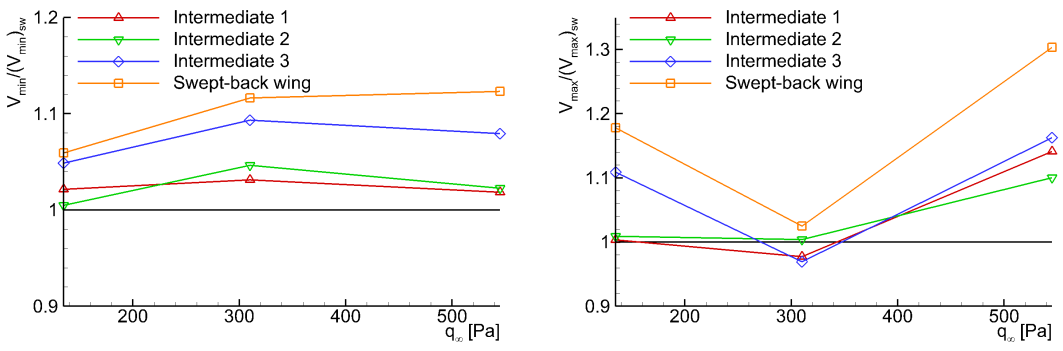

(a) (b)

Figure 5.14: Effect of the wing configuration on the minimum and maximum speeds.

Concerning the maximum speed (cf. Fig. 5.14b), the swept-back wing provides always the largest maximum speed as a result of the small planform area and of the comparatively small values of the zero-lift drag coefficient associated with this configuration (cf. Fig. 5.8a). However, the relative gain in V_{max} is very sensitive to the flow conditions because it depends on C_{D0} which is itself very sensitive to the flow conditions and membrane deformation. The relative gain in maximum speed corresponding to the swept-back varies between 1.02 and 1.3 times the

maximum speed of the straight wing depending on the flow conditions.
The largest performance gain concerning the minimum and the maximum speed is always reached with one of the extreme configurations. The performance values corresponding to the intermediate configurations are always in between.

5.2.2 Maximum range and endurance

The range and the endurance were recognized to be directly proportional to the lift-to-drag ratio (cf. Eqs. 1.28 and 1.29). As a result, the maximum range and endurance are obtained when the airplane flies at $(L/D)_{max}$. The relative change in maximum range and endurance compared to the performance values corresponding to the straight wing can be evaluated with the relation given by Eq. 5.7.

$$\frac{E_{max}}{(E_{max})_{sw}} = \frac{R_{max}}{(R_{max})_{sw}} = \frac{(L/D)_{max}}{[(L/D)_{max}]_{sw}} \tag{5.7}$$

Figure 5.15 presents the relative variation of the maximum range and the maximum endurance with the planform configuration. Here again, the effect of the planform shape is very sensitive to the flow conditions. At q_∞ = 135 Pa and q_∞ = 310 Pa, the straight wing provides clearly the best performance because it is associated with comparatively large values of the maximum lift-to-drag ratio (cf. Fig. 5.13). At q_∞ = 310 Pa, the relative maximum range and endurance decrease monotonically from 1 to 0.7 as the planform changes from the straight wing to the swept-back wing configuration according to the monotonic decrease in the maximum lift-to-drag ratio occurring at this flow condition. At q_∞ = 135 Pa, the effect of the planform is not as univocal as at q_∞ = 310 Pa. All configurations exhibit a maximum range and a maximum endurances that is smaller by a factor between 0.86 and 0.89 compared to the performance of the straight wing. At q_∞ = 545 Pa, the best performance is obtained with the intermediate 1 configuration although all configurations are relatively near to each other at this flow conditions.

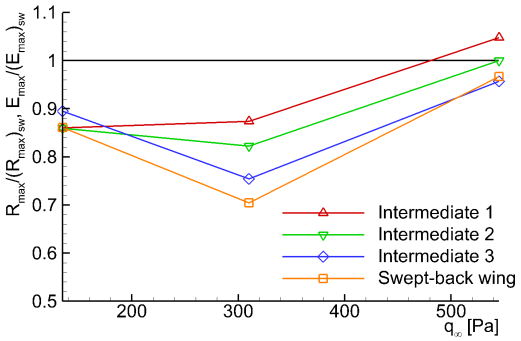

Figure 5.15: Effect of the wing configuration on the maximum range and endurance.

5.2.3 Minimum turn radius

The minimum turn radius was recognized to be proportional to the ratio of the lift-dependent drag factor to the wing area (level turn, cf. Eq. 1.30). Consequently, the minimum turn ra-

dius associated with a given planform relatively to the minimum turn radius associated with the straight wing can be evaluated by Eq. 5.8.

$$\frac{r_{min}}{(r_{min})_{sw}} = \frac{(K/S)}{(K/S)_{sw}} \tag{5.8}$$

Figure 5.16 indicates the relative variation of the minimum turn radius with the planform at different free-stream dynamic pressures. The smallest turn radius is always obtained with the straight wing as a result of its comparatively large planform area and small lift-dependent drag factor (cf. Fig. 5.8b). It increases monotonically as the planform is changed towards the swept-back wing because of the decreasing planform area and of the increasing lift-induced drag factor. Consequently, the swept-back wing exhibits the largest values of r_{min}, which are larger by a factor between 1.57 and 1.89 times the minimum turn radius of the straight wing configuration depending on the flow conditions.

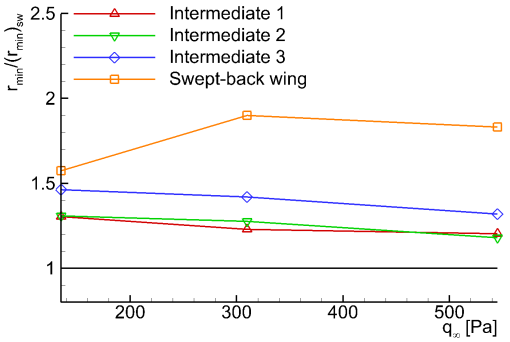

Figure 5.16: Effect of the wing configuration on the minimum turn radius.

6 Wing characteristics with modified membrane properties

The study of the wing characteristics presented in the previous chapters revealed that the passive deflection of the wing surface dominates the wing behavior and leads to an pronounced dependency of the aerodynamic characteristic and flight performances on the flow conditions. In this chapter, the wing characteristics resulting from specific structural modifications of the baseline membrane cover aiming to provide additional control over the wing shape and to limit this passive dependency are presented. First, the impact of a continuous variation of the membrane pre-stress is studied. Further, the wing characteristics obtained with the two alternative membrane covers shown in section 2.1.3.4 are discussed. The results presented in this chapter were obtained with the last version of the articulated structure (cf. section 2.1.1).

6.1 Variation of the membrane pre-stress

In order to influence the surface deformation and to allow for additional control of the wing shape, a continuous variation of the membrane properties is required. The solution considered here is the variation of the pre-stress, induced by moving the trailing-edge spar as introduced in section 2.1.3.3. With the straight wing, the intermediate 2, and the swept-back wing, the pre-stress was modified by moving the trailing-edge spar into four different positions corresponding to root chord lengths of 0.24 m, 0.26 m, 0.28 m, and 0.3 m. The root chord length used so far was 0.27 m. The membrane pre-stress and the geometric characteristics associated with these configurations are listed in Table 2.4. In the following, the different pre-stress settings are referred to by the parameter K_m defined as the ratio of the pre-stress to the free-stream dynamic pressure as defined in Eq. 2.17. The values of this parameter corresponding to each planform shape, pre-stress, and flow condition are given in Table 2.6.

As discussed in chapter 4, the character of the boundary layer has a significant effect on the deflection amplitude at large free-stream dynamic pressures in the case of the straight wing configuration. The force measurements presented in the following were performed with a clean wing surface and thus correspond to the free-transition case. For the deflection measurements, markers were placed over the complete wing surface and disturb the surface flow. Therefore, the boundary layer is turbulent over the complete wing surface in this case. As a result, the deflection amplitude of the straight wing at q_∞ = 545 Pa is expected to be underestimated compared to the deflection amplitude that occurred during the force measurements as explained in section 4.2.2.

6.1.1 Effect on the wing camber

Figures 6.1 to 6.3 show the influence of the pre-stress on the deflected wing geometries at α = 10°, represented by the airfoil section at $2y/b$ = 0.3. The pre-stress has a significant effect on the deflection of the wing surface [71, 72]. The camber at a given free-steam dynamic pressure decreases as the pre-stress is augmented. However, the effect on the camber is not the same for all configurations because of the intrinsic influence the planform has on the initial pre-stress (cf. section 2.1.3.3). The straight wing configuration (cf. Fig. 6.1) exhibits the largest deflection amplitudes as well as the largest variation in camber as the pre-stress is varied. The reason is that this configuration is associated with a relatively small pre-stress (i.e. small K_m) and that it additionally experiences a comparatively large aerodynamic load as a result of its large aspect ratio as already explained in section 4.1. At q_∞ = 545 Pa and with the smallest pre-stress (k_m = 460), the wing shows a very thick airfoil with a relative camber of about 0.14. At this flow condition, increasing the pre-stress allows keeping the relative camber to a more usual amplitude (i.e. < 0.1). In the case of the intermediate 2 configuration (cf. Fig. 6.2), the deflection is much smaller and the variation of the pre-stress results in a narrower range of cambers compared to the straight wing configuration. The main reason for this is that the initial pre-stress is larger with this configuration, which is directly reflected by the comparatively large values of the parameter K_m. In the case of the swept-back wing configuration (cf. Fig. 6.3), the pre-stress affects the airfoil shapes with a similar amplitude as in the case of the intermediate 2 configuration. Further, the camber is also much smaller than in the case of the straight wing, although this configuration is associated with K_m values that are even slightly smaller than for the straight wing. In this case, the smaller deflection is uniquely attributed to the effect of the smaller aspect ratio as discussed in section 4.1.

Figure 6.4 shows a synthesis of the effect of the pre-stress on the wing camber. The relative camber of the airfoil sections at $2y/b$ = 0.3 occurring at α = 5° and α = 10° is plotted as a function of the parameter K_m. The data points represented by the square, the delta, and the diamond symbols indicate the values obtained from the measurements performed at q_∞ = 135 Pa, q_∞ = 310 Pa, and q_∞ = 545 Pa, respectively, and the continuous lines (red), the dashed lines (green), and the dash-dotted lines (blue) represent the data sets corresponding to the straight wing, the intermediate 2, and the swept-back wing configurations, respectively. Further, each group of four data points with the same symbol and line style correspond to the four values of the pre-stress used at a given flow condition and wing planform. The leftmost one of those four points therefore always corresponds to the smallest pre-stress, i.e. the one obtained with c_r = 0.24 m. There is an inverse dependency between the wing camber and the parameter K_m. Overall, the camber decreases as K_m increases. The sensitivity of the camber to a change in K_m is further much larger at low values than at large values of this parameter. At large values, the relative camber of all three wing configurations converges towards f/c = 0.025, which corresponds to the camber of the airfoil section with the undeflected membrane. As K_m decreases, the straight wing configuration exhibits always the largest camber, because its large aspect ratio leads to comparatively larger aerodynamic load at equivalent flow conditions. The maximum relative camber associated with this configuration is f/c = 0.11 at α = 5° and f/c = 0.14 at α = 10°.

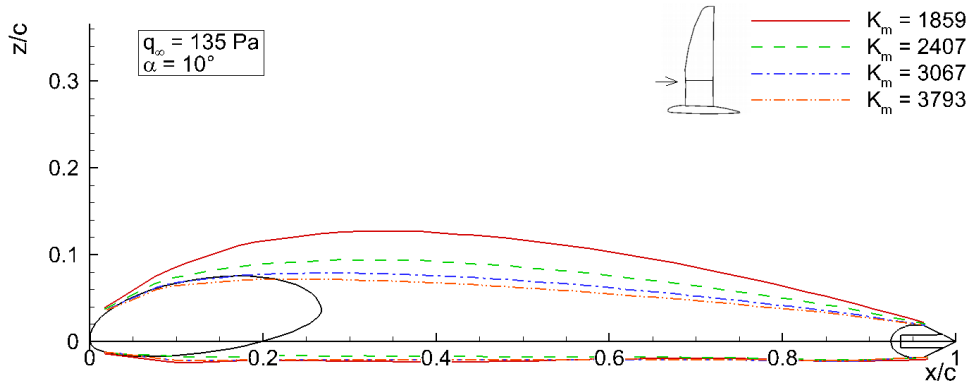

(a)

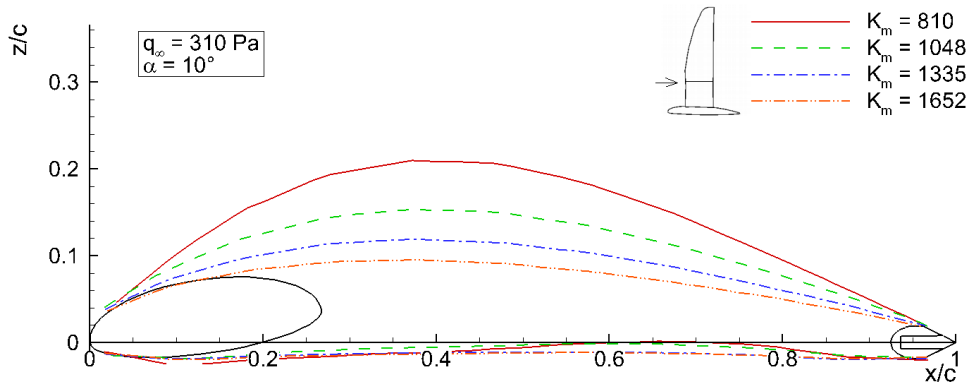

(b)

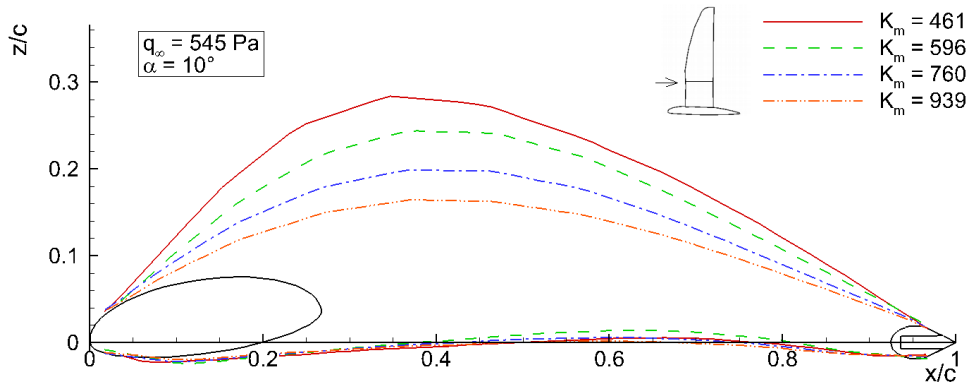

(c)

Figure 6.1: Effect of a variation of the pre-stress on the deflected airfoil shapes of the straight wing configuration (wing section at $2y/b = 0.3$).

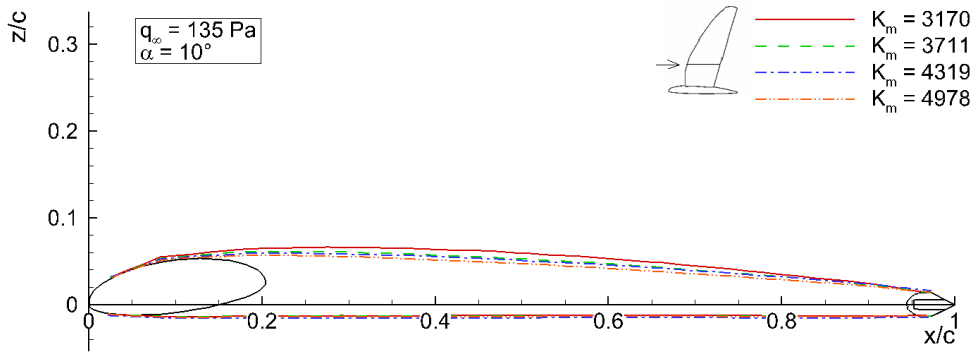

(a)

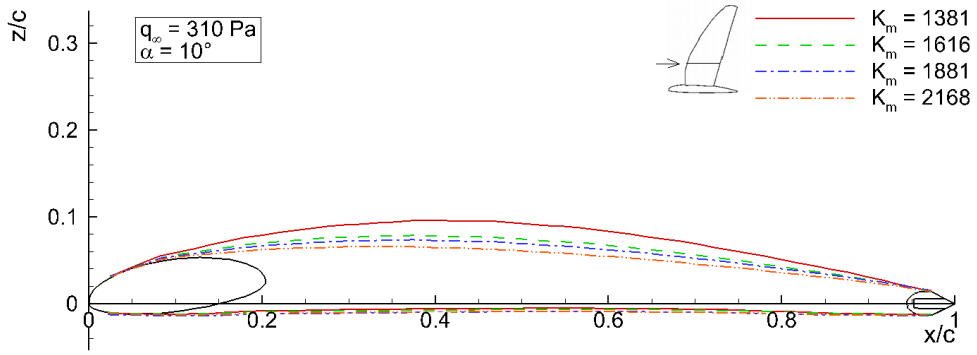

(b)

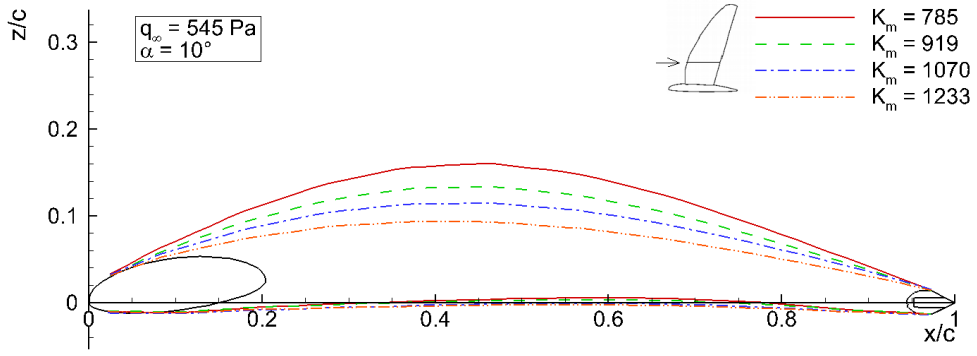

(c)

Figure 6.2: Effect of a variation of the pre-stress on the deflected airfoil shapes of the intermediate 2 configuration (wing section at $2y/b = 0.3$).

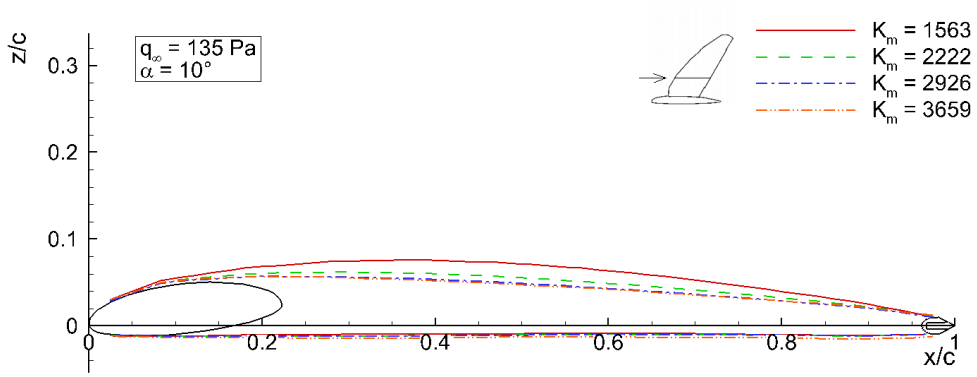

(a)

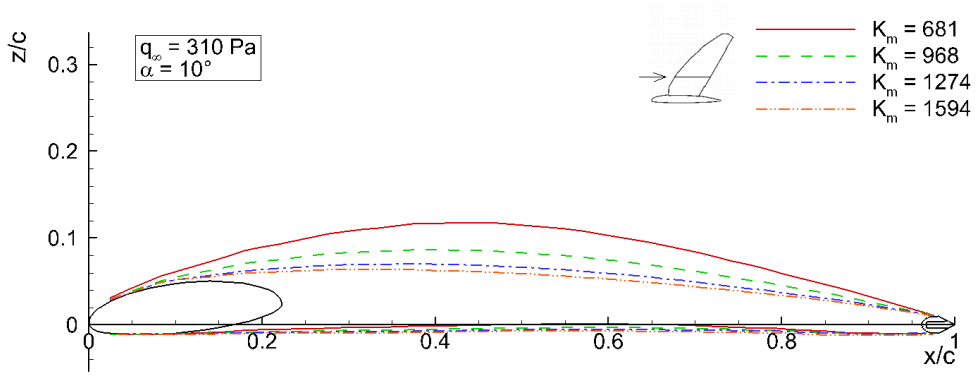

(b)

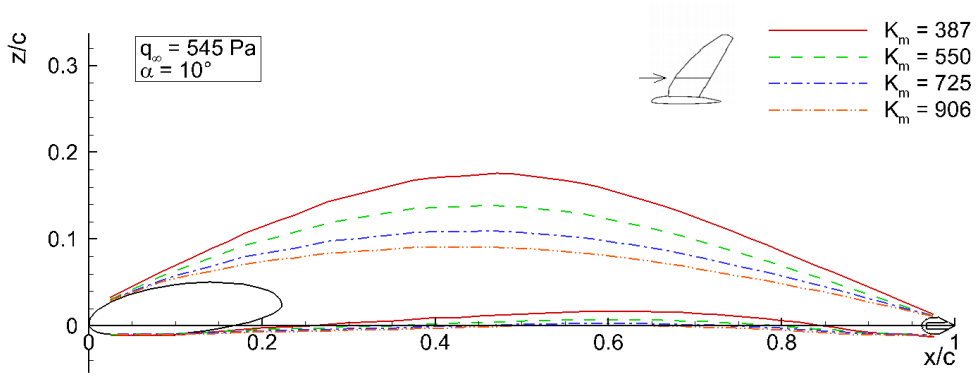

(c)

Figure 6.3: Effect of a variation of the pre-stress on the deflected airfoil shapes of the swept-back wing configuration (wing section at $2y/b = 0.3$).

At $\alpha = 5^\circ$, the camber corresponding to the straight wing reaches its largest value at $K_m = 596$ and drops abruptly as K_m decreases. In this particular case, the downward deflection of the wing lower side that occurs at $\alpha = 0^\circ$ persists in the positive range of angles of attack (hysteresis effect, cf. chapter 4), lowering thus the camber. The swept-back wing configuration is always associated with the smallest camber at a given value of K_m because it has the smallest aspect ratio and thus, the membrane is subjected to smaller aerodynamic loads. At the lowest value of K_m associated with this configuration, the relative camber is $f/c = 0.079$ at $\alpha = 5^\circ$ and $f/c = 0.094$ at $\alpha = 10^\circ$. Finally, the camber of the intermediate 2 configuration at a given value of K_m is always between the two other configurations. The largest relative camber in this case is $f/c = 0.064$ at $\alpha = 5^\circ$ and $f/c = 0.081$ at $\alpha = 10^\circ$.

For a given planform shape, the wing camber does not perfectly scale with K_m since at an equivalent value of this parameter but obtained with a different combination of pre-stress and dynamic pressure, a different wing camber results. The camber is always larger with a low pre-stress and a low dynamic pressure than with a large dynamic pressure and a large pre-stress. This effect is especially pronounced in the case of the straight wing configuration between the datasets corresponding to $q_\infty = 135$ Pa and $q_\infty = 310$ Pa. These differences can be due to several reasons. Principally, the parameter K_m reflects only the local characteristics of the membrane (pre-stress taken at a single position on the wing surface, cf. section 2.1.3) but the wing is three-dimensional and the membrane deflection in the wing section considered here is influenced by the entire membrane surface. Also, the variation in Reynolds number associated with a variation of the free-stream dynamic pressure also influences the membrane deformation.

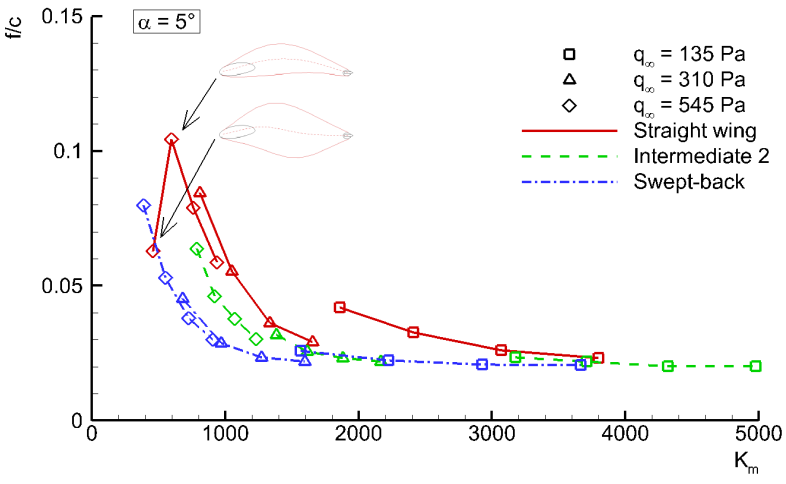

(a)

Figure 6.4: Relative camber of the wing section at $2y/b = 0.3$ as a function of the parameter K_m.

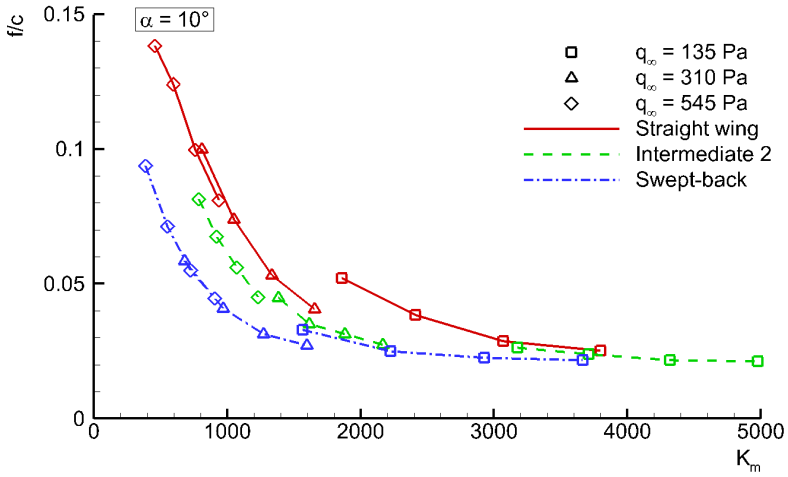

(b)

Figure 6.4 continued.

6.1.2 Effect on the aerodynamic characteristics

The analysis of the membrane deflection in the previous section showed that a variation of the pre-stress can be used to adjust the wing camber within a certain range at a given flow condition. In the following, the resulting effect on the aerodynamic characteristics is discussed.

6.1.2.1 Hysteresis

Force measurements were carried out during the increasing and the decreasing angle of attack slopes to detect the presence of any hysteresis effects as discussed in chapter 4. The results reveal that the hysteresis effect becomes significant at low values of K_m. Figure 6.5 shows the lift and drag polars corresponding to the straight wing configuration measured during the increasing and the decreasing angle of attack slopes at q_∞ = 545 Pa to illustrate the influence of the pre-stress on the hysteresis. With the lowest pre-stress (K_m = 461), the hysteresis is pronounced and extends between α = -13° and α = 4°. Accordingly, the hysteresis in the drag polar is also very large. The lift and the drag are larger during the decreasing angle of attack phase because the camber remains longer positive for $\alpha < 0°$ as discussed in chapter 4. As the pre-stress increases, the size of the hysteresis diminishes and disappears completely at K_m = 939. A synthesis of the influence of the pre-stress on the amplitude of the hysteresis for each planform configuration is given in Fig. 6.6. The upper plot shows ΔC_{L0}, the difference between the C_{L0} values corresponding to the α-increasing and the α-decreasing lift curves, as a function of K_m. The lower plot shows ΔC_{D0}, the difference in zero-lift drag coefficient between the α-increasing and the α-decreasing drag polars, as a function of K_m. The hysteresis becomes significant when K_m is lower than 1000. Consequently, no hysteresis effect is observed for the intermediate 2 configuration because this configuration is associated with larger values of K_m for the conditions considered here.
The aerodynamic characteristics presented in the following are averaged between the α-increasing and the α-decreasing curves for clarity.

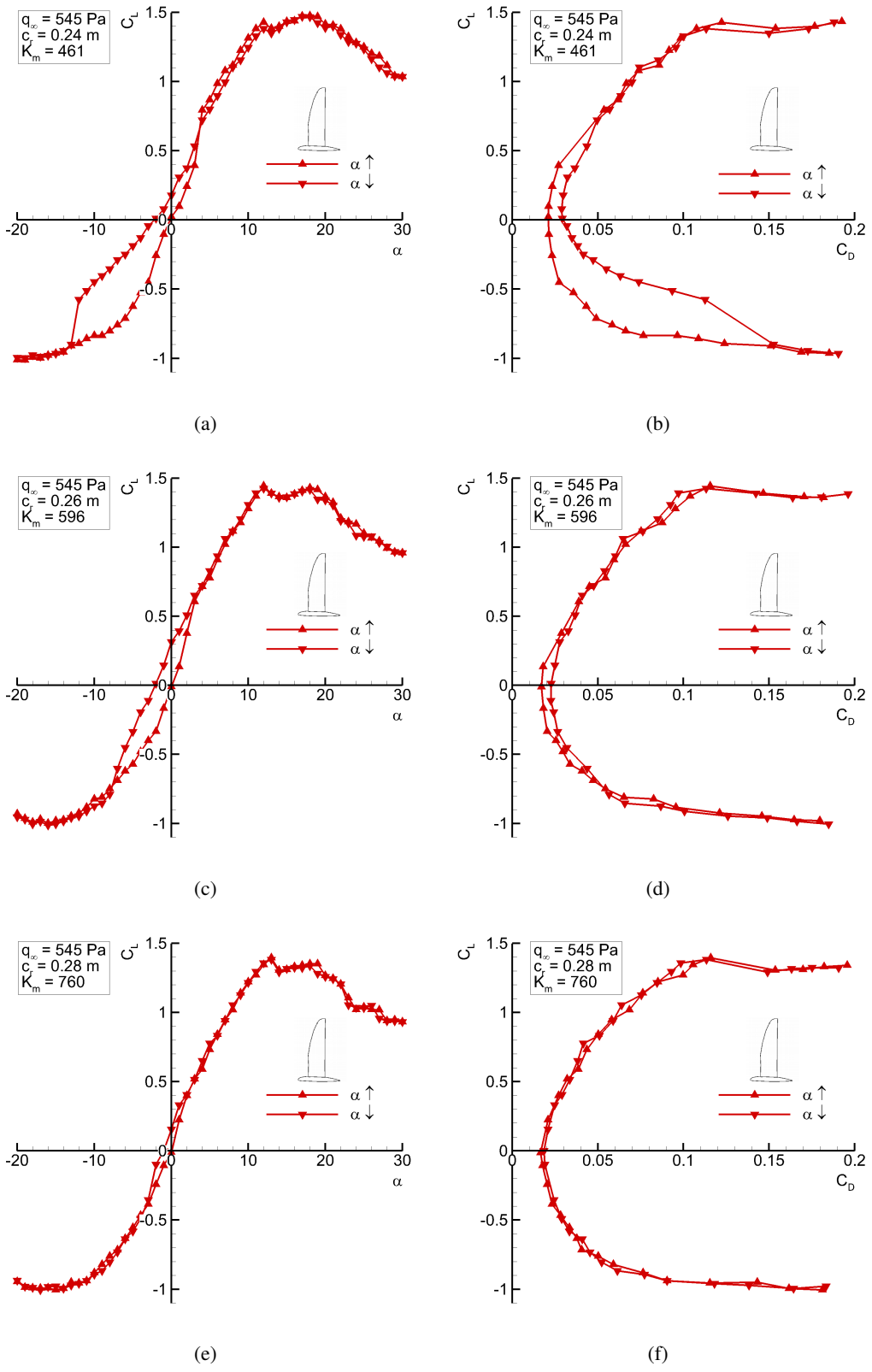

Figure 6.5: Lift curves of the straight wing configuration corresponding to the α-increasing and to the α-decreasing slopes at q_∞ = 545 Pa.

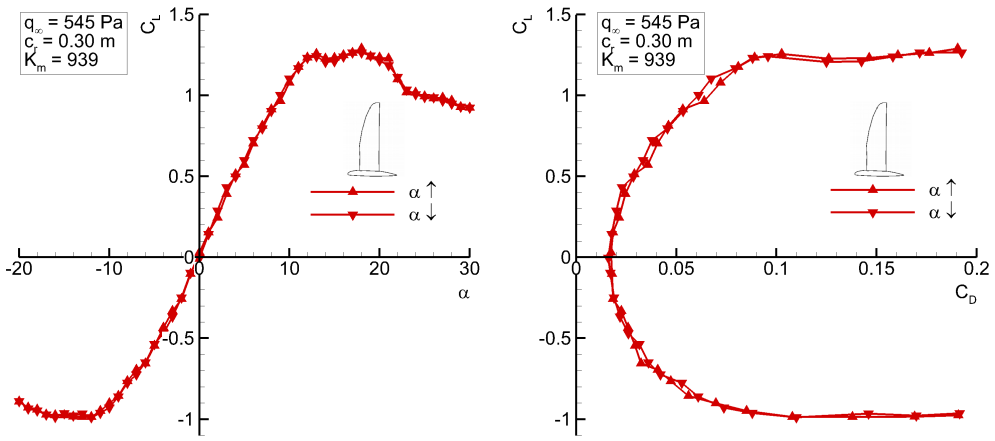

(g) (h)

Figure 6.5 continued.

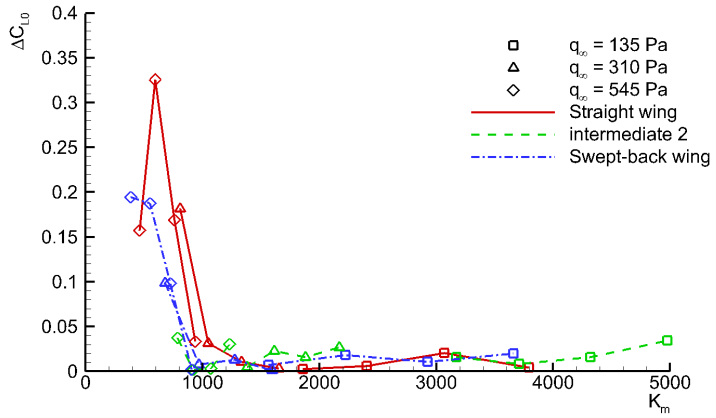

(a)

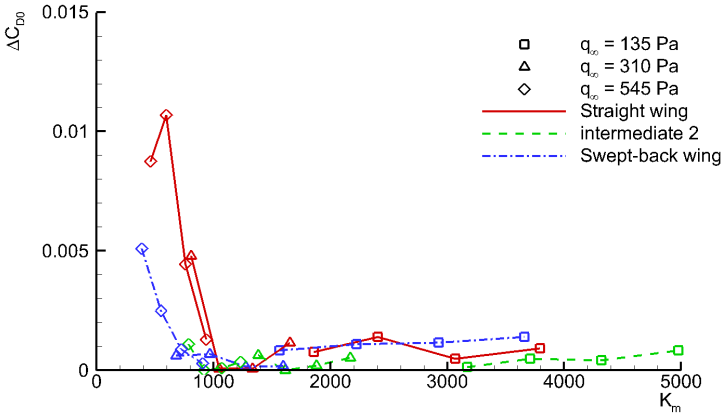

(b)

Figure 6.6: Amplitude of the hysteresis effect as a function of K_m.

6.1.2.2 Lift polars

Figure 6.7 illustrates the effect of the pre-stress on the lift polars of the straight wing configuration at q_∞ = 135 Pa, q_∞ = 310 Pa, and q_∞ = 545 Pa. In general, the lift increases with decreasing pre-stress as a result of the larger camber (cf. Fig. 6.1). However, the pre-stress is found to influence the slope of the lift curves rather than to just shift the curves as could be expected from the variation of the camber. The explanation for this is that the wing at $\alpha = 0^\circ$ exhibits a symmetric airfoil shape due to the deflection of both wing sides into opposite directions as discussed in chapter 4. As a result, the wing produces almost no lift at $\alpha = 0^\circ$ independently of the pre-stress. As the angle of attack increases, the camber becomes positive and grows with a rate that depends on the pre-stress, explaining thus the difference in the lift curve slopes. In addition to this, increasing the root chord length leads also to a slight reduction of the aspect ratio (cf. Table 2.4) which also has an influence on the lift curve slope. At q_∞ = 135 Pa and q_∞ = 310 Pa, the slope of the lift curve increases monotonically with decreasing K_m. At q_∞ = 545 Pa, the lift curve slope increases monotonically up to K_m = 596 but not further. Moreover, the lift curve corresponding to K_m = 461 exhibits a pronounced non-linearity for $\alpha < 5^\circ$. The explanation for this is that the curves presented here are averaged from the two lift curves associated with the α-increasing and the α-decreasing angle of attack slopes shown in Fig. 6.5a, where a pronounced hysteresis occurs. In addition to the lift curve slope, the pre-stress also affects the stall characteristics. For instance, the maximum lift is found to increase with decreasing pre-stress, which is directly related to the increasing camber. The effect of the pre-stress on the lift curves corresponding to the intermediate 2 configuration is shown in Fig. 6.8. In this case, the impact of the pre-stress on the lift curve slope is much smaller than in the case of the straight wing configuration according to the larger values of K_m associated with this configuration. At q_∞ = 135 Pa and q_∞ = 310 Pa, the influence of the pre-stress is very small but still consequent because the largest slopes and the largest maximum lift occur for the smallest value of K_m. At q_∞ = 545 Pa, a larger effect on the lift curve slope is observed according to the larger membrane deformation occurring at this flow condition. Finally, the lift polars corresponding to the swept-back wing are shown in Fig. 6.9. In this case, the impact of the pre-stress on the lift polar is also much smaller than in the case of the straight wing but still larger than in the case of the intermediate 2 configuration.

Figure 6.10 shows a synthesis of the influence of the pre-stress on the lift characteristics in terms of the lift curve slope, $C_{L,\alpha}$, and the maximum lift coefficient, C_{Lmax}, as a function of the parameter K_m. The values of $C_{L,\alpha}$ presented here were obtained by the same method as in chapter 5. Although the lift curves are in general non-linear, especially at lower values of K_m, this approximation still allows capturing the main trends. $C_{L,\alpha}$ decreases with increasing K_m according to the trend observed during the analysis of the lift curves in Figs. 6.7 to 6.9. At large values of K_m, $C_{L,\alpha}$ converges towards a constant value which is near to the theoretical lift curve slope of a rigid wing (cf. section 3.1. The straight wing is associated with the largest values of $C_{L,\alpha}$ over the whole range of K_m due to its comparatively large aspect ratio. Accordingly, the swept-back wing exhibits always the smallest values of $C_{L,\alpha}$. In the case of the straight wing configuration, the lift curve slope reaches a maximum value of approximately 7.4 at K_m = 760. This value is larger than the theoretical maximum of 2π associated with a wing of infinite span. Such large

values of $C_{L,\alpha}$ are effectively possible in the case of the elasto-flexible wing because the camber varies with the angle of attack. At this lower values of K_m, the airfoil changes from a symmetric shape at $\alpha = 0^\circ$ to a cambered airfoil with $f/c = 0.1$ at $\alpha = 10^\circ$ (cf. Fig. 6.4b), explaining the large values of $C_{L,\alpha}$ captured by the linear approximation of the lift curves. Also, the maximum value of $C_{L,\alpha}$ obtained here is larger than the one presented in chapter 5 in Fig. 5.4a. The reason for this is that both data sets were obtained with a different version of the wing structure as explained in section 2.1.1. The swept-back wing configuration exhibits a behavior similar to the straight wing but with overall smaller values of $C_{L,\alpha}$ due to its smaller aspect ratio. It reaches a maximum of $C_{L,\alpha} = 5.5$ at $K_m = 540$. In comparison to the other two configurations, the intermediate configuration shows a narrower variation of $C_{L,\alpha}$ because it is associated with larger values of K_m due to the larger initial pre-stress. The largest value of $C_{L,\alpha}$ in this case is 6.08.

The maximum lift coefficient (cf. Fig. 6.10b) increases with decreasing K_m according to the trend observed in the lift polars (cf. Figs. 6.7 to 6.9). The straight wing exhibits the overall smallest and the overall largest maximum lift with values between 0.91 at $K_m = 3793$ and 1.46 at $K_m = 461$. The intermediate 2 configuration is associated with maximum lift coefficients between 0.94 at $K_m = 4319$ and 1.28 at $K_m = 785$. The narrowest range of C_{Lmax} values is found in the case of the swept-back wing configuration with values between 1.09 at $K_m = 1563$ and 1.33 at $K_m = 387$. Moreover, this configuration exhibits comparatively large values of C_{Lmax} in the range of K_m values corresponding to $q_\infty = 135$ Pa. A similar behavior was already observed in section 5.1.1 and it was explained by the larger sweep angle associated with the swept-back wing configuration. Finally, the values of C_{Lmax} shown here are significantly larger than those presented in section 5.1.1. As for differences in the lift curve slopes mentioned above, the explanation is that the results presented here were obtained with a different version of the articulated structure. Mainly, the thin rounded spar used in the inner part of the leading-edge in the second version of the structure can be responsible for the smaller values of the maximum lift presented in chapter 5.

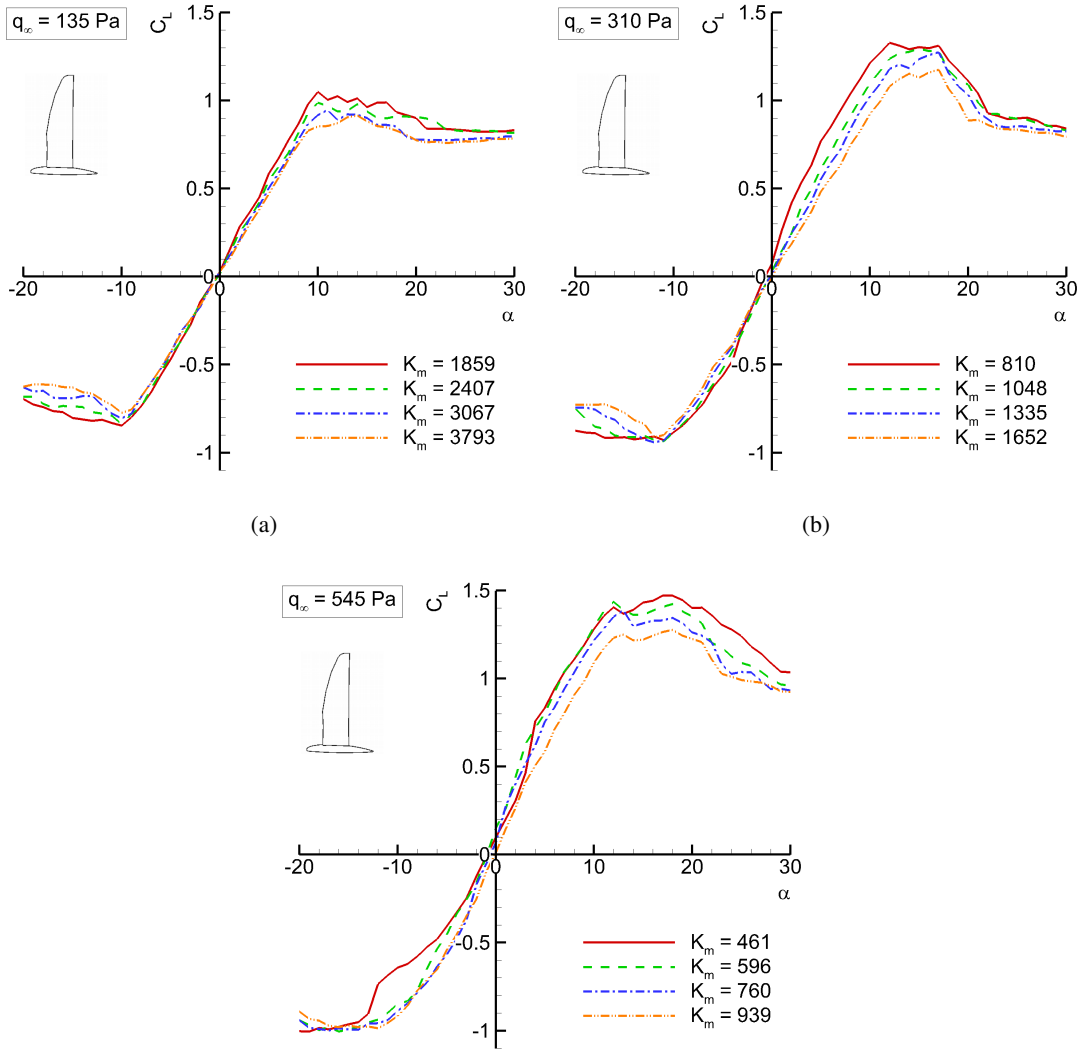

Figure 6.7: Effect of a variation of the pre-stress on the lift polars of the straight wing configuration.

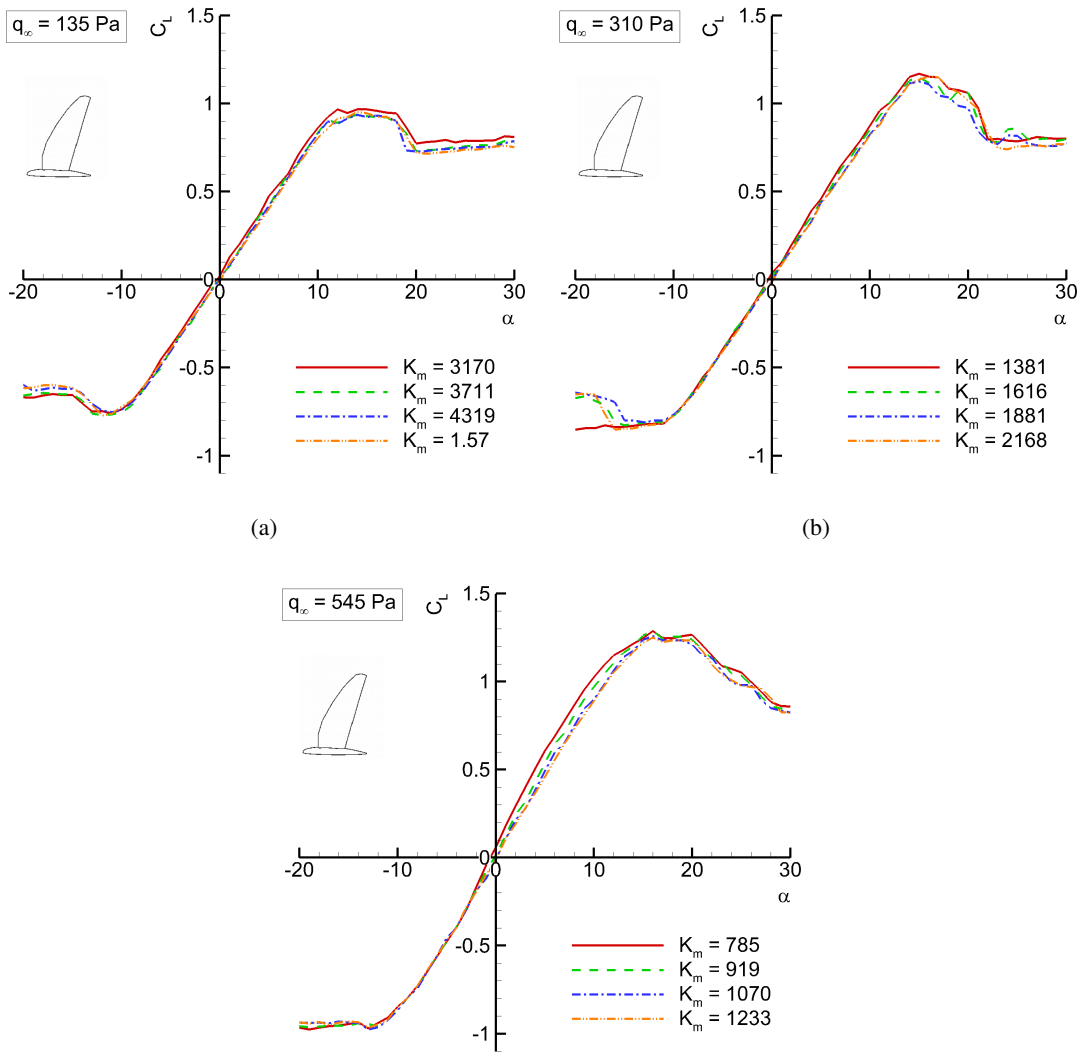

Figure 6.8: Effect of a variation of the pre-stress on the lift polars of the intermediate 2 configuration.

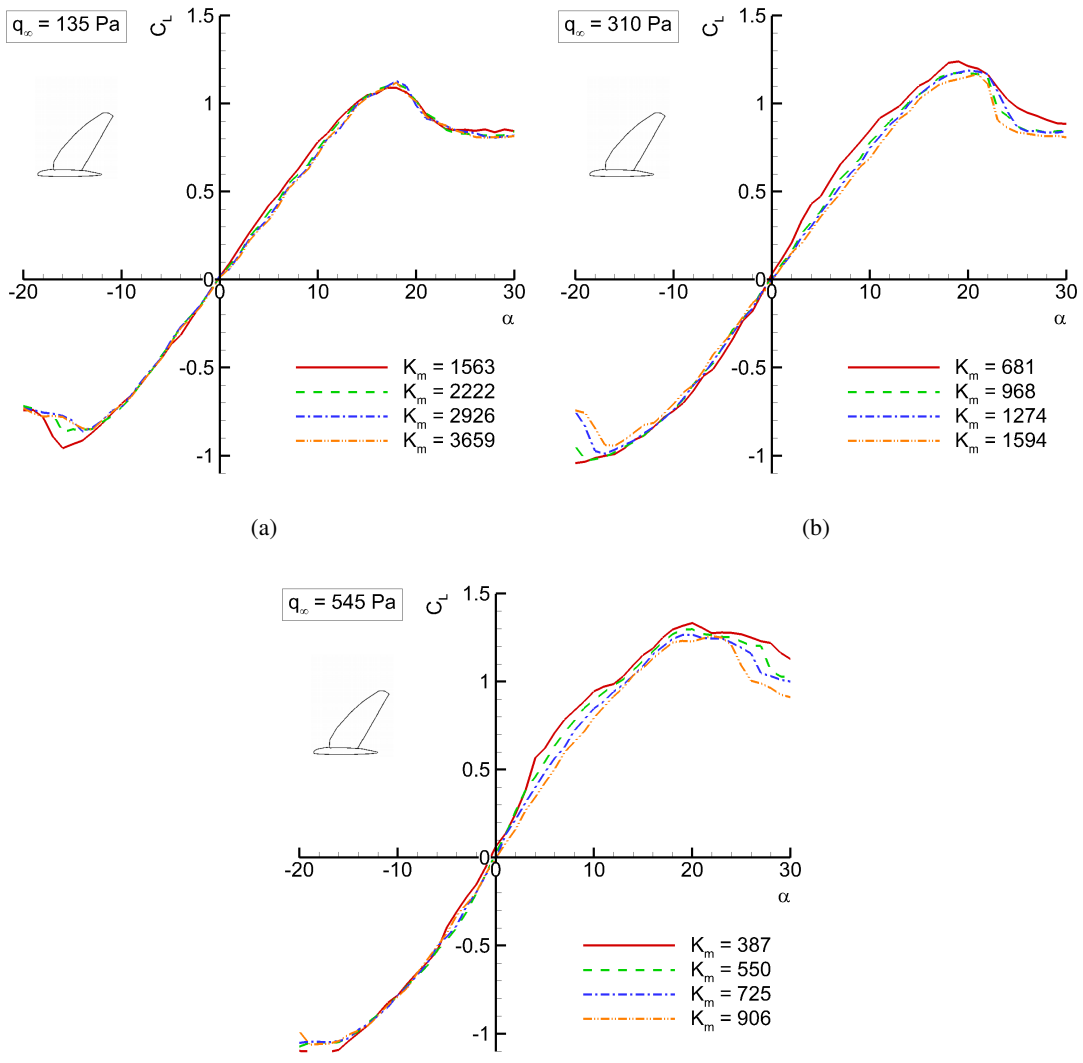

Figure 6.9: Effect of a variation of the pre-stress on the lift polars of the swept-back wing configuration.

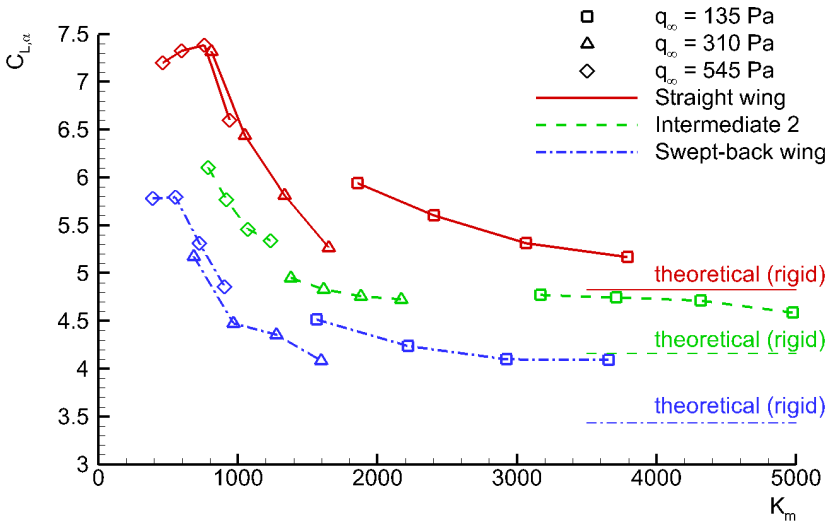

(a)

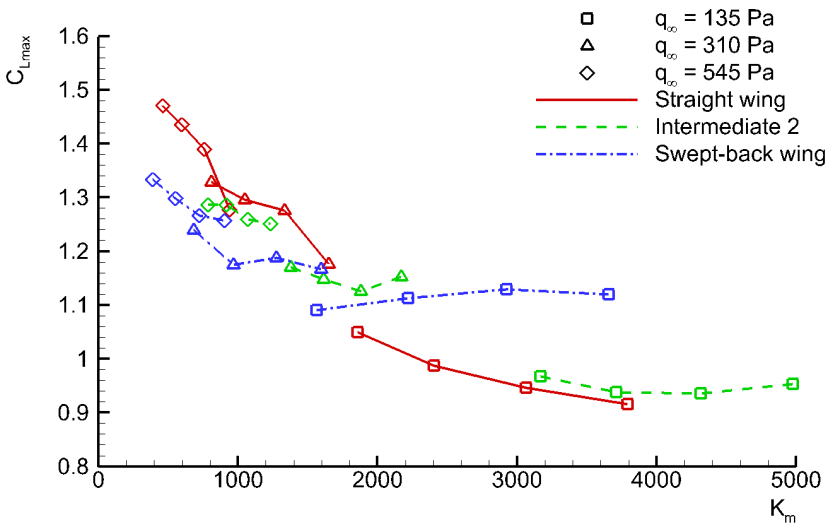

(b)

Figure 6.10: Synthesis of the lift characteristics in terms of the lift curve slope ($C_{L,\alpha}$) and maximum lift coefficient (C_{Lmax}) as a function of the parameter K_m.

6.1.2.3 Drag polars

Figure 6.11 shows the effect of the pre-stress on the drag polars of the straight wing configuration at q_∞ = 135 Pa, q_∞ = 310 Pa, and q_∞ = 545 Pa. At q_∞ = 135 Pa and q_∞ = 310 Pa, the pre-stress does not affect the zero-lift drag, but an effect is observed on the lift-dependent drag. Indeed, the lift-dependent drag in the upper range of positive C_L and in the lower range of negative C_L decreases with decreasing K_m. This is attributed mainly to the larger maximum lift associated with a smaller pre-stress as discussed above (cf. Fig. 6.7). In addition to this, the slight increase in aspect ratio coming along with the decreasing pre-stress resulting from the movement of the trailing-edge spar (cf. Table 2.4) also contributes to a reduction of the lift-dependent drag. At q_∞ = 545 Pa, a large impact on the zero-lift drag and on the lift-dependent drag occurs. At this flow condition, the zero-lift drag is the largest with the smallest pre-stress (K_m = 461), and decreases as the pre-stress increases. This is due to the excessively large camber and thickness the wing exhibits at very small values of K_m (cf. Fig. 6.1c). The effect of the pre-stress on the drag polars of the intermediate 2 configuration is shown in Fig. 6.12. The pre-stress in this case has a much smaller impact on the drag polars according to the smaller effect it has on the wing shape (cf. Fig. 6.2), which was explained by the larger values of K_m associated with this configuration due to its larger initial pre-stress. The zero-lift drag remains fairly constant as the pre-stress varies at all flow conditions. Only a slight decrease in the lift-dependent drag is observed with increasing pre-stress, as explained in the case of the straight wing by the larger maximum lift occurring with small pre-stress (cf. Fig. 6.8) as well as by the effect of the varying aspect ratio. Finally, the drag polars of the swept-back wing configuration are shown in Fig. 6.13. As in the case of the straight wing (cf. Fig. 6.11), the zero-lift drag remains fairly constant at q_∞ = 135 Pa and q_∞ = 310 Pa, but increases significantly with decreasing pre-stress at q_∞ = 545 Pa. Concerning the lift-dependent drag, it is also observed to increase with decreasing pre-stress.

Figure 6.14 presents a synthesis of the drag characteristics in terms of the zero-lift drag coefficient, C_{D0}, and the lift-dependent drag factor, K. The values of C_{D0} and K are obtained with the same method as used in section 5.1.3.1. The quantity C_{D0} remains fairly constant within each dataset corresponding to the same dynamic pressure. However, it is observed to diminish with increasing dynamic pressure, which is likely to be an effect of the increasing Reynolds number. However, at q_∞ = 545 Pa, C_{D0} increases rapidly with decreasing K_m in the cases of the straight wing and of the swept-back wings. This is due to the massive camber and thickness occurring at small values of K_m (cf. Figs. 6.1c and 6.3c), which produce a “blunt body” effect. Using a larger pre-stress at this flow condition is therefore advantageous to reduce the drag. Concerning the effect of the planform shape, it can be seen that C_{D0} is always the largest in the case of the straight wing and the smallest in the case of the swept-back wing according to the trend expected from the change in aspect ratio. The variation of the lift-dependent drag factor with the parameter K_m is shown in Fig. 6.14b. Overall, K decreases slightly with decreasing K_m according to the trend observed in Figs. 6.11 to 6.13. Only in the case of the straight wing at q_∞ = 545 Pa, the lift-dependent drag factor K is larger at the smallest value of K_m. Finally, the lift-dependent drag factor is the largest in the case of the swept-back wing and the smallest in the case of the straight wing. This once again matches well with the trend expected from rigid wing theory.

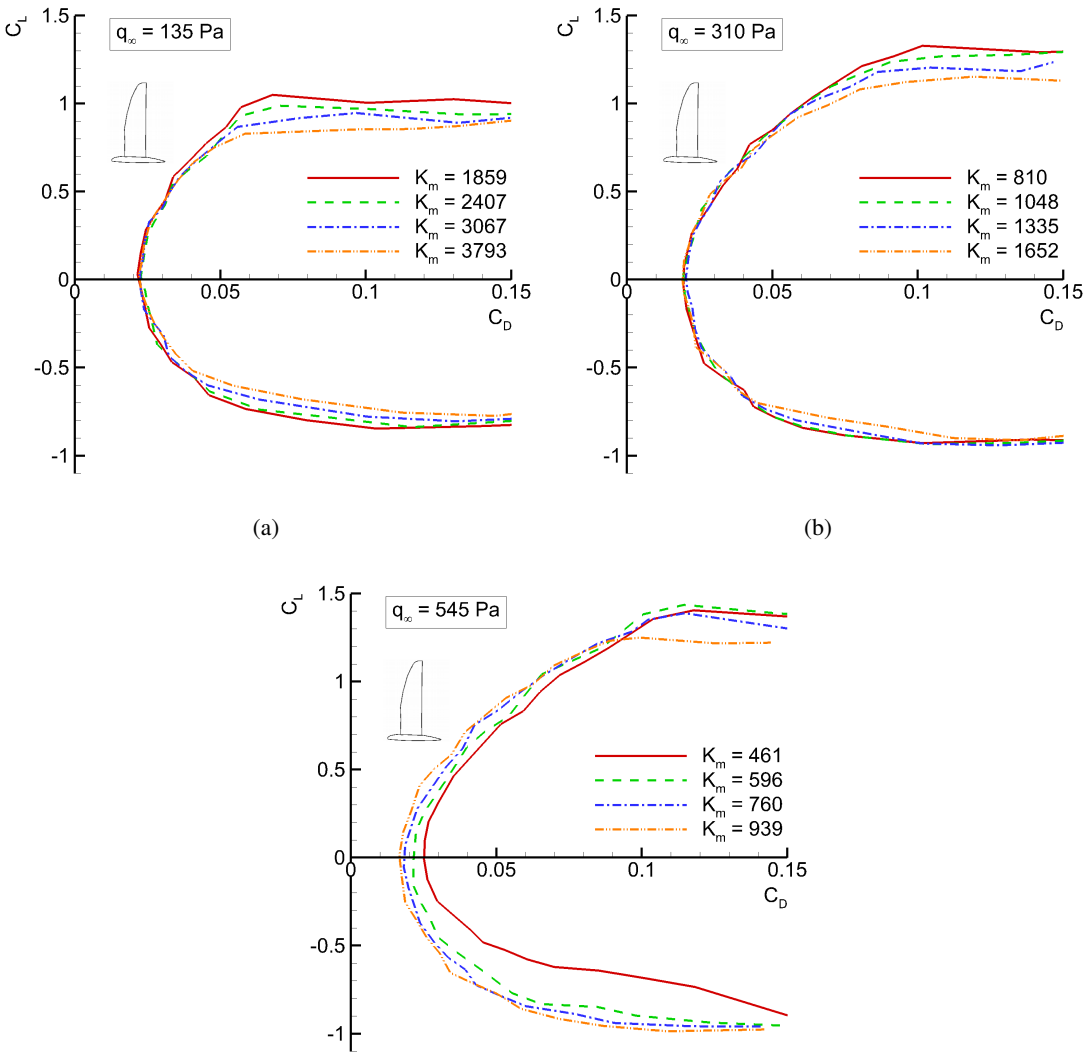

Figure 6.11: Effect of a variation of the pre-stress on the drag polars of the straight wing configuration.

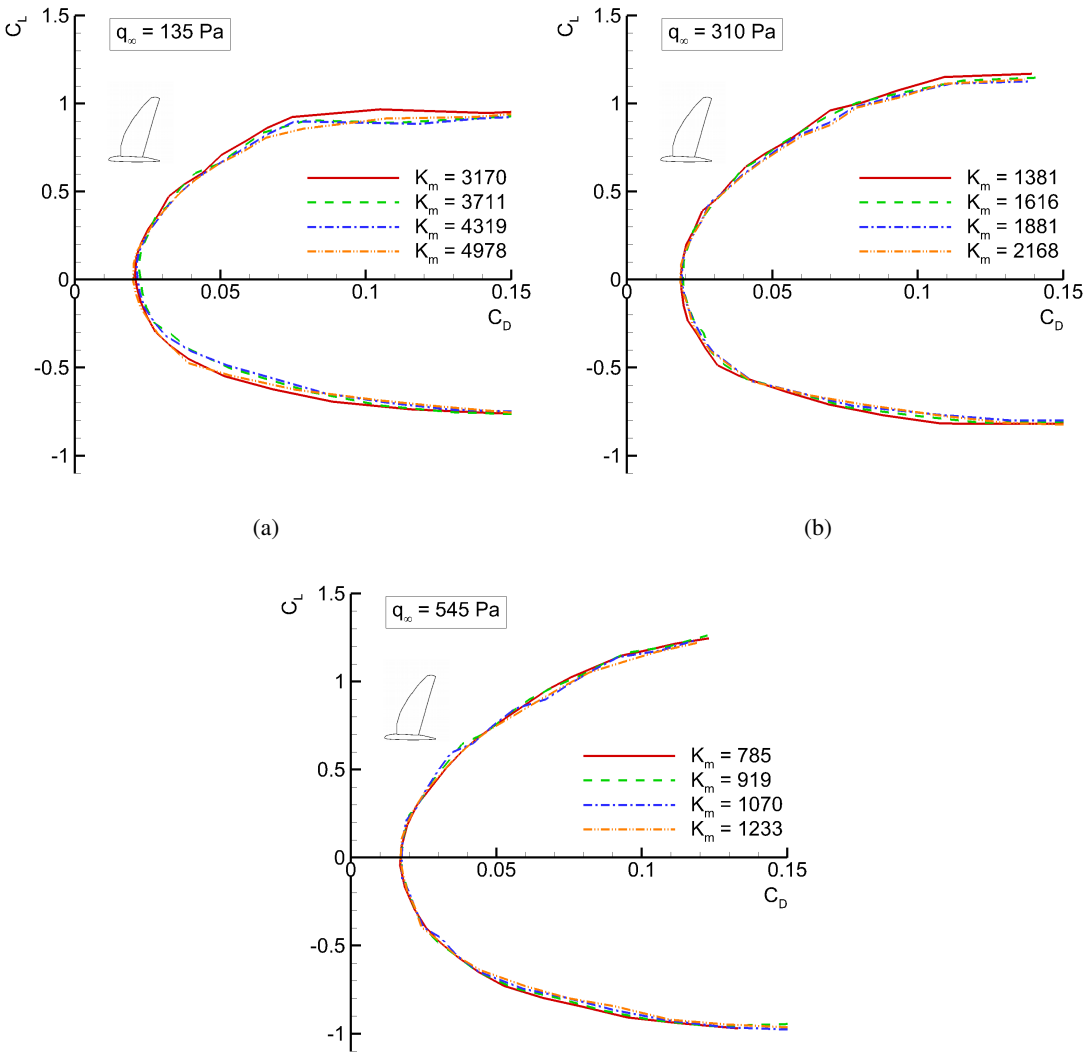

Figure 6.12: Effect of a variation of the pre-stress on the drag polars of the intermediate 2 configuration.

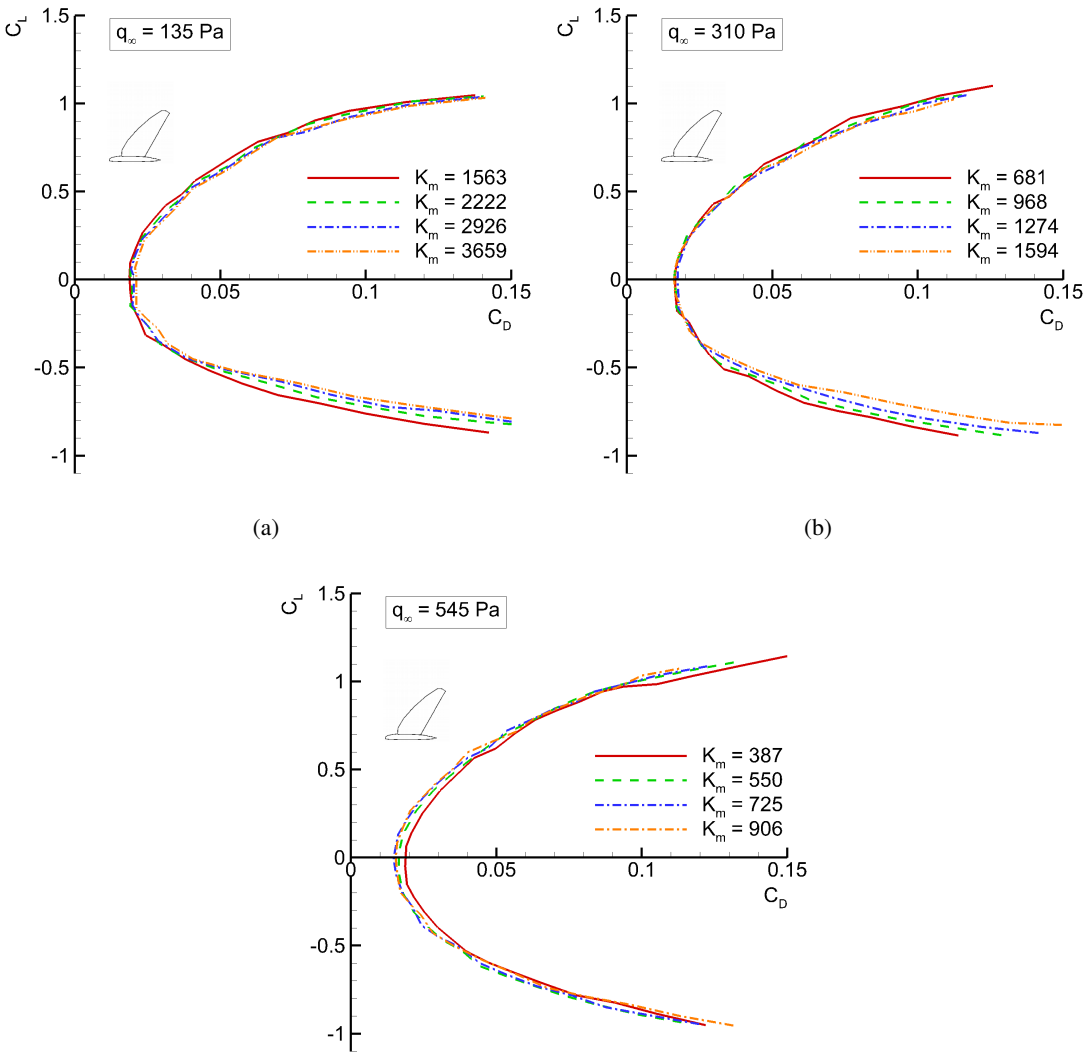

Figure 6.13: Effect of a variation of the pre-stress on the drag polars of the swept-back wing configuration.

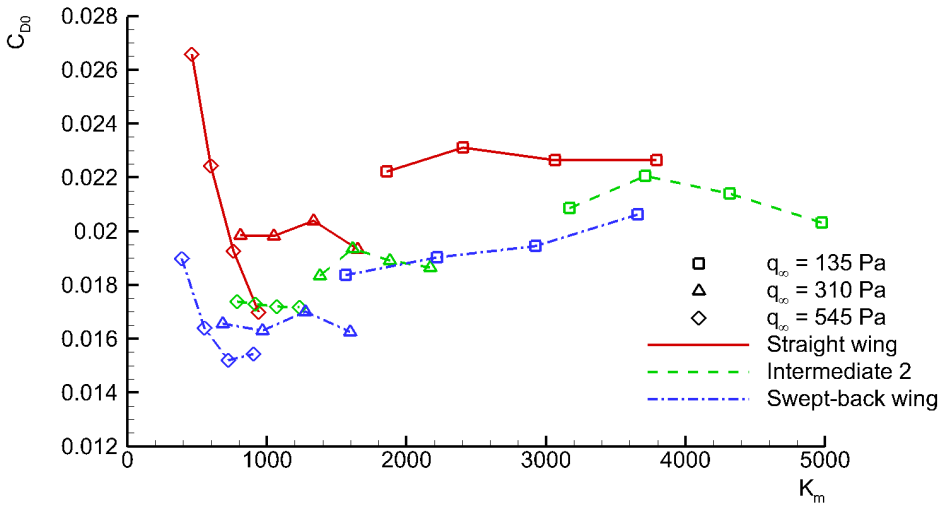

(a)

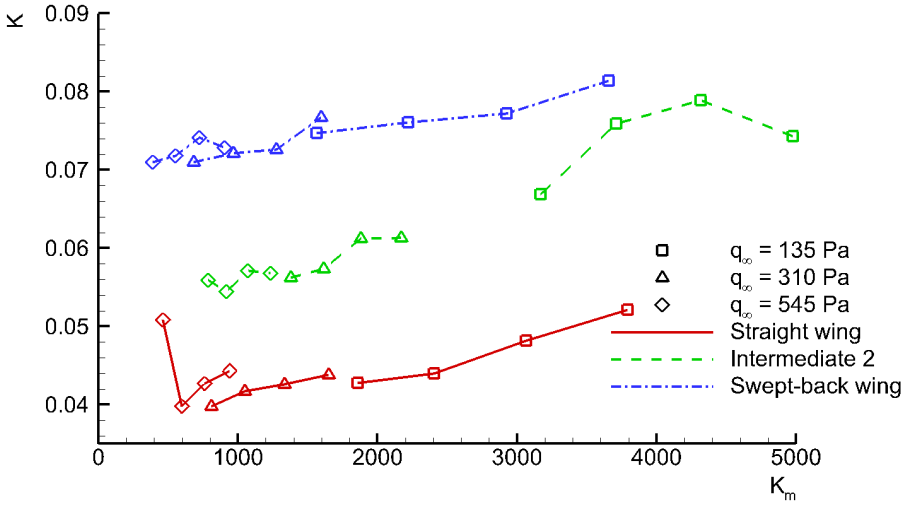

(b)

Figure 6.14: Synthesis of the drag characteristics in terms of the zero-lift drag coefficient (C_{D0}) and lift induced drag factor (K) as a function of the parameter K_m.

6.1.2.4 Lift-to-drag ratio

Figure 6.15 shows the effect of the pre-stress on the lift-to-drag ratio characteristics of the straight wing configuration at q_∞ = 135 Pa, q_∞ = 310 Pa, and at q_∞ = 545 Pa. At q_∞ = 135 Pa, the best aerodynamic efficiency is obtained with the lowest pre-stress (K_m = 1859). In this case, the increase in efficiency as the pre-stress decreases is due to an increase in lift and a decrease in drag as shown in the corresponding lift and drag polars (cf. Figs. 6.7a and 6.11a, respectively). In contrast, the best L/D characteristics at q_∞ = 545 Pa is obtained with the largest pre-stress (K_m = 939). In this case, a large pre-stress is advantageous to limit the deflection and avoid the drag increment coming along with excessively large cambers. At this flow condition, the higher efficiency is dominated by the reduction of the drag because the lift decreases with increasing pre-stress (cf. Figs. 6.7c and 6.11c). At q_∞ = 310 Pa, the effect of the pre-stress is not as clear as for the two other flow conditions. Similar maximum values of L/D are reached with all of the four pre-stress settings considered here. The lift-to-drag ratio characteristics of the intermediate 2 configuration are shown in Fig. 6.16. The impact of the pre-stress is smaller in this case according to the small variation in lift and drag discussed in Figs. 6.8 and 6.12. Finally, the lift-to-drag ratio characteristics of the swept-back wing are shown in Fig. 6.17. The global effect of the pre-stress in this case occurs in a similar manner than for the straight wing. Indeed, the largest lift-to-drag ratios at q_∞ = 135 Pa are obtained with the smallest pre-stress (K_m = 1563) and at q_∞ = 545 Pa, the best efficiency is obtained with a large pre-stress (K_m = 906).
A synthesis of the lift-to-drag ratio characteristics in terms of its maximum value, $(L/D)_{max}$, as a function of the parameter K_m is given in Fig. 6.18. With all three planform configurations, the largest values of $(L/D)_{max}$ occur at similar values of the parameter K_m. In the case of the straight wing, the maximum value of $(L/D)_{max}$ is equal to 18.1 and occurs around K_m = 900. With the intermediate 2 configuration, the maximum is equal to 17.2 and occurs at K_m = 1080. The maximum with the swept-back wing is 14.9 and occurs at K_m = 908. The values of $(L/D)_{max}$ reported here are relatively large considering the low Reynolds number at which the measurements were performed (cf. Table 2.5). Further, an univocal trend concerning the influence of the planform configuration on the values of $(L/D)_{max}$ can be recognized. The largest values of $(L/D)_{max}$ are obtained with the straight wing configuration, whereas the smallest occur in the case of the swept-back configuration. This agrees well with the trend expected from the variation of the aspect ratio. Finally, the results presented here indicate that a variation of the pre-stress can be effectively used to adjust the lift-to-drag ratio compared to the constant pre-stress case and to improve the flight performance such as range and endurance (cf. section 1.3.3).

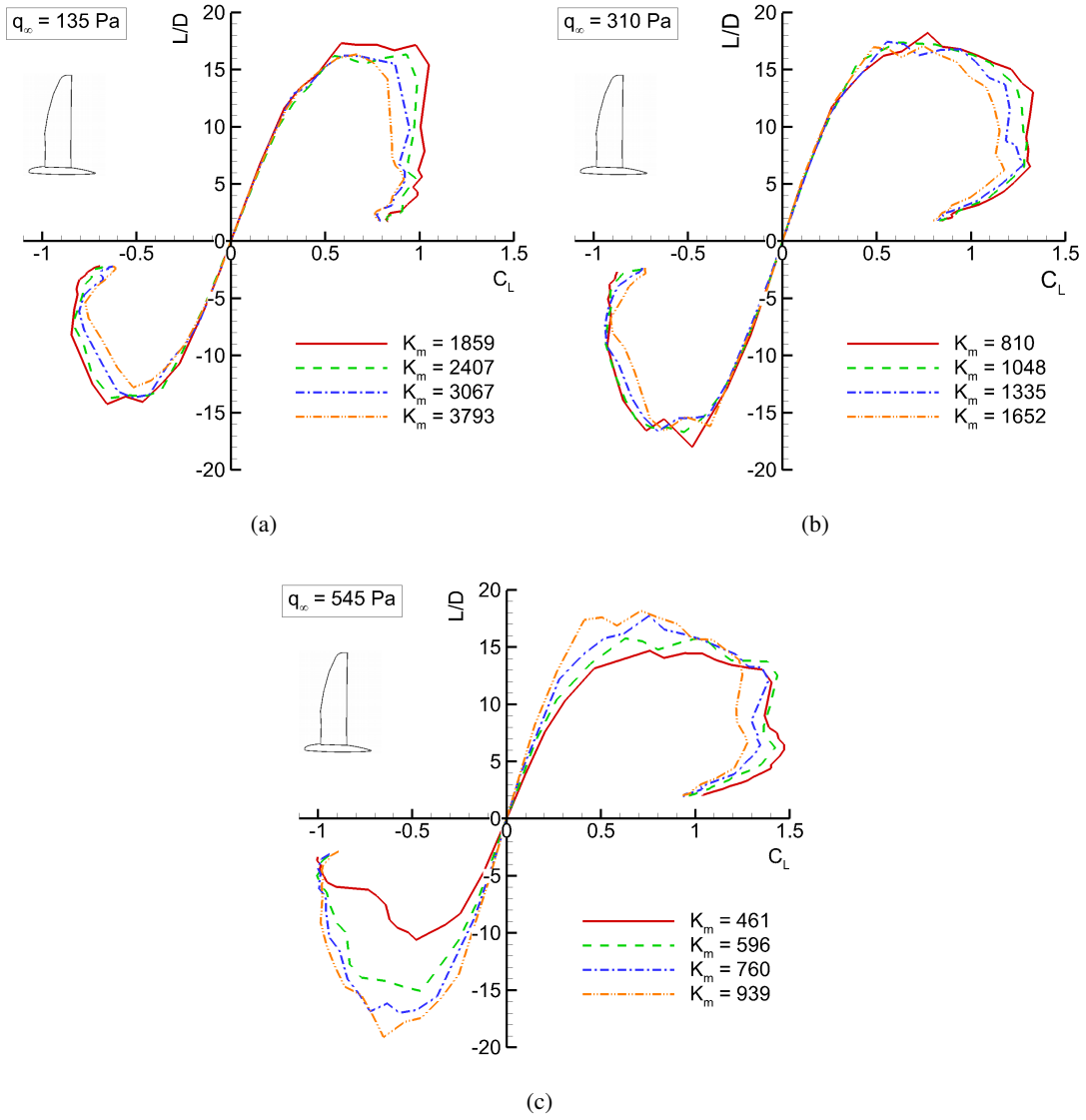

Figure 6.15: Effect of a variation of the pre-stress on the lift-to-drag ratio characteristics of the straight wing configuration.

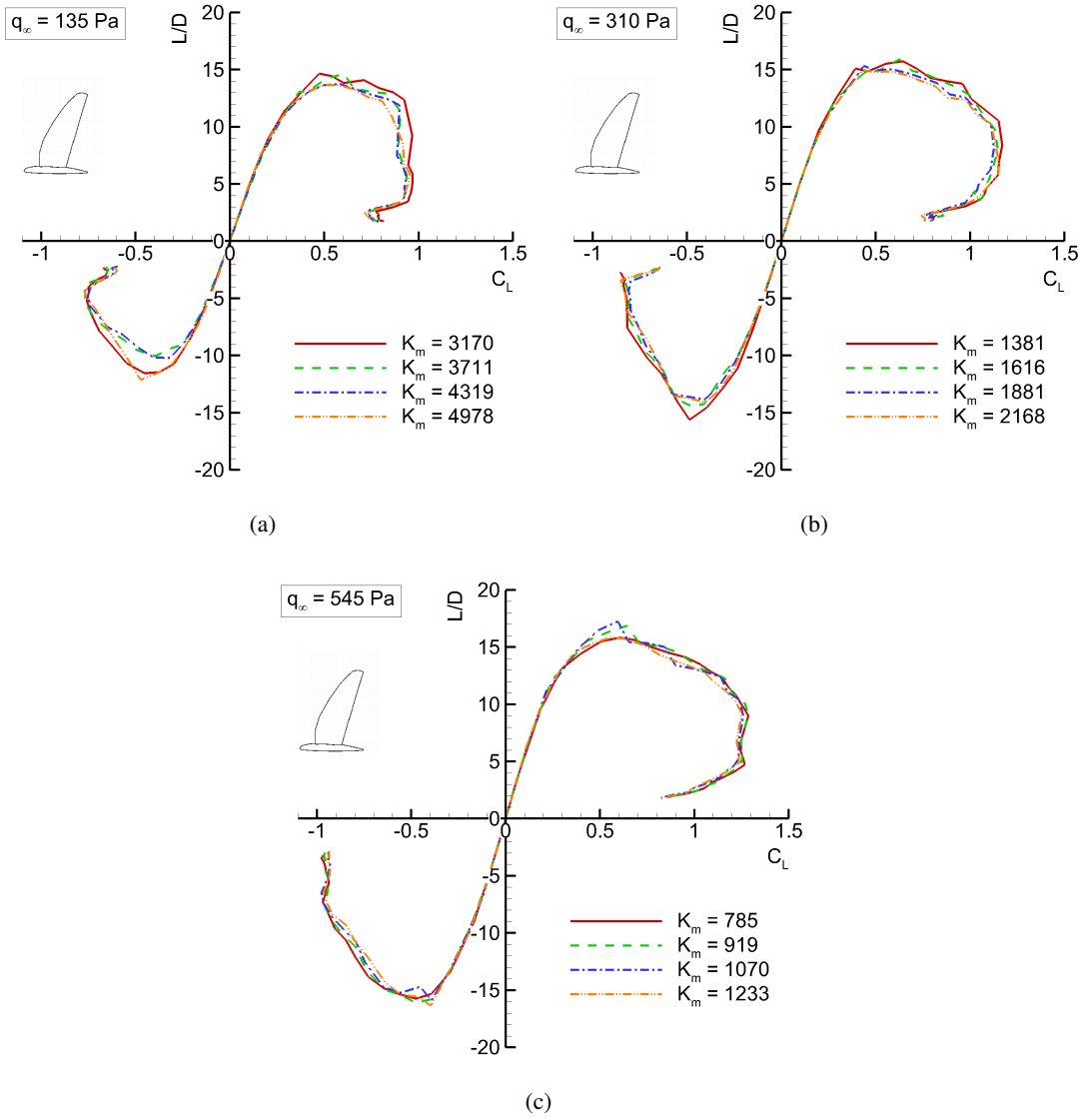

Figure 6.16: Effect of a variation of the pre-stress on the lift-to-drag ratio characteristics of the intermediate 2 configuration.

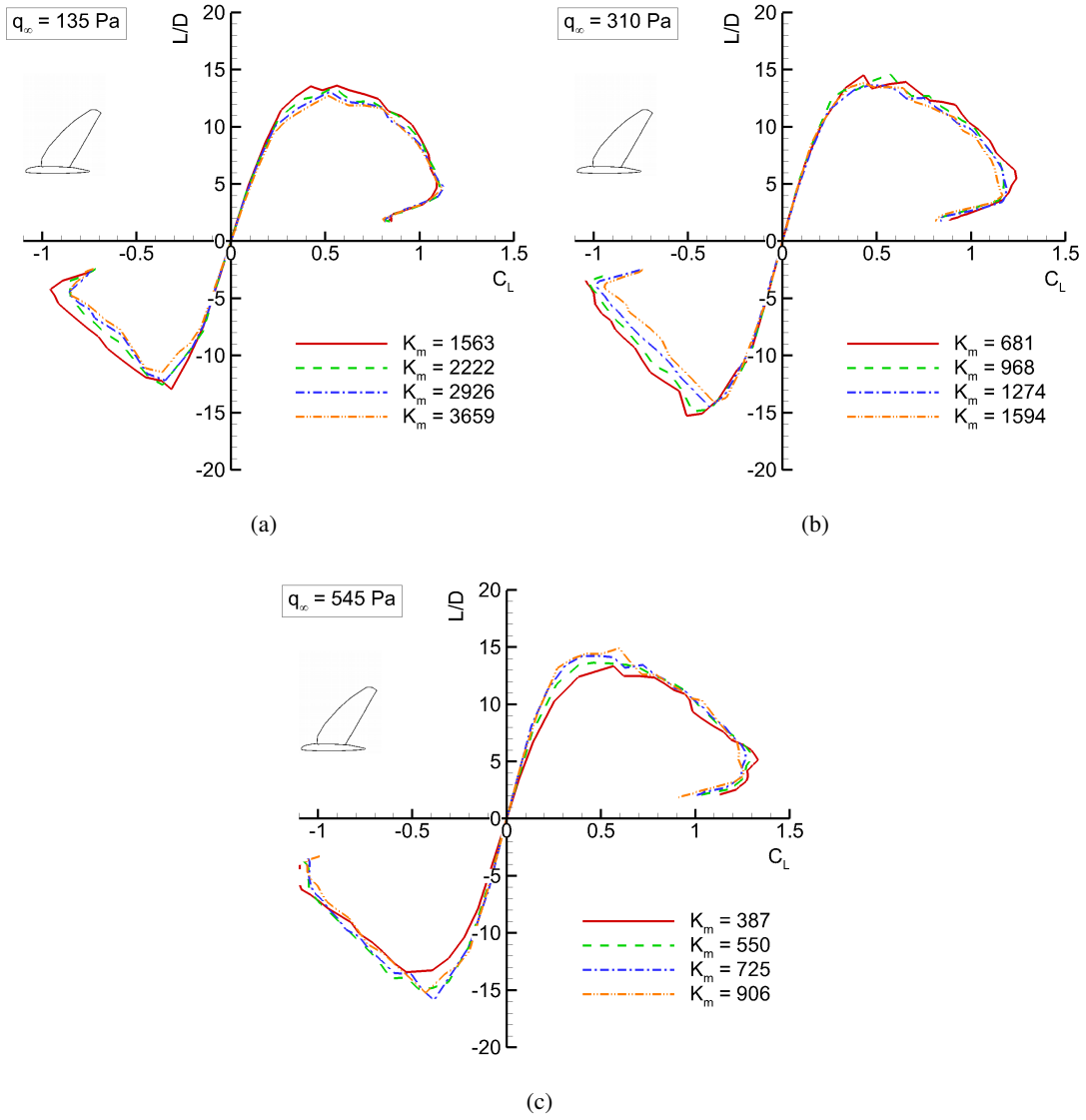

Figure 6.17: Effect of a variation of the pre-stress on the lift-to-drag ratio characteristics of the swept-back configuration.

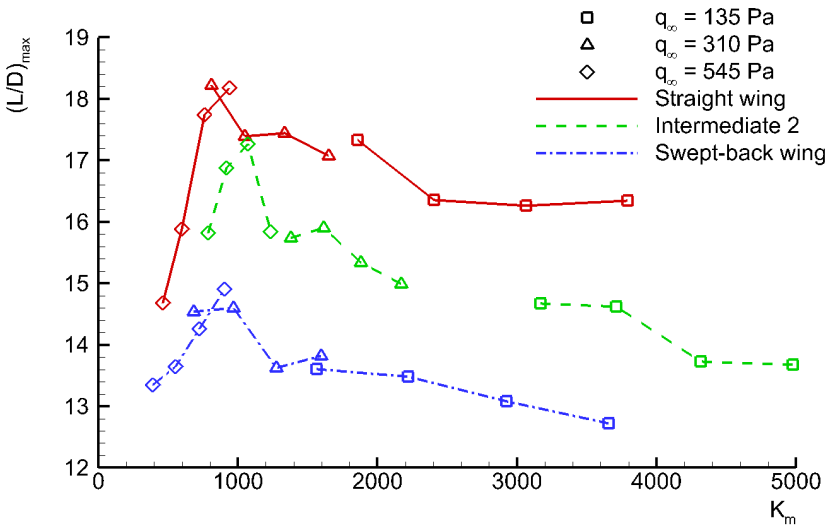

Figure 6.18: Synthesis of the lift-to-drag ratio characteristics in terms of the maximum lift-to-drag ratio ($(L/D)_{Lmax}$) as a function of the parameter K_m.

6.2 Modified membrane covers

The previous section showed that the deflection of the wing surface can be significantly influenced by a continuous adjustment of the membrane pre-stress. However, the high flexibility of the wing surface still leads to large deformations at large free-stream dynamic pressures. Here, the effect of structural modifications of the baseline membrane cover to increase its stiffness and limit the deformations is investigated. For this, the two alternative membrane covers presented in section 2.1.3.4 are tested on the straight wing configuration. In the following, the wing characteristics with the modified membranes are compared to the wing characteristics with the baseline membrane cover. For this, the results presented in chapter 4 (free transition case) are used.

6.2.1 Effect on the deflection of the wing surface

The markers for the deflection measurements were placed on the wing surface along six spanwise sections as indicated in Fig. 6.19. The sections 1, 3, and 5 are placed where the wing surface is modified, whereas the sections 2, 4, and 6 are placed in between. The section 3, which is placed around $2y/b = 0.3$, coincides with the single spanwise section measured on the wing with the baseline membrane cover presented in chapter 4. For this reason, the deflected wing shape corresponding to this spanwise position are focused on in the following.

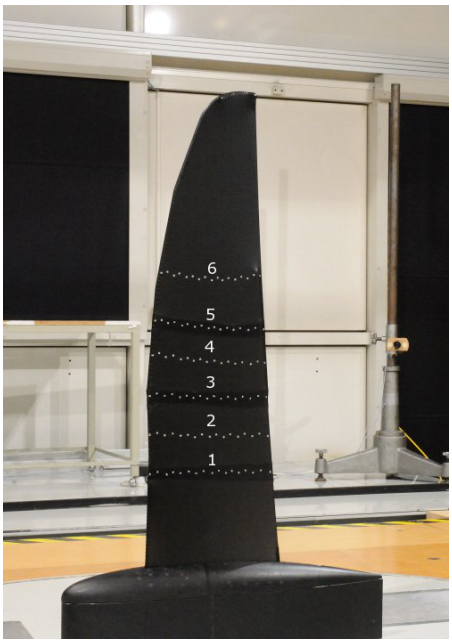

Figure 6.19: Position of the markers placed on the wing surface for the measurement of the deflected wing shapes.

Figure 6.20 shows the deflected wing shapes at $\alpha = 6^{\circ}$ obtained with the two modified membrane covers compared to the baseline case. The dynamic pressure dependency of the wing shape is considerably smaller with the modified membrane covers because the deflection at $q_\infty = 310$ Pa and $q_\infty = 545$ Pa is significantly smaller in the cases related to the strips and the battens. At q_∞

= 135 Pa, the upper side of the airfoil corresponding to the membrane cover with the battens has a positive camber. However, this is not due to the deflection of the membrane but due to the cambered shape of the battens (cf. section 2.1.3.4). This membrane cover experiences also the smallest deflection among the three designs considered here. In addition to this, the camber of the wing surface remains fairly the same at all dynamic pressures, whereas it significantly changes for the baseline case and for the strips case due to the flexibility of the wing surface. Therefore, using rigid battens is an effective mean to have a large control over the wing shape and provide the wing with a certain camber even at low free-stream dynamic pressures.
Figure 6.21 presents the deflected airfoil shapes measured at α = -6° to illustrate the behavior of the wing with the modified membrane covers at negative angles of attack. In the baseline case and in the strips case, both wing sides are deflected downwards. In contrast, the wing upper side of the membrane cover with the battens keeps a positive camber at all free-stream dynamic pressures due to the presence of the rigid batten. However, the wing lower side with the straight batten is significantly deflected downwards at q_∞ = 310 Pa and q_∞ = 545 Pa because the batten is not fixed to the wing structure but only attached to the membrane cover. The presence of the straight batten is clearly visible as suggested by the discontinuity in curvature around x/c = 0.2.
Figure 6.22 shows a synthesis of the relative camber of the wing section no. 3 corresponding to the different membrane designs as a function of the angle of attack at q_∞ = 135 Pa, q_∞ = 310 Pa, and q_∞ = 545 Pa. These diagrams illustrate well the large influence the membrane design has on the wing geometry. At q_∞ = 135 Pa, the camber remains positive over the whole range of angles of attack in all three cases, because the deflection of the wing lower side at negative angles of attack is too small to cause a negative camber. At α = 0°, the camber of the wing with the battens is slightly larger than in the two other cases due to the cambered battens used for the wing upper surface. Further, the dependency of the camber on the angle of attack is the smallest in the case of the cover with the battens according to the larger stiffness of the wing surface. It varies between f/c = 0.023 at α = -10° and f/c = 0.035 at α = 20°. In the two other cases, the dependency of the camber on α is slightly more pronounced according to the larger flexibility of the wing surface. At q_∞ = 310 Pa, the influence of the membrane design on the relative camber is much more pronounced. The baseline case shows overall the broadest range of cambers with values between f/c = -0.037 at α = -12° and f/c = 0.08 at α = 12°. Due to its larger stiffness, the wing with the strips exhibits a narrower range of cambers providing values between f/c = -0.022 at α = -10° and f/c = 0.063 at α = 18°. The camber corresponding to the membrane cover with the battens remains positive over the whole angle of attack range. It varies between f/c = 0.016 at α = -10° and f/c = 0.045 at α = 16°. At q_∞ = 545 Pa, the large hysteresis effect that occurs in the baseline case (as described in chapter 4) is not present with both modified membrane covers due to their larger stiffness. The relative camber corresponding to the membrane cover with the battens remains still positive over the whole range of angles of attack at this flow condition although it gets very small in the negative α-range (f/c = 0.005 at α = -8°). While the baseline case reaches very large cambers with values up to f/c = 0.12 at α = 10°, the increased membrane stiffness corresponding to the strips case allows keeping the camber below f/c = 0.1.

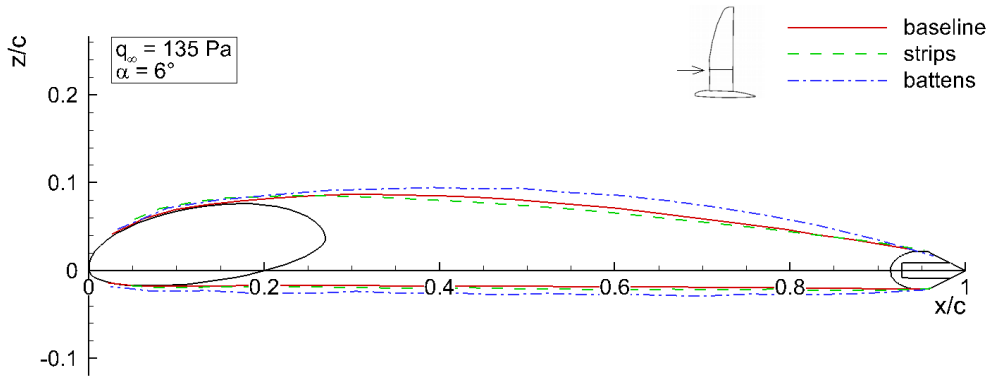

(a)

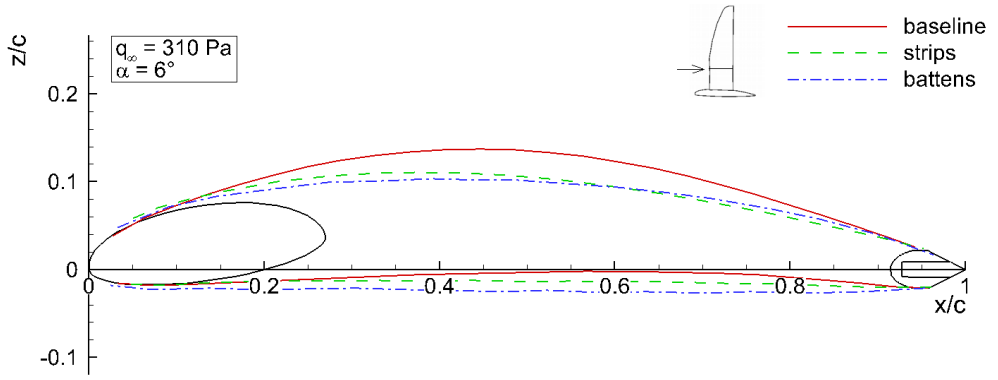

(b)

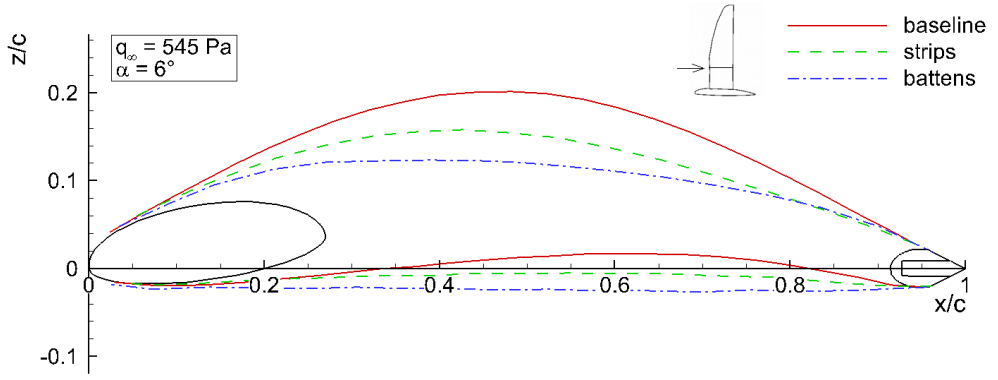

(c)

Figure 6.20: Deflected airfoil shapes at $\alpha = 6^{\circ}$ resulting from the different membrane covers (wing section no. 3 at $2y/b = 0.3$, statistically averaged from hundred instantaneous measurements).

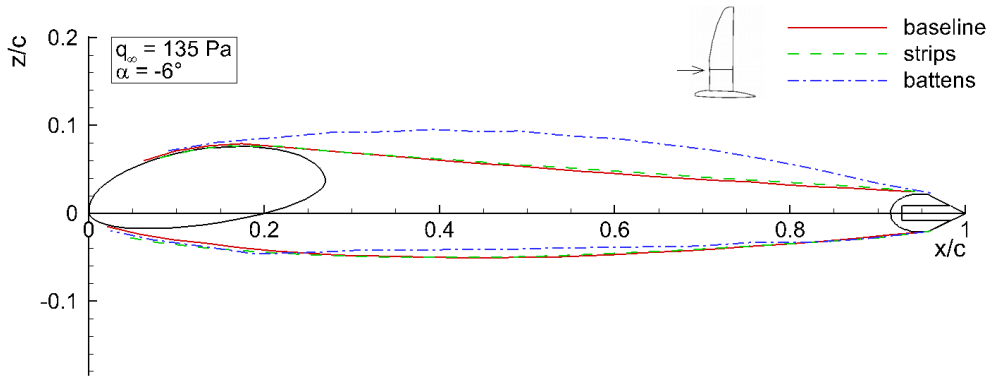

(a)

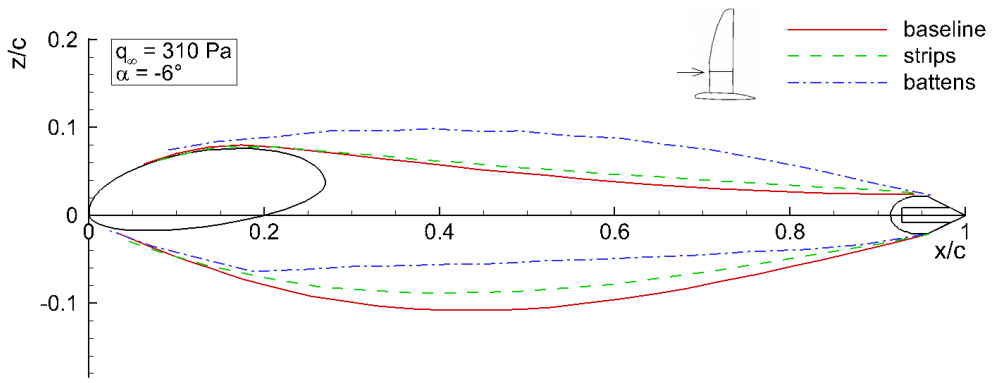

(b)

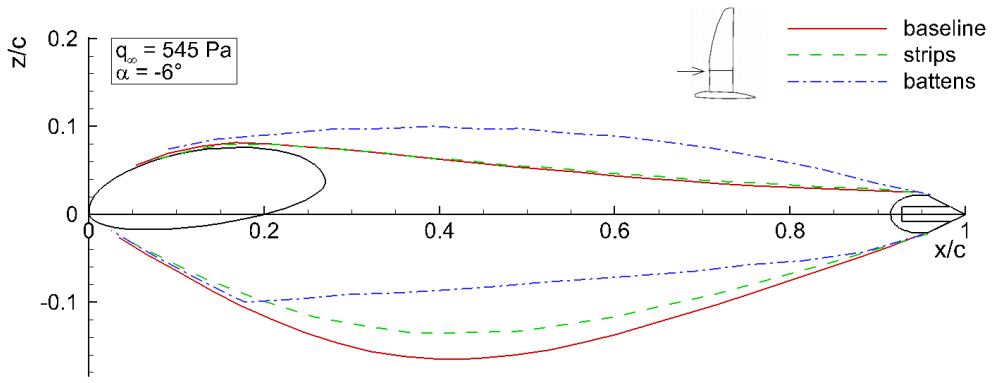

(c)

Figure 6.21: Deflected airfoil shapes at α = -6° resulting from the different membrane covers (wing section no. 3 at $2y/b = 0.3$, statistically averaged from hundred instantaneous measurements).

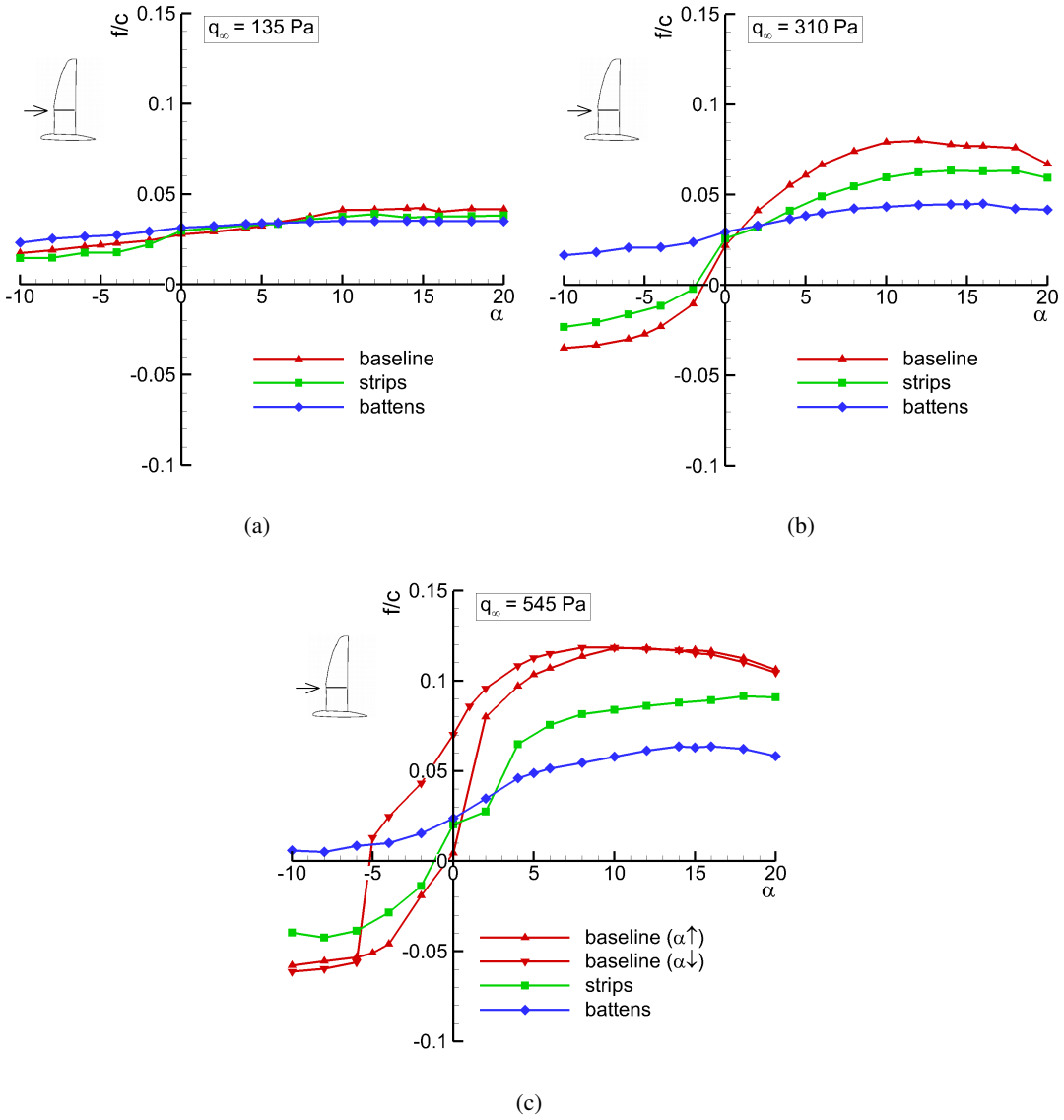

Figure 6.22: Relative camber at $2y/b = 0.3$ (airfoil section no. 3) as a function of the angle of attack and flow conditions.

In the following, the three-dimensional geometry of the wing surface reconstructed from the measurements of the wing sections no. 1 to 6 is analyzed to assess the influence of the local modifications of the membrane cover on the spanwise distribution of the deflection. Figure 6.23 shows the geometry of the wing upper side corresponding to the membrane cover with the strips measured at $\alpha = 10^{\circ}$. At $q_\infty = 135$ Pa and $q_\infty = 310$ Pa, the deflection of the membrane along the span is maximum at section no. 2 and decreases smoothly above and below this section. At $q_\infty = 545$ Pa, a different pattern occurs with several local maxima located at the sections no. 2, 4, and 6, i.e. between the sections where the membrane is modified. However, the differences are small and the wing surface remains fairly smooth along the span at all three flow conditions. Figure 6.24 presents the spanwise distribution of the relative camber corresponding to the different free-stream dynamic pressures. The maximum camber of the deflected wing occurs in section no. 2

($2y/b = 0.22$) at all flow conditions. Further, the camber distribution remains relatively smooth even if the membrane cover is modified only at discrete spanwise positions.

The deflected geometries of the wing upper surface in the case of the membrane cover with the battens measured at $\alpha = 10^{\circ}$ are shown in Fig. 6.25. At $q_\infty = 135$ Pa, the largest values of z are found at the sections no. 1, 3, and 5 where the cambered battens are placed. In between, z is smaller, indicating that the deflection of the membrane is smaller than the height of the cambered battens. At $q_\infty = 310$ Pa, the deflection of the membrane between the battens (sections no. 2, 4 and 6) has increased and a smoother wing surface results. At $q_\infty = 545$ Pa, a pattern opposite to the one occurring at $q_\infty = 135$ Pa occurs because the largest values of z are found at sections no. 2, 4, and 6, i.e. between the battens. In this case, the deflection of the membrane between the battens is larger than the height of the battens. However, the differences are small, which indicates that using battens at specific positions along the span already provides a large control on the geometry of the wing surface. The spanwise distribution of the relative camber as a function of the flow conditions is shown in Fig. 6.26. It is relatively smooth, except at $q_\infty = 545$ Pa where the larger deflection of the membrane between the battens (sections no. 2, 4, and 6) leads to larger relative camber than on the battens (sections no. 1, 3, and 5).

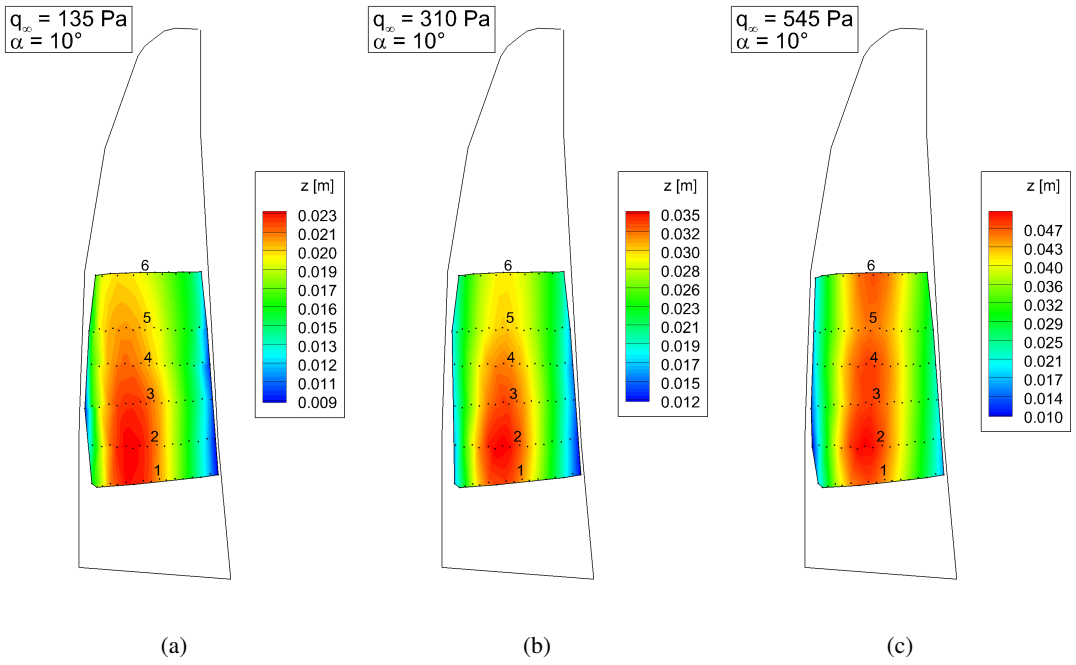

(a) (b) (c)

Figure 6.23: Contour plots showing the deflected geometries of the wing upper side in the case of the membrane cover with the strips.

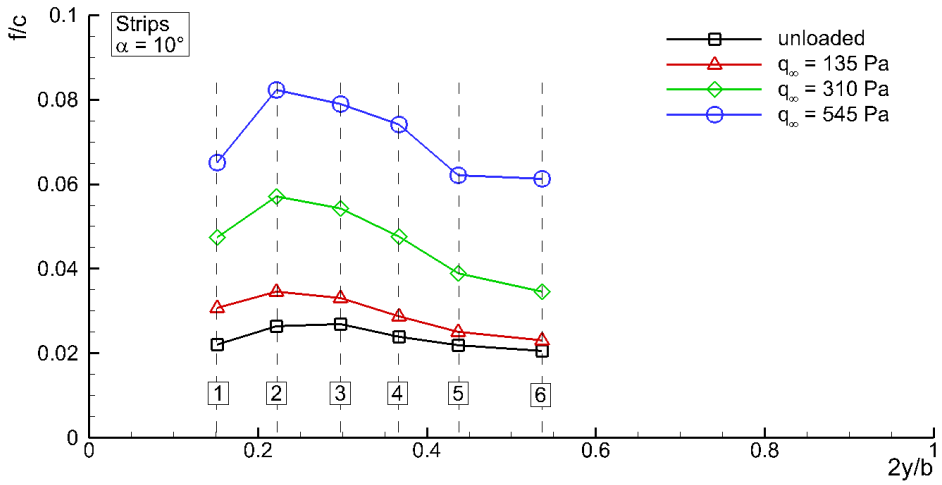

Figure 6.24: Spanwise distribution of the relative camber in the case of the membrane cover with the strips.

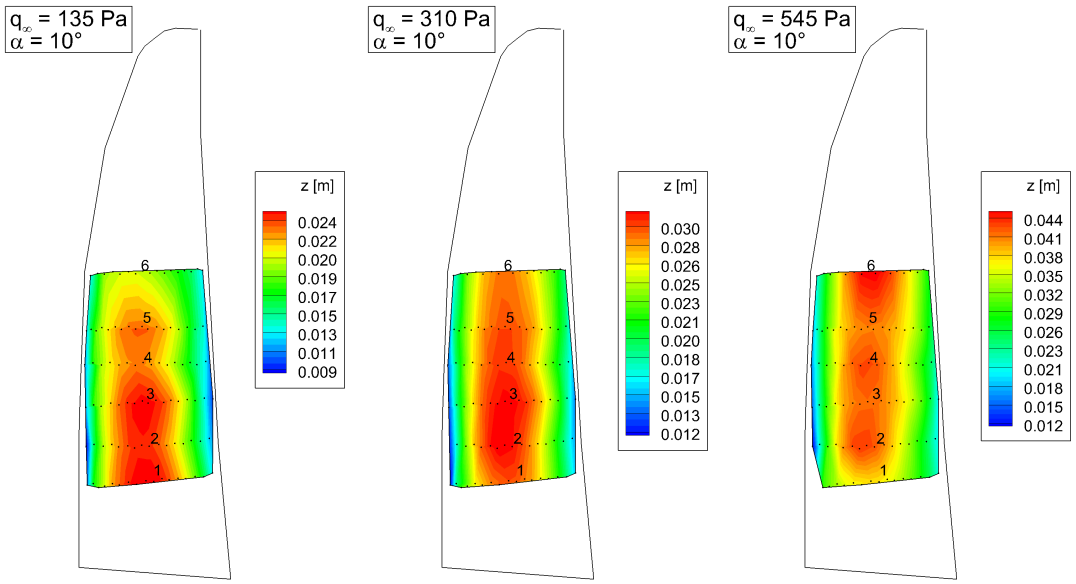

(a) (b) (c)

Figure 6.25: Contour plots showing the deflected geometries of the wing upper side in the case of the membrane cover with the battens.

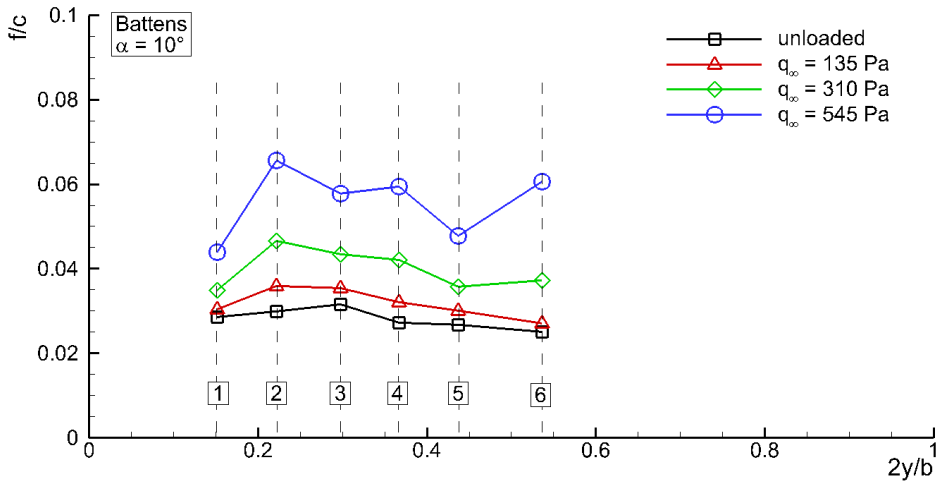

Figure 6.26: Spanwise distribution of the relative camber in the case of the membrane cover with the battens.

6.2.2 Effect on the aerodynamic characteristics

6.2.2.1 Lift polars

Figure 6.27 shows the lift polars corresponding to the different membrane designs at q_∞ = 135 Pa, q_∞ = 310 Pa, and q_∞ = 545 Pa. At q_∞ = 135 Pa, all three lift curves exhibit similar slopes which are moreover near to the theoretical prediction because the deformation at this flow condition is small and does not influence much the lift characteristics. As the free-stream dynamic pressure increases, significant differences occur. The slope of the lift curves corresponding to the baseline cover increases largely as a result of the large deformations. In contrast, the lift curves corresponding to the two modified membrane covers are less affected according to the increased membrane stiffness. Indeed, the two polars corresponding to the modified membrane covers remain near to the theoretical lift curve even at q_∞ = 545 Pa. This confirms the effectiveness of an increased membrane stiffness to limit the intensity of the passive dynamic pressure dependency of the aerodynamic characteristics. The wing can therefore operate at larger speeds before strong non-linearities occur. The wing with the battens produces also less negative lift at negative angles of attack compared to the two other cases because the camber remains positive over the whole angle of attack range (cf. Fig. 6.22). The hysteresis occurring at large free-stream dynamic pressure with the baseline case is completely eliminated with both modified membrane covers.

Concerning the stall behavior, the wing with the baseline membrane cover exhibits the largest maximum lift (C_{Lmax} = 1.02) and latest stall (α_{max} = 15°) at q_∞ = 135 Pa. At this flow condition, the wing with the strips stalls slightly earlier (α_{max} = 12°) but shows a similar maximum lift coefficient as the baseline case (C_{Lmax} = 1.01). The wing with the battens is the first to stall (α_{max} = 10°) and exhibits the smallest maximum lift with (C_{Lmax} = 0.925). At q_∞ = 310 Pa, the maximum lift is around 1.2 and occurs around α = 17° in all three cases. However, the onset of stall in the baseline case occurs much earlier. At q_∞ = 545 Pa, the baseline and the strips cases

exhibit similar maximum lift (C_{Lmax} = 1.27 at α_{max} = 19°). The wing with the battens at this flow condition exhibits a slightly smaller maximum lift (C_{Lmax} = 1.2) and stalls at α_{max} = 14° already.

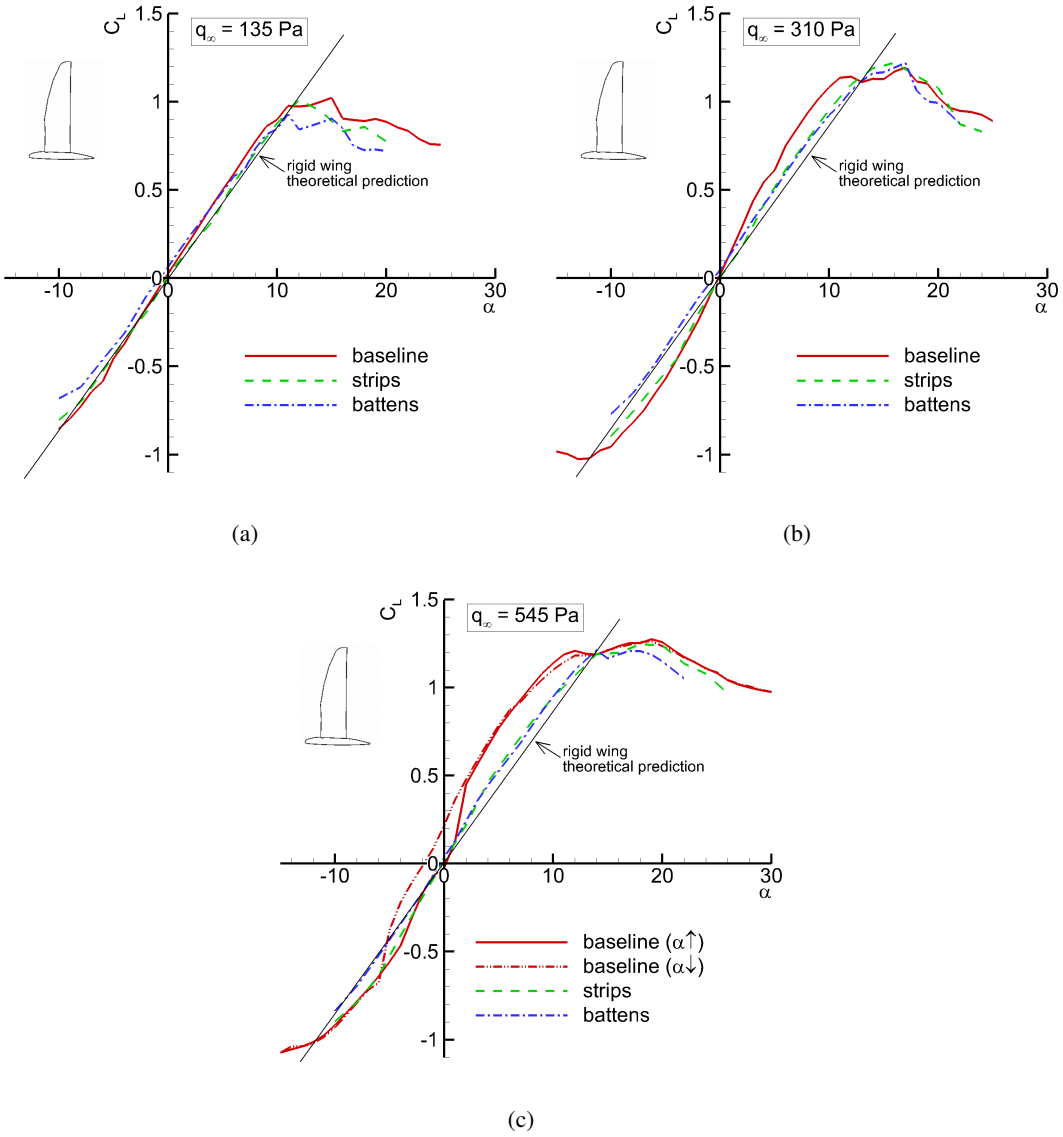

Figure 6.27: Comparison between the lift characteristics associated with the different membrane covers.

6.2.2.2 Drag polars

Figure 6.28 shows the drag polars corresponding to the three different membrane designs. At q_∞ = 135 Pa and q_∞ = 310 Pa, the baseline case exhibits the smallest drag over the whole range of lift coefficient. The wing with the battens shows the largest drag, especially in the negative range of lift coefficients. The reason for this is that the camber remains positive even at negative angles of attack as highlighted in Fig. 6.22, leading to larger drag compared to the negatively cambered airfoils occurring in the two other cases. At q_∞ = 545 Pa, there is less difference in the negative range of lift coefficients. At this flow condition, the largest drag in the positive range

of lift coefficients occurs in the case of the membrane cover with the strips. The difference in zero-lift drag between the α-increasing and α-decreasing polars corresponding to the baseline case was already explained in chapter 4.

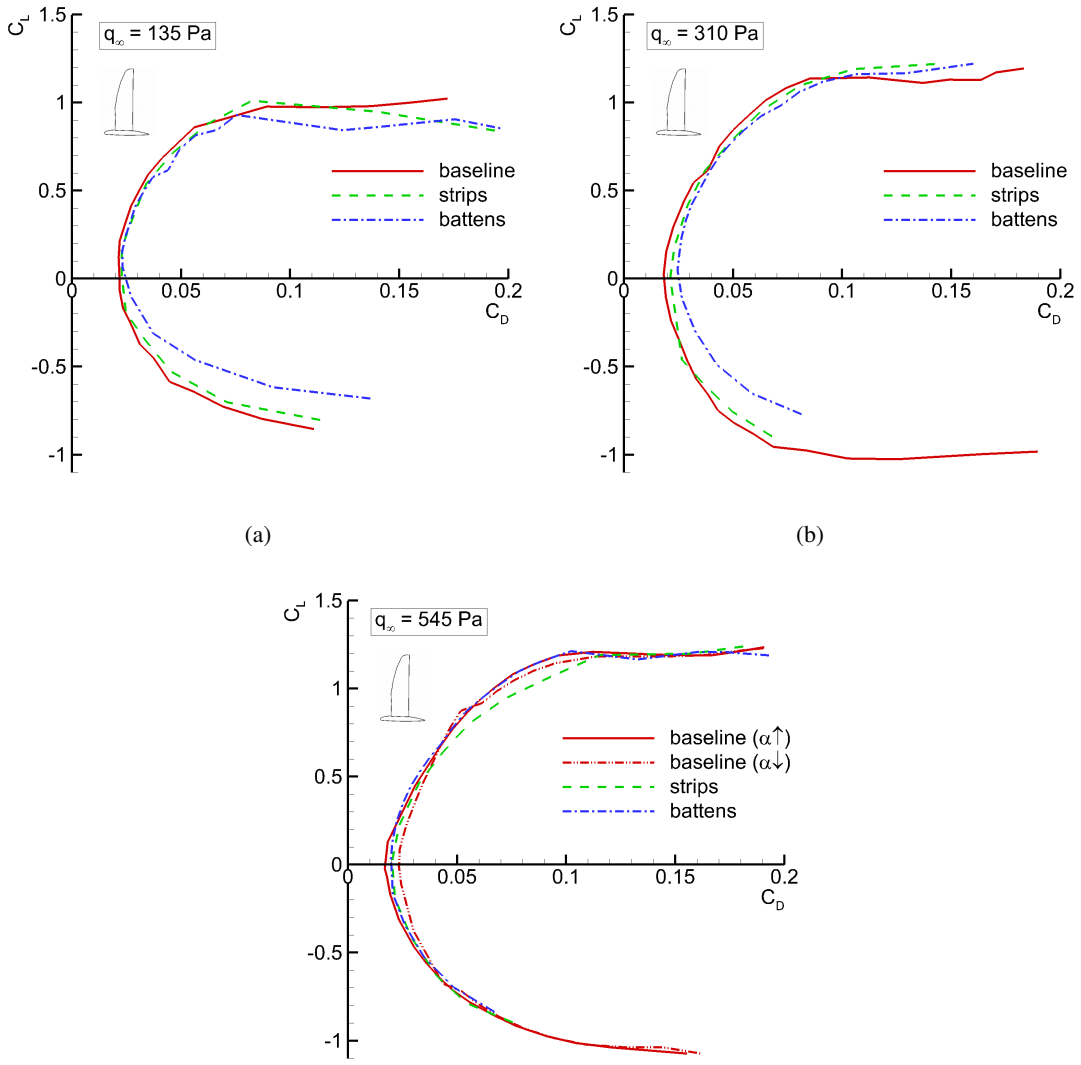

Figure 6.28: Comparison between the drag polars associated with the different membrane covers.

6.2.2.3 Lift-to-drag ratio

Figure 6.29 presents a comparison between the lift-to-drag ratio characteristics corresponding to the different membrane designs. At q_∞ = 135 Pa and q_∞ = 310 Pa, the best characteristics over the whole range of lift coefficients is obtained with the baseline model with a maximum lift-to-drag ratio of 16.9 at q_∞ = 135 Pa and 17.2 at q_∞ = 310 Pa. The superiority of the baseline cover is due to a smaller drag and a larger lift as shown in Figs. 6.27 and 6.28. The wing with the battens exhibits the smallest values of L/D over the whole range of lift coefficients. The

difference is especially pronounced in the negative range of lift coefficients, because the camber remains always positive with this cover design as shown in Fig. 6.28. At q_∞ = 545 Pa, the trend is mixed. For $C_L < 0.7$, the membrane cover with the battens offers the largest values of L/D because the battens prevent the occurrence of too large deflections. Above $C_L > 0.7$, the battens and the baseline cases have similar values of L/D and the membrane with the strips shows the smallest values of L/D over the whole range of positive lift coefficients.

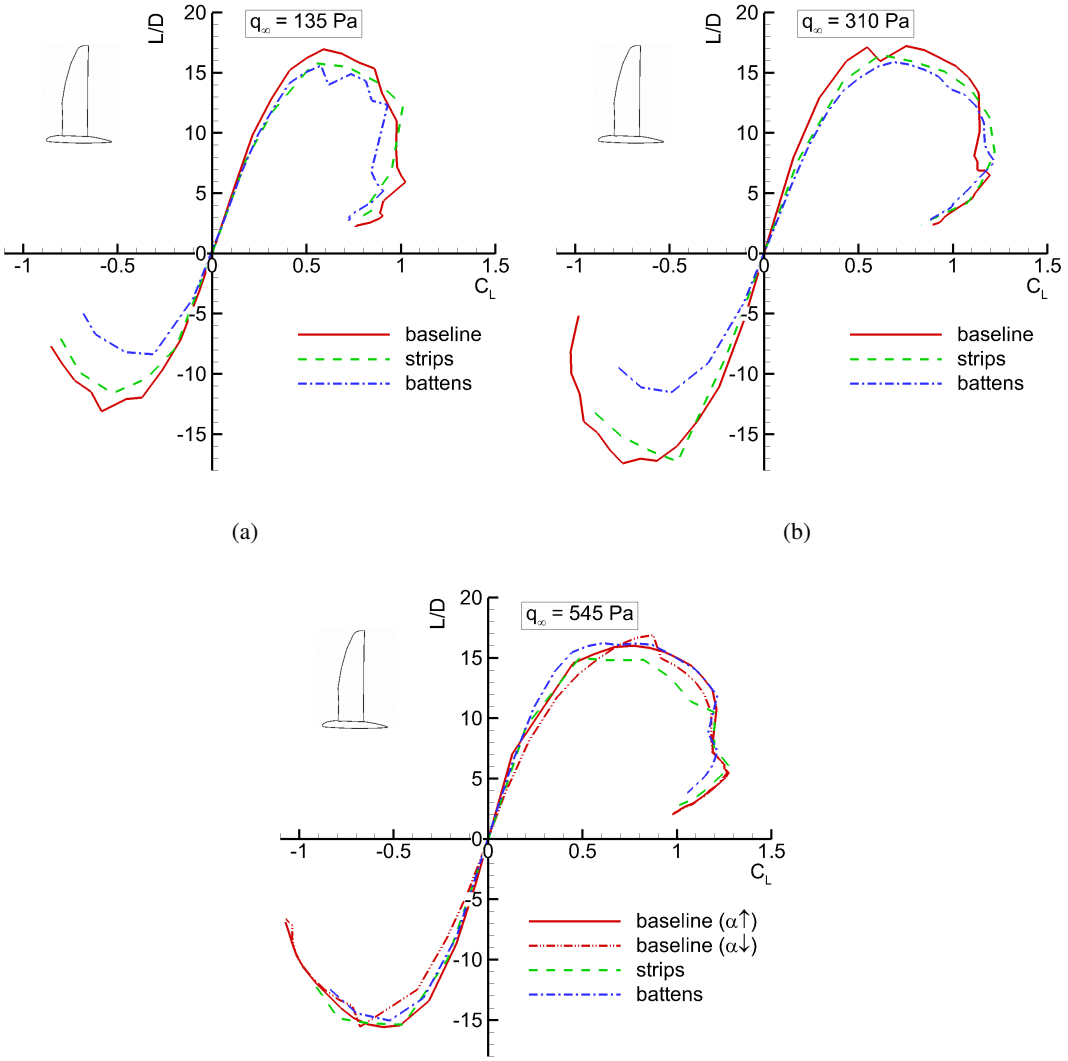

Figure 6.29: Comparison between the lift-to-drag ratio characteristics associated with the different membrane covers.

Although a significant reduction of the membrane deflection and a large effect on the lift characteristics was observed, none of the modified membrane covers considered here lead to a significant performance improvement in terms of lower drag and maximum lift compared to the baseline design. However, the alternative membrane designs tested here were not optimized to reach target performance values, but rather to assess the global effect of a modification of the

membrane design. The principal benefit shown at this stage is that using a stiffer membrane cover allows the wing to operate at larger dynamic pressures before very large deflection amplitudes occur. Also, using battens allows to provide the wing surface with a certain camber even at flow conditions where the aerodynamic load is too small to deflect the wing surface.

7 Conclusions and outlook

This work focuses on the investigation of an elasto-flexible morphing wing concept allowing large variation of the planform and airfoil geometry and destined for subsonic UAV application. Variable geometry wings are considered as having a great potential to provide aircraft with extended mission capabilities compared to conventional fixed wing configurations. Indeed, in-flight adaption of the wing shape to varying mission requirements is the only way to avoid performance drop at off-design conditions. The construction of the morphing wing concept studied in this work is biologically inspired. It consists of an articulated inner frame structure with an elasto-flexible membrane cover spanned on it forming the aerodynamic surface. The kinematics of the articulated structure allows the wing planform to be continuously changed between a straight wing configuration with a large aspect ratio and no sweep, and a swept-back wing configuration with a low aspect ratio and large sweep. The elastic membrane cover used for the wing surface naturally adapts to the changing planform shape and provides a seamless wing contour. However, the wing surface deflects when subjected to pressure loads. Therefore, the airfoil shape is not fixed in advance like a conventional rigid wing but depends on the flow conditions.

The investigations carried out in this work are based on a combination of wind tunnel tests and numerical simulations. An articulated semi-span model of the wing with a maximum span of one meter was developed for the experimental tests. The wing structure uses an asymmetric spar for the leading-edge to avoid sharp suction peaks and a telescopic spar for the trailing-edge which length adapts to the current planform shape. A stepper motor is used to actuate the structure and change the wing configuration. For the wing surface, a commercial off-the-shelf impermeable anisotropic elastic membrane is used. The basic design consists of a simple cover sewed out of the membrane material with a cut providing a certain amount of pre-stress when mounted on the articulated structure. However, the pre-tension can further be adjusted by moving the trailing-edge spar of the articulated frame structure via a linear screw guide at the wing root. In addition to this basic membrane cover, two other membrane covers were used to investigate the impact of specific structural modifications on the wing performance. The first one has an increased membrane thickness at specific locations along the span to increase the stiffness of the wing surface. The second one has rigid cambered battens attached to the wing surface, providing increased control over the airfoil shape. The experimental tests include force measurements, stereo particle image velocimetry, wool tuft surface flow visualizations, and surface deflection measurements with stereo-photogrammetry. The experiments were conducted in a low speed wind tunnel facility with an open test section at free-stream dynamic pressures ranging from 135 Pa to 545 Pa, corresponding to velocities between 15 m/s and 30

m/s and to mean chord based Reynolds numbers between 230000 and 600000. This range of flow conditions was determined under consideration of the deformation of the wing surface. The numerical investigations are based on a self-developed program implementing a non-linear analytical model of a two-dimensional elastic membrane airfoil coupled with the flow solver Xfoil. This program was used to analyze the aero-elastic behavior of membrane airfoils having a structure similar to a section of the wind tunnel model.

The detailed analysis of the deformation of the wing surface revealed how the camber and thickness of the wing depends on the flow conditions. The flow-structure interaction phenomena are strongly non-linear because the deformation and the aerodynamic load influence each other. The variation of the planform shape further increases the complexity of the interaction because it influences both, the membrane pre-stress and the aerodynamic load. As a result, the membrane deflection at equivalent flow conditions occurs with different amplitudes depending on the planform configuration. For a given wing planform, the free-stream dynamic pressure influences the overall amplitude of the deflection and thus, the wing camber. The angle of attack affects the remaining aspects of the airfoil geometry such as the sign of the camber and the location of the maximum camber along the chord. The pressure distribution deflects the membrane in such a way that the wing takes a positive camber at positive angles of attack and a negative camber at negative angles of attack. Around the zero-lift angle of attack, both wing sides are deflected in opposite directions resulting in fairly symmetric airfoil shapes. The deflection of the wing surface is found to be very stable in the attached flow regime. Significant vibrations of the membrane are only observed in the separated flow regime. The analysis of the membrane deformation during the increasing and the decreasing angle of attack slopes further revealed that, under certain conditions, the transition from a negative to a positive camber (and vice versa) can occur at a different angle of attack. The result is a pronounced hysteresis loop in the corresponding aerodynamic performance values. This phenomenon occurred only in cases where the ratio of the membrane pre-stress to the free-stream dynamic pressure was below 1000. Further, the deflection of the wing surface was found to be significantly influenced by the nature of the boundary layer. Experimental tests using a zig-zag tape placed at the leading-edge to force transition revealed that, at large dynamic pressures, the deflection is significantly smaller in the case of a fully turbulent boundary layer compared to the case where the boundary layer remains laminar over a larger portion of the wing. The detailed investigation of this phenomenon by means of numerical simulations indicated that this behavior is closely related to the fact that the natural transition, when the deflection is large, occurs in the rear part of the wing through a laminar separation bubble. The presence of this local flow separation delays the growth of the boundary layer, which is significantly thinner in the rear part of the airfoil compared to the fully turbulent case where it grows monotonically along the complete wing surface. Consequently, trailing-edge flow separation occurs earlier in the fully turbulent case, which in turn limits the pressure load on the wing surface and explained the smaller amplitude of the deflection.

According to the passive deformation of the wing surface, the aerodynamic characteristics of the wing show a pronounced dependency on the flow conditions. In particular, the lift curve slope increases and becomes non-linear with increasing free-stream dynamic pressure as a result of the varying camber. At the flow conditions where the deflection is large, the passive adaption of the wing surface to the separated flow leads to very smooth and delayed stall characteristics. As a result, the flexible wing surface acts like a natural flow control mechanism mitigating stall. Concerning the drag characteristics, both the zero-lift and the lift-dependent drag are found to decrease with increasing deformation except in the case where the deflection is excessively large because significant trailing-edge flow separation occurs at any angle of attack. This indicates that there is a flow condition at which the membrane reaches an optimal deformation state regarding the aerodynamic efficiency. Further, the comparison of the aerodynamic characteristics of five different wing configurations revealed that the basic effect of the planform shape on the aerodynamic characteristics is consistent with the theoretical expectations, although the behavior of the wing is strongly affected by the deformation of its surface. For instance, configurations with smaller aspect ratios are associated with smaller lift curve slopes, and configurations with larger sweep angles are associated with steeper pitching moment characteristics. The dynamic pressure dependency of the wing shape produces a global shift of the absolute performance values such as the slopes of the lift or pitching moment curves, but the general trend concerning the effect of the planform shape remains consistent at a given flow condition. Concerning the longitudinal stability, the aerodynamic center is found to move backwards with increasing membrane deformation as a result of the increasing angle of attack dependency of the camber. This indicates that the longitudinal stability of the wing increases with increasing free-stream dynamic pressure. The comparison of the drag polars associated with the different wing planforms confirmed the potential of a variation of the wing planform to increase the global aerodynamic efficiency compared to a fixed wing. In fact, the swept-back wing configuration, due to its small aspect ratio, exhibits a comparatively smaller drag in the lower range of lift coefficients. In contrast, the straight wing configuration, due to its large aspect ratio, shows a comparatively smaller drag in the upper range of lift coefficients. As a result, the maximum lift-to-drag ratios corresponding to these two configurations occur at distinct lift coefficients, and varying the wing planform can be effectively used to improve the overall aerodynamic efficiency depending on the required lift coefficient (i.e. flight conditions). However, the performance gain from planform morphing depends largely on the flow conditions due to the influence of the membrane deformation. All intermediate wing configurations exhibit aerodynamic characteristics which are fairly between the values associated with the straight wing and the swept-back wing. Therefore, they do not provide an own improvement potential in terms of drag. Further, an evaluation of flight performance criteria based on the experimentally obtained aerodynamic parameters revealed that the best performance in terms of minimum speed, maximum range, maximum endurance, and minimum turn radius is always obtained with the straight wing. The other configurations provide better performance only in terms of the maximum speed, which is the largest with the swept-back wing configuration.

The results of the investigations with modified membrane properties revealed that the wing characteristics can be effectively manipulated by changing the properties of the membrane cover. The variation of the membrane pre-stress is found to be an effective way to influence the passive deflection of the wing surface, allowing thus to adjust the wing camber within a certain range at a given flow condition. In particular, a low pre-stress enables more deflection and can be used to obtain a larger camber at low velocities. In contrast, a larger pre-stress is useful to limit the deflection at large free-stream dynamic pressures and prevent drag penalties associated with an excessive camber. The study of the lift and drag polars corresponding to different membrane pre-stress indicates further that an effective improvement of the lift-to-drag ratio characteristics can be reached compared to the case where the pre-stress is constant. The modified membrane cover with the increased stiffness showed a significant reduction of the deformation amplitude compared to the baseline design. Consequently, the passive dynamic pressure dependency of the wing shape and of the performance values is significantly reduced, too. Finally, the tests performed with the membrane cover containing the battens showed that this solution is the most effective one to limit the passive dependency of the wing shape and of the aerodynamic characteristics. In particular, the battens can be used to provide the wing surface with a certain camber even at flow conditions where the aerodynamic load is too small to deflect the wing surface. Although both modified membrane designs have a large impact on the behavior of the wing surface compared to the baseline case, none of them leads to an improvement of the aerodynamic performance in terms of maximum lift and minimum drag compared to the wing characteristics with the basic membrane cover. However, a significant benefit provided by the modified membrane covers is, that due to the larger stiffness of the wing surface, the wing can operate at much larger dynamic pressures before very large deformations of the wing surface and non-linearities in the aerodynamic performance values occur.

The experimental and numerical investigations carried out in this work allowed to gather a comprehensive database of the wing performance as a function of the wing configuration and membrane deformation over a range of flow conditions. In addition, a deep understanding of the aero-elastic phenomena involved could be gained, and critical design aspects and their effects on the performance could be identified. Based on these findings, further development of the aero-elasto-flexible morphing wing should concentrate on the optimization of the membrane cover. This includes the development of an advanced cover with optimized properties allowing the wing surface to deflect into a given shape at given flow conditions. For this, a membrane material with specific anisotropic characteristics customized for this application is required. The possibility to integrate actuators in the wing surface, e.g. actuated battens to regulate the wing camber or active elements for a local adjustment of the pre-tension, should also be investigated to provide extended control over the wing shape. Beside this, further aerodynamic investigations using a full-span model are needed to extend the aerodynamic database to the characteristics of the lateral motion. In particular, the potential of using asymmetric wing configurations and/or asymmetric membrane adaption for lateral control needs to be assessed. Aerodynamic investigations to assess the aero-elastic response of the wing in unsteady flow conditions would also be

an important aspect of future research. Eventually, the development of a flyable version of the wing should be considered to perform flight tests and to assess the potential of this wing under real conditions.

Bibliography

[1] T. Weisshaar, “Morphing Aircraft Systems: Historical Perspectives and Future Challenges”, *Journal of Aircraft*, Vol. 50, No. 2, 2013, pp. 337-353.

[2] S. Vasista, L. Tong, K. C. Wong, “Realization of Morphing Wings: A Multidisciplinary Challenge”, *Journal of Aircraft*, Vol. 49, No. 1, 2012, pp. 11-28.

[3] W. W. Gilbert, “Mission Adaptive Wing System for Tactical Aircraft”, *Journal of Aircraft*, Vol. 18, No. 7, 1981, pp. 597-602.

[4] S. B. Smith, D. W. Nelson, “Determination of the Aerodynamic Characteristics of the Mission Adaptive Wing”, *Journal of Aircraft*, Vol. 27, No. 11, 1990, pp. 950-958.

[5] R. Hardy, “AFTI/F-111 Mission Adaptive Wing Technology Demonstration Program”, *Aircraft Prototype and Technology Demonstrator Symposium*, 1983.

[6] R. W. Wlezien, G. C. Horner, A. R. McGowan, S. L. Padula, M. A. Scott, R. J. Silcox, J. O. Simpson, “The Aircraft Morphing Program”, *39th Structures, Structural Dynamics, and Materials Conference and Exhibit*, Apr. 20-23, 1998, Long Beach, Canada, AIAA 98-1927.

[7] A. R. McGowan, M. R. Waszak, “NASA’s Morphing Project Research Summaries in Fiscal Year 2002”, NASA/TM-2005-213266.

[8] D. L. Raney, R. C. Montgomery, L. L. Green, M. A. Park, “Flight Control using Distributed Shape-Change Effector Arrays”, *41th AIAA/ASME/ASCE/AHS/ASC Structures, Structural Dynamics, and Materials Conference and Exhibit*, Apr. 3-6, Atlanta, 2000, AIAA-2000-1560.

[9] D. L. Raney, R. H. Cabell, A. R. Sloan, W. G. Barnwell, S. T. Lion, B. A. Hautamaki, “Wind Tunnel Test of an RPV with Shape-Change Control Effector and Sensor Arrays”, *AIAA Guidance, Navigation, and Control Conference and Exhibit*, Aug. 16-19, Providence, Rhode Island, 2004, AIAA 2004-5114.

[10] A. R. McGowan, D. E. Cox, B. S. Lazos, M. R. Waszak, D. L. Raney, E. J. Siochi. P. S. Pao, “Biologically-Inspired Technologies in NASA’s Morphing Project”, *Proceedings of SPIE*, Vol. 5051, 2003.

[11] K. Richter, H. Rosemann, “Numerical Investigation on the Aerodynamic Effect of Mini-TEDs on the AWIATOR Aircraft at Cruise Conditions”, *25th Congress of the International Council of the Aeronautical Sciences*, Hamburg, Germany, Sept. 3-8, 2006, ICAS 2006-3.9.3.

[12] G. Dargel, H. Hansen, J. Wild, T. Streit, H. Rosemann, K. Richter, "Aerodynamische Flügelauslegung mit multifunktionalen Steuerflächen", *Proceedings of the German Aerospace Congress 2002*, Stuttgart, Germany, 2002, DGLR-2002-096.

[13] O. Criou, "A350 XWB family and technologies", *Presentation at Hamburg University of Applied Sciences*, Sept. 20, 2007.

[14] E. Pendelton, "Back to the Future - How Active Aero-elastic Wings are a Return to Aviations Beginnings and Small Step to Future Bird-like Wings", *RTO AVT Symposium on Active Technology for Enhanced Performance Operational Capabilities of Military Aircraft, Land Vehicles and Sea Vehicles*, Braunschweig, Germany, May 8-11, 2000.

[15] E. Pendelton, P. Flick, D. Paul, D. Voracek, E. Reichenbach, K. Griffin, "The X-53 a Summary of the Active Aeroelastic Wing Flight Research Program", *48th AIAA/ASME/ASCE/AHS/ASC Structures, Structural Dynamics, and Materials Conference*, Apr. 23-26, 2007, Honolulu, Hawaii, AIAA 2007-1855.

[16] R. Pecora, F. Amoroso, L. Lecce, "Effectiveness of Wing Twist Morphing in Roll Control", *Journal of Aircraft*, Vol. 49, No. 6, pp. 1666-1674, 2012.

[17] N. S. Khot, K. Appa, F. E. Eastep, "Optimization of Flexible Wing Without Ailerons for Rolling Maneuver", *Journal of Aircraft*, Vol. 37, No. 5, 2000, pp. 892-897.

[18] H. P. Monner, D. Sachau, E. Breitbach, "Design Aspects of the Elastic Trailing Edge for an Adaptive Wing", *RTO AVT Specialists' Meeting on Structural Aspects of Flexible Aircraft Control*, Ottawa, Canada, Oct. 18-20, 1999.

[19] F. Gandhi, P. Anusonti-Inthra, "Skin design studies for variable camber morphing airfoils", *Smart Materials and Structures*, Vol. 17, No. 1, 2008.

[20] C. Breitsamter, "Aerodynamic Efficiency of High Maneuverable Aircraft Applying Adaptive Trailing-Edge Section", *24th Congress of the International Council of the Aeronautical Sciences*, Yokohama, Japan, Aug. 29-Sept. 3, 2004, ICAS-2004-4-3-2.

[21] J. A. Hetrick, R. F. Osborn, S. Kota, P. M. Flick, D. B. Paul, "Flight Testing of Mission Adaptive Compliant Wing", *48th AIAA/ASME/ASCE/AHS/ASC Structure, Structural Dynamics, and Materials Conference and Exhibit*, Honolulu, Hawaii, Apr. 23-26, 20067, AIAA-2007-1709.

[22] C. Thill, J. Etches, I. Bond, K. Potter, P. Weaver, "Morphing Skins", *The Aeronautical Journal*, Vol. 112, No. 1129, 2008, pp. 117-139.

[23] A. R. Rodriguez, "Morphing Aircraft Technology Survey", *45th AIAA Aerodpace Sciences Meeting and Exhibit*, Reno, Nevada, Jan. 8-11, 2007, AIAA-2007-1258.

[24] D. Moorhouse, S. Sanders, M. von Spakovsky, J. Butt, "Benefits and Design Challenges of Adaptive Structures for Morphing Aircraft", *The Aeronautical Journal*, Paper No. 3012, 2006, pp. 157-162.

[25] J. Valasek, "Morphing Aerospace Vehicles and Structures", 1^{st} edition, Wiley, 2012.

[26] J. Bowman, B. Sanders, B. Cannon, J. Kudva, S. Joshi, T. Weisshaar, "Development of Next Generation Morphing Aircraft Structures", *48^{th} AIAA/ASME/ASCE/AHS/ASC Structure, Structural Dynamics, and Materials Conference and Exhibit*, Honolulu, Hawaii, Apr. 23-26, 2007, AIAA-2007-1730.

[27] J. S. Flanagan, R. C. Strutzenberg, R. B. Myers, J. E. Rodrian,, "Develpment and Flight Testing of a Morphing Aircraft, the NextGen MFX-1", *48^{th} AIAA/ASME/ASCE/AHS/ASC Structure, Structural Dynamics, and Materials Conference and Exhibit*, Honolulu, Hawaii, Apr. 23-26, 2007, AIAA-2007-1707.

[28] T. G., Ivanco, R. C. Scott, M. H. Love, S. Zink, T. A. Weisshaar, "Validation of the Lockheed Martin Morphing Concept with Wind Tunnel Testing", *48^{th} AIAA/ASME/ASCE/AHS/ASC Structure, Structural Dynamics, and Materials Conference and Exhibit*, Honolulu, Hawaii, Apr. 23-26, 2007, AIAA-2007-2235.

[29] M. Abdulrahim, "Flight Performance Characteristics of a Biologically Inspired Morphing Aircraft", *43^{rd} AIAA Aerospace Sciences Meeting and Exhibit*, Jan. 10-13, 2005, Reno, Nevada, AIAA-2005-345.

[30] D. T. Grant, M. Abdulrahim, R. Lind, "Flight Dynamics of a Morphing Aircraft Utilizing Multiple-Joint Wing Sweep", *AIAA Atmospheric Flight Mechanics Conference and Exhibit*, Aug. 21-24, 2006, Keystone, Colorado, AIAA-2006-6505.

[31] A. Song, X. Tian, E. Israeli, R. Galvano, K. Bishop, S. Swartz, K. Breuer, "Aeromechanics of Membrane Wings with Implications for Animal Flight", *AIAA Journal*, Vol. 46, No. 8, 2008, pp. 2096-2106.

[32] R. M. Waldmann, A. J. Song, D. K. Riskin, S. M. Swartz, K. S. Breuer, "Aerodynamic Behavior of Compliant Membranes as Related to Bat Flight", *38^{th} Fluid Mechanics Conference and Exhibit*, Jun. 23-26, 2008, Seattle, Washington, AIAA-2008-3716.

[33] H. Hu, M. Tamai, T. Murohy, T., "Flexible-Membrane Airfoils at Low Reynolds Numbers", *Journal of Aircraft*, Vol.45, No. 5, 2008, pp. 1767-1777.

[34] W. Shyy, F. Klevebring, M. Nilsson, J. Sloan, B. Caroll, C. Fuentes, "Rigid and Flexible Low Reynolds Number Airfoils", *Journal of Arcraft*, Vol. 36, No. 3, 1999, pp. 523-529.

[35] M. R. Waszak, J. B. Davidson, P. G. Ifju, "Simulation and Flight Control of an Aeroelastic Fixed Wing Micro Aerial Vehicle", *AIAA Atmospheric Flight Mechanics Conference*, Monterey, California, Aug. 5-8, 2002, AIAA-2002-4875.

[36] M. R. Hays, J. Morton, B. Dickinson, U. K. Chakravarty, W. S. Oates, "Aerodynamic control of micro air vehicle wings using electrostatic membranes", *Journal of Intelligent Material Systems ans Structures*, Vol. 23, No. 8, 2012.

[37] L. Yongsheng, W. Shyy, "Shape Optimization of a Membrane Wing for Micro Air Vehicles", *AIAA Journal*, Vol. 42, No. 2, 2004, pp. 424-426.

[38] L. Yongsheng, W. Shyy, "Laminar-Turbulent Transition of a Low Reynolds Number Rigid or Flexible Airfoil", *AIAA Journal*, Vol. 45, No. 7, 2007, pp. 1501-1513.

[39] M. D. Maughmer, "A Comparison of the Aerodynamic Characteristics of Eight Sailwing Airfoil Sections", Technical Report, Princeton University, 1979.

[40] M. P. Fink, "Full-scale Investigation of the Aerodynamic Characteristics of a Sailwing of Aspect Ratio 5.9", *Nasa Technical Note*, 1969, NASA TN D-5047.

[41] H. Muray, S. Maruyama, "Theoretical Investigation of the Aerodynamics of Double Membrane Sailwing Airfoil Sections", *Journal of Aircraft*, Vol. 17, No. 5, 1980, pp. 294-290.

[42] H. Muray, S. Maruyama, "Theoretical Investigation of Sailwing Airfoils Taking Account of Elasticities", *Journal of Aircraft*, Vol. 19, No. 5, 1982, pp. 385-389.

[43] K. Padian, J. Rayner, "The wings of pterosaurs", *American Journal of Science*, Vol. 293, 1993, pp. 91-166.

[44] M. T. Wilkinson, "Sailing the skies: the improbable aeronautical success of the pterosaurs", *The Journal of Experimental Biology*, No. 210, 2007, pp. 1663-1671.

[45] J. H. McMasters, "Aerodynamics of the Long Pterosaur Wing", Science, Vol. 191, No. 4230, 1976, pp. 898-899.

[46] J. D. Anderson, "Aircraft Performance and Design", 2^{nd} edition, McGraw-Hill International Editions, 1996.

[47] J. D. Anderson, "Fundamentals of Aerodynamics", 5^{th} edition, McGraw-Hill International Editions, 2010.

[48] W. F. Phillips, "Mechanics of Flight", 2^{nd} edition, Wiley, 2010.

[49] T. Hubel, "Untersuchungen zur Instationären Aerodynamik an einem Vogelähnlichen Flügelschlagmodell", Ph. D. Dissertation, Faculty of Biology, TU Darmstadt, 2006.

[50] J. Uhlemann, N. Stranghoener, H. Schmidt, K. Saxe, "Effects on Elastic Constants of Technical Membranes Applying the Evaluation Methods of MSAJ/M-02-1995", *Membranes 2011, International Conference on Textile Composite and Inflatable Structures*, Oct. 5-7, 2011, Barcelona, Spain.

[51] "ANSYS Mechanical APDL Operations Guide", Release 15, 2013.

[52] M. Raffel, C. E. Willert, S. T. Wereley, J. Kompenhans, "Particle Image Velocimetry", 2^{nd} edition, Springer, 2007.

[53] FlowManager, Software Package, Ver. 4.50, Dantec Dynamics.

[54] A. K. Martinov, “Practical Aerodynamics”, International Series of Monographies in Aeronautics and Astronautics, Division II: Aerodynamics, Vol. 4, Pergamon Press, 1965.

[55] T. Luhmann, S. Robson, S. Kyle, I. Harley, “Close Range Photogrammetry”, 1^{st} edition, Wittles Publishing, 2006.

[56] R. C. Pankhurst, D. W. Holder, “Wind-Tunnel Technique”, 1^{st} edition, Pitman press, Bath, 1952.

[57] M. Drela, H. Youngren, “Athena Vortex Lattice (AVL)”, Software Package, Version 3.15, http://web.mit.edu/drela/Public/web/avl.

[58] M. Drela, “XFOIL: An Analysis and Design System for Low Reynolds Number Airfoils”, Low Reynolds Number Aerodynamics, Lecture Notes in Engineering Vol. 54, 1989, pp. 1-12.

[59] M. Drela, M. B. Giles, “Viscous-Inviscid Analysis of Transonic and Low Reynolds Number Airfoils”, *AIAA Journal*, Vol. 25, No. 10, 1987, pp. 1347-1355.

[60] M. Drela, H. Youngren, “Xfoil”, Software Package, Version 6.97, http://web.mit.edu/drela/Public/web/xfoil.

[61] T. J. Mueller, “The Influence of Laminar Separation and Transition on Low Reynolds Number Airfoil Hysteresis”, *Journal of Aircraft*, Vol.22, No. 9, 1985, pp. 763-770.

[62] J. L. van Ingen, “The e^N method for transition prediction. Historical review of work at TU Delft”, *38^{th} Fluid Dynamics Conference and Exhibit*, Seattle, Washington, Jun. 23-26, 2008, AIAA-2008-3830.

[63] http://www.aer.mw.tum.de [cited May 2014]

[64] http://www.schoeller-textiles.com/eschler/technische-textilien.html [cited May 2014]

[65] C. Breitsamter, N. Adams, W. Wall, “Entwicklung und Analyse eines formadaptiven aeroelastoflexiblen Nurflüglers”, *Gemeinschaftsantrag des Lehrstuhls für Aerodynamik und des Lehrstuhls für Numerische Mechanik der TU München auf Gewährung einer Sachbeihilfe*, 2007.

[66] B. Béguin, C. Breitsamter, N. Adams, ”Aerodynamic Investigations on an Aeroelastoflexible Morphing Wing Configuration”, *27^{th} Congress of the International Council of the Aeronautical Sciences*, Nice, France, Sept. 19-24, 2010, ICAS 2010-2.10.4.

[67] B. Béguin, C. Breitsamter, N. Adams, “Aerodynamic Investigations of a Morphing Membrane Wing”, *AIAA Journal*, Vol. 50, No. 11, 2012, pp. 2588 - 2599.

[68] B. Béguin, C. Breitsamter, N. Adams, “Aerodynamic Analysis of an Elasto-flexible Morphing Wing Configuration”, *60. Deutscher Luft- und Raumfahrtkongress*, Sept. 27-29, 2011, Bremen, Germany.

[69] B. Béguin, C. Breitsamter, N. Adams, "Investigation of an Elastoflexible Morphing Wing Configuration", *Membrane 2011, International Conference on Textile Composites and Inflatable Structures*, Oct. 5-7, 2011, Barcelona, Spain.

[70] B. Béguin, C. Breitsamter, N. Adams, "Wake Measurements to Assess the Flow-Structure Interaction of an Elasto-Flexible Morphing Wing Configuration", *New Results in Numerical and Experimental Fluid Mechanics VIII*, NNFM 121, 2013, pp. 43-50.

[71] B. Béguin, C. Breitsamter, N. Adams, "Aerodynamic Optimization of a Morphing Membrane Wing", *28th Congress of the International Council of the Aeronautical Sciences*, Brisbane, Australia, Sept. 23-28, 2012, ICAS 2012-3.6.3.

[72] B. Béguin, C. Breitsamter, "Effects of Membrane Pre-stress on the Aerodynamic Characteristics of an Elasto-flexible Morphing Wing", *Aerospace Science and Technology*, Manuscript Ref. No. AESCTE-D-13-00351R1, accepted for publication May 2014.